ELEMENTAL AND STRUCTURAL BEHAVIORS OF BIMETALLIC NANOPARTICLES UNDER REACTIVE ENVIRONMENTS AND ITS IMPLICATION IN CATALYST DESIGN, PROCESSING, AND PERFORMANCE

BY

YUNG-TIN PAN

DISSERTATION

Submitted in partial fulfillment of the requirements
for the degree of Doctor of Philosophy in Chemical Engineering
in the Graduate College of the
University of Illinois at Urbana-Champaign, 2017

Urbana, Illinois

Doctoral Committee:

Professor Hong Yang, Chair
Professor Edmund G. Seebauer
Assistant Professor David W. Flaherty
Professor Jian-Min Zuo

Abstract

Bimetallic nanocatalyst often shows enhanced performance where the key lies not only on the overall composition but more importantly, is related to the specific atomic arrangement of the two metal elements on the and near surface regions. In order to make the most out of bimetallic nanocatalyst, it is important to understand how to control its near surface elemental arrangement as well as how it behaves under the complex reaction environments.

In this dissertation, the structural and elemental rearrangements of various bimetallic nanocatlyst were studied focusing on the processing and identifying the structure of a working catalyst. The first part emphasizes on how post-synthesis thermal process of bimetallic nanocatlyst for improved catalytic performance, which includes the thermally driven composition redistribution of Pt-Ni octahedral oxygen reduction reaction (ORR) nanocatalyst, the formation of Ag-Pt compositional intermetallics from alloy nanoparticles for formic acid oxidation (FAOR), and the regioselective atomic rearrangement of Ag-Pt octahedral catalysts by chemical vapor-assisted treatment. The second part is dedicated to identifying the actual structures of the bimetallic nanocatalysts under reaction conditions and how it affects performance, with more emphasis on product selectivity. The two model systems are metal-on-metal Rh-on-Pd for CO_2 hydrogenation and Cu@CuAg nanocatalyst for propylene epoxidation.

Environmental transmission electron microscopy was utilized in most of the projects mentioned above and provided critical information with high spatial resolution in realtime. The in situ microscopic observations showes good correlation with ex situ microscoscopic, surface sensitive spectroscopic, electrochemical, and chromotagraphic analysis as well as densitiy functional theory (DFT) calculations.

The discovery in this dissertation indicates how the multiple governing factors

determines the restructuring of different bimetallic nanocatalyst under various reactive thermal-chemical environments. It provides insights not just in the synthesis and processing of bimetallic nanocatalysts but also on the design of reaction conditions for the optimum working structure that leads to the best performance.

Acknowledgments

First of all, I would like to thank my research advisor, Professor Hong Yang, for his wholehearted support and patient guidance during my Ph.D. study. Prof. Yang and I joined UIUC in the same year. I can still recall those days clearly when we worked together very diligently to set up the lab space from scratch and when we took turns to drive to Rochester for valuable instrumentations in his previous lab. I remember how both of us suffered from my overly broad interest in everything but lacking focus on in-depth investigation in any one of them. However, with the tremendous amount of support and the opportunities I have received from him, I believe I have improved and become a more independent researcher. Prof. Yang is not only my academic adviser, but also given me the warmth of a family with his considering attention to my physical and mental wellbeing, as well as ensuring my success in the future. If there is anything that I can say to express my deepest gratitude to Prof. Yang, it would be this saying in Chinese: 一日為師，終身為父。

I would like to thank my committee members, Prof. Edmund Seebauer, Prof. David W. Flaherty, and Prof. Jian-Min Zuo, for their dedicated service, great suggestions, and generosity with their precious time.

I would like to thank the Ministry of Education of Taiwan for granting me the Governmental Scholarship for Overseas Study (GSOS) which initiated my Ph.D. era and financially supported me during the first three years of my graduate study. I would like to thank the Dow Chemical Company for their financial support during my fourth and fifth year of graduate study and I would like to thank the Graduate College of University of Illinois at Urbana-Champaign for granting me with the “Dissertation Completion Fellowship” to finish up

my dissertation.

I spent a wonderful time in Prof. Yang's group with a team of excellent, intelligent, passionate people. I would like to thank my lab mates, Dr. Jianbo Wu, Dr. Xi Yin, Dr. Jaemin Kim, Dr. Na Zhang, Steven Warren, Kai-Chieh Tsao, Yuqi Yan, Thao Ngo, Pei-Chieh Shih, Dr. Qiang Wang, Dr. Shaohua Fang, Dr. Baoliang Lyu, Dr. Panpan Li, Dr. Wei Zhou, Dr. Tao Yang, Kam Sang Kwok, Adam Dornford, Lingqing Yan, Yayuan Liu, and Wenjin Zhu for their great help and friendship.

I want to thank my wonderful collaborators in the Kong research group, especially Dr. Cartney Smith and Jinrong Chen for their input in the study of Pd nanosheets for cancer cell treatments. I want to thank my fabulous collaborators in the Zuo research group who educated me enormously on the knowledges of electron microscopy. I would like to thank Yu-Tsun Shao for his effort in the atomic scale characterization using the high angle annular dark field scanning transmission electron microscopy. I would like to thank Dr. Wenpei Gao and Dr. Honggyu Kim for their tremendous contribution in setting up the environmental TEM and gas handling system. I would like to thank Dr. Wenpei Gao again for his training and mentoring on the environmental TEM.

I also want to thank the wonderful people I met at UIUC. I am grateful to our staff at the School of Chemical Sciences and the Materials Research Laboratory for their assistance during my PhD research. In particular, I would like to thank Dr. Danielle L. Gray, Dr. Jeffery Bertke, Dr. Richard Haasch, Dr. Julio Soares, Dr. James Mabon, Dr. Honghui Zhou, Dr. Changqiang Chen, and Dr. Wacek Swiech for their great assistance and helpful discussion. I would like to express my gratitude to Professor Hyun Joon Kong and David W. Flaherty for their great help and advice. I would also like to thank my friends in the TSA badminton club, the UIPO, and the Champaign

Grilled Chicken Club. I would also like to thank my girlfriend – Yi-Hung Ma for her unconditional support during my graduate study.

Finally, I would like to express my heartfelt gratitude to my parents, which are both UIUC alumni, for their unconditional love and support in my life. I would like to thank my grandparents who supported my father's education regardless of the financial difficulties back then. I could not have been who I am without their visionary actions. I would like to thank my family and friends who have been very supportive during my graduate study. I wouldn't have made it this far without your warmhearted encouragements.

Table of Contents

Chapter 1

Introduction to Elemental Rearrangements in Bimetallic Nanoparticle Catalyst

1.1 Introduction

Bimetallic nanocatalyst is now widely utilized in thermal,[1] photo,[2] and electrochemical[3] reaction systems due to their proven improved activity as well as selectivity, when compared to their monometallic counterparts. Based on the spatial distribution of two metal atoms, bimetallic nanoparticles can be synthesized into a wide variety of different structures, such as, random alloy, intermetallic, core-shell, and other complex forms. It is well known that for bimetallic nanocatalyst, the structure and composition of surface and subsurface layers greatly affect its electronic property and hence catalytic activity. For example, Pt shell on Ru core (Ru@Pt) was shown to be very active for preferential oxidation of CO over H_2 at low temperature compared to other types of arrangements.[1] For oxygen reduction reaction (ORR), the most active Pt-Ni bimetallic catalyst has been reported to be the {111} surface with a composition of Pt_3Ni. Octahedral shaped Pt_3Ni nanocrystals turn out to be the most active form of nanoparticles.[3] There is a clear need for such kind of precision in the design and synthesis of bimetallic nanocatalyst with controlled size and structure. However, the structure and composition are often dependent on each other in the synthesis of bimetallic nanoparticles.[4] For example, in the synthesis of Pt-Ni nanoparticles using carbon monoxide as the reducing agent through the GRAILS method, the geometry of the synthesized nanocrystal strongly depends on the feeding Pt/Ni ratio. Formation of nanocubes dominates with pure Pt feed and nano octahedra become the main product under the addition of Ni precursors.[5] Another example of composition dependent morphology lies in

the synthesis of Ag-Pt bimetallic nanoparticles, where a Ag rich feed favored the formation of nanospheres and Pt rich feed favored the formation of warm like nanostructures.[6] In addition to geometry, surface composition of these as-made nanocatalyst is determined by either kinetically, *i.e.*, reaction/deposition rate of precursor molecules, or thermodynamically by approaching the configuration with a minimum surface energy. It is due to this lack of flexibility in controlling over surface composition that the shaped bimetallic nanocatalyst often shows unexpected low performance.[7]

Fortunately, the surface composition of bimetallic catalyst can be modified via post-synthesis processes, such as treatments under thermal-chemical and electrochemical environments. Some of the early work in this area was performed using the in-situ ambient pressure X-ray photoelectron spectroscopy (APXPS) to study the composition and valence states of surface and near surface elements of bimetallic nanoparticles under gaseous environments. The metallic elements that have been studied by this technique ranges from noble metal (Au, Ag, Pt, Pd), to precious metal (Rh, Ru), and to other transition metals (Cu, Ni, Co).[8-16] In certian bimetallic combinations, such as RhPd, the surface composition is extremely responsive to the gas environment in a reversible way where the surface is dominated with RhO_x species under oxidizing gas and became metallic with an equivalent amount of Rh and Pd under reducing atmosphere.[17] Such kind of dynamic response reveals that the working state of a bimetallic nanocatalyst might be far from the as-prepared state which, at first sight, seems to be detrimental to "rationally-designed" bimetallic catalyst. One can however, take advantage of this phenomenon to design post-synthesis thermal processes under desired conditions in order to adjusting the structure of bimetallic nanocatalyst for preferred reaction systems, *i.e.*, photo or electrochemical systems, or reactions where the catalysts are utilized at mild conditions.

In addition to spectroscopy based techniques, in situ environmental transmission electron microscopy (ETEM), a technique with much higher spatial resolution, has widely been utilized to study the working state of nano-catalyst under reaction atmospheres. Gaseous species such as CO, H_2, O_2, and methane (CH_4) have been introduced into the specimen area to directly observe the dynamic response of catalyst particles under working conditions. With such kind of capability, researchers are now able to observe the dynamic response of morphology and composition of bimetallic nanocatalyst in situ with atomic scale details.[18-25]

In the following sections, I will provide an overview on the research development regarding the structure and compositional behaviors of bimetallic nanocatalysts under reactive environments. The principles behind thermal and gaseous environment driven reconstruction will be first introduced, followed by a review on the utilization of in situ TEM for bimetallic nanoparticle research. Finally I will present the aim and overview of my thesis work.

1.2 Factors Governing the Restructuring of Bimetallic Nanocatalyst

Restructuring of bimetallic nanocatalyst is a complex process which can be affected by various factors. It not only shares identical behaviors as monometallic nanocatalyst, *i.e.*, sintering, but also exhibits intricate composition distribution due the additional metallic species introduced. In this section, the major governing factors will be discussed. Although the discussions are discrete, it should be noted that the surface composition and atomic arrangement of bimetallic nanocatalyst are determined simultaneously by multiple factors described below.

1.2.1 Inhomogeneous composition distribution and solid state diffusion

Bimetallic nanocatalyst can possess a wide variety of different structures. Depending on their elemental distribution, bimetallic can exist in the form of ordered structure (such as, intermetallic compound), random alloy, or heterostructures (such as, core-shell and Janus particles) (Figure 1.1).

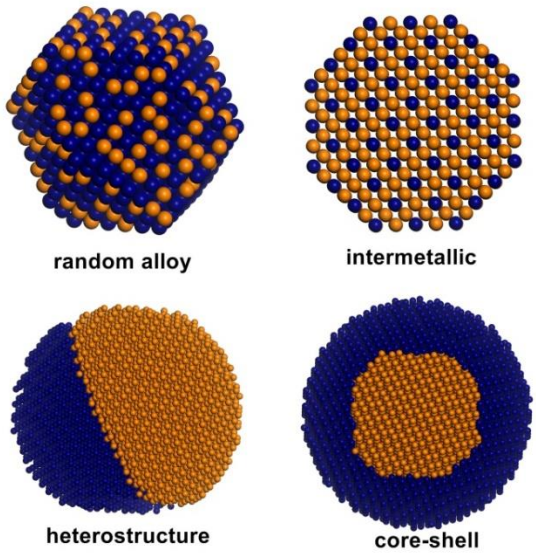

Figure 1.1 Schematic of some possible structures of bimetallic nanoparticles.

Bimetallic heterostructured nanoparticle inherently provides the chemical potential to drive the counter diffusion of the two metal species and is susceptible to undergo composition redistribution when provided with sufficient energy to overcome the diffusion barrier. Diffusion coefficient D_0 and activation energy of the two given metal species can be significantly different. For example, in a Ag host crystal, D_0 is 0.20 $cm^2 \cdot s^{-1}$ for Cu atoms and 0.40 $cm^2 \cdot s^{-1}$ for Ag atoms.[26] The difference between the diffusion rates results in the formation of "vacancies" which are created due to the fast moving species. This phenomenon is referred as the "Kirkendall Effect" and is the major reason accounted for the formation of hollows in bimetallic nanoparticles. González et al. showed the double hollow formation from the core@shell Ag@Au nanocube.[27] Due to the faster diffusion rate of Ag atoms in Au lattices as oppose to Au atoms in Ag lattices, the core Ag atoms diffused faster towards the shell, leaving vacancies behind, resulting in the formation of hollow cubes (Figure 1.2).

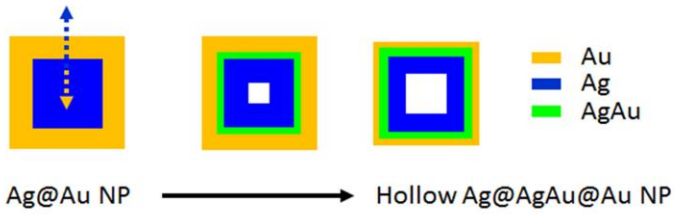

Figure 1.2 Schematic showing the formation of hollow structure in a Ag@Au core@shell nanoparticle due to the Kirkendall effect.

1.2.2 Thermodynamic factors governing intra-particle restructuring

The final configuration of a bimetallic nanocatalyst is governed by thermodynamics and approaches a most stable state under specific conditions. There are four major factors involved in determining the final structure of a bimetallic nanocatalyst. They are equilibrium phase for

binary metallic systems, intrinsic surface energy of metals, adsorption of gaseous molecules on metal surfaces, and chemical reaction between external molecules with the surface metal atoms (Figure 1.3).

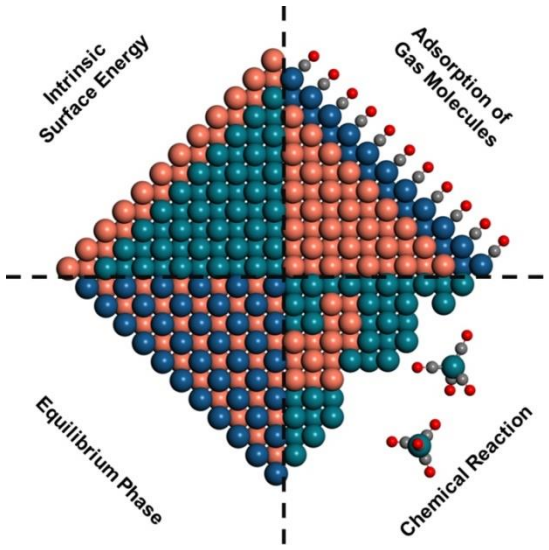

Figure 1.3 Schematic of the four major factors governing the structure of a bimetallic nanocatalyst.

1.2.2.1 Equilibrium phase of binary metal systems

The equilibrium phase of a specific pair of metals refers to the thermodynamically most stable state that exhibits a specific composition and atomic arrangement at a specific temperature. This information is readily available from binary phase diagrams which are well documented in various database, such as the alloy phase diagram database from the American Society of Metals International.[28] The phase diagram contains critical information of miscibility and intermetallic composition, if any, of a binary metallic system. The phase information of a few bimetallic systems relevant to this dissertation research is summarized in Table 1.1. This piece of information is important in determining the final state of a bimetallic catalyst.

Table 1.1 Phase information of selected bimetallic systems.

Entry	Metal A	Metal B	Alloy	Intermetallic phase
1[29]	Pt	Ag	No	Yes
2[30]	Pd	Rh	No	No
3[31]	Ag	Cu	No	No
4[32]	Au	Pd	Yes	Yes
5[33]	Ni	Pt	Yes	Yes

1.2.2.2 Intrinsic surface energy of metals

The surface energy plays an important role in determining the total energy of nano sized particles and its contribution increases as the particle size decreases. Under vacuum or inert gaseous atmosphere, the intrinsic surface energy of individual metals determines the surface composition of a bimetallic nanoparticle (Table 1.2).[34] At a given temperature, the thermodynamically most stable state should have a surface layer that has the lowest surface energy. For immiscible metals, the surface should be dominated by the one of lower intrinsic surface energy. However, due to the complexity of possible configurations, the surface composition of miscible alloys requires further experimental and theoretical studies.

Table 1.2 Intrinsic surface energy (in eV/atom) of low index surfaces of transition metals.[34]

Metal	(111)	(100)	(110)
Pt	1.004	1.378	2.009
Pd	0.824	1.152	1.559
Ag	0.553	0.653	0.953
Au	0.611	0.895	1.321
Cu	0.707	0.906	1.323
Rh	1.002	1.310	1.919
Ni	0.695	0.969	1.337

1.2.2.3 Adsorption of gas molecules on metal surfaces

Surface metal atoms are under-coordinated, *i.e.*, the metal surfaces possess many dangling bonds which make them susceptible to react with external atoms/molecules. This process is usually exothermic, resulting in a thermodynamically more stable state. When a bimetallic nanoparticle is exposed to a gaseous environment with strong adsorbing molecules, the surface is dominated by the composition and atomic arrangements that exhibit the lowest energy. Carbon monoxide (CO) is one of the gaseous molecules that bind strongly to most except group XI transition metal surfaces (Table 1.3). It has been applied in many studies on bimetallic nanoparticles composed of a combination of group XI and other metals because of the significant difference in adsorption energy.[12, 35-42]

Table 1.3 Binding energy (in eV/molecule) of CO and oxygen on selected metal surfaces.[43]

Metal	CO on (111)	$O_{(ad)}$ on (211)
Pt	-1.9	0.2
Pd	-1.75	0.5
Ag	-0.2	0.5
Au	-0.4	0.89
Cu	-0.6	0
Rh	-1.85	-0.81
Ni	-1.7	-0.85

1.2.2.4 Reaction of surface metal atoms with gas molecules

Chemical reactions between metal and gas are common and used in different applications, such as extracting Ni metal from its mines. The “Mond“ process utilized the reaction between Ni and CO (Eq.1), forming gaseous nickel carbonyl $Ni(CO)_5$ at low temperatures to extract Ni from NiCu minerals. Pure Ni is then recovered by decomposing

$Ni(CO)_5$ at a higher temperature (Eq.2)

$$Ni_{(s)} + 5CO_{(g)} \rightarrow Ni(CO)_{5(g)} \quad (1)$$

$$Ni(CO)_{5(g)} \rightarrow Ni_{(s)} + CO_{(g)} \quad (2)$$

It is clear that such reactions significantly alter the composition of bimetallic nanocatalyst. Another example is the formation of Pd carbonyl clusters which was shown to facilitate the surface diffusion and clustering of Pd atoms on iron oxide.[44] Oxidation of transition metals is another common reaction between metal and gas molecules. When exposed to oxygen, the metal species with a higher oxidation potential will dominate the surface, forming an oxide layer. Since the oxidation involves the counter diffusion of O and metal atoms, Kirkendall process is very likely to take place, which results in hollow nanostructures.[45-47] Depending on the partial pressure of O_2, the valence state may change and the surface oxide layers may vary from amorphous to crystalline.

1.2.3 Interparticle interaction - sintering

Sintering of metal crystallites/clusters into large particles is a common problem for high temperature heterogeneous catalysts, which leads to a dramatic loss in the active surface area. Moreover, sintering of small clusters significantly decreases the amount of active sites, usually under-coordinated surface atoms, which deactivates the catalyst completely in some cases.[48] The primary factors affecting the sintering of supported metal catalyst, are temperature and atmosphere,[49] which also play important roles in restructuring of bimetallic nanocatalyst as

mention above.[50] The nature of the support and the level of metal loading are critical.[51] With a few exceptions, anti-sintering ability of supported metal catalyst generically correlates well with the melting point of metal species.[52]

For bimetallic nanocatalyst, sintering is a very complex process which may be accompanied with phase transition, such as dealloying and the formation of intermetallics. Furthermore, since sintering is predominantly governed by temperature, diffusivity or melting point of individual metal species may be more critical than surface energy in determining the final surface composition.

1.3 Restructuring of Bimetallic Nanoparticles: A Brief Literature Review

1.3.1 Au-Pd and Au-Pt

Au-Pd and Au-Pt bimetallic nanoparticles have been widely studied possibly due to its potential applications as active and selective catalysts for oxidation and partial oxidation reactions, such as CO oxidation,[12, 53] methane to methanol conversion,[54] hydrogen peroxide (H_2O_2) formation,[55] and formic acid oxidation,[38] etc. The dispersity of Pd/Pt atoms or clusters on the catalyst surface plays critical role in determining the product selectivity. This leads to the investigation of Au-Pd and Au-Pt bimetallic nanocatalyst under reactive gaseous environments to probe the catalyst under working conditions or to discover processing conditions to optimize the surface composition. In situ X-ray techniques reveal a uniform alloy throughout the particle under vacuum at room temperature (RT) turned into one with a Pd rich surface when exposed to CO at 350°C for Au-Pd nanoparticles.[56] However, segregated structure was observed for Au-Pt nanoparticles where Au migrated to the surface under vacuum and Pt dominated the surface

under CO.[57] Based on the phase diagram, Au and Pd are completely miscible with each other and form stable intermetallics at specific ratios and temperatures (Figure 1.4a).[32] On the other hand, Au and Pt only form a alloy at low Pt concentration (Figure 1.4b).[33] This explains the different outcome of the two systems under vacuum although Pd and Pt share considerable similarities. This difference also suggests that multiple factors need to be considered in the restructuring of bimetallic nanoparticles. For Au-Pd, even though it exhibits a much lower surface energy then Pd (Table 1.1), Au does not compensate the energy penalty to form segregated structures. For Au-Pt, since segregation is preferred, the surface is dominated by the metal with lower intrinsic surface energy, *i.e.*, Au. When CO molecules are introduced, due to the strong affinity between CO and Pd and Pt atoms (Table 1.2), the surface becomes rich in these metal elements. The enrichment of Pd on surface was also observed under the coexistence of CO and O_2, suggesting it being the actual state of an working catalyst.[12]

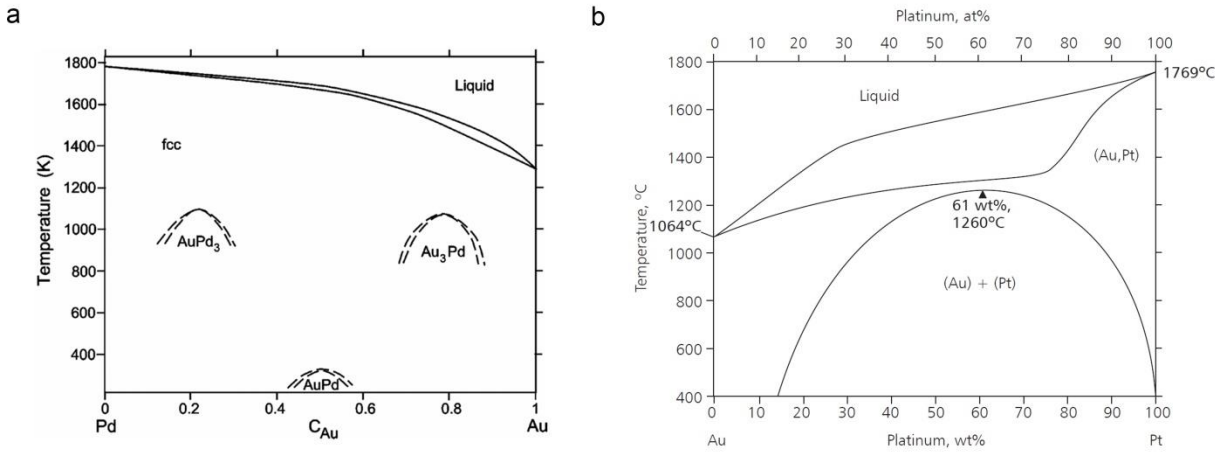

Figure 1.4 Binary phase diagrams of Au-Pd (a) and Au-Pt (b).[32-33]

1.3.2 Rh-Pd

Rh-Pd is a good catalyst for the three-way catalytic convertor,[17] as well as the selective methanol reforming reaction.[58] Tao et el studied the Rh-Pd catalyst under NO, CO, and O_2 and

revealed the compositional restructuring of RhPd nanoparticles under oxidation and reduction conditions. The XPS data unambiguously showed that surface composition, oxidation state, and atomic arrangements varied reversibly under reductive and oxidative gaseous environment. When exposed to oxidative environment with NO or O_2, the surface was mostly covered by Rh oxide species, while Pd metallic species dominated the surface when a reducing gas (CO) was introduced (Figure 1.5). Unlike the bimetallic system between Au and Pd, Rh and Pd are immiscible (Table 1)[30] with Pd exhibiting lower intrinsic surface energy. Rh and Pd share similar affinity towards CO however, O atoms adsorbs much stronger on Rh than Pd (Table 3). This difference explains the reversible surface Rh to Pd ratios under alternating reducing (CO) and oxidizing (NO, O_2) atmospheres. Under CO atmosphere, the determining factor for surface composition becomes the intrinsic surface energy since the CO adsorption energies are similar. When exposed to oxidizing environments, the adsorption and reaction of oxygen with Rh take over and become the dominant factors that minimize the energy of the system.

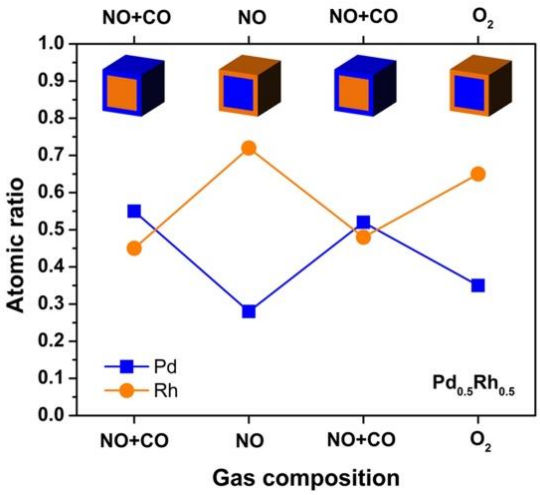

Figure 1.5 Composition variations of Rh-Pd nanoparticles under reactive gas environment, adapted and redrawn from Tao et al.[17]

1.3.3 Other bimetallic systems

Table 1.4 lists a range of reported bimetallic nanoparticle systems studied under reactive gaseous environments, which include the binary systems of interest, the utilized techniques, the segregation behaviors, and the controlling factors of structure. Once again, it can be clearly seen that the restructuring of most bimetallic nanoparticle systems studied can be addressed by one or a combination of the major governing factors described above.

Table 1.4 Reported bimetallic nanoparticle systems examined under reactive gas environments.

Bimetalllic system	Technique	Conditions & segregation effect	Conditions & segregation effect	Factors controlling structure
AuCu[59]	*In-situ* XANES	500 ºC H_2 Cu migrates to core	3-400 ºC O_2/CO CuO_x surface patches	N/A
AuPd[56]	*In-situ* SAFS, PDF, and DRIFTS	Vac; RT uniform alloy	350 ºC CO Pd rich surface	CO-Pd bond formation
AuPt[57]	IR CO stretching	Vac; RT Au migrates to surface	140 ºC CO Pt enrich on surface	Workfunction vs M-CO bond
SnPt[60]	*In-situ* XAFS/QXAFS	400 ºC O_2 SnO_2 on surface	400 ºC H_2 returns to Pt_3Sn	Structural oxidation
PtRh[61]	AP-XPS	300 ºC NO Rh surface segregation	300 ºC H_2 Pt enriched surface	ΔH_f(oxide) vs. surface free energy
PdRh[17, 58]	AP-XPS	300 ºC NO Rh surface segregation	300 ºC NO+CO or H_2 Pd enriched surface	Rh oxide formation
PtPd[61]	AP-XPS	300 ºC NO Pd remians on surface	300 ºC NO+CO or H_2 Pd remains on surface	ΔH_f(oxide) vs. surface free energy
PtCu[56]	*In-situ* SAFS, PDF, and DRIFTS	Vac; RT Cu rich surface	350 ºC CO Pt rich surface	CO-Pt surface adsorption
PtCo[42]	Electrochemistry	200 ºC CO Pt surfaec segregation		Segregatio vs surface mixing; Pt-CO vs Co-CO
PtCo[11]	AP-XPS	125 ºC H_2 Pt surface segregation	125 ºC in CO/O_2 Co segregates to surface, not oxidzed	Adsorbate induced restructuring
AgCu[62]	AP-XPS	247 ºC O_2 and O_2/C_2H_4 Cu enriched at surface	247 ºC C_2H_2 less Cu at surface	Surface energies and CuO formation
NiCu[13]	AP-XPS	H_2; Ni rich surface	O_2; Cu rich surface	

1.4 Utilization of In Situ Environmental (E)TEM for Bimetallic Nanoparticle Research

In situ environmental TEM is a promising technique to study the dynamic response of bimetallic nanoparticles under reactive gaseous environments with high temporal and spatial resolution. The bright field imaging can be used to directly observe the variations of geometrical structures. Electron diffraction (ED) can be carried out to identify the phase and sometimes composition. If coupled with energy dispersive X-ray (EDX) detector and electron energy loss spectrometer (EELS), the composition and valence state can be investigated in more details. In the following section, a few examples on how ETEM has been used to address various aspects of bimetallic nanocatalyst ranging from preparation[63-64] to behaviors under thermal and reactive gaseous environments.[12, 65-68]

1.4.1 In situ preparation of TiO_2 supported Cu-Ni[21]

Using ETEM installed with EELS detector, the Croizer group was able to investigate the formation of Cu-Ni catalyst on the precursor impregnated TiO_2 support. Real time imaging under H_2 at 300 ºC revealed the dynamic process of particle formation followed by ripening and particle-particle coalescence. In situ STEM-EELS revealed the sequential formation of Cu followed by Ni nanoparticles as well as the time-resolved spatial distribution of Cu and Ni species in which their conclusion on the formation of Cu-Ni alloy was based on.

1.4.2 Restructuring of Pt-Co nanoparticle under oxygen and hydrogen atmospheres[22]

Zhang et al. studied the redistribution of Pt and Co atoms of a Pt-Co nanoparticle under

O_2 and H_2 atmosphere. The growth kinetics of surface CoO layer under oxygen at 250 °C was analyzed using in situ HRTEM. In situ STEM-EELS, on the others hand, was performed under H_2 atmospheres to investigate the reduction of CoO surface layer. Based on the Z-contrast STEM images and EELS linescan of Co, the final structure of reduced Pt-Co nanoparticle was shown to compose of a Pt skin and Co subsurface layer on an alloy core.

1.5 Aim and Overview of Thesis

The structure of bimetallic nanocatalyst plays a critical role in determining its effectiveness towards specific reactions. When boiled down to the atomic level, it is the near surface atomic arrangement, which governs the surface electron configuration and the reaction energetic landscape of the reaction pathways. Although the synthetic method for structurally defined bimetallic crystals is approaching maturity, it remains a grand challenge to control the elemental distribution within the well-defined facets.

Post-synthesis thermal treatment under chemical vapor environments is a promising process to further adjust the structure of a bimetallic nanocatalyst. When conditions are controlled appropriately, usually at low temperature regimes, the composition distribution can be adjusted without altering the initial size and shape of the nanocatalyst. The first aim of this thesis is to develop such process focusing on the fundamental understanding on the behaviors of structurally well-defined bimetallic nanocatalyst under thermal and reactive gaseous environments. In Chapter 2, the composition rearrangement of bimetallic Pt-Ni octahedral nanocatalysts under thermal conditions studied by of ETEM and other surface probing techniques such as XPS and electrochemical methods will be presented. Chapter 3 focuses on the

near surface composition rearrangement bimetallic Ag-Pt octahedral nanocatalyst under thermal-chemical conditions studied by HAADF-STEM, ETEM, XPS, etc. Density Functional Theory (DFT) calculations are used in understanding the surface energetics of different elemental configurations. The chemical vapor assisted homogenization and segregation of near surface elemental arrangements were observed both in situ and ex situ. The structure-property relation was investigated for electrocatalysis and gas phase heterogeneous catalysis. The atomic arrangements of bimetallic nanocatalyst can also be defined by thermodynamics, *i.e.*, the equilibrium intermetallic phase. In Chapter 4, the transition of Ag-Pt alloy nanoparticle to disordered compositional intermetallics was studied. To the best of our knowledge, it is the first time that a phase-pure Ag-Pt intermetallic has ever been experimentally identified.

Bimetallic catalysts are designed to facilitate surface reactions, *i.e.*, they are working in reactive environments. In this regard, another aim of this thesis is to provide thorough understanding on the working state of a bimetallic catalyst, focusing on the relation among the gas environment, structure, and product selectivity. To address this question for hydrogenation reactions, Rh-on-Pd metal-on-metal nanocatalyst was investigated in situ by the ETEM under CO_2 hydrogenation conditions in Chapter 5. Adsorption energetics of CO on metal surfaces was calculated by DFT to explain and predict the structure-property relation. Gas phase heterogeneous reactions were carried out to confirm the in situ results and theoretical discoveries. In Chapter 6, Cu@CuAg nanocatalyst was studied for its structure-property relation for the epoxidation of propylene with molecular O_2. In situ studies were carried out in the ETEM under propylene and O_2. The main focus lies in understanding how the environment, *i.e.*, propylene to O_2 ratio, affects the structure of the Cu@CuAg nanocatalyst and its implication to the product distribution.

1.6 References

1. Alayoglu, S.; Nilekar, A. U.; Mavrikakis, M.; Eichhorn, B., *Nat. Mater.* **2008,** *7*, 333-338.
2. Sugano, Y.; Shiraishi, Y.; Tsukamoto, D.; Ichikawa, S.; Tanaka, S.; Hirai, T., *Angew. Chem. Int. Ed.* **2013,** *52*, 5295-5299.
3. Wu, J.; Yang, H., *Acc. Chem. Res.* **2013,** *46*, 1848-1857.
4. Gan, L.; Cui, C.; Heggen, M.; Dionigi, F.; Rudi, S.; Strasser, P., *Science* **2014,** *346*, 1502-1506.
5. Wu, J.; Gross, A.; Yang, H., *Nano Lett.* **2011,** *11*, 798-802.
6. Peng, Z.; You, H.; Yang, H., *ACS Nano* **2010,** *4*, 1501-1510.
7. Cui, C.; Gan, L.; Li, H.-H.; Yu, S.-H.; Heggen, M.; Strasser, P., *Nano Lett.* **2012,** *12*, 5885-5889.
8. Languille, M. A.; Ehret, E.; Lee, H. C.; Jeong, C. K.; Toyoshima, R.; Kondoh, H.; Mase, K.; Jugnet, Y.; Bertolini, J. C.; Aires, F. J. C. S.; Mun, B. S., *Catal. Today* **2016,** *260*, 39-45.
9. Lee, A. F.; Ellis, C. V.; Wilson, K.; Hondow, N. S., *Catal. Today* **2010,** *157*, 243-249.
10. Park, J. Y.; Zhang, Y.; Joo, S. H.; Jung, Y.; Somorjai, G. A., *Catal. Today* **2012,** *181*, 133-137.
11. Zheng, F.; Alayoglu, S.; Pushkarev, V. V.; Beaumont, S. K.; Specht, C.; Aksoy, F.; Liu, Z.; Guo, J.; Somorjai, G. A., *Catal. Today* **2012,** *182*, 54-59.
12. Delannoy, L.; Giorgio, S.; Mattei, J. G.; Henry, C. R.; El Kolli, N.; Méthivier, C.; Louis, C., *ChemCatChem* **2013,** *5*, 2707-2716.
13. Beaumont, S. K.; Alayoglu, S.; Pushkarev, V. V.; Liu, Z.; Kruse, N.; Somorjai, G. A., *Faraday. Discuss.* **2013,** *162*, 31-44.

14. Renzas, J. R.; Huang, W.; Zhang, Y.; Grass, M. E.; Hoang, D. T.; Alayoglu, S.; Butcher, D. R.; Tao, F.; Liu, Z.; Somorjai, G. A., *Phys. Chem. Chem. Phys.* **2011,** *13*, 2556-2562.

15. Tao, F.; Salmeron, M., *Science* **2011,** *331*, 171-174.

16. Alayoglu, S.; Beaumont, S.; Zheng, F.; Pushkarev, V.; Zheng, H.; Iablokov, V.; Liu, Z.; Guo, J.; Kruse, N.; Somorjai, G., *Top. Catal.* **2011,** *54*, 778-785.

17. Tao, F.; Grass, M. E.; Zhang, Y.; Butcher, D. R.; Renzas, J. R.; Liu, Z.; Chung, J. Y.; Mun, B. S.; Salmeron, M.; Somorjai, G. A., *Science* **2008,** *322*, 932-934.

18. Chenna, S.; Crozier, P. A., *ACS Catal.* **2012,** *2*, 2395-2402.

19. Chenna, S.; Banerjee, R.; Crozier, P. A., *ChemCatChem* **2011,** *3*, 1051-1059.

20. Jinschek, J. R., *Chem. Commun.* **2014,** *50*, 2696-2706.

21. Li, P.; Liu, J.; Nag, N.; Crozier, P. A., *J. Catal.* **2009,** *262*, 73-82.

22. Xin, H. L.; Alayoglu, S.; Tao, R.; Genc, A.; Wang, C.-M.; Kovarik, L.; Stach, E. A.; Wang, L.-W.; Salmeron, M.; Somorjai, G. A.; Zheng, H., *Nano Lett.* **2014,** *14*, 3203-3207.

23. Vendelbo, S. B.; Elkjær, C. F.; Falsig, H.; Puspitasari, I.; Dona, P.; Mele, L.; Morana, B.; Nelissen, B. J.; van Rijn, R.; Creemer, J. F.; Kooyman, P. J.; Helveg, S., *Nat. Mater.* **2014,** *13*, 884-890.

24. Yoshida, H.; Kuwauchi, Y.; Jinschek, J. R.; Sun, K.; Tanaka, S.; Kohyama, M.; Shimada, S.; Haruta, M.; Takeda, S., *Science* **2012,** *335*, 317-319.

25. Benavidez, A. D.; Kovarik, L.; Genc, A.; Agrawal, N.; Larsson, E. M.; Hansen, T. W.; Karim, A. M.; Datye, A. K., *ACS Catal.* **2012,** *2*, 2349-2356.

26. Kittel, C., *Introduction to Solid State Physics*. 8 ed.; John Wiley & Sons, Inc.: Hoboken, NJ, 2005.

27. González, E.; Arbiol, J.; Puntes, V. F., *Science* **2011,** *334*, 1377-1380.

28. Piccinin, S.; Nguyen, N. L.; Stampfl, C.; Scheffler, M., *J. Mater. Chem.* **2010,** *20*, 10521-10527.

29. Durussel, P.; Feschotte, P., *J. Alloys Compd.* **1996,** *239*, 226-230.

30. Calculated Pd-Rh phase diagram. 2005 ed.; National Physical Laboratory: 2005.

31. Sanchez, J. M.; Stark, J. P.; Moruzzi, V. L., *Phys. Rev. B* **1991,** *44*, 5411-5418.

32. Okamoto, H.; Massalski, T. B., *Bull. Alloy Phase Diagr.* **1985,** *6*, 229-235.

33. T. B. Massalski, H. O., P.R. Subramanian, L. Kacprzak, *Binary Alloy Phase Diagrams*. ASM International: Ohio, USA, 1990.

34. Vitos, L.; Ruban, A. V.; Skriver, H. L.; Kollár, J., *Surf. Sci,* **1998,** *411*, 186-202.

35. Carenco, S., *Chem. Eur. J.* **2014,** *20*, 10616-10625.

36. Vestergaard, E. K.; Vang, R. T.; Knudsen, J.; Pedersen, T. M.; An, T.; Lægsgaard, E.; Stensgaard, I.; Hammer, B.; Besenbacher, F., *Phys. Rev. Lett.* **2005,** *95*, 126101.

37. Murdoch, A.; Trant, A. G.; Gustafson, J.; Jones, T. E.; Noakes, T. C. Q.; Bailey, P.; Baddeley, C. J., *Sur. Sci.* **2015**.

38. Lee, S.-Y.; Jung, N.; Cho, J.; Park, H.-Y.; Ryu, J.; Jang, I.; Kim, H.-J.; Cho, E.; Park, Y.-H.; Ham, H. C.; Jang, J. H.; Yoo, S. J., *ACS Catal.* **2014,** *4*, 2402-2408.

39. McCue, A. J.; Anderson, J. A., *J. Catal.* **2015,** *329*, 538-546.

40. Yao, Y.; Goodman, D. W., *Phys. Chem. Chem. Phys.* **2014,** *16*, 3823-3829.

41. Tenney, S. A.; He, W.; Roberts, C. C.; Ratliff, J. S.; Shah, S. I.; Shafai, G. S.; Turkowski, V.; Rahman, T. S.; Chen, D. A., *J. Phys. Chem. C* **2011,** *115*, 11112-11123.

42. Mayrhofer, K. J. J.; Juhart, V.; Hartl, K.; Hanzlik, M.; Arenz, M., *Angew. Chem. Int. Ed.* **2009,** *48*, 3529-3531.

43. Studt, F.; Sharafutdinov, I.; Abild-Pedersen, F.; Elkjær, C. F.; Hummelshøj, J. S.; Dahl, S.; Chorkendorff, I.; Nørskov, J. K., *Nat. Chem.* **2014,** *6*, 320-324.

44. Parkinson, G. S.; Novotny, Z.; Argentero, G.; Schmid, M.; Pavelec, J.; Kosak, R.; Blaha, P.; Diebold, U., *Nat. Mater.* **2013,** *12*, 724-728.

45. Railsback, J. G.; Johnston-Peck, A. C.; Wang, J.; Tracy, J. B., *ACS Nano* **2010,** *4*, 1913-1920.

46. Wang, W.; Dahl, M.; Yin, Y., *Chem. Mater.* **2013,** *25*, 1179-1189.

47. Fan, H. J.; Knez, M.; Scholz, R.; Hesse, D.; Nielsch, K.; Zacharias, M.; Gösele, U., *Nano Lett.* **2007,** *7*, 993-997.

48. Mavrikakis, M.; Bäumer, M.; Freund, H.-J.; Nørskov, J. K., *Catal. Lett.* **2002,** *81*, 153-156.

49. Behafarid, F.; Pandey, S.; Diaz, R. E.; Stach, E. A.; Cuenya, B. R., *Phys. Chem. Chem. Phys.* **2014,** *16*, 18176-18184.

50. Wanke, S. E.; Flynn, P. C., *Catal. Rev.* **1975,** *12*, 93-135.

51. Morikawa, A.; Tanabe, T.; Hatanaka, M.; Takahashi, N.; Sato, A.; Kuno, O.; Suzuki, H.; Shinjoh, H., *Appl. Catal. A* **2015,** *493*, 33-39.

52. Kip, B. J.; Duivenvoorden, F. B. M.; Koningsberger, D. C.; Prins, R., *J. Catal.* **1987,** *105*, 26-38.

53. Alayoglu, S.; Tao, F.; Altoe, V.; Specht, C.; Zhu, Z.; Aksoy, F.; Butcher, D.; Renzas, R.; Liu, Z.; Somorjai, G., *Catal. Lett.* **2011,** *141*, 633-640.

54. Ab Rahim, M. H.; Forde, M. M.; Jenkins, R. L.; Hammond, C.; He, Q.; Dimitratos, N.; Lopez-Sanchez, J. A.; Carley, A. F.; Taylor, S. H.; Willock, D. J.; Murphy, D. M.; Kiely, C. J.; Hutchings, G. J., *Angew. Chem. Int. Ed.* **2013,** *125*, 1318-1322.

55. Wilson, N. M.; Flaherty, D. W., *J. Amer. Chem. Soc.* **2016,** *138*, 574-586.

56. Oxford, S. M.; Lee, P. L.; Chupas, P. J.; Chapman, K. W.; Kung, M. C.; Kung, H. H., *J. Phys. Chem. C* **2010,** *114*, 17085-17091.

57. Lang, H.; Maldonado, S.; Stevenson, K. J.; Chandler, B. D., *J. Amer. Chem. Soc.* **2004,** *126*, 12949-12956.

58. Divins, N. J.; Angurell, I.; Escudero, C.; Pérez-Dieste, V.; Llorca, J., *Science* **2014,** *346*, 620-623.

59. Liu, X.; Wang, A.; Li, L.; Zhang, T.; Mou, C.-Y.; Lee, J.-F., *J. Catal.* **2011,** *278*, 288-296.

60. Uemura, Y.; Inada, Y.; Bando, K. K.; Sasaki, T.; Kamiuchi, N.; Eguchi, K.; Yagishita, A.; Nomura, M.; Tada, M.; Iwasawa, Y., *J. Phys. Chem. C* **2011,** *115*, 5823-5833.

61. Tao, F.; Grass, M. E.; Zhang, Y.; Butcher, D. R.; Aksoy, F.; Aloni, S.; Altoe, V.; Alayoglu, S.; Renzas, J. R.; Tsung, C.-K.; Zhu, Z.; Liu, Z.; Salmeron, M.; Somorjai, G. A., *J. Am. Chem. Soc.* **2010,** *132*, 8697-8703.

62. Piccinin, S.; Zafeiratos, S.; Stampfl, C.; Hansen, T. W.; Hävecker, M.; Teschner, D.; Bukhtiyarov, V. I.; Girgsdies, F.; Knop-Gericke, A.; Schlögl, R.; Scheffler, M., *Phys. Rev. Lett.* **2010,** *104*, 035503.

63. Wu, Q.; Duchstein, L. D. L.; Chiarello, G. L.; Christensen, J. M.; Damsgaard, C. D.; Elkjær, C. F.; Wagner, J. B.; Temel, B.; Grunwaldt, J.-D.; Jensen, A. D., *ChemCatChem* **2014,** *6*, 301-310.

64. Damsgaard, C. D.; Duchstein, L. D. L.; Sharafutdinov, I.; Nielsen, M. G.; Chorkendorff, I.; Wagner, J. B., *Microscopy* **2014,** *63*, 397-401.

65. Johns, T. R.; Goeke, R. S.; Ashbacher, V.; Thüne, P. C.; Niemantsverdriet, J. W.; Kiefer, B.; Kim, C. H.; Balogh, M. P.; Datye, A. K., *J. Catal.* **2015,** *328*, 151-164.

66. Holse, C.; Elkjær, C. F.; Nierhoff, A.; Sehested, J.; Chorkendorff, I.; Helveg, S.; Nielsen, J. H., *J. Phys. Chem. C* **2015,** *119*, 2804-2812.

67. Chenna, S.; Crozier, P., *Microsc. Microanal.* **2011,** *17*, 1602-1603.

68. Sharma, R.; Chee, S.-W.; Herzing, A.; Miranda, R.; Rez, P., *Nano Lett.* **2011,** *11*, 2464-2471.

Chapter 2

In Situ ETEM Study of Composition Redistribution in Pt-Ni Octahedral Catalysts for Electrochemical Reduction of Oxygen[1]

2.1 Introduction

Electrocatalysts are important for a range of important applications, such as polymer electrolyte membrane fuel cell (PEMFC),[1] battery,[2,3] and solar-fuel device.[4] Heterogeneous electrocatalysis usually involves the adsorption of reactant (molecule or ion), electron transfer, and desorption of product from the surface. Thus surface state is a key parameter in electrocatalytic reaction, and the ability to manipulate composition and atomic structure on or near the catalyst surface can have great impact on the performance in both activity and stability. In this context, bimetallic catalyst becomes increasingly important for electrochemical reaction because the electrochemical process can be extremely sensitive to surface structure and composition.[1,5-7] For the control of catalysts with well-defined surfaces, solution phase synthesis is proved to be a promising route, because this method is capable for producing monodisperse nanoparticles with uniform shape and overall composition.[8,9] These structural parameters are not always independently tunable though,[8,10] because several factors determine the final surface composition, which can be related to global surface energy and phase behavior (alloy or intermetallic).[9,11]

Surface composition and structure of a pristine bimetallic nanoparticle are usually determined by the element that has the lower intrinsic surface energy. However, when the

[1] Modified with permission, from Pan, Y.-T.; Wu, J.; Yang, H. *AIChE J*. **2016**, *62*, 399-407.

particle is exposed to a reactive environment or in the presence of capping ligand in solution, the dominant surface species becomes the one that has a lower overall energy, which is a combination of intrinsic surface energy and adsorption energy of molecules on specific atomic sites.[12,13] It has been demonstrated the surface composition of bimetallic nanoparticle can be very sensitive to reactive environments using in situ X-ray spectroscopy-based techniques.[12-18] Moreover, the surface composition responds dynamically to the environment, showing reversibility under cyclic gas atmospheres.[12] In addition to X-ray based techniques, using the latest environmental transmission electron microscope (ETEM),[19-22] one can expect to obtain valuable information on the structural or morphological changes of nanoparticles in situ at high spatial resolution under reactive atmospheres.[23] A combination of both X-ray and ETEM techniques can therefore provide a comprehensive picture of the dynamic behavior of bimetallic nanoparticles to develop optimal processing conditions and design principles.

In this chapter, we present the detail of structural changes of as-made Pt-Ni octahedral catalysts in situ during the post-synthesis thermal treatment under processing temperatures using ETEM. The corresponding as-made and thermally-treated carbon-supported Pt-Ni octahedral catalysts were studied for the reduction of oxygen under acidic conditions. So far, a large number of Pt-based alloy nanoparticles were shown to be excellent ORR catalysts.[1,7,8,10,24-29] Transition metal segregated in the subsurface is a critical feature of these ORR catalysts of Pt-M (M=transition metal) nanoparticles.[30-33] The optimization in structure has often been done via post-synthesis treatment thermally or electrochemically.[34,35] Among the alloys of Pt and transition metals, Pt_3Ni was shown to be the optimal alloy compositions that have the highest ORR performance. The as-made octahedral Pt_3Ni catalyst tends to have high Ni content preferentially segregated on surface of {111} facets.[32] Upon treatment in chemical or

electrochemical environments, these Ni atoms leached out preferentially from the {111} facets, and the catalyst particles evolved into various etched structures, such as, concave octahedron, hexapod, or nanoframe.[36-38]

We choose carbon-supported, sandwich-type Pt-Ni octahedral nanoparticles in this work. The in situ ETEM study was carried out at a mild annealing temperature of 200~210 ºC under vacuum. This condition was also used to post treat as-made Pt-Ni octahedral nanoparticle catalysts on carbon support. Ex situ X-ray photoelectron spectroscopy (XPS) was used to study both the as-made and annealed (210 ºC, vacuum) Pt-Ni nanoparticle catalysts; while cyclic voltammetry and polarization curve were used to examine their ORR performance.

2.2 Experimental

2.2.1 Materials and chemicals

All chemicals were used as received without further purification. Platinum acetylacetonate ($Pt(acac)_2$, Strem Chemical, 98%); nickel acetylacetonate ($Ni(acac)_2$, Sigma-Aldrich, 95%); oleylamine (OAm, Sigma-Aldrich, technical grade, 70%); oleic acid (OAc, Sigma-Aldrich, technical grade, 90%); diphenyl ether (Sigma-Aldrich, 99%); n-butylamine (Sigma-Aldrich, 99.5%); hexane (Sigma-Aldrich, >95%); chloroform (Macron, >99%); ethanol (Decon Labs, 200 proof); methanol (macron, >99%); argon gas (Ar, Airgas, C.P. grade); carbon monoxide gas (CO, Airgas, C.P. grade).

2.2.2 Synthesis of Pt-Ni octahedral nanoparticles

To synthesize Pt-Ni octahedral nanoparticles, a solution of 20 mg (0.05 mmol) of $Pt(acac)_2$, 7 mg (0.027 mmol) of $Ni(acac)_2$ was dissolved in 9 mL of oleylamine (OAm), 1 mL of diphenyl ether and 50 μL of oleic acid (OA) in a 25-mL three-neck round bottom flask immersed in an oil bath at 130 °C. The flask was connected to a Schlenk line through a condenser. The reaction mixture turned into a transparent yellowish solution at this temperature after 2 min. The flask was then evacuated with a rotary pump (Edward RV 12) and purged with Ar (supplier) for 6 cycles to remove air and moisture. The solution was then bubbled with CO gas and transferred to a second oil bath at 210 ºC. Throughout the process, the flask was connected to the Schlenk line. The typical flow rate of CO gas was set at 120 cm^3/min and the reaction time was 30 min. The rest of steps followed the procedure for synthesis of Pt-Ni octahedral nanoparticles reported previously.[8] The solid products were washed and separated by dispersing the reaction mixture in 2 mL of chloroform and 10 mL of ethanol, followed by centrifugation at 5000 rpm for 5 min. This procedure was repeated three times. The final products were dispersed in hexane for further characterization.

2.2.3 Preparation of carbon-supported catalysts

Carbon black (Vulcan XC-72) was used as support for making platinum nickel catalysts (Pt-Ni/C). In a standard preparation, carbon black particles were dispersed in chloroform and sonicated for 1 h. A designed amount of Pt-Ni nanoparticles suspension in hexane was added to this dispersion of carbon black at the nanoparticle-to-carbon-black mass ratio of 20:80. This mixture was further sonicated for 30 min and stirred overnight. The resultant solids were precipitated out by centrifugation and dried under an argon stream. The solid product was then

re-dispersed in n-butylamine at a concentration of 0.5 mg-catalyst/mL in a capped glass vial. The mixture was kept under stirring for 3 days under ambient air conditions and then collected using a centrifuge at a rate of 5000 rpm for 5 min. The precipitate was re-dispersed in 10-mL methanol by sonicating for 15 min and then separated by centrifugation. This procedure was repeated three times. The final samples were dispersed in ethanol for further characterization. For ex situ thermal treatment, carbon-supported catalysts were annealed at 210 ºC in a tube furnace (GSL-1500X, MTI Corporation) for 1 h and cooled down under vacuum (9.8 kPa or 0.097 atm). The treated catalyst was then used for electrochemical measurements.

2.2.4 Characterization

Transmission electron microscopy (TEM) and high-resolution transmission electron microscopy (HR-TEM) micrographs were taken on a FEI TECNAI F-20 field emission microscope at an accelerating voltage of 200 kV. Scanning transmission electron microscopy (STEM) micrographs and energy dispersive X-ray (EDX) elemental spot analysis and line scans were carried out using the high-angle annular dark field (HAADF) mode on JEOL 2010F STEM with Schottky field emitter at an accelerating voltage of 200 kV. Inductively coupled plasma optical emission spectrometry (ICP-OES) was performed using a Perkin Elmer 2000DV ICP-OES spectrometer. X-ray photoelectron spectroscopy (XPS) was acquired using Kratos Axis ULTRA (Manchester UK) spectrometer with a monochromatic Al source. The XPS spectrum analysis was done using CasaXPS software with Shirley type baseline. To make an XPS specimen, as-made Pt-Ni octahedral nanoparticles, after extensive washing with chloroform, were drop-casted on Si wafer and treated under the same condition as mentioned above. The

atomic ratio between Pt and Ni were calculated by integrating Pt 4f (60-84 eV) and Ni 2p (845-885 eV) peaks with a sensitivity factor of 6.115 and 3.845, respectively.

2.2.5 In situ ETEM study

In situ heating experiment was conducted using a Hitachi H9500 ETEM at an accelerating voltage of 200 kV. This ETEM is equipped with a variable-temperature heating holder made of a tungsten wire. Carbon-supported catalyst dispersed in ethanol was loaded on the tungsten heating wire, which was pre-mounted on the in situ holder, using a fine-tip paint brush. The catalyst was transferred by dipping the brush in the ethanol solution and deposited on the heating wire by gentle brushing. The catalyst-deposited heating wire was then left sitting on bench for 30 min to allow the evaporation of ethanol. The holder was then introduced into the Hitachi H9500 ETEM and connected to a DC power supply for resistive heating.

Survey of the sample was done at room temperature under standard operating conditions. Once the particle of interest was located, electron beam was blocked by closing the gun valve and temperature of heating wire was raised. Temperature of the sample was determined by the current-temperature relation chart (Hitachi). The current was slowly increased to 390 mA (200 ^{o}C) and maintained throughout the rest of the experiment. Once the current reached 390 mA, TEM micrographs were recorded using the Gatan Orius SC200 CCD camera, and Gatan digital micrograph software. The TEM images were recorded by taking screen shot videos with CamStudio software during the course of experiment. Electron irradiation was kept minimized during the course of experiment and the gun valve was opened only during image acquisition, which was typically less than 1 min with a current density of 1.18×10^{-11} A/cm^2. The sample was then left in dark for another 5 min before the next imaging cycle. Image analysis and processing

was done using Digital Micrograph (DM, Gatan) and ImageJ software. Detail procedures for image processing are described in supporting information.

2.2.6 Electrochemical measurements

A three-electrode cell was used to measure the electrochemical properties of these alloy catalysts. The working electrode was a glassy-carbon rotating disk electrode (RDE) (area: 0.196 cm^2). A 1 cm^2 platinum foil was used as the counter electrode and a HydroFlex hydrogen electrode was used as the reference, which was placed in a separate compartment. Hydrogen evolution reaction (HER) was used to calibrate this hydrogen electrode before the tests. All potentials were referenced to the reversible hydrogen electrode (RHE). The electrolyte was 0.1-M $HClO_4$ aqueous solution, diluted from 70% double-distilled perchloric acid (GFS Chemicals, USA) with MilliporeQ ultra-pure water. The mass of metal in each Pt-Ni/C catalyst was determined by thermogravimetric analysis (TGA) using an SDT-Q600 TGA/DSC system from TA Instruments at a ramp rate of 10 °C/min to 600 °C in air followed by annealing at 600 °C for 30 min under a forming gas of 5 % hydrogen in argon at a flow rate of 50 ml/min. To prepare the working electrode, 5 mg of the Pt-Ni/C catalyst (20% based on the weight of alloy nanoparticles) was dispersed in 10 mL of the mixed solvent and sonicated for 5 min. The solvent contained a mixture of de-ionized water, isopropanol, and 5% Nafion at the volumetric ratio of 8:2:0.05. 20 μL of the suspension was added onto the RDE by a pipette and dried in air. The loading amount of Pt-Ni alloy nanocatalysts on the RDE was determined to be 9.3 $\mu gPt/cm^2$. The CV measurement was carried in argon-saturated 0.1-M $HClO_4$ solution at room temperature with a scan rate of 50 mV/s. Oxygen reduction reaction (ORR) activity was determined in a 0.1-M $HClO_4$ solution which was purged with oxygen for 30 min prior to, and during testing. The scan

rate for ORR measurement was set at 10 mV/s in the positive direction. Data were used without iR-drop correction.

2.3 Results and Discussion

2.3.1 Electron microscopy characterization of sandwich-structured Pt-Ni octahedral nanoparticle

Figure 2.1 shows the electron microscopy (EM) micrographs, EDX line scan, and a three dimensional (3D) illustration of as-made Pt-Ni octahedral catalysts. These nanoparticles showed monodispersity and were uniform in size and shape (Figure 2.1a). The average edge length of these octahedral nanoparticles was 11.3 ± 1.3 nm. The vast majority of the particles had a dark contrast core and shell with a light contrast layer sandwiched in between. High resolution TEM (HRTEM) images showed the lattice fringes had a *d*-spacing of 2.15 Å in the core, 2.20 Å in the shell, and 2.09 Å in the layer sandwiched in between (Figure 2.1b). High angular dark field STEM was used to further analyze this unique three-layered structure, because Z contrast is quite distinctive for these two metal elements in such STEM micrographs (Figure 2.1c, 2.1d). The STEM study shows unambiguously the core and shell had higher intensity (heavier metal, *i.e.*, Pt) than the middle layer. Average size of the core was about 5 nm and thickness of the outer surface layer was 1.5 nm, approximately equivalent to 7 atomic layers. Thickness of the middle region was ~5 nm.

The EDX line scan (Fig. 1e) provides a semi-quantitative compositional analysis along the trajectory in Fig. 1d. The Pt L_α line had three peaks located in the outer shell and core regions (blue squares fitted with green line), while Ni K_α line had two peaks (orange triangles fitted with

red curve) in the subshell layer. A quantitative spot analysis shows that the composition of as-made Pt-Ni octahedral nanoparticle was $Pt_{77}Ni_{23}$ in the central region, $Pt_{54}Ni_{46}$ in the subshell-layer and $Pt_{71}Ni_{29}$ in the outer shell region (Figure 2.2). The ICP-OES analysis showed that the nanoparticles have a Pt to Ni of 54:46. These convergence evidences indicates Pt and Ni did not distribute uniformly in as-made octahedral particles, instead they had a sandwiched nanostructure with Pt rich in both the core and shell regions, as being illustrated in Fig. 1f.

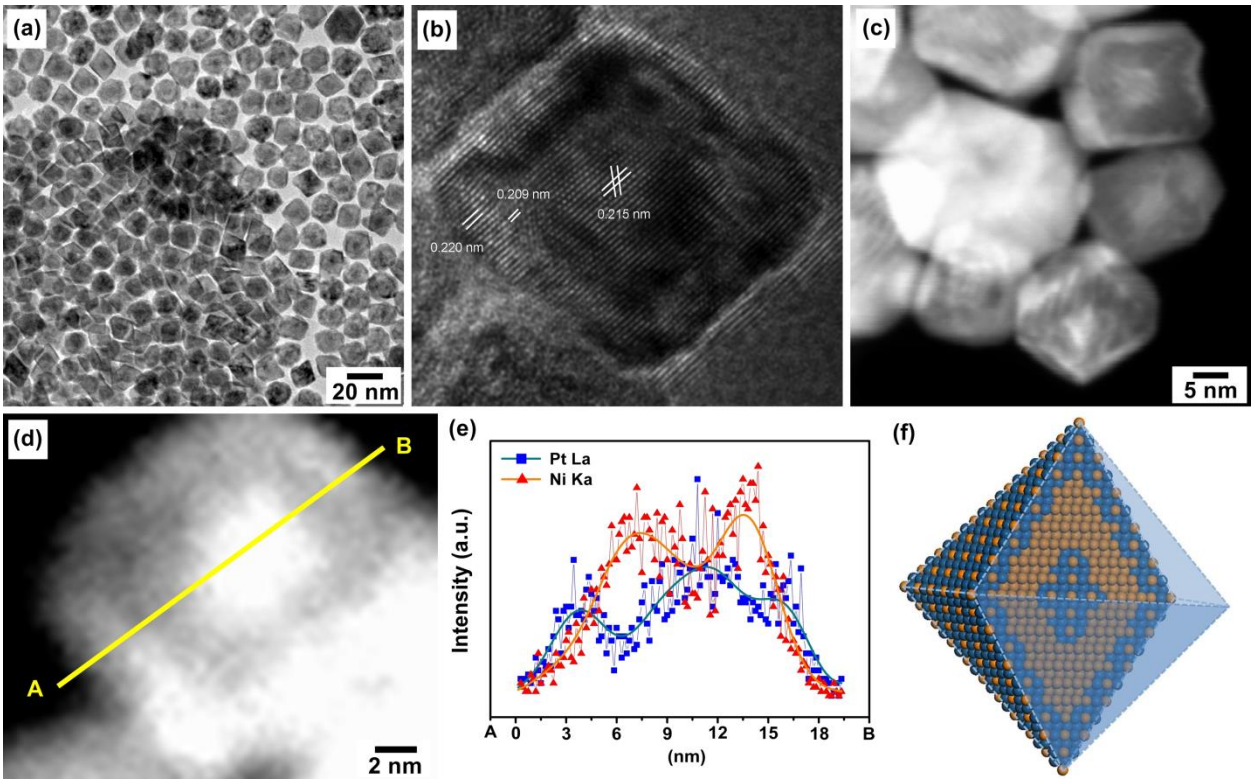

Figure 2.1 EM characterization of as-made Pt-Ni octahedral nanocrystals: (a) low and (b) high magnification TEM micrographs, (c) low and (d) high magnification dark-field STEM images, (e) EDX line scans for Pt and Ni elements, and (f) schematic drawing of the sandwich like three-layered structures (square: Pt, triangle: Ni). (Figure 2.1a and b is taken by Jianbo Wu)

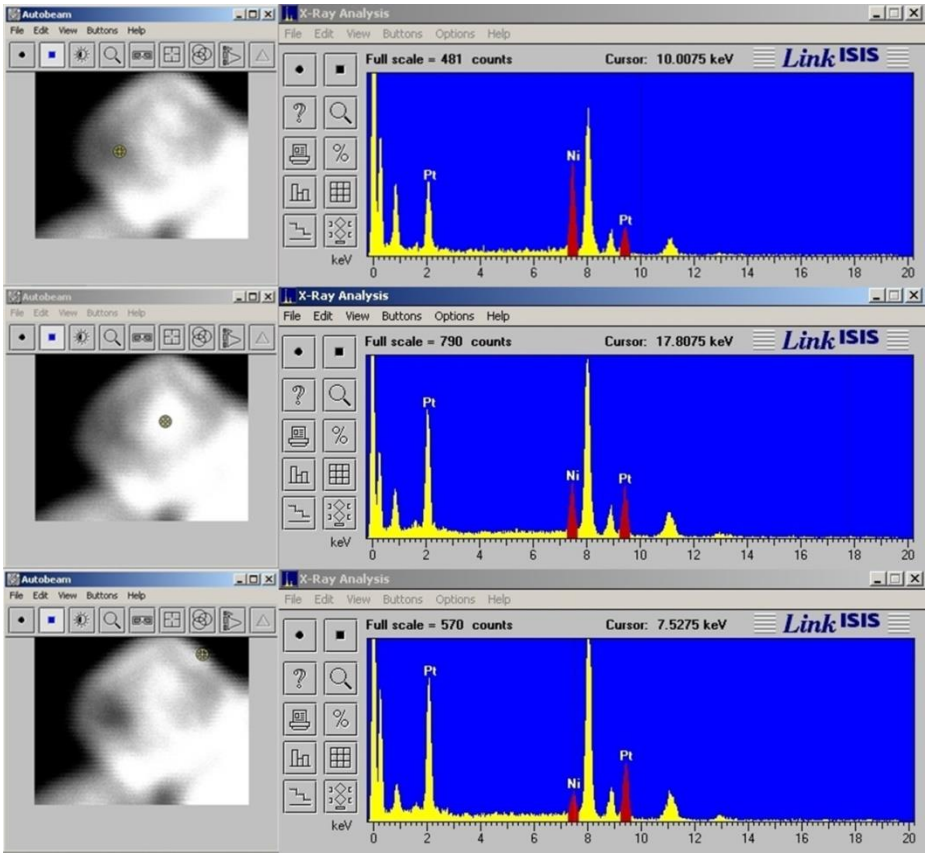

Figure 2.2 STEM-EDX spot analysis on different regions of as-made Pt-Ni nanoparticle.

2.3.2 In situ ETEM observation of single Pt-Ni octahedral nanocatalyst under thermal-vacuum conditions

Figure 2.3 shows a series of in situ HRTEM micrographs of a representative Pt-Ni octahedral nanoparticle taken at 200 ºC for a time period of 25 min. These micrographs were taken with 5-min intervals with an exposure time of 15 to 30 s to electron beam during image acquisition. The contrast inside these TEM nanoparticles varied, reflecting the change in composition and structure, especially those features related to lattice strain. Upon annealing, boundaries of the 2-nm thick outer shell became less distinguishable over time, accompanied with rounding off of the facets of octahedral nanoparticles. The heterogeneity in composition

created strong driving force for atoms to move within the as-made Pt-Ni octahedral nanoparticle at elevated temperatures, resulting in redistribution of both Pt and Ni elements.

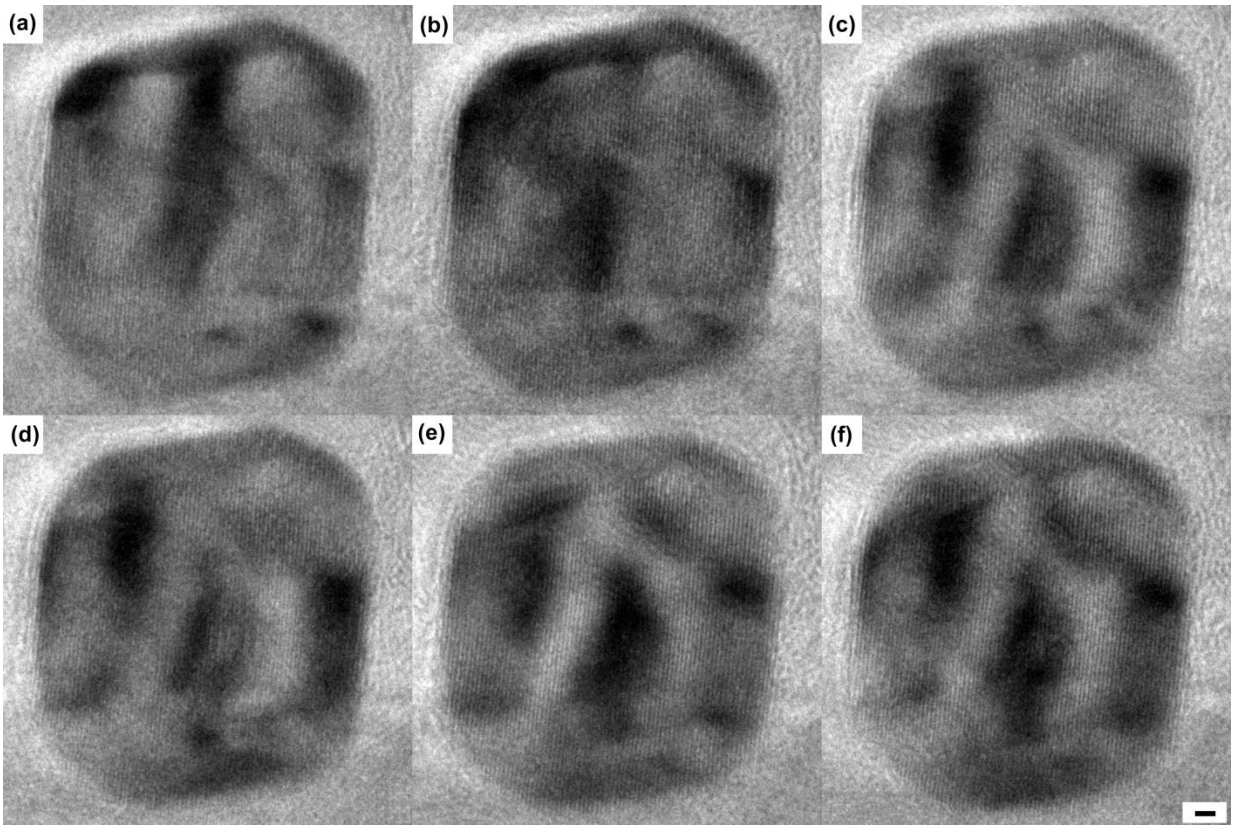

Figure 2.3 In situ TEM micrographs taken under vacuum annealing conditions at 200 ºC, over a time period of (a) 0, (b) 4, (c) 10, (d) 15, (e) 20, and (f) 25 min, respectively. Scale bar is 2 nm, applicable to all.

2.3.3 Image processing, analysis, and identification of dislocations

To extract the lattice movement information from these TEM images, we used the inverse Fourier transform (IFFT) technique to generate filtered images based on diffraction patterns obtained using FFT. As shown in Figure 2.4, after applying mask on the diffraction spots of interest, a filtered image preserving the diffraction information can be obtained. The filtered

image can then be overlaid with the original micrograph, which provides clean information on the lattice fringes in the <111> direction (Figure 2.5).

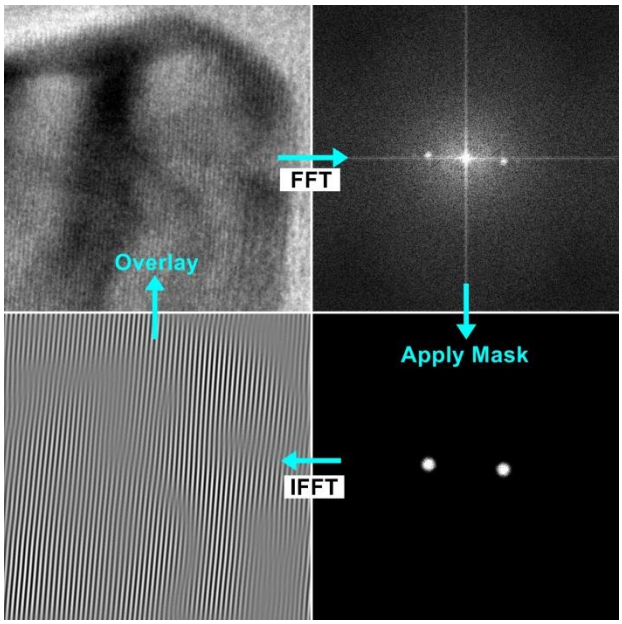

Figure 2.4 Schematic showing the process of acquiring a filtered image using the digital micrograph (DM) software. The TEM micrographs (Figure 2.3) were taken as screenshots and save as JPEG file. The image file was then converted to "REAL" in the DM. A fast Fourier transform (FFT) was performed to acquire the reciprocal space image and a mask was placed to block off all other information except the diffraction pattern of interest. After applying inverse FFT to the masked diffraction pattern, a filtered image was generated with clear lattice fringes.

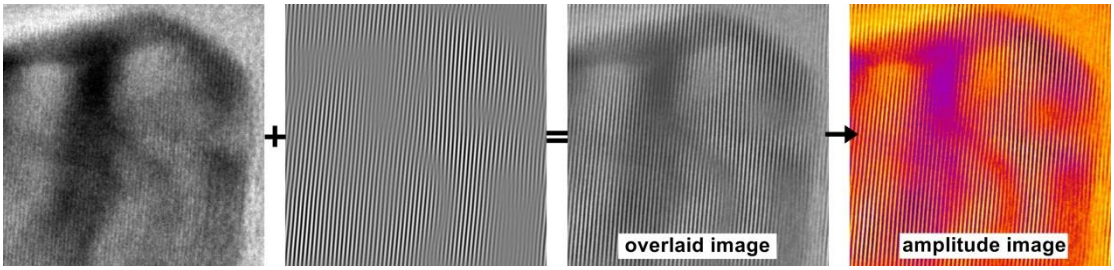

Figure 2.5 Schematic showing the process of generating amplitude image. A filtered image was overlaid with the original one and transformed to amplitude image by ImageJ.

Figure 2.6 shows a representative filtered amplitude image of upper right region of the octahedral nanoparticle shown in Figure 2.3a. The positions of dislocation, highlighted with dashed white circles, were clearly visible in multiple places. Since the values of intrinsic (111) lattice spacing between Pt and Ni are quite different (2.265 vs. 2.034 Å), these dislocations likely originated from the misfit at the boundary between Pt-rich core/shell and the Ni-rich sub-shell layer in between.

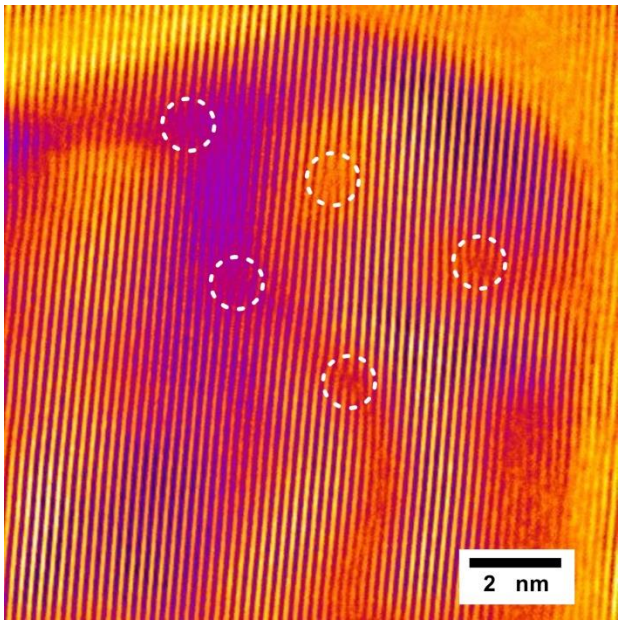

Figure 2.6 Representative filtered amplitude image of the corner region of an octahedral nanoparticle. This image was generated using the top right portion of the image shown in Figure 2.3a. Positions of the dislocations are marked with white dashed circles.

2.3.4 Migration of dislocation pairs along <111> and <100> directions

Figure 2.7 shows the TEM micrographs and the fitting curves of the dislocation movement for the octahedral nanoparticle. The locations of observed dislocations were highlighted with white squares. These dislocations moved outwards and eventually settled near the surface during the course of experiment (Figure 2.7a-b,). Since dislocation tend to exist at the position where large lattice mismatch occurs, *i.e.*, the dislocations tend to concentrate at the boundaries between the shell and subshell or the sub-shell and core regions, the migration of dislocations suggest the movement of Ni in the sub-shell layer towards the surface, or effective counter diffusion of Pt and Ni atoms in the particle. Migration of dislocations towards the surface occurred along both <111> and <100> directions (Figure 2.7). The dislocation moved about 1.2 nm towards the {100} surfaces over a period of 25 min (Figure 2.7c), and 0.78 nm in 20 min towards the {111} surfaces (Figure 2.7d). The final positions of the dislocations were about 2.4 nm from the {100} surfaces and 1.6 nm from the {111} surfaces. Distance between the position of dislocation and surface had an exponential decay relationship with respect to time along both directions (Figure 2.7c-d). Our data also show migration along the <111> direction reaching final stage, *i.e.*, steady-state, faster than the <100> direction.

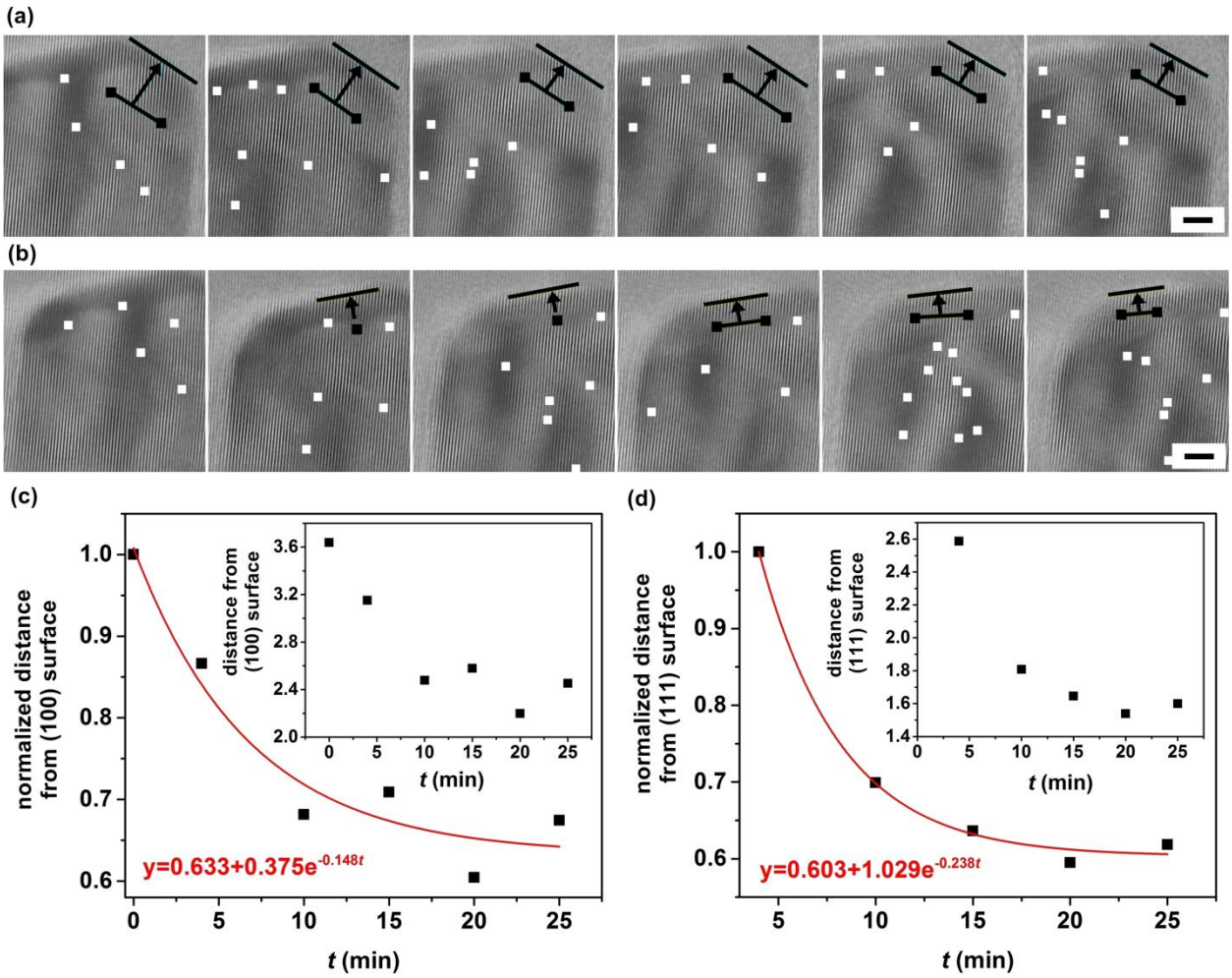

Figure 2.7 (a-b) TEM micrographs and (c-d) fitting curve of dislocation movement as a function of time along (a, c) <100> and (b, d) <111> directions, respectively. The fitting curves were drawn based on the Fick's law. The squares highlight the positions of the edge of dislocation planes. The black squares were used to obtain the distances from the surface. Scale bar is 2 nm, applicable to all.

Fick's second law of one-dimensional diffusion was used to gain semi-quantitative understanding of the dislocation movement.

$$\frac{\partial C}{\partial t} = D\frac{\partial^2 C}{\partial x^2} \quad (1)$$

where C is a function describing the concentration of either Pt or Ni as a function of time (t) and position (x). D is the diffusion coefficient. The solution of the time dependent term has the general formula of:

$$C(x,t) = A(x) \cdot T(t) \quad (2)$$

$$T(t) = e^{-Dk^2 t} \quad (3)$$

where the constant k is inversely proportional to the distance between the two boundaries. Eq. (3) is essentially describing how fast the metal atoms reach equilibrium. Upon reaching equilibrium the dislocation seized to move towards the surface. Thus there should be a correlation between the movement of dislocations and the migration of metal atoms. If one of the two boundaries is set at the surface and the other is in close proximity to the dislocations, the initial location of the dislocations were 2.59 nm (L_{111}) and 3.64 nm (L_{100}) away from {111} and {100} surfaces, respectively. The ratio between the square of L_{100} and L_{111} (L_{100}^2/L_{111}^2) is 1.975. From Figure 2.7c-d, the fitted rate constant for dislocations migrating along the (111) Dk_{111} and (100) Dk_{100} directions are 0.238 and 0.148 min^{-1} respectively, with a ratio of 1.608 between the two. If the diffusivity inside a crystal is independent of the diffusion direction, the ratio should be identical between the fitted rate constant Dk_{100}/ Dk_{111} and L_{111}^2/L_{100}^2 based on eq. (3). The calculation shows a nearly 20% variation between the two values using highly simplified model, indicating that the diffusion coefficient of the dislocation along the <111> and <100> directions might be different, with the diffusion coefficient about 1.23 times larger in the <100> direction. This phenomena may origin from the different packing density of atoms in the (100) and (111) surfaces, with less densely packed planes along the <100> direction. The calculated values of

diffusion coefficient are on the order of 10^{-2} to 10^{-1} nm^2/min (10^{-22} to 10^{-21} m^2/s) along the <100> and <111> directions. While these values are very rough estimations since the assumption of the fixed boundary conditions could not really be applicable directly in the solid catalyst, they are much higher than the volume diffusion coefficient of Pt and Ni extrapolated from high temperature measurements (8.63×10^{-8} nm^2/min, or 1.44×10^{-27} m^2/s).[39-41] Hence the movement of the dislocation should reflect the grain boundary like diffusion assisted by the local atomic movement around the end regions of dislocation planes.[42] A control experiment was performed on the Pt-Ni octahedral nanoparticle at room temperature under similar operation procedure to evaluate the effects of electron beam (Figure 2.8 2.9). We did not observe the outward movement of dislocations, although we did observe variations is dislocation position.

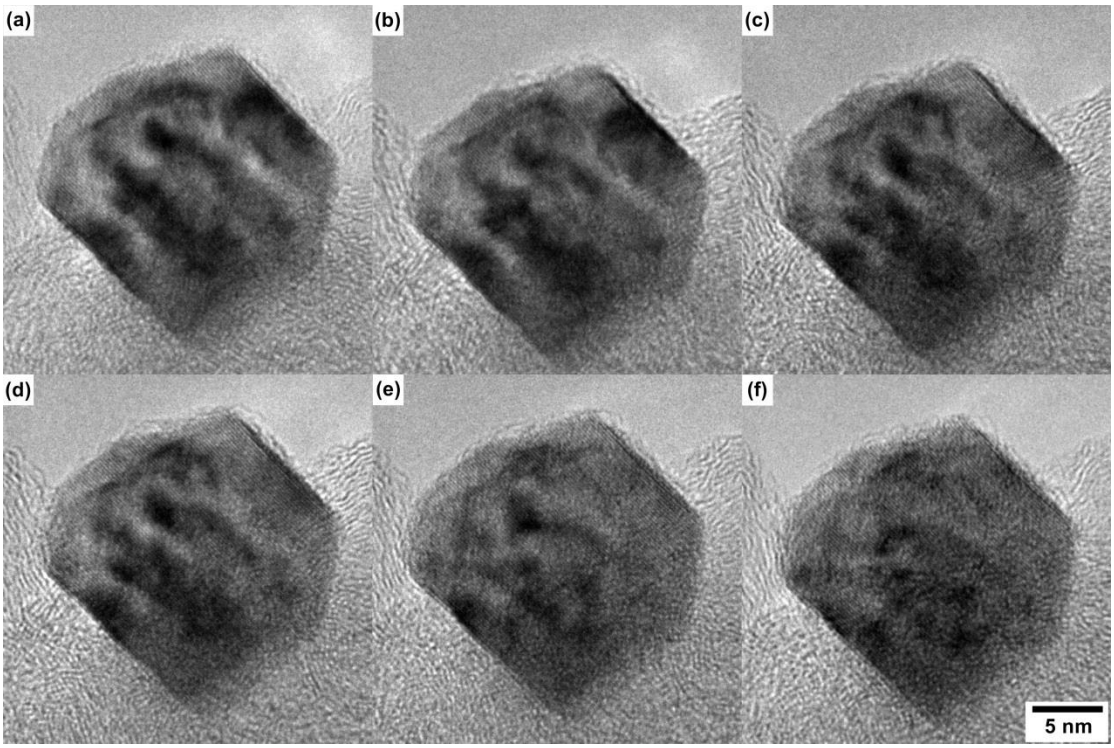

Figure 2.8 In situ TEM micrographs taken under vacuum at RT, over a time period of (a) 0, (b) 5, (c) 10, (d) 15, (e) 20, and (f) 25 min, respectively.

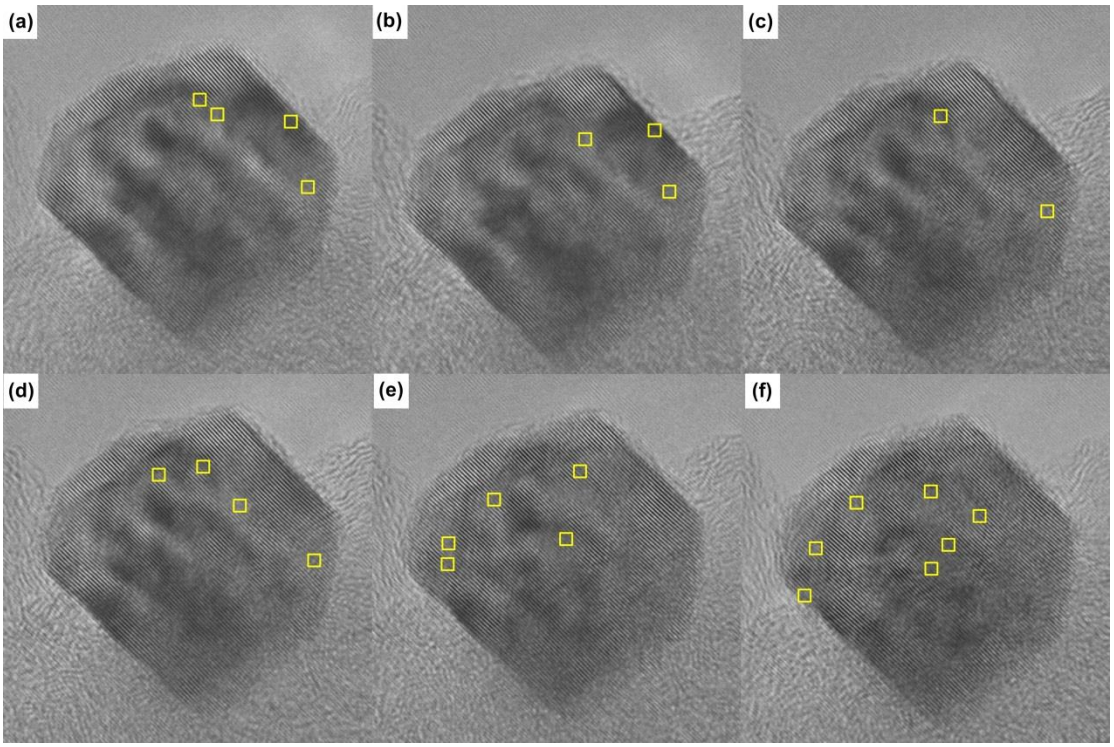

Figure 2.9 Corresponding FFT enhanced images of those shown in Figure 2.8. The yellow squares highlight the positions edges of the dislocation planes.

2.3.5 Surface composition analysis by XPS

XPS spectroscopy was performed on the carbon-supported Pt-Ni octahedral nanoparticles before and after annealing in vacuum at 210 ºC for 1 h (Figure 2.10). The survey scans indicate the surface contains Pt, Ni, C, and O. Pt existed as pure metallic form, judging by the position and shape of the binding energy peaks for Pt 4f lines. Surface Ni was present in both metal and oxide forms, with oxide as the dominant phase, judging by the position of Ni 2*p* lines. Thus the binding energy peak at 531 eV, which corresponds to O 1s line, could come from both the surface adsorb species and nickel oxides. The observation of surface nickel oxides was expected, since the samples were not stored under inert atmosphere and Ni metal atoms reacted readily

with oxygen to form NiO_x upon exposure to air. Our XPS data show the surface, including the near surface region, was composed of 90 atomic percent (at%) of Pt and 10 at% of Ni for the as-made Pt-Ni octahedral catalyst. The composition changed to 51 at% of Pt and 49 at% of Ni for the surface regions after the sample was treated at 210 ºC under vacuum for 1 h. The increase of surface Ni content was accompanied with the increase of oxide form of Ni species. Similar relation between surface Ni ratio and its oxidation state was also reported for PdNi.[42] The XPS analysis provides direct evidence of surface enrichment of Ni after the thermal treatment and agrees well with the composition change resulting from the outward movements of dislocation observed by in situ ETEM.

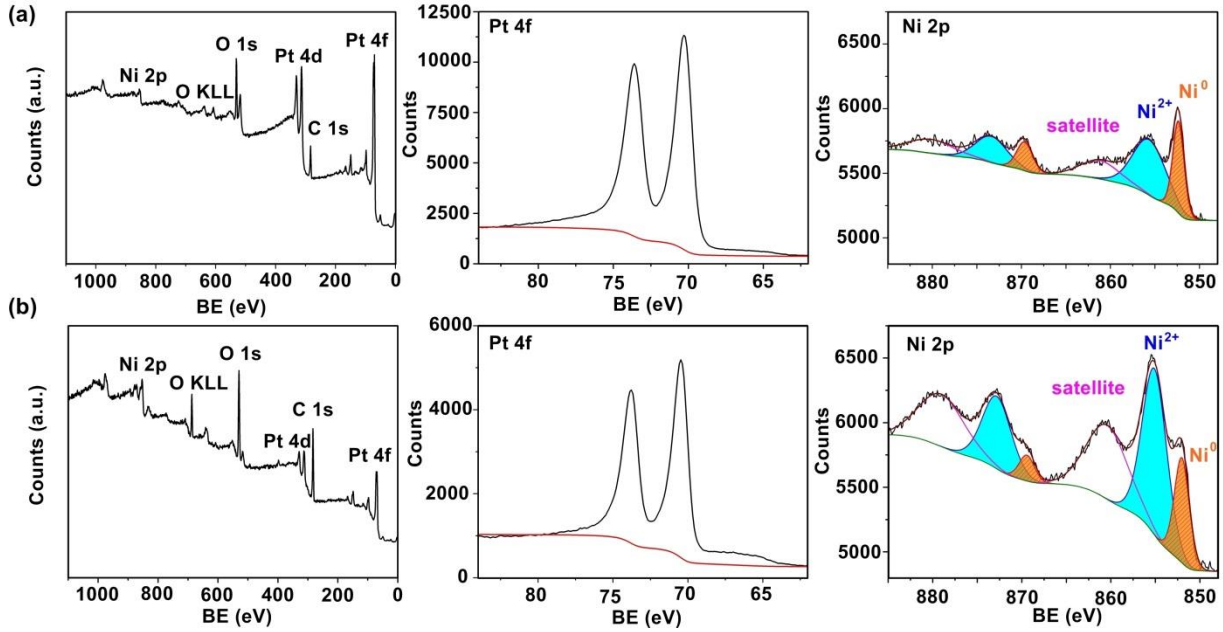

Figure 2.10 XPS spectroscopy of (a) as-made and (b) vacuum-annealed Pt-Ni octahedral catalysts, showing the survey scan (left), Pt 4f (middle), and Ni 2p (right) regions, respectively.

2.3.6 Surface composition and electrochemical reduction of oxygen

A direct consequence of redistribution of metal elements in a bimetallic nanoparticle catalyst is the change of its catalytic activity. Under the harsh acidic condition for ORR, activated surface of Pt-Ni or other Pt-based bimetallic catalyst typically consists of a Pt skin and Ni or other metal subsurface layer.[30] The carbon-supported Pt-Ni octahedral nanoparticle catalyst transformed the top 1.5-nm Pt-rich shell with more Ni contents upon thermal treatment (Scheme 1). The cyclic voltammetry (CV) shows flat curves for the hydrogen adsorption/desorption regions, indicating Pt(111) facet-dominant surfaces. Interestingly, the OH adsorption and desorption peaks between 0.6 and 0.8 V (vs. RHE) decreased continuously during the initial five CV cycles (Figure 2.11). The disappearance of these OH related peaks can be attributed to the dissolution of non-Pt metal from the surface, which was observed previously in other bimetallic electrocatalysts (Pt-Co and Pt-Cu).[32,33] After 20 CV cycles, most Ni atoms on the outmost surface of the treated catalysts were dissolved into the acidic electrolyte, resulting in the formation of Pt skin.

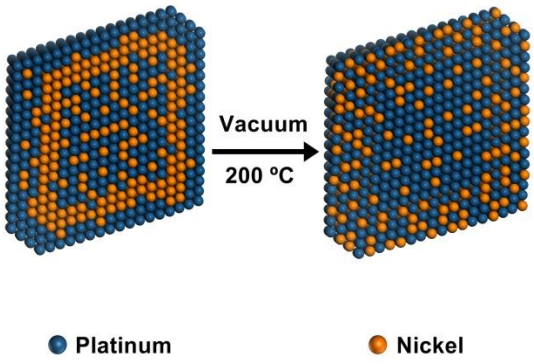

Scheme 2.1 Proposed change in composition of the sandwich-structured octahedral Pt-Ni ORR catalyst after post-synthesis thermal treatments.

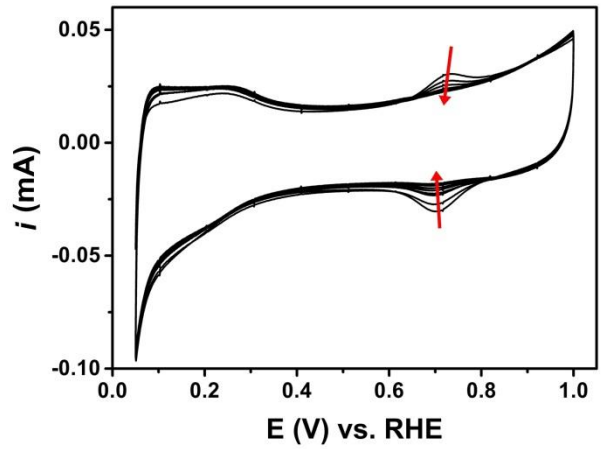

Figure 2.11 Initial CV scans of thermally-treated Pt-Ni/C octahedral catalysts. The CV was carried out in 0.1-M $HClO_4$ under Ar. Dissociation of surface Ni was evident judging by the disappearance of Ni redox peaks between 0.6 and 0.8 V (vs. RHE). (Measurement was carried out by Jianbo Wu)

These octahedral catalysts with Pt skin were then used as catalyst for ORR. A huge positive shift of 58 mV was observed in the ORR polarization measurement after the first two cycles (Figure 2.12). The ORR polarization shifted by another 28 mV in the same direction in the subsequent cycles before the curve was finally stabilized. The initial big jump of 0.58 mV could be attributed to the optimization of surface structure by removing additional Ni atoms, most likely in the top surface region. The gradual shift during the subsequent ORR polarization cycles was from the leaching of Ni atoms from the more inner and subsurface regions. Besides the applied potential, strong affinity between Ni and O atoms should also contribute to this process.[31,33] The surface structure, composing of Pt skin on Ni-containing subsurface, further optimized the reaction of oxygen with surface Pt atoms by shifting the binding energy more negatively than Pt_3Ni, namely, towards the value corresponding to the maximum current density

of volcano plot. The kinetic current density (i_s) at 0.9 V had a 6-time increase, changing from 0.42 to 2.49 mA/cm^2, and the half-wave potential ($V_{half\text{-}wave}$) increased from 0.78 V for the initial to 0.866 V for the final ORR sweeps (Fig. 7 inset). The catalyst had a final specific surface activity of 4.8 mA/cm$^2_{Pt}$ and mass activity of 1.4 A/mg$_{Pt}$. On the contrary, the as-made Pt-Ni sandwich catalysts had an ORR surface specific activity of 1.2 mA/cm$^2_{Pt}$ with little change over CV and ORR cycles (Figure 2.13).

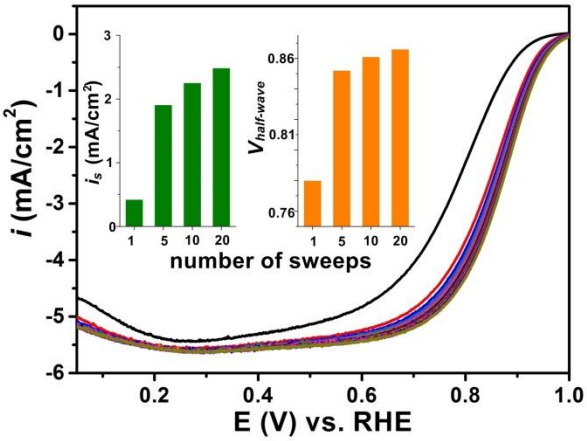

Figure 2.12 ORR polarization curves of thermally-treated Pt-Ni octahedral catalyst after CV treatments. Insets show the area specific and mass activity values after the designated number of cycles. (Measurement was carried out by Jianbo Wu)

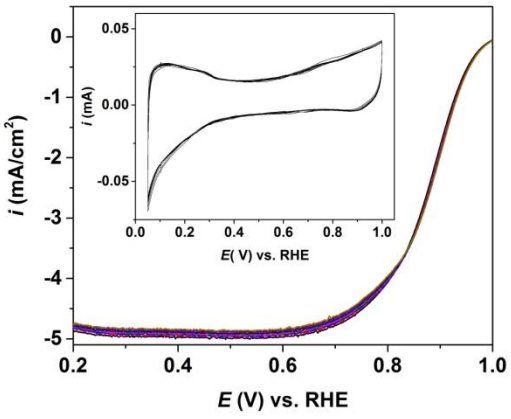

Figure 2.13 ORR polarization curves over ten repetitive cycles of as-made Pt_3Ni octahedral catalyst. Inset shows ten CV cycles performed prior to ORR. All tests were done in 0.1-M $HClO_4$ solutions under O_2 for ORR and Ar for CV.

A careful examination of CV curves shows the hydrogen adsorption/desorption region became narrower after cycling, (Figure 2.14, inset). This change could be due to the oxygen-induced enrichment of Ni at surface and subsurface layer, which also altered the OH adsorption. Theoretical studies suggest that the adsorption strength of oxygen on the (111) surface of Pt-Ni with a Pt skin layer is slightly weaker than that required for maximum ORR activity.[44] Our study suggests that the formation of Ni-enriched near surface alloy layer changed the adsorption strength of oxygen in comparison to a pure Ni subsurface layer, because Ni in Pt causes the upshift of the d-band center of the {111} surface of Pt-Ni towards the value expected for maximum ORR activity.[44,45] Based on the above TEM, XRD, XPS observations and ORR characterization, a composition-redistribution process can thus be derived and is summarized in Scheme 2.2.

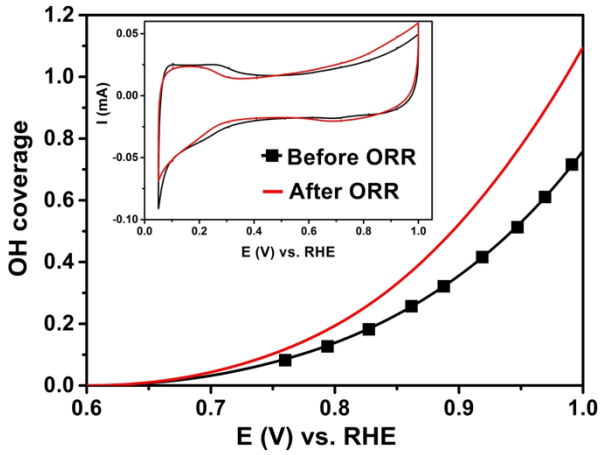

Figure 2.14 Coverage of hydroxyl group on surface of the Pt-Ni octahedral catalyst before and after ORR tests. Inset shows the corresponding CV curves. (Measurement was carried out by Jianbo Wu)

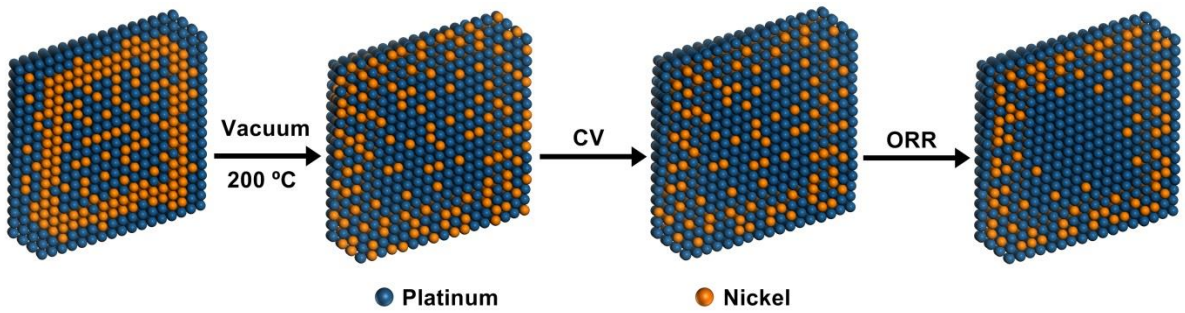

Scheme 2.2 Proposed change in composition of the sandwich-structured octahedral Pt-Ni ORR catalyst after post-synthesis thermal treatments.

2.4 Conclusions

In sum, in situ ETEM study under reacting conditions, together with XPS data, provide direct evidence to show dislocation movement is one structural factor likely to be the origin for much enhanced ORR catalytic performance. The three-layered structure of Pt-Ni octahedral nanoparticle catalyst that has Pt-rich shell and core is rather unique and worthwhile for further exploration. The degree of enhancement in ORR activity (1.4 A/mg_{Pt} in mass activity and 4.8 mA/cm^2_{Pt} in area specific activity) is very high. This study highlights the tremendous potentials of post-synthesis thermal treatments and usefulness of in situ ETEM in understanding the structural origins, and subsequently the design principle of optimal electronic and surface geometric configurations for catalyst.

2.5 References

1. Wu, J.; Yang, H., *Acc. Chem. Res.* **2013,** *46*, 1848-1857.

2. Hummelshøj, J. S.; Blomqvist, J.; Datta, S.; Vegge, T.; Rossmeisl, J.; Thygesen, K. S.; Luntz, A. C.; Jacobsen, K. W.; Nørskov, J. K., *J. Chem. Phys.* **2010,** *132*, 071101.

3. Jung, H.-G.; Hassoun, J.; Park, J.-B.; Sun, Y.-K.; Scrosati, B., *Nat. Chem.* **2012,** *4*, 579-585.

4. Kim, T. W.; Choi, K.-S., *Science* **2014,** *343*, 990-994.

5. Alayoglu, S.; Nilekar, A. U.; Mavrikakis, M.; Eichhorn, B., *Nat. Mater.* **2008,** *7*, 333-338.

6. Wu, J.; Li, P.; Pan, Y.-T.; Warren, S.; Yin, X.; Yang, H., *Chem. Soc. Rev.* **2012,** *41*, 8066-8074.

7. Huang, X.; Zhao, Z.; Cao, L.; Chen, Y.; Zhu, E.; Lin, Z.; Li, M.; Yan, A.; Zettl, A.; Wang, Y. M.; Duan, X.; Mueller, T.; Huang, Y., *Science* **2015,** *348*, 1230-1234.

8. Wu, J.; Gross, A.; Yang, H., *Nano Lett.* **2011,** *11*, 798-802.

9. Xia, Y.; Xiong, Y.; Lim, B.; Skrabalak, S. E., *Angew. Chem. Int. Ed.* **2009,** *48*, 60-103.

10. Carpenter, M. K.; Moylan, T. E.; Kukreja, R. S.; Atwan, M. H.; Tessema, M. M., *J. Am. Chem. Soc.* **2012,** *134*, 8535-8542.

11. Vitos, L.; Ruban, A. V.; Skriver, H. L.; Kollár, J., *Surf. Sci.* **1998,** *411*, 186-202.

12. Tao, F.; Grass, M. E.; Zhang, Y.; Butcher, D. R.; Renzas, J. R.; Liu, Z.; Chung, J. Y.; Mun, B. S.; Salmeron, M.; Somorjai, G. A., *Science* **2008,** *322*, 932-934.

13. Beaumont, S. K.; Alayoglu, S.; Pushkarev, V. V.; Liu, Z.; Kruse, N.; Somorjai, G. A., *Faraday. Discuss.* **2013,** *162*, 31-44.

14. Mayrhofer, K. J. J.; Juhart, V.; Hartl, K.; Hanzlik, M.; Arenz, M., *Angew. Chem. Int. Ed.* **2009,** *48*, 3529-3531.

15. Tenney, S. A.; Ratliff, J. S.; Roberts, C. C.; He, W.; Ammal, S. C.; Heyden, A.; Chen, D. A., *J. Phys. Chem. C* **2010,** *114*, 21652-21663.

16. Tao, F.; Salmeron, M., *Science* **2011,** *331*, 171-174.

17. Zheng, F.; Alayoglu, S.; Pushkarev, V. V.; Beaumont, S. K.; Specht, C.; Aksoy, F.; Liu, Z.; Guo, J.; Somorjai, G. A., *Catal. Today* **2012,** *182*, 54-59.

18. Cui, C.; Ahmadi, M.; Behafarid, F.; Gan, L.; Neumann, M.; Heggen, M.; Cuenya, B. R.; Strasser, P., *Faraday Discuss.* **2013**, *162*, 91-112.

19. Chenna, S.; Crozier, P., *Microsc. Microanal.* **2011,** *17*, 1602-1603.

20. Chenna, S.; Crozier, P. A., *Micron* **2012,** *43*, 1188-1194.

21. Chenna, S.; Crozier, P. A., *ACS Catal.* **2012,** *2*, 2395-2402.

22. Yoshida, H.; Kuwauchi, Y.; Jinschek, J. R.; Sun, K.; Tanaka, S.; Kohyama, M.; Shimada, S.; Haruta, M.; Takeda, S., *Science* **2012,** *335*, 317-319.

23. Xin, H. L.; Alayoglu, S.; Tao, R.; Genc, A.; Wang, C.-M.; Kovarik, L.; Stach, E. A.; Wang, L.-W.; Salmeron, M.; Somorjai, G. A.; Zheng, H., *Nano Lett.* **2014,** *14*, 3203-3207.

24. Strasser, P., *Science* **2015**, *349*, 379-380.

25. Peng, Z.; Yang, H., *Nano Today* **2009**, *4*, 143-164.

26. Wu, J.; Qi, L.; You, H.; Gross, A; Li, J.; Yang, H., *J. Am. Chem. Soc.* 2012,*134*, 11880-11883.

27. Wu, J.; Zhang, J.; Peng, Z.; Yang, S.; Wagner, F. T.; Yang H., *J. Am. Chem. Soc.* **2010**, *132*, 4984-4985.

28. Zhang, J.; Yang, H.; Fang, J.; Zou, S., *Nano Lett.* **2010**, *10*, 638-644.

29. Choi, S.-I.; Xie, S.; Shao, M.; Odell, J. H.; Lu, N.; Peng, H.-C.; Protsailo, L.; Guerrero, S.; Park, J.; Xia, X.; Wang, J.; Kim, M. J.; Xia, Y., *Nano Lett*. **2013**, *13*, 3420-3425.

30. Stamenkovic, V. R.; Fowler, B.; Mun, B. S.; Wang, G. F.; Ross, P. N.; Lucas, C. A.; Markovic, N. M., *Science* **2007,** *315*, 493-497.

31. Ma, Y.; Balbuena, P. B., *Surf. Sci.* **2008,** *602*, 107-113.

32. Cui, C.; Gan, L.; Heggen, M.; Rudi, S.; Strasser, P., *Nat. Mater.* **2013,** *12*, 765-771.

33. Callejas-Tovar, R.; Balbuena, P. B., *Surf. Sci.* **2008,** *602*, 3531-3539.

34. Strasser, P.; Koh, S.; Anniyev, T.; Greeley, J.; More, K.; Yu, C.; Liu, Z.; Kaya, S.; Nordlund, D.; Ogasawara, H.; Toney, M. F.; Nilsson, A., *Nat. Chem.* **2010,** *2*, 454-460.

35. Kim, J.; Lee, Y.; Sun, S., *J. Am. Chem. Soc.* **2010,** *132*, 4996-4997.

36. Chen, C.; Kang, Y.; Huo, Z.; Zhu, Z.; Huang, W.; Xin, H. L.; Snyder, J. D.; Li, D.; Herron, J. A.; Mavrikakis, M.; Chi, M.; More, K. L.; Li, Y.; Markovic, N. M.; Somorjai, G. A.; Yang, P.; Stamenkovic, V. R., *Science* **2014,** *343*, 1339-1343.

37. Gan, L.; Cui, C.; Heggen, M.; Dionigi, F.; Rudi, S.; Strasser, P., *Science* **2014,** *346*, 1502-1506.

38. Zhang, L.; Roling, L.T.; Wang, X.; Vara, M.; Chi, M.; Liu, J.; Choi, S-I.; Park, J.; Herron, J. A.; Xie, Z.; Mavrikakis, M.; Xia, Y., *Science* **2015**, *349*, 412-416.

39. Markus, S.; Michael, L.; Manuel, R.; Bogdan, S., *J. Phy.-Condens. Mat.* **2013,** *25*, 065401.

40. Leitner, M.; Sepiol, B.; Stadler, L.-M.; Pfau, B.; Vogl, G., *Nat. Mater.* **2009,** *8*, 717-720.

41. Gong, W.; Zhang, L.; Yao, D.; Zhou, C., *Scripta Mater.* **2009,** *61*, 100-103.

42. Herzig, C.; Divinski, S. V., *Mater. Trans.* **2003,** *44*, 14-27.

43. Shen, S. Y.; Zhao, T. S.; Xu, J. B.; Li, Y. S., *J. Power Sources* **2010,** *195*, 1001-1006.

44. Stamenkovic, V.; Mun, B. S.; Mayrhofer, K. J. J.; Ross, P. N.; Markovic, N. M.; Rossmeisl, J.; Greeley, J.; Nørskov, J. K., *Angew. Chem. Int. Ed.* **2006,** *45*, 2897-2901.

45. Hammer, B.; Nørskov, J. K., Theoretical surface science and catalysis—calculations and concepts. In *Advances in Catalysis*, Bruce C. Gates, H. K., Ed. Academic Press: 2000; Vol. Volume 45, pp 71-129.

Chapter 3

Regioselective Atomic Rearrangement of Ag-Pt Octahedral Catalysts by Chemical Vapor-Assisted Treatment[1]

3.1 Introduction

Heterogeneous catalyst plays an essential role in a wide range of applications ranging from chemical synthesis,[1] to environmental engineering,[2-3] to energy-related processes.[4-5] Among the various catalytic materials, bimetallic nanoparticles serve as an important class of catalyst for thermally[6-7] and electrochemically[8] driven reactions where the performance depends strongly on the shape and surface structures, including elements on the top layer and subsurface regions.[9-10] While synthetic procedures are available to produce monodisperse bimetallic nanoparticles with uniform size and shape,[11-12] these structurally well-defined bimetallic nanoparticles often do not show the optimal performance as catalysts. A main reason lies in the fact there exists a mismatch between the surface structure and composition of as-made nanoparticles and those required for the optimal performance. Thus, it is desirable to develop a facile approach that is capable of restructuring the surface without significantly modifying the preferred shape of catalysts, and it remains an experimental challenge to engineer the surface and near surface atomic arrangements of shape- and size-defined bimetallic catalysts to maximize the facet-dependent performance.[13]

Thermal treatment in air or inert gas atmosphere has been the main post-synthesis processing method for catalysts, though this approach often results in uncontrollable changes in the nanoparticle shape and size due to the requirement of high processing temperature. Surface

[1] Modified with permission, from Pan, Y.-T.; Yan, L.; Shao, Y.-T.; Zuo, J.-M.; Yang, H. *Nano Lett.* **2016**, *16*, 7988-7992.

composition of spherical bimetallic nanoparticles, however, were found to change almost reversibly through thermal treatments under reactive gaseous environments.[14-17] In situ environmental transmission electron microscopy (ETEM) is a major technique for studying the dynamics of structural changes.[18-20] Compared to ambient pressure X-ray photoelectron spectroscopy (AP-XPS), which has excellent surface chemical sensitivity, ETEM is capable of analyzing local elemental distribution in bimetallic nanoparticles at both high spatial and temporal resolutions.[21] For instance, in situ ETEM was successfully used recently to examine the detailed dynamics in the surface and bulk composition changes of Pt-Ni sandwiched octahedral nanoparticles during the process of thermal treatment.[19]

In this work, we show that by simply using CO or argon (Ar) vapors, one can effectively regulate site-preferred elemental distribution of surface atoms for Ag-Pt octahedral nanoparticle catalysts. In situ ETEM was used to gain the critical insight into the atomic-level regioselective dynamics of bimetallic structures under different chemical vapors (CO and Ar). Density functional theory (DFT) calculations were carried out to analyze the energetics of the relevant Ag, Pt and AgPt metal surfaces with and without CO gas to account for the observed chemical vapor-regulated surface atomic structures.

3.2 Experimental

3.2.1. Materials and chemicals

Silver nitrate ($AgNO_3$, 99.85%, ACROS); potassium tetrachloroplatinate(II) (K_2PtCl_4, 46.4% Pt, Alfa Aesar); polyallylamine hydrochloride (PAH, Alfa Aesar); formaldehyde (HCHO, 37%, MACRON Fine Chemicals); acetic acid (AA, >99.7%, Glacial, Fisher Scientific);

ammonium hydroxide (NH_4OH, MACRON Chemicals); carbon black (Vulcan XC-72, Cabot); α-Al_2O_3 (Alfa-Aesar); perchloric acid (70%, VERITAS double distilled, GFS chemicals); formic acid (88%, GFS chemicals); propanol (LC-MS Reagent, J.T.Baker); Nafion 117 solution (Sigma-Aldrich); carbon monoxide (CO, research grade, Airgas); argon (Ar, UHP grade, Airgas); propylene (PP, UHP, Airgas); H_2 (5% balanced N_2, Airgas). All were used as received.

3.2.2 Preparation of stock solutions

Stock solution of K_2PtCl_4 (0.05 M) was made by dissolving 103.77 mg of K_2PtCl_4 into 5 mL of deionized water. $AgNO_3$ stock solution (0.05 M) was prepared by dissolving 42.4 mg of $AgNO_3$ in 5 mL of deionized water. PAH stock solutions (0.5 M) were prepared by dissolving 472.5 mg of PAH into 10 mL of deionized water.

3.2.3 Synthesis of Ag-Pt octahedral nanoparticles

Ag-Pt octahedral nanoparticles were prepared via a modified hydrothermal method reported elsewhere.[22] In short, 0.5 mL of 0.05-M potassium tetrachloroplatinate (K_2PtCl_4), 0.5 mL of 0.05-M silver nitrate ($AgNO_3$), and 1.0 mL of 0.5-M polyallylamine hydrochloride (PAH) were well mixed by continuous stirring at 500 rpm in 7.5 mL of water in a 25-mL Teflon liner for 15 min. Then, 1.0 mL of HCHO solution (37%) was added into the mixture and stirred for another min. The Teflon liner was then sealed, placed into a stainless-steel autoclave, and transferred into an oven that was preheated to 180 ºC for reaction. After reaction for 4 h, the autoclave was cooled down under ambient conditions and the products were separated by centrifugation. The products were then washed with deionized (DI) water by sonication and

centrifugation cycles for five times using aqueous acetic acid solution (5 vol%) as the dispersing agent and aqueous ammonium hydroxide solution (10 vol%) as the precipitation agent.

3.2.4. Preparation of carbon-supported catalysts

Carbon black (Vulcan XC-72) was used as support for making Ag-Pt catalysts (Ag-Pt/C). In a standard preparation, carbon black particles were dispersed in ethanol and sonicated for 1 h. A designed amount of octahedral Ag-Pt nanocrystal suspension in water was added to this dispersion of carbon black at the nanoparticle-to-carbon-black mass ratio of 20:80. This mixture was further sonicated for 30 min and stirred overnight. The resultant solids were precipitated out by centrifugation and dried in a vacuum oven at 60 ºC for 2 h.

A calibration curve was measured and used to accurately determine the amount of different octahedral Ag-Pt nanocrystal catalysts deposited on the rotating disk electrode. The calibration curve was constructed based on the measurement of extinction at 700 nm the UV-Vis spectra, showing a linear relationship with the concentration (Figure 3.1). The ink was made by using carbon black dispersed in a stock solution containing water, propanol and nafion with a ratio of 80:20:0.05. The mass concentration was 1 mg carbon per mL of stock solution. The predetermined concentration for all catalyst samples was adjusted to 0.8 mg/mL by the UV-Vis spectrometer. A total of 30 μg of catalyst was deposited on the RDE by drop casting in three times, using 12.5 μL of the ink each time.

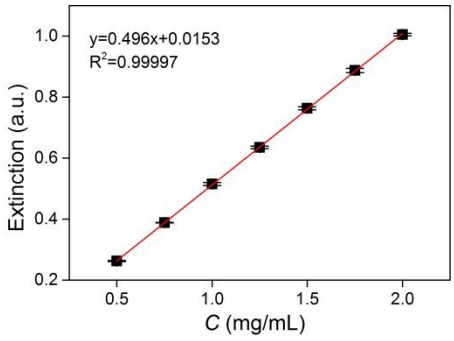

Figure 3.1 Calibration curve showing the relation between the mass concentration of carbon in water versus extinction at 700 nm measured by UV-Vis spectrometer.

3.2.5. Preparation of α-Al_2O_3 supported catalysts

α-Al_2O_3 (Vulcan XC-72) support Ag-Pt catalysts was prepared by physically mixing the Ag-Pt colloids with dispersion of α-Al_2O_3 powders in 50mL of DI-water on a stir plate at room temperature. The mass concentration of the Ag-Pt colloid was determined by measuring the mass of the dry powders after evaporating a known amount of solvent. The Ag-Pt was 1 wt% of α-Al_2O_3. The mixture was vigorously stirred overnight, separated by centrifugation, and dried in a 50 °C vacuum oven (Symphony Vacuum Oven, VWR) for 5h.

3.2.6 Chemical vapor treatment of Ag-Pt octahedral nanoparticles and catalysts

Ex situ treatment of Ag-Pt octahedral nanoparticles were performed using a tube furnace (Lindburg/Blue M, Thermo Scientific) under alternating CO or Ar atmosphere. The Ag-Pt octahedral particles for TEM study were either deposited on a TEM grid, on a carbon support, or a α-Al_2O_3 support. The flow rate was set at 100 sccm for CO gas and 300 sccm for Ar. The

temperature for heat treatment was ramped to the predetermined value at a heating rate of 10 ºC/min and then kept constant throughout the course of the experiment. The temperature was then cooled down naturally to room temperature under CO or Ar. All treatments were carried out using the same batch to exclude any errors that would potentially be introduced during synthesis and loading processes.

3.2.7 Characterization

TEM and STEM characterization was performed using JEOL Cryo 2100 and JEOL 2010F (S)TEM TEM at an accelerating voltage of 200 kV. Cs-corrected HAADF-STEM was carried out in the JEOL 2200 FS STEM with Schottky field emitter and a spherical aberration corrector (Cs-corrector) at an accelerating voltage of 200 kV. XRD patterns were acquired using a Bruker D8 Venture Duo diffractometer. XPS measurements were carried out using a Kratos Axis ULTRA spectrometer with monochromatic Al source and the spectrums were analyzed by CasaXPS software.

3.2.8 In situ ETEM study

In situ TEM study was carried out using a Hitachi H9500 Environmental Transmission Electron Microscope (ETEM) at an accelerating voltage of 300 kV (3μA) and a current density of 4.15×10^{-11} A/cm^2. AgPt octahedral nanoparticles were deposited using fine tip brush onto a tungsten heating wire, which serves as a heating element in the variable-temperature gas injection holder. The holder was then introduced into the Hitachi H9500 ETEM and connected to a DC power supply for resistive heating. The temperature of the heating element was referred to

the current-temperature relation chart (Hitachi). The current was set to 110 mA, correlating to a temperature of 50 ºC, and maintained throughout the course of experiments. Carbon monoxide gas was introduced through a mass flow controller (Brooks Instrument, SLA 5850S1SAB1C2A1) into the specimen chamber at a flow rate of 0.2 mL/min. TEM micrographs were recorded using the Gatan Orius SC200 CCD camera, and Gatan digital micrograph software. Electron irradiation was kept minimized during the course of the experiment in which the gun valve was opened only during image acquisition. The sample was left in dark before the next imaging cycle. Image analysis and processing were done using Digital Micrograph (DM, Gatan) and ImageJ software, respectively. Detail procedures for image processing are described elsewhere[19].

3.2.9 Electrochemical oxidation of formic acid

Electrochemical characterization of treated carbon-supported Ag-Pt octahedral catalyst was carried out in a three-electrode cell. The working electrode was prepared by depositing 30 μg of catalyst on a glassy-carbon rotating disk electrode (RDE) (area: 0.196 cm^2). A 1-cm^2 Pt foil was used as the counter electrode, and a HydroFlex hydrogen electrode as the reference. Hydrogen evolution reaction (HER) was used to calibrate this hydrogen electrode before the tests. Cyclic voltammetry was performed to determine the electrochemical active surface area (ECSA) based on proton adsorption and activity towards formic acid oxidation under Ar-saturated 0.1-M perchloric acid ($HClO_4$). A mixture of 0.1-M $HClO_4$ with 0.5-M formic acid (HCOOH) was used for study the oxidation of formic acid.

3.2.10 Propylene hydrogenation reaction

Propylene hydrogenation reaction was performed in a ¼" diameter quartz tube packed with α-Al_2O_3 supported Ag-Pt octahedral catalyst post chemical vapor treatments. The reaction was carried out under room temperature with a total flow rate of 20 mL/min (2% propylene and 5% H_2 balanced with N_2). The catalyst was pretreated under CO or Ar atmosphere at 100 ºC and quenched to room temperature for the hydrogenation reaction. In order to clean off the adsorbed CO without altering the surface atomic arrangements, the catalyst was further purged with oxygen at room temperature after the 100 ºC CO treatment. The products were analyzed online by a GC (SRI, Multigas #3) with a TCD and FID detector equipped with a methanizer with He as the carrier gas.

3.2.11 Computational details for density functional theory calculation

The DFT calculation was carried out using the plane-wave basis code CASTEP[23] with ultrasoft pseudopotentials.[24] The generalized gradient approximation (GGA) with the revised Perdew-Burke-Ernzerhof (RPBE)[25] function was applied to treat the electronic exchange and correlation. The plane-wave basis set cut-off energy was set to 300 eV. The lattice constant of an Ag_1Pt_1 unit cell was first optimized and used for building Ag-Pt slabs. The total energy was calculated for a (3×3) periodic surface with varying surface Ag/Pt ratios on (111) surface of an fcc structure slabs The edges of the octahedral nanoparticle was modeled by introducing adsorbed Ag/Pt atoms on the AgPt (110) surface. The total energy was calculated for (3x3) periodic surface by varying the surface Ag/Pt from pure Ag, Ag_1Pt_1, to pure Pt on the fcc structure (110) slabs. In all simulations, the position and composition in the second and third layers fixed to Ag_1Pt_1 (or $Ag_{50}Pt_{50}$). The Monkhorst-Pack scheme k-point grid sampling was set

to 3×4×1 for the surface and Gamma point for single CO and H_2 molecule, with a total size of 10×10×20 Å. The tolerance for convergence was 1×10^{-5} eV/atom in energy, 3×10^{-2} eV/Å in force, and 1×10^{-3} Å in displacement. The same settings were applied for calculation both in vacuum and with adsorbed CO or H_2 molecule. The CO and H_2 adsorption energy term was also calculated using the following equation:

$$E_{ad} = E(\text{molecule/surface}) - E(\text{molecule}) - E(\text{surface})$$

where E_{ad} is the adsorption energy, E(molecule) is the energy of the free molecule, E(surface) is the energy of the surface, and E(molecule/surface) is the energy of the adsorption system. E_{ad} served as a criterion to determine whether would bind and be considered as part of the surface.

3.3 Results and Discussion

3.3.1 Synthesis and characterization of alloy Ag-Pt octahedral nanoparticle

Well-defined Ag-Pt octahedral nanoparticles were synthesized using potassium tetrachloroplatinate (K_2PtCl_4) and silver nitrate ($AgNO_3$) as metal precursors in a mixture of polyallylamine hydrochloride (PAH/HCl), formaldehyde (HCHO) and water by a modified hydrothermal method reported elsewhere.[22] Powder XRD pattern shows these nanoparticles had a typical face-centered cubic (FCC) phase with the diffraction peaks positioned in between those of Ag and Pt metals, indicating the formation of Ag-Pt alloy (Figure 3.2). TEM micrograph shows the as-synthesized Ag-Pt nanocrystals have octahedral morphology (Figure 3.2, inset, Figure 3.3). High resolution (HR) TEM, scanning transmission electron microscopy (STEM), and energy dispersive X-ray spectroscopy (EDX) line-scan were also carried out to characterize the as-synthesized particles (Figure 3.4). The d-spacing was measured to be 2.29 Å, which

corresponds to the (111) lattice of Ag-Pt alloy. EDX line-scan shows similar intensity profiles between Ag L_α and Pt M_β lines, indicating both elements are evenly distributed in the Ag-Pt alloy octahedral nanocrystal.

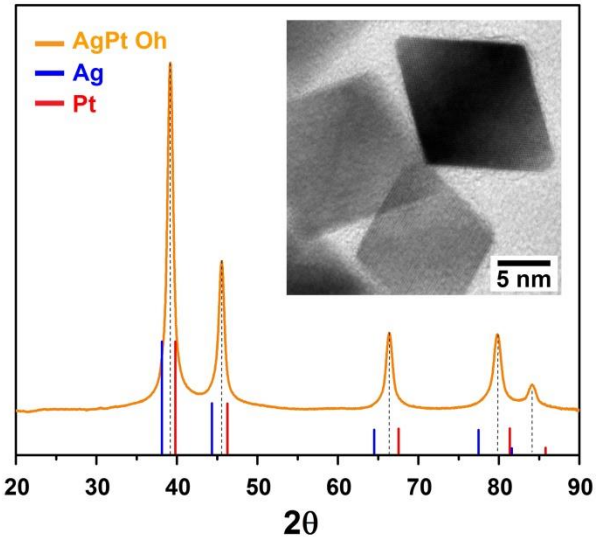

Figure 3.2 XRD and TEM characterizations of as-synthesized Ag-Pt octahedral nanocrystals.

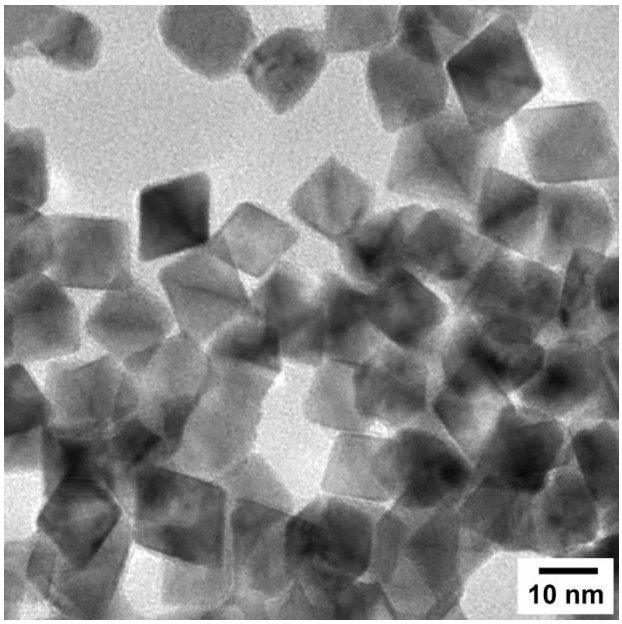

Figure 3.3 Low magnification TEM micrograph of as-prepared octahedral Ag-Pt nanocrystals.

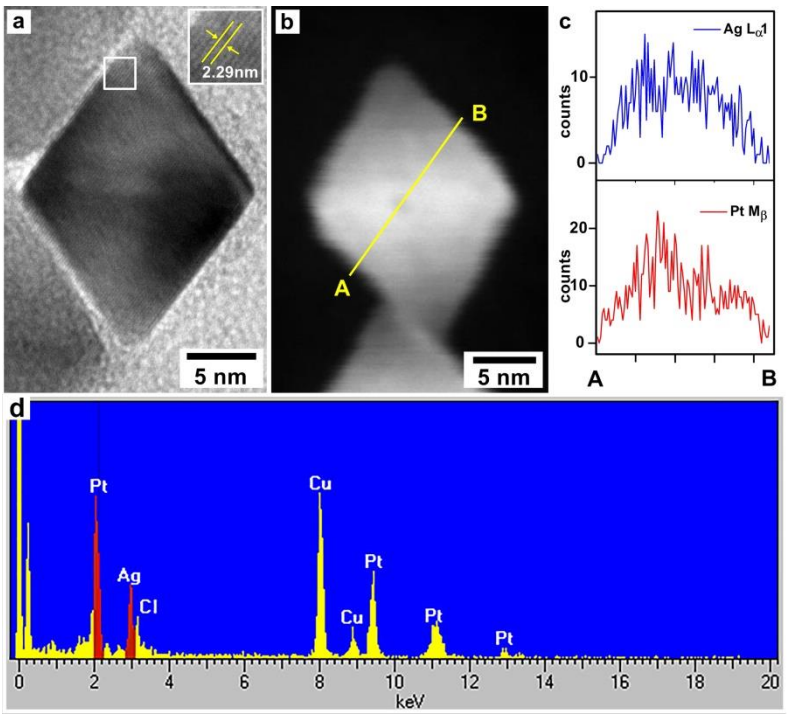

Figure 3.4 (a) HETEM micrograph, (b) STEM image, (c) EDX line scans, and (d) overall spot analysis of as-prepared Ag-Pt octahedral nanocrystals. Inset in (a) shows the lattice has the spacing of 2.29 Å.

3.3.2 Chemical vapor assisted elemental rearrangement verified by high angle annular dark field (HAADF) scanning transmission electron microscopy (STEM)

Low-temperature treatments of as-made octahedral Ag-Pt nanocrystals were carried out at 100 ºC under alternating CO and Ar atmospheres. This low temperature was designed to ensure the change of the surface composition through chemical affinity with reactive vapor molecule without the high thermal energy that could cause the change of the octahedral shape of Ag-Pt nanocrystals. CO gas was selected as its adsorption energy on these two metal surfaces are very different, *i.e.*, 0.07 eV/molecule for Ag versus -1.22 eV/molecule for Pt, showing opposite

binding trend in comparison with the intrinsic values of surface energy (0.553 eV/atom for pure Ag versus, 1.004 eV/atom for pure Pt).[26, 27] The ability of using CO gas to selectively stabilize surface Pt atoms makes it a potentially useful reagent to modify the surface composition.

Figure 3.5 shows the Z-contrast micrographs and intensity profiles of the Ag-Pt nanocrystals treated at 100 ºC under CO using high angle annular dark field (HAADF) STEM. These nanocrystals preserved the well-defined octahedral shape with a uniform intensity distribution correlated well with the geometry when they were viewed along the <110> or <100> zone axis (Figure 3.5a, b). The intensity profile of the boxed area shows a continuous decrease towards the surface, corresponding to the structural thinning near the edge (Figure 3.5a from position I to II). Meanwhile, intensity profile shows fairly even distribution along the edge (Figure 3.5b, III to IV), indicating the uniform distribution of Ag and Pt atoms at this region. When atmosphere was switched to Ar vapor however, surface distributions of Ag and Pt atoms changed dramatically and became heterogeneous. Contrast at the edge regions turned bright if viewed along the <110> zone axis, indicating Pt atoms segregated preferentially around this region (Figure 3.5c). The corresponding intensity profile in the boxed area shows a local maximum across position V and VI, indicating that Pt atoms located preferably at the edge or surface regions. If viewed from the <100> zone axis, strong intensity originated from Pt atoms formed a bright cross pattern with the maxima at the ends (Figure 3.5d, VII to VIII). This observation shows Pt atoms concentrate near the edge and corner regions. These collective evidences indicate the Ag-Pt octahedral nanoparticle changes from random alloy into a structure with Pt rich in the edge and center regions and Ag rich at the central regions of the surfaces.

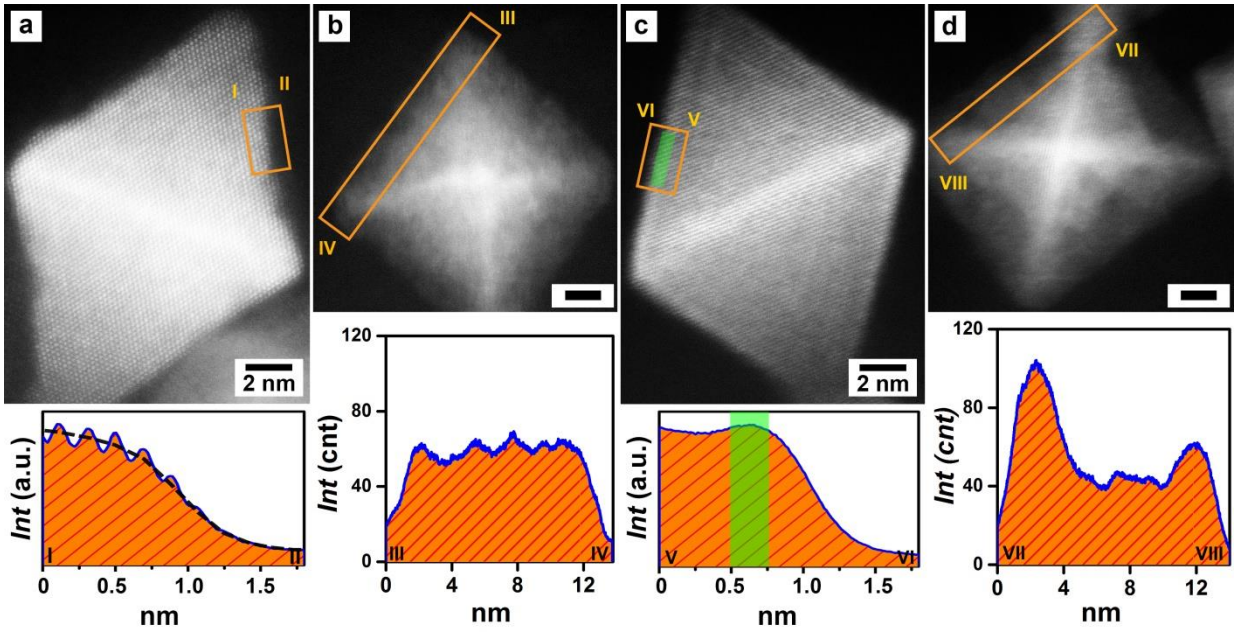

Figure 3.5 HAADF-STEM micrographs and corresponding intensity profiles of Ag-Pt ctahedral nanoparticles after ex situ treatments under CO gas at 100 ºC imaged along (a), <110> and (b), <100> zone axes; treated first under CO followed by Ar at 100 ºC: imaged along (c), <110> and (d), <100> zone axis. Scale bars are 2 nm.

The overall surface composition of Ag-Pt octahedral nanoparticles, measured by X-ray photoelectron spectroscopy (XPS), showed nearly constant Ag/Pt ratio after treatments under alternating CO/Ar atmospheres suggesting the atoms were only rearranging laterally in the near surface regions, i.e., 1.5-2 nm below the surface (Figure 3.6-7, Table 3.1).

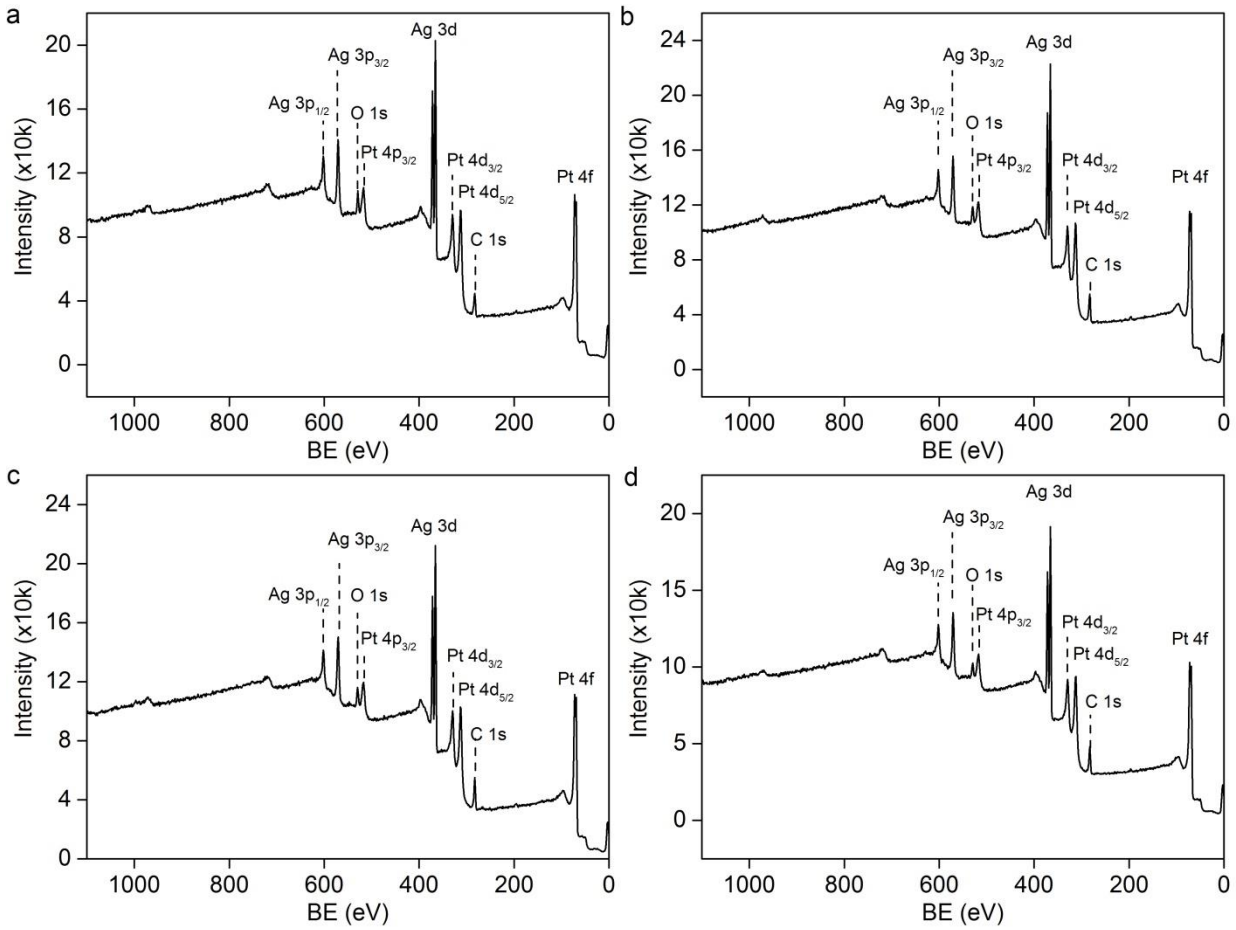

Figure 3.6 XPS survey spectra measured for Ag-Pt Oh nanoparticles treated at 100 ºC under (a) CO, (b) CO followed by Ar, (c) alternating CO-Ar-CO, and (d) CO-Ar-CO-Ar atmospheres at 100 ºC with 1 h intervals.

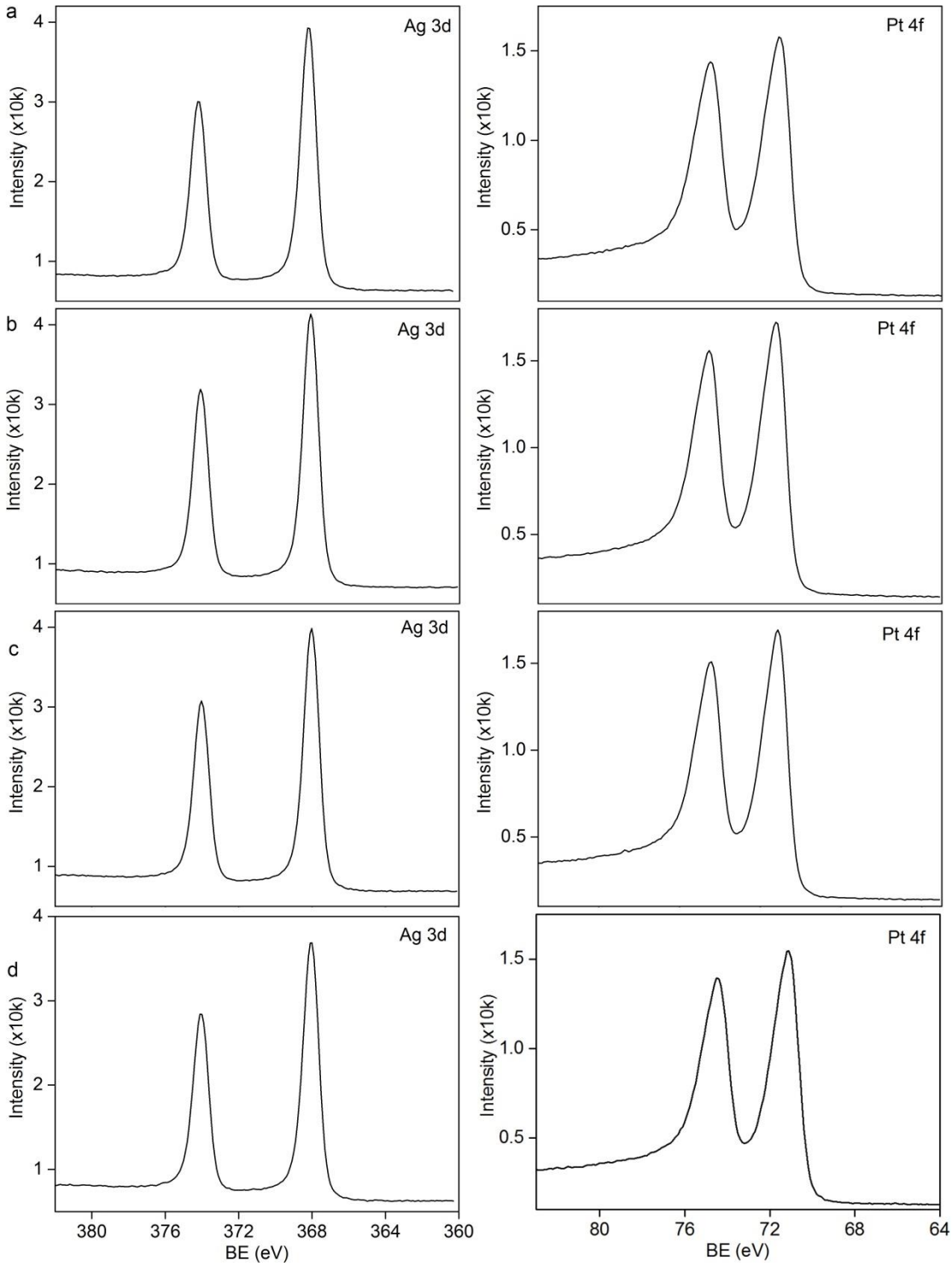

Figure 3.7 XPS Ag 3d and Pt 4f spectra measured for Ag-Pt Oh nanoparticles treated at 100 ºC under (a) CO, (b) CO followed by Ar, (c) alternating CO-Ar-CO, and (d) CO-Ar-CO-Ar atmospheres at 100 ºC with 1 h intervals.

Table 3.1 Surface Ag:Pt ratios of Ag-Pt Oh NPs treated at 100 ºC under alternating CO and Ar atmospheres measured by XPS.

Chemical vapor	CO	CO-Ar	CO-Ar-CO	CO-Ar-CO-Ar
Ag : Pt	51 : 49	50 : 50	50 : 50	50.5 : 49.5

3.3.3 In situ ETEM investigation

Variable-temperature environmental TEM (ETEM) was used to examine the dynamics of structural changes in these Ag-Pt octahedral nanocrystals in situ. The atmosphere in the sample chamber was alternated between vacuum and CO gas at a constant heating current of 110 mA, which is correlated to 50 ºC. HRTEM micrographs were acquired to analyze the dynamics in d-spacing and dislocation movements within the Ag-Pt octahedral nanocrystals using a protocol reported elsewhere.[19]

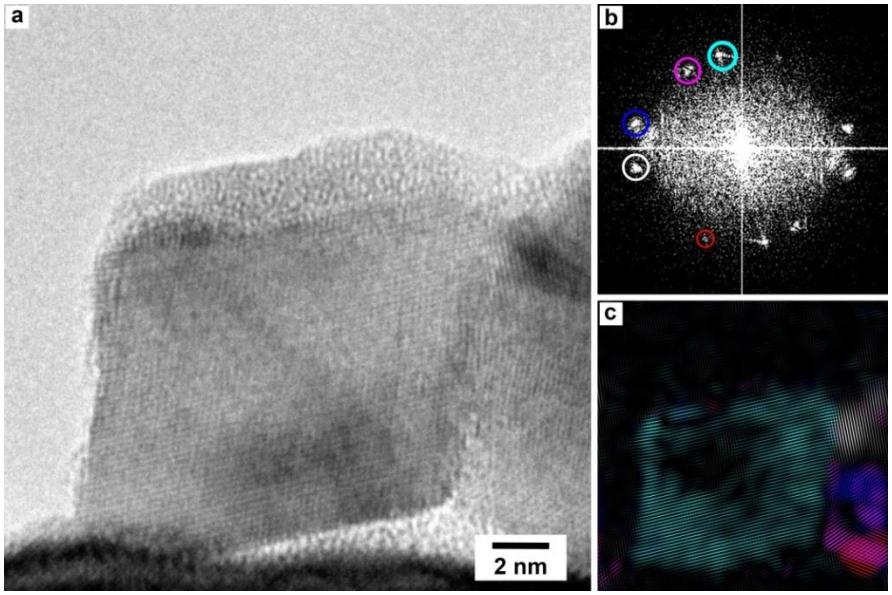

Figure 3.8 (a) As-acquired TEM micrograph, (b) the corresponding FFT image and (c) the color-coded inversed FFT image.

Figure 3.8a is a typical as-acquired TEM micrograph of the Ag-Pt octahedral nanocrystal with its corresponding fast Fourier transform (FFT, Figure 3.8b). Filtered inverse FFT (IFFT) images can be constructed on individual sets of diffraction spots where the spatial distribution of corresponding lattice fringes can be mapped out (Figure 3.8c). Since our focus is on the octahedral particle, the diffraction spot circled in cyan will be used to construct FFT enhanced images for further analysis. Using this technique, the in situ acquired micrographs of the Ag-Pt nanocrystals were studied in detail. The Ag-Pt nanocrystal was first exposed in vacuum where a series of micrographs was acquired (Figure 3.9).[1]

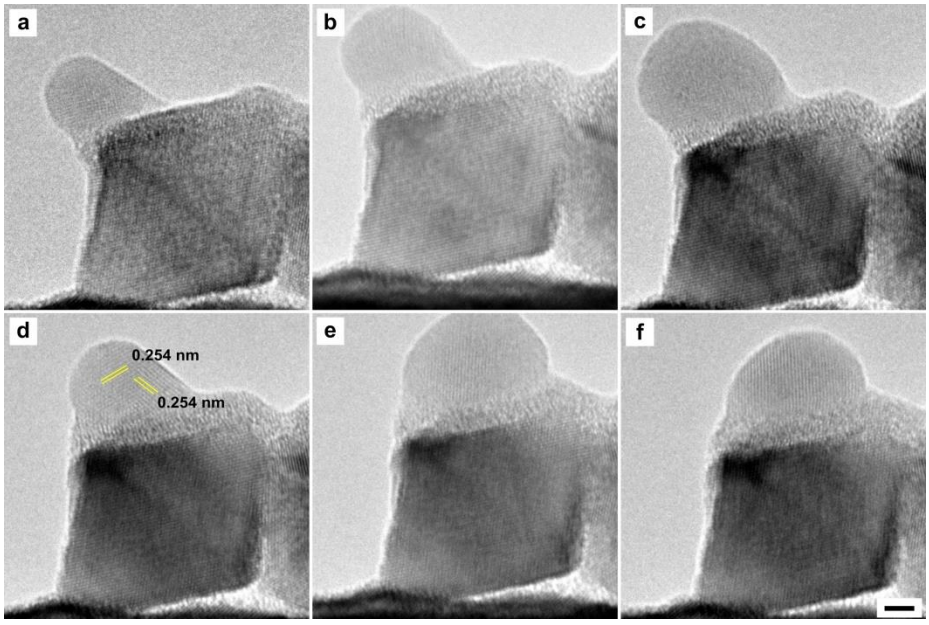

Figure 3.9 In situ ETEM micrographs showing the evolution of representative Ag-Pt octahedral nanoparticle under vacuum at 50 ºC (110 mA) as a function of time: (a) 0, (b) 6, (c) 9, (d) 16, (e) 23, (f) 27 min, respectively. Scale bar is 2 nm, applicable to all images.

[1] Lattice at the upper top left corner of the Ag-Pt octahedral nanocrystal was heavily influenced by the over-layer of AgCl salt, which passivated the upper surface and prevented it from exposing to the chemical vapor environment. The formation of AgCl salt was due to the reaction between the surface Ag and residual chlorine species from PAH/HCl which was used as the capping agent in the synthesis .

Figure 3.10 shows the FFT of the Figure 3.8 which was then used to construct the FFT enhanced images (Figure 3.11), using the approach described in Chapter 2, where the dislocations can be clearly identified (Figure 3.12).

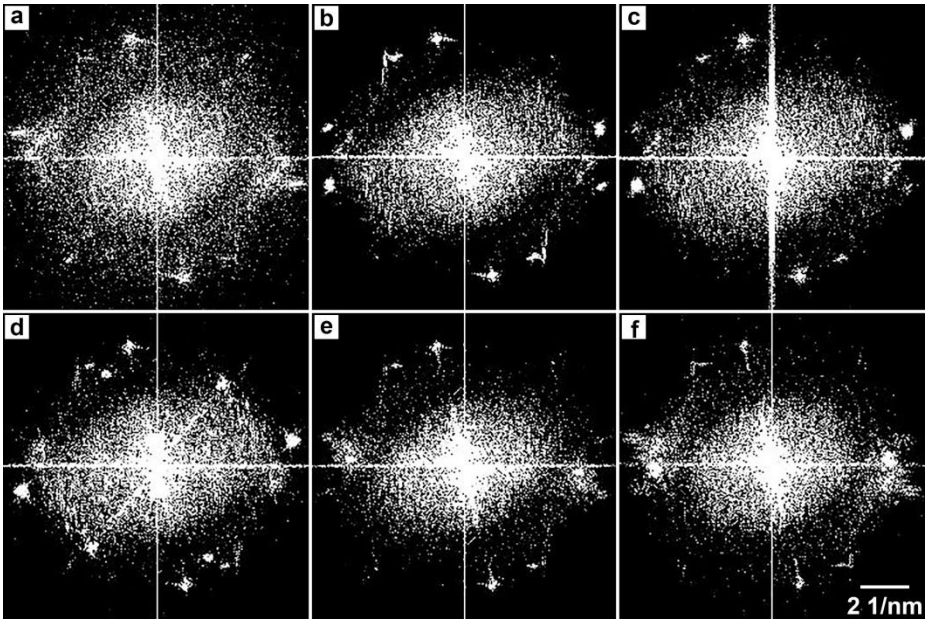

Figure 3.10 FFT images of representative ETEM micrographs in Figure 3.7 acquired under vacuum at 50 ºC (110 mA) as a function of time: (a) 0, (b) 6, (c) 9, (d) 16, (e) 23, (f) 27 min, respectively. Scale bar is 2 1/nm, applicable to all images.

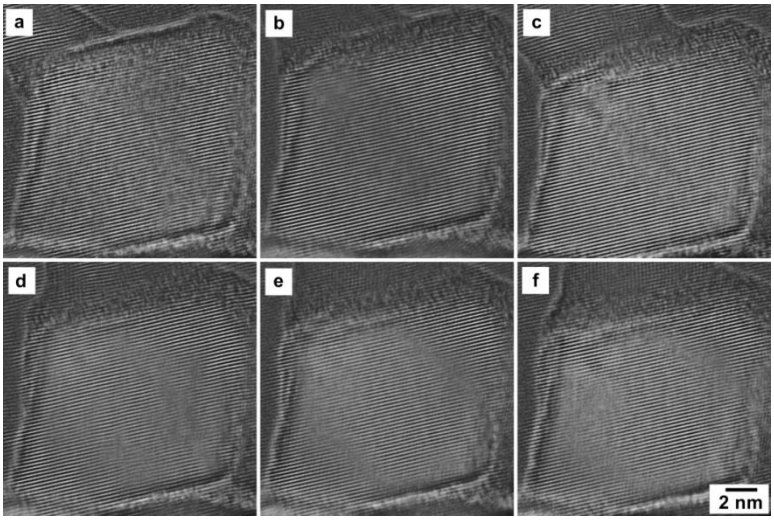

Figure 3.11 FFT-enhanced images of representative ETEM micrographs in Figure 3.7 acquired under vacuum at 50 ºC (110 mA) as a function of time: (a) 0, (b) 6, (c) 9, (d) 16, (e) 23, (f) 27 min, respectively. Scale bar is 2 nm, applicable to all images.

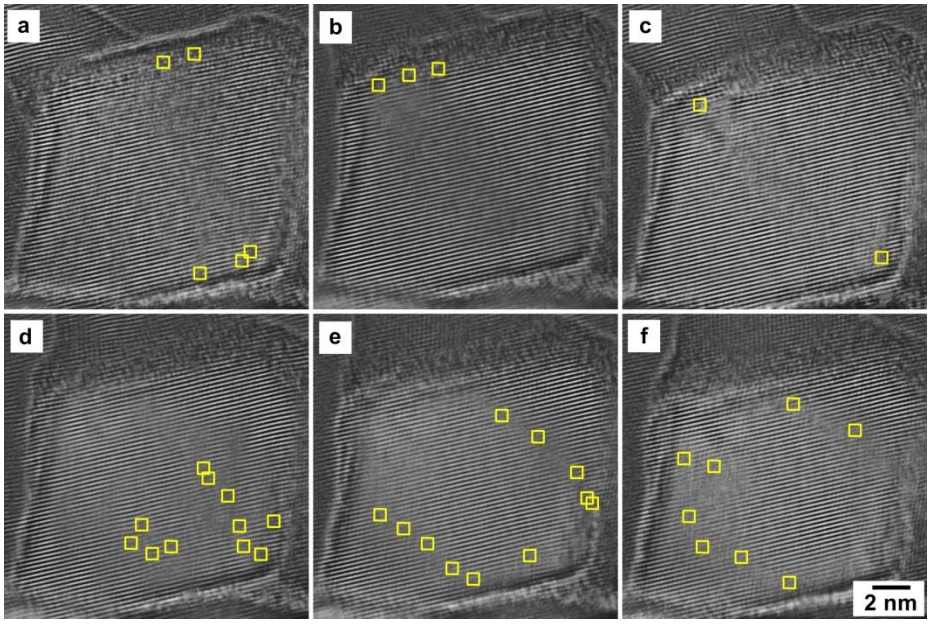

Figure 3.12 FFT-enhanced images highlighting the dislocations in representative ETEM micrographs in Figure 3.7 acquired under vacuum at 50 ºC (110 mA) as a function of time: (a) 0, (b) 6, (c) 9, (d) 16, (e) 23, (f) 27 min, respectively. Scale bar is 2 nm, applicable to all images.

The Ag-Pt nanocrystal was then exposed to CO environment (Figure 3.13-3.16) for extended period of time and back to vacuum where the acquired micrographs was analyzed using the same approach describe above. (Figure 3.17-3.20)

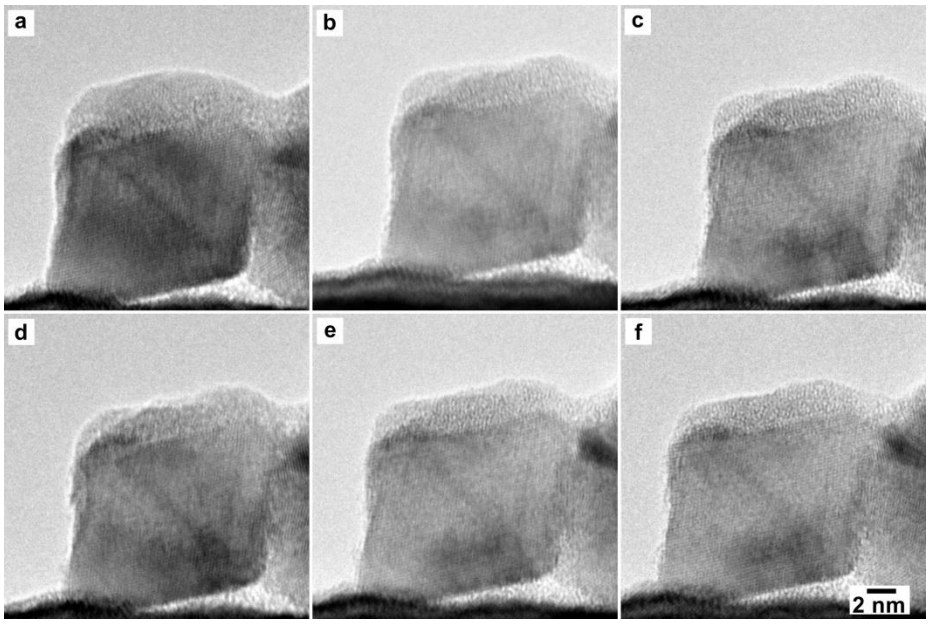

Figure 3.13 In situ ETEM micrographs showing the evolution of representative Ag-Pt octahedral nanoparticle under CO gas atmosphere at 50 ºC (110 mA): (a) 0, (b) 5, (c) 9, (d) 13, (e) 18, and (f) 24 min, respectively. The first micrograph was taken 7 min after the last image acquired in vacuum. Scale bar is 2 nm, applicable to all images.

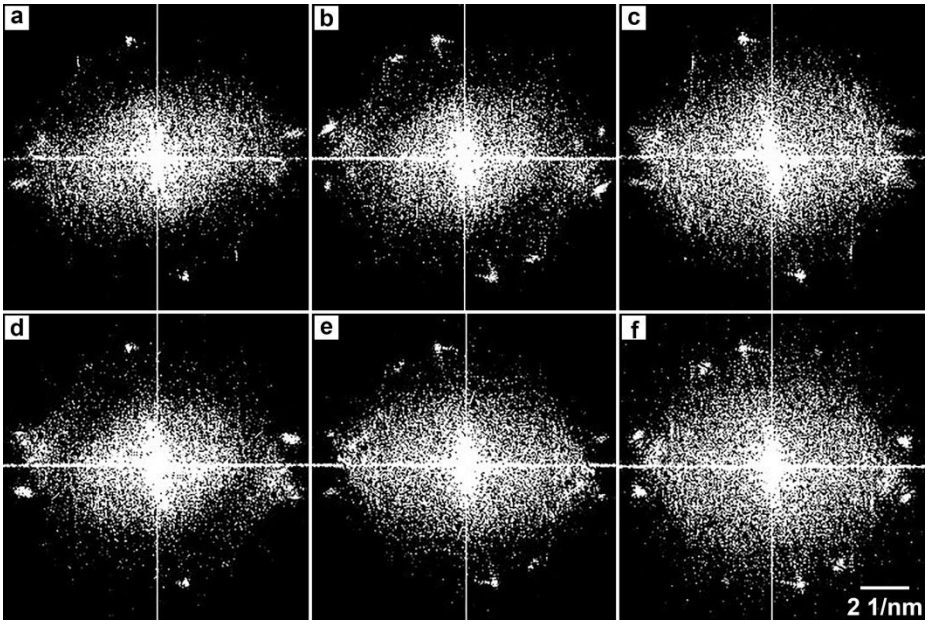

Figure 3.14 FFT-enhanced images of representative ETEM micrographs in Figure 3.11 acquired under vacuum at 50 ºC (110 mA) as a function of time: (a) 0, (b) 5, (c) 9, (d) 13, (e) 18, (f) 24 min, respectively. Scale bar is 2 1/nm, applicable to all images.

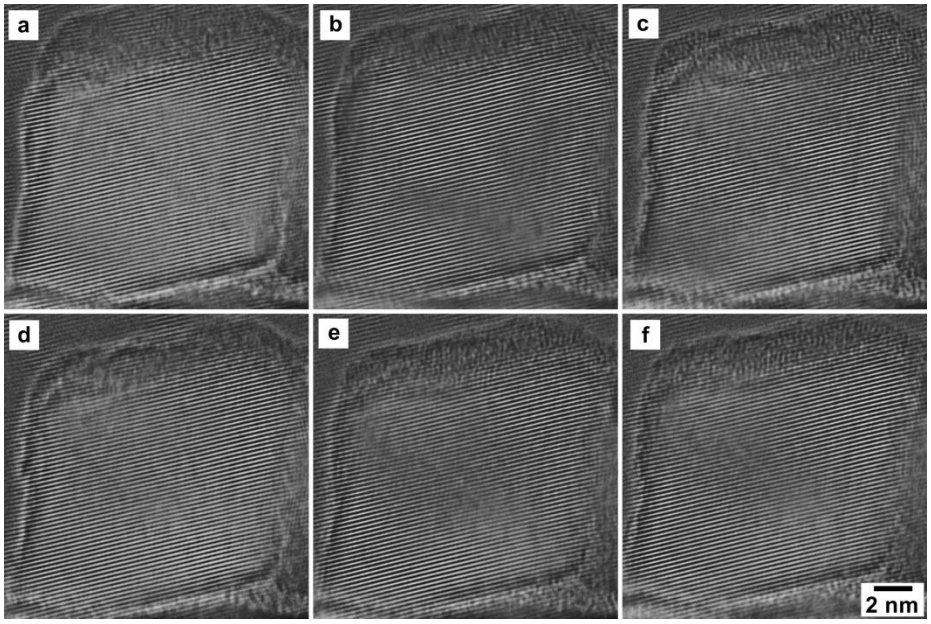

Figure 3.15 FFT-enhanced images of representative ETEM micrographs in Figure 3.11 acquired under vacuum at 50 ºC (110 mA) as a function of time: (a) 0, (b) 5, (c) 9, (d) 13, (e) 18, (f) 24 min, respectively. Scale bar is 2 nm, applicable to all images.

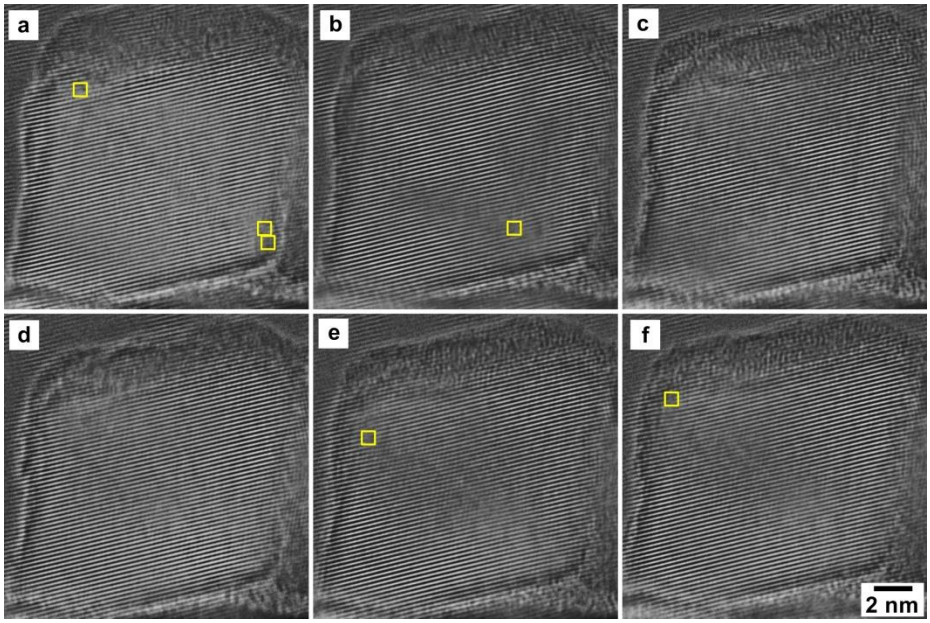

Figure 3.16 FFT-enhanced images highlighting dislocations of representative ETEM micrographs in Figure 3.11 acquired under vacuum at 50 ºC (110 mA) as a function of time: (a) 0, (b) 5, (c) 9, (d) 13, (e) 18, (f) 24 min, respectively. Scale bar is 2 nm, applicable to all images.

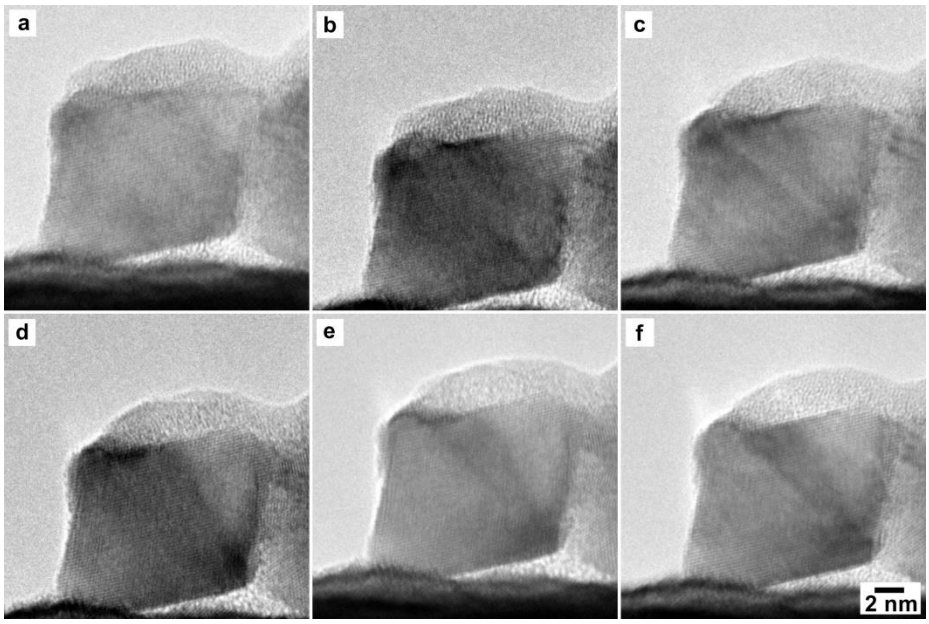

Figure 3.17 In situ ETEM micrographs showing the evolution of the Ag-Pt octahedral nanoparticle under vacuum at 50 ºC (110 mA) as a function of time: (a) 0, (b) 3, (c) 8, (d) 14, (e) 22, (f) 30 min, respectively. The first micrograph was taken 6 min after the last image acquired in CO gas. Scale bar is 2 nm, applicable to all images.

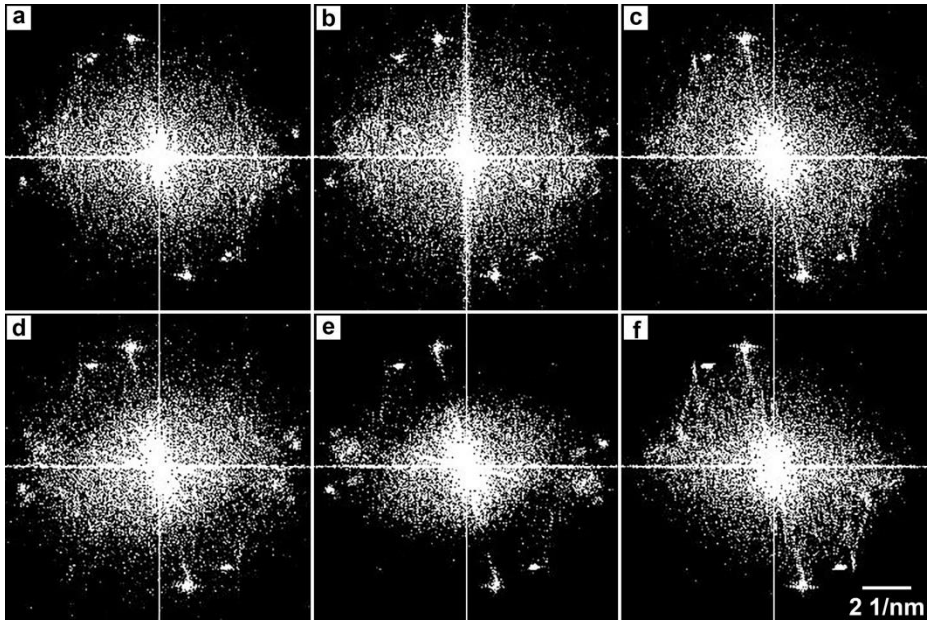

Figure 3.18 FFT images of representative ETEM micrographs in Figure 3.15 acquired under vacuum at 50 ºC (110 mA) as a function of time: (a) 0, (b) 3, (c) 8, (d) 14, (e) 22, (f) 30 min, respectively. Scale bar is 2 1/nm, applicable to all images.

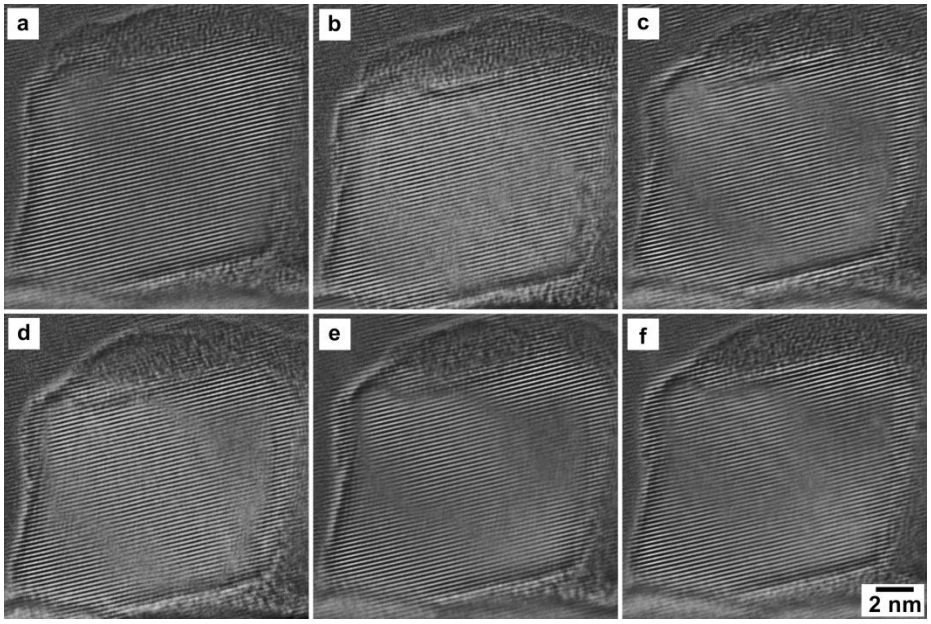

Figure 3.19 FFT-enhanced images of representative ETEM micrographs in Figure 3.15 acquired under vacuum at 50 ºC (110 mA) as a function of time: (a) 0, (b) 3, (c) 8, (d) 14, (e) 22, (f) 30 min, respectively. Scale bar is 2 nm, applicable to all images.

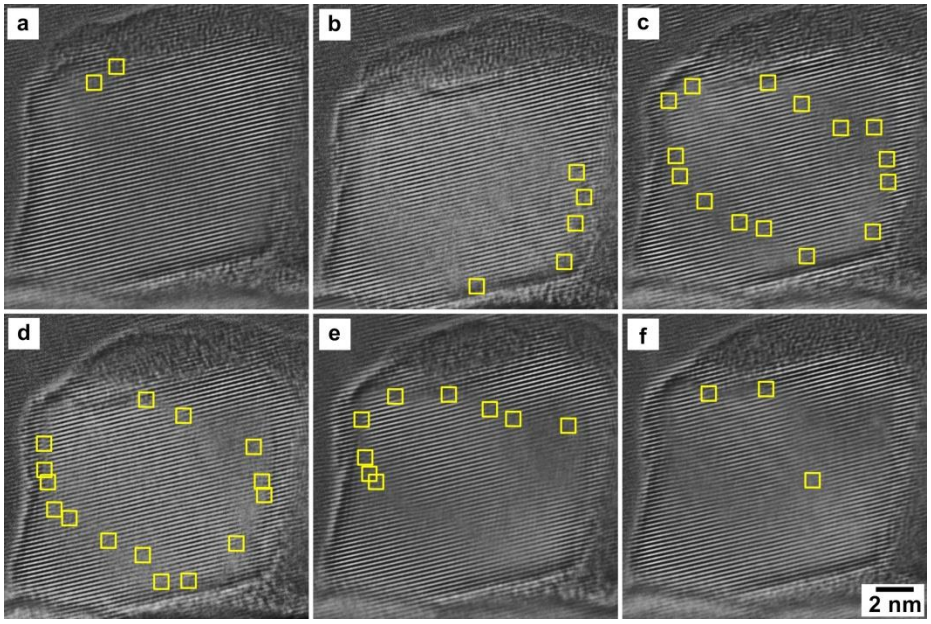

Figure 3.20 FFT-enhanced images highlighting dislocations of representative ETEM micrographs in Figure 3.15 acquired under vacuum at 50 ºC (110 mA) as a function of time: (a) 0, (b) 3, (c) 8, (d) 14, (e) 22, (f) 30 min, respectively. Scale bar is 2 nm, applicable to all images.

The number of dislocations was plot against time in Figure 3.21a. There existed a clear relation between the number of dislocations and the type of chemical vapor environment, that is, dislocations appeared in large numbers under vacuum and disappeared rapidly when CO gas was introduced or re-introduced. The observed dislocations, which are associated with the dynamics of atomic movement in solid,[19] were related to the inhomogeneous distribution of Ag and Pt atoms that have different sizes. Thus, the evolution or elimination of dislocations should be a good indicator for the dynamic rearrangements of Ag and Pt atoms within the Ag-Pt octahedral nanoparticles when they were exposed to CO or Ar atmosphere. Our results show that dislocation disappeared at a faster rate than its evolution, suggesting desorption of CO molecule should limit the redistribution of surface elements at low temperature.

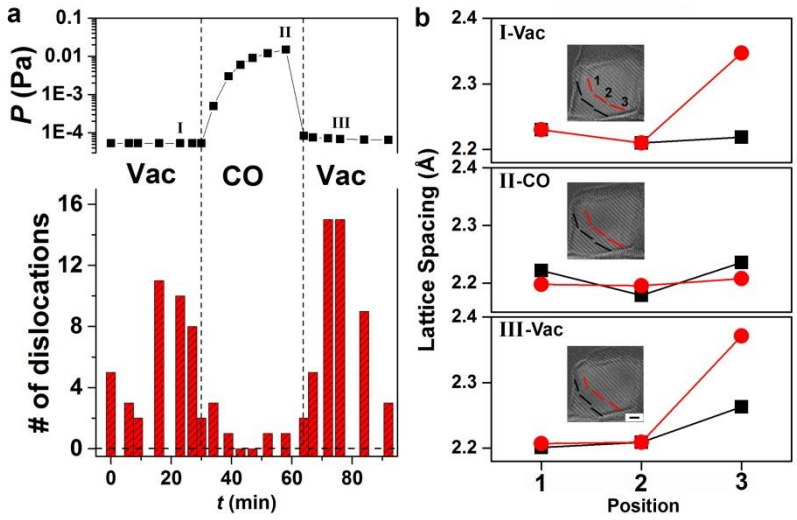

Figure 3.21 ETEM observations on the number of dislocations (a) and lattice spacing measurements (b) on a single Ag-Pt Oh nanoparticle under switching gas environments.

The FFT-enhanced images show mismatched lattices were observed in the Ag-Pt octahedral nanocrystal when it was exposed to vacuum (Figure 3.11, 3.19). This mismatch provides additional information in analyzing the change of composition within the nanoparticle, thus the movement of metal atoms. The lattice spacing was measured for selected FFT enhanced images in each alternating environment, i.e, vacuum, CO, and vacuum; Figure 3.12e, Figure 3.16f, and Figure 3.20d), across three positions along the mismatched regions, resulting in two sets of lattice spacing (red and black lines in Figure 3.21b).

The results show while the center of the particle (Position 1 and 2) had no obvious change in lattice spacing, there was a clear inverse relationship near the surface under different chemical vapor atmospheres (Position 3). This result indicates the change in composition near the surface was much more responsive to the exterior environment than in the center of the

nanoparticles and most likely responsible for the observed dislocations. The CO induced dynamic behavior of surface atoms was also reported previously for Pd atoms on FeO_2[28] as well as for Pt stepped surfaces at room temperature.[29] At Position 3, the lattice spacing near the bottom right corner was larger than those near the bottom left corner under vacuum and became similar to the center under CO gas, suggesting the surface composition became homogeneous under CO gas and turned heterogeneous under vacuum with regions closer to the bottom left corner rich in Pt (Figure 3.21b). To confirm the observed dynamic change in surface composition using CO gas as reactive chemical vapor, we carried out separate experiments on a different octahedral Ag-Pt nanoparticle under alternating vacuum and CO atmospheres using in situ ETEM. The same reversible dynamics for the evolution of dislocations under vacuum and their disappearance under CO vapor were readily observed (Figure A.1-13, Appendix A). This in situ ETEM result is in good agreement with that observed in the HAADF-STEM study in terms of dynamic change in surface composition (Figure 3.5).

3.3.4 Theoretical study of surface energetics by density functional theory calculation

DFT calculations were carried out to examine the energetics of Ag-Pt octahedral (111) surfaces with different Ag/Pt ratios and arrangements under vacuum or with adsorbed CO in order to gain insights on the relationship between the distribution of surface elements and environment of chemical vapors (Figure 3.22). A slab with subsurface layers having a fixed Ag/Pt ratio of 1:1 was used in the calculation of total energy. Six types of top surface layers were compared, which include Pt, AgPt, Ag_3Pt, and Ag under vacuum, and AgPt and Ag_3Pt with adsorbed CO molecule.

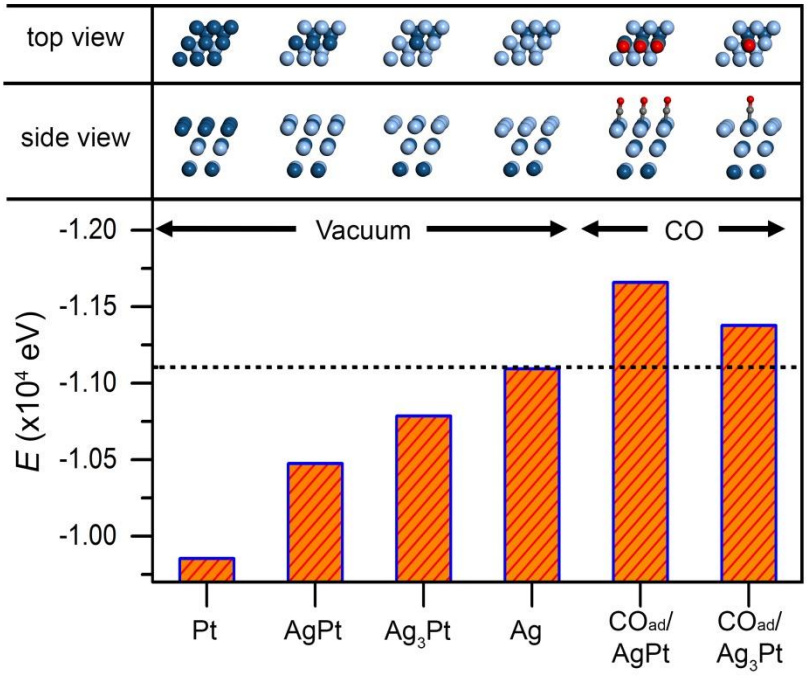

Figure 3.22 DFT calculation of the total energy of (111) surfaces of Ag, Pt, Ag_xPt under vacuum and with adsorbed CO gas. The dashed line shows the threshold energy where the CO adsorbed surface must exceed in order to stabilize Pt atoms on the surface.

The DFT calculation results suggest the value of total system energy was in a linear relation with respect to surface Ag/Pt ratio. Top surface of pure Ag has the lowest energy, thus thermodynamically the most stable structure, which is in good agreement with the literature.[26] When they were introduced to the surface, CO molecules may or may not be part of the surface depending on the composition and configuration of the adsorbed CO molecule (Table 3.2). Our DFT calculation suggests CO does not adsorb on Ag top surface, showing a positive adsorption energy, agreeing with the literature, and hence, it was not account as part of the surface in the calculation of system energy.[27] On the other hand, DFT calculation shows negative adsorption energies for CO on Pt atoms regardless of the neighboring atoms being Pt or Ag, thus adsorbed

CO needs to be considered as part of the surface. Under CO atmosphere, Ag_3Pt and AgPt (111) surfaces became more stable in comparison with pure Ag surface.

Table 3.2 Adsorption energy of CO on (111) surface of Ag_xPt_y alloys

Ag_xPt_y	Ag_1Pt_0	Ag_3Pt_1	Ag_1Pt_1	Ag_0Pt_1	Pt(111)*
$CO_{(ad)}$ (eV/molecule)	+0.1245 (atop)	-1.39 (atop)	-1.043 (atop)	-0.92 (bridge)	-1.232 (atop)

* calculated for a pure Pt(111) slab

The energetics of the edges of a Ag-Pt octahedral particle was modeled by introducing a single row of metal atoms (Ag, Pt, or mix) on the Ag-Pt (110) surface (Figure 3.23). The calculated results shows identical behavior as the (111) surface, where the Ag_1Pt_1 edge is most stable under CO (Table 3.3)

Table 3.3 Adsorption energy of CO on octahedral particle edges

Ag_xPt_y	Ag_1Pt_1	Ag_0Pt_1
$CO_{(ad)}$ (eV/molecule)	-1.062	-0.932

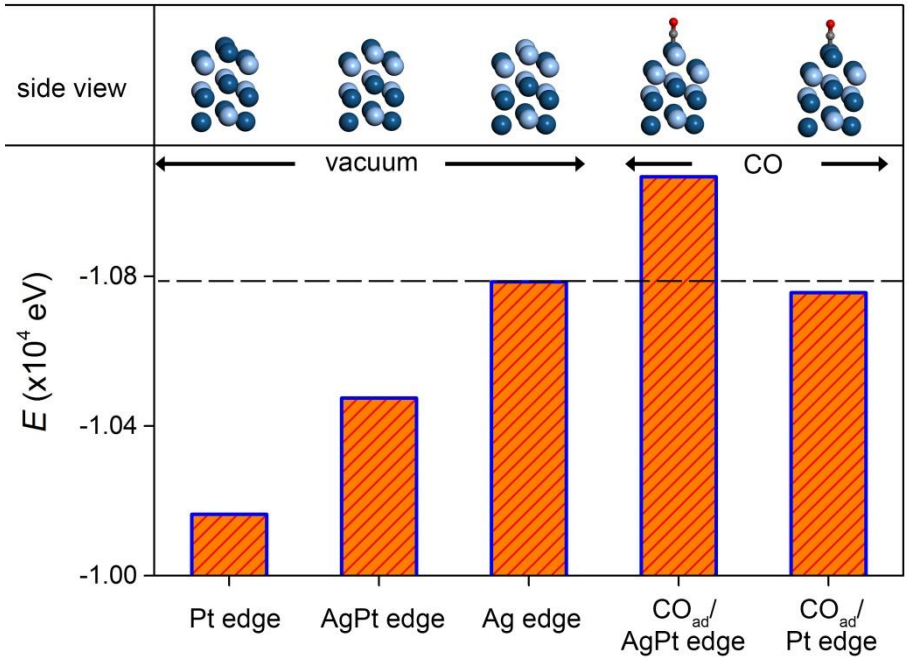

Figure 3.23 DFT modeling and calculation of the total energy of the edge of Ag-Pt Oh nanoparticles under vacuum and with adsorbed CO gas. The dashed line shows the threshold energy where the CO adsorbed surface must exceed in order to stabilize Pt atoms on the edge sites.

Although it appears that the surface that maximizes the number of adsorbed CO should be most stable under CO atmosphere, i.e., a pure Pt surface, one should consider the negative effect of high coverage on the average CO adsorption energy on Pt (111) surface.[30] However, such limitation can be overcome by the Ag_3Pt surface due to the separation of isolated Pt atoms by surrounded Ag atoms which maintains its strongest CO adsorption energy among other configurations (Table 3.2 & 3.3) even at high CO coverages. When the environment was switched to vacuum, driven by the tendency to phase separate, it is expected that Ag and Pt atoms would segregated to different sites.[31] The enrichment of Pt on edge sites was also reported

on PtNi octahedras[32, 33] where Pt was also the element with higher intrinsic surface energy,[26] similar to the case in the present study. When switched back to CO once again, the reversible process of dispersing Pt atoms in the near surface regions took place again, which could be driven by the lateral concentration gradient as well as the tendency to minimize the overall surface energy.

3.3.5 Performance evaluation of chemical vapor treated Ag-Pt octahedral catalyst

Formic acid oxidation reaction (FAOR) was carried out to examine the catalytic performance of these Ag-Pt octahedral nanoparticles upon chemical vapor-assisted treatment. FAOR is uniquely suited for such study because this reaction is very sensitive to the degree of alloying of Pt atoms with another metal atom, and the activity was reported to be the highest when Pt atom was isolated by Ag or Au atoms.[34-36] Cyclic voltammetry (CV) was used to characterize the carbon-supported catalysts of octahedral Ag-Pt nanocrystals upon various treatments under alternating CO and Ar atmospheres (Figure 3.24). The proton adsorption in an Ar-saturated $HClO_4$ solution shows little difference between the CO and Ar treated catalyst indicating surface Pt content was not altered substantially by the treatments (Figure 3.24a inset). Figure 3.24a shows the CV curves for electrocatalytic FAOR using Ag-Pt octahedral nanoparticle catalyst treated in CO and Ar gases, respectively. The relatively high activity towards FAOR was observed for the Ag-Pt octahedral catalyst after CO-assisted treatment, in line with the observed surface structure of highly dispersed Pt in Ag. The dependence of activity on treatment atmospheres indicated a reversible response on the surface elemental distribution under CO and Ar, which is in good agreement with ETEM observations (Figure 3.24b, Table 3.4 and 3.5).

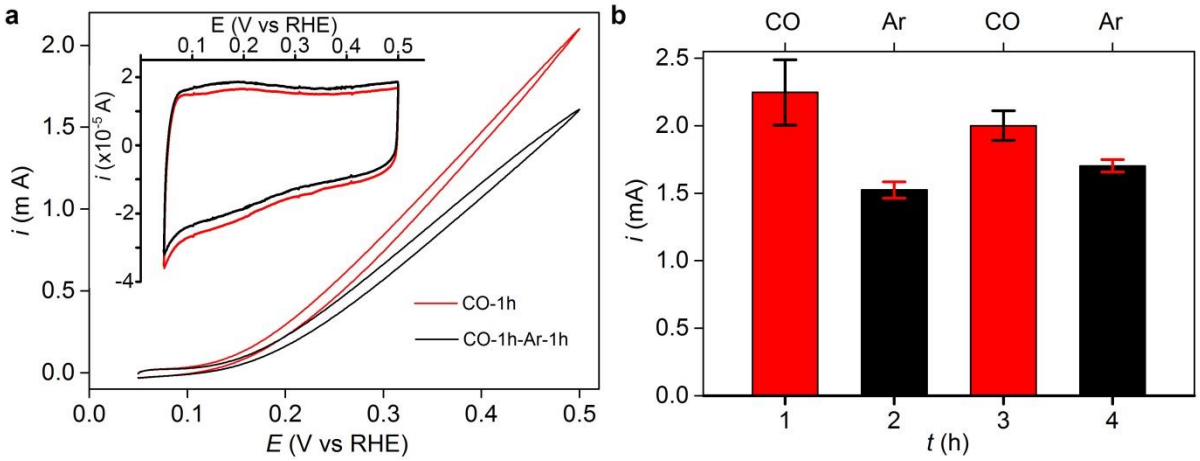

Figure 3.24 Electrocatalytic study of carbon-supported Ag-Pt octahedral nanoparticle catalysts after sequential chemical-vapor assisted treatments in CO and Ar gases at 100 ºC. a. CV curves recorded in Ar-saturated 0.5-M HCOOH aqueous solution with 0.1-M $HClO_4$ as the supporting electrolyte, b. activity for the oxidation of formic acid by Ag-Pt catalysts after various CO and Ar vapor-assisted treatments.

Table 3.4 FAOR current (mA) of Ag-Pt catalysts treated with CO and Ar gases*

# of measurement	CO	CO-Ar	CO-Ar-CO	CO-Ar-CO-Ar
1	2.59	1.61	2.12	1.74
2	2.10	1.50	1.85	1.73
3	2.05	1.47	2.03	1.64

*: All currents were measured at 0.5 V (vs RHE).

Table 3.5 ECSA value (cm^2_{Pt}) of Ag-Pt catalysts treated with CO and Ar gases

# of measurement	CO	CO-Ar	CO-Ar-CO	CO-Ar-CO-Ar
1	0.21	0.20	0.26	0.26
2	0.23	0.21	0.29	0.28
3	0.26	0.22	0.31	0.30

Propylene hydrogenation reaction was also carried out with the chemical vapor treated Al_2O_3 supported Ag-Pt octahedral nanocatalyst. Such catalytic reaction plays an important role for the production of high quality liquid fuel.[37, 38] Conversion of propylene to propane was shown to depend heavily on the treatment conditions for the Ag-Pt catalysts. The steady-state conversion was around 82-84% for the catalysts treated with CO, and decreased to 55% for those with subsequent treatment by Ar (Figure 3.25). The difference in observed conversion should originate from the arrangements of surface Pt and Ag atoms of octahedral catalysts. Dissociative adsorption of H_2 could occur spontaneously on Pt (111), but was endothermic on Ag (111),[39, 40] that is, hydrogenation of alkene by molecular H_2 occurred readily on Pt but not on Ag. Table 3.6 summarizes the DFT calculation results of dissociative energy terms of H_2 on monolayer Ag, Ag_3Pt, and Pt on an Ag-Pt alloy (111) slab. The results indicate the dissociative adsorption of H_2 is exothermic on Pt surface and endothermic on Ag surface. H_2 also dissociated exothermically (-0.191 eV/molecule) on Ag_3Pt (111) surface, suggesting a uniform alloy surface should favor the catalytic hydrogenation of propylene to propane. On the other hand, when Ag and Pt atoms form surface clusters, H_2 dissociation becomes active only on Pt-segregated edge regions, which exhibited lower conversion towards propylene hydrogenation because of reduced active surface area.

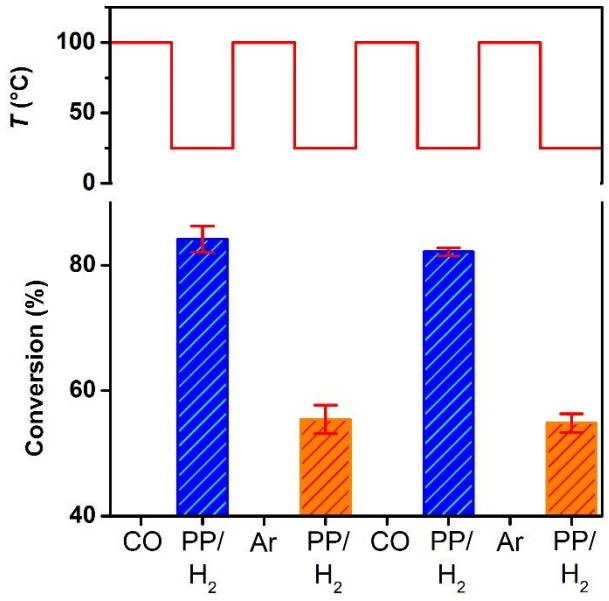

Figure 3.25 Conversion of propylene to propane using Al_2O_3 supported Ag-Pt octahedral nanocatalyst pretreated under different chemical vapors.

Table 3.6 Dissociative adsorption energy of H_2 on (111) surface of Ag_xPt_y alloys.

surf. comp.	Ag	Pt	Ag_3Pt	Ag_3Pt
ad. config.	hollow	atop	bidentate	$atop_{Pt}$ $hollow_{Ag}$
H_{diss} (eV/mol.)	0.405	-0.596	-0.715	-0.191
side view	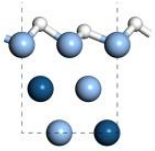	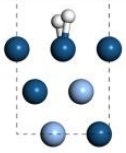	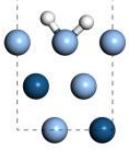	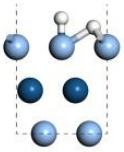
top view	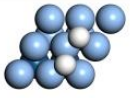		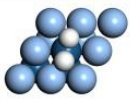	

3.4 Conclusions

A low temperature, chemical vapor-assisted treatment method is developed to control surface atomic structures of Ag-Pt octahedral nanoparticles dynamically and regioselectively. Under CO treatment Ag and Pt atoms become uniformly distributed on surface, while in vacuum Pt atoms preferably segregate to the edge regions. Using chemical vapor to effectively lowering the total surface energy allows for low or room temperature approach to the post-synthesis treatment of surface atomic arrangements without altering the shape, resulting in preferred surface structures (Pt in Ag) for catalysis. In situ ETEM in this regard is a valuable tool in the design of post-synthesis processing condition. The principle of chemical vapor-assisted processing demonstrated in this study represents a new design paradigm for making high performance bi- or multi-metallic catalysts.

3.5 References

1. Sankar, M.; Dimitratos, N.; Miedziak, P. J.; Wells, P. P.; Kiely, C. J.; Hutchings, G. J. *Chem. Soc. Rev.* **2012,** 41, 8099-8139.
2. Zhou, S.; Varughese, B.; Eichhorn, B.; Jackson, G.; McIlwrath, K. *Angew. Chem. Int. Ed,* **2005,** 117, 4615-4619.
3. Nutt, M. O.; Hughes, J. B.; Wong, M. S. *Environ. Sci. Technol.* **2005,** 39, 1346-1353.
4. Wu, J.; Yang, H. *Acc. Chem. Res.* **2013,** 46, 1848-1857.
5. Singh, S. K.; Singh, A. K.; Aranishi, K.; Xu, Q. *J. Am. Chem. Soc.* **2011,** 133, 19638-19641.
6. Freakley, S. J.; He, Q.; Harrhy, J. H.; Lu, L.; Crole, D. A.; Morgan, D. J.; Ntainjua, E. N.; Edwards, J. K.; Carley, A. F.; Borisevich, A. Y.; Kiely, C. J.; Hutchings, G. J. *Science* **2016,** 351, 965-968.
7. Wilson, N. M.; Flaherty, D. W. *J. Am. Chem. Soc.* **2016,** 138, 574-586.
8. Strasser, P. *Science* **2015,** 349, 379-380.
9. Yu, W.; Porosoff, M. D.; Chen, J. G. *Chem. Rev.* **2012,** 112, 5780-5817.
10. Wang, X.; Choi, S.-I.; Roling, L. T.; Luo, M.; Ma, C.; Zhang, L.; Chi, M.; Liu, J.; Xie, Z.; Herron, J. A.; Mavrikakis, M.; Xia, Y. *Nat. Commun.* **2015,** 6.
11. Peng, Z.; Yang, H. *Nano Today* **2009,** 4, 143-164.
12. Wang, D.; Li, Y. *Adv. Mater.* **2011,** 23, 1044-1060.
13. Wu, J.; Gross, A.; Yang, H. *Nano Lett.* **2011,** 11, 798-802.
14. Divins, N. J.; Angurell, I.; Escudero, C.; Pérez-Dieste, V.; Llorca, J. *Science* **2014,** 346, 620-623.

15. Tao, F.; Grass, M. E.; Zhang, Y.; Butcher, D. R.; Renzas, J. R.; Liu, Z.; Chung, J. Y.; Mun, B. S.; Salmeron, M.; Somorjai, G. A. *Science* **2008,** 322, 932-934.

16. Tao, F.; Salmeron, M. *Science* **2011,** 331, 171-174.

17. Nierhoff, A.; Conradsen, C.; McCarthy, D.; Johansson, T. P.; Knudsen, J.; Chorkendorff, I. *Catal. Today* **2015,** 244, 130-135.

18. Hansen, T. W.; Wagner, J. B. *ACS Catal.* **2014,** 4, 1673-1685.

19. Pan, Y.-T.; Wu, J.; Yin, X.; Yang, H. *AIChE J.* **2016,** 62, 399-407.

20. Pan, Y.-T.; Yan, Y.; Shao, Y.-T.; Zuo, J.-M.; Yang, H. *Nano Lett.* **2016**.

21. Xin, H. L.; Alayoglu, S.; Tao, R.; Genc, A.; Wang, C.-M.; Kovarik, L.; Stach, E. A.; Wang, L.-W.; Salmeron, M.; Somorjai, G. A.; Zheng, H. *Nano Lett.* **2014,** 14, 3203-3207.

22. Fu, G.-T.; Ma, R.-G.; Gao, X.-Q.; Chen, Y.; Tang, Y.-W.; Lu, T.-H.; Lee, J.-M. *Nanoscale* **2014,** 6, 12310-12314.

23. Clark Stewart, J.; Segall Matthew, D.; Pickard Chris, J.; Hasnip Phil, J.; Probert Matt, I. J.; Refson, K.; Payne Mike, C. *Kristallogr.* **2005**; *220*, 567-570.

24. Vanderbilt, D. *Phys. Rev. B* **1990,** 41, 7892-7895.

25. Hammer, B.; Hansen, L. B.; Nørskov, J. K. *Phys. Rev. B* **1999,** 59, 7413-7421.

26. Vitos, L.; Ruban, A. V.; Skriver, H. L.; Kollár, J. *Surf. Sci.* **1998,** 411, 186-202.

27. Carenco, S. *Chem-Eur. J.* **2014,** 20, 10616-10625.

28. Parkinson, G. S.; Novotny, Z.; Argentero, G.; Schmid, M.; Pavelec, J.; Kosak, R.; Blaha, P.; Diebold, U. *Nat. Mater.* **2013,** 12, 724-728.

29. Tao, F.; Dag, S.; Wang, L.-W.; Liu, Z.; Butcher, D. R.; Bluhm, H.; Salmeron, M.; Somorjai, G. A. *Science* **2010,** 327, 850-853.

30. Sachtler, J. W. A.; Somorjai, G. A. *J. Catal.* **1983,** 81, 77-94.

31. Durussel, P.; Feschotte, P. *J. Alloys Compd.* **1996,** 239, 226-230.

32. Cui, C.; Gan, L.; Heggen, M.; Rudi, S.; Strasser, P. *Nat. Mater.* **2013,** 12, 765-771.

33. Chen, C.; Kang, Y.; Huo, Z.; Zhu, Z.; Huang, W.; Xin, H. L.; Snyder, J. D.; Li, D.; Herron, J. A.; Mavrikakis, M.; Chi, M.; More, K. L.; Li, Y.; Markovic, N. M.; Somorjai, G. A.; Yang, P.; Stamenkovic, V. R. *Science* **2014,** 343, 1339-1343.

34. Yang, S.; Lee, H. *ACS Catal.* **2013,** 3, 437-443.

35. Suntivich, J.; Xu, Z.; Carlton, C. E.; Kim, J.; Han, B.; Lee, S. W.; Bonnet, N.; Marzari, N.; Allard, L. F.; Gasteiger, H. A.; Hamad-Schifferli, K.; Shao-Horn, Y. *J. Am. Chem. Soc.* **2013,** 135, 7985-7991.

36. Zhong, W.; Wang, R.; Zhang, D.; Liu, C. *J. Phys. Chem. C* **2012,** 116, 24143-24150.

37. Batts, B. D.; Fathoni, A. Z. *Energ. Fuels* **1991,** 5, 2-21.

38. Oasmaa, A.; Kuoppala, E. *Energ. Fuels* **2003,** 17, 1075-1084.

39. Lee, G.; Plummer, E. W. *Phys. Rev. B* **1995,** 51, 7250-7261.

40. Montoya, A.; Schlunke, A.; Haynes, B. S. *J. Phys. Chem. B* **2006,** 110, 17145-17154.

Chapter 4

Ag-Pt Compositional Intermetallics Made of Alloy Nanoparticles[1]

4.1 Introduction

Heterogeneous catalytic reaction generally follows the Sabatier principle that the reaction rate depends greatly on the affinity between reactive species and surface sites.[1] The binding strength cannot be too strong nor too weak in order to reach the highest turnover frequency. Transition metals have been shown to be active towards catalyzing a wide variety of reactions, although achieving the optimized binding strength of key intermediates is often challenging, if not impossible, with a single metal element.[2, 3] Incorporation of a second metal species can however effectively adjust surface electronic structures to obtain the appropriate binding energy in a bimetallic catalyst.[4]

Structures of a bimetallic catalyst can range from heterogeneous core-shell nanoparticle, to homogeneous random alloy, and ordered intermetallic.[5] Intermetallic compounds are unique and stable bimetallic structures with long range order in atomic arrangement that fall in the thermodynamic minimum.[6, 7] Since electron is usually more localized in an intermetallic compound, thermal and electrical conductivities are usually lower than those of its corresponding individual metals.[8] As catalyst, intermetallic phase can be most effective in both separating the active surface sites and adjusting the surface electronic properties.[6, 9] For instance, intermetallic Pd_xGa_y and $Al_{13}Fe_4$ catalysts were reported to be highly selective for partial hydrogenation of alkyne to alkene.[10-13] Intermetallic Pd_2Ga was active for methanol synthesis from CO_2.[14, 15]

[1] Modified with permission, from Pan, Y.-T.; Yan, Y.; Shao, Y.-T.; Zuo, J.-M.; Yang, H. *Nano Lett.* **2016**, *16*, 7988-7992.

Intermetallic $NaAu_2$ catalyst was used for low temperature CO oxidation in the absence of metal oxide supports.[16] PtCo,[17] PtFe,[18, 19] and PtPd intermetallic skin (on Pd octahedral nanoparticles)[20] were shown to be very active and stable for oxygen reduction reaction (ORR).

While they are often favored for catalytic applications, intermetallic compounds do not always form through metallurgy approach for two given metal elements and are often element specific. For instance, while Au and Cu form intermetallic phases, Ag and Cu are almost immiscible in a board range of composition. Ag and Pt is one interesting pair of metals which are immiscible in bulk phase. A computational study suggested that the $L1_1$ structure might exist within a narrow composition window, though no pure Ag-Pt intermetallic phase has ever been observed experimentally so far.[21, 22] Alloying of Ag and Pt in the form of nanoparticles, however, was shown to be possible from molecular precursors using a solution phase synthesis.[23] In this chapter, we demonstrate the preparation of phase-pure compositional intermetallic Ag-Pt by thermally treating Ag_xPt_y alloy nanoparticles of different Ag/Pt atomic ratio at 700 °C in nitrogen. Simulated powder X-ray diffraction (PXRD) patterns were used to identify a brand new, mixed hexagonal and cubic closely packed phase (HCP/CCP). ETEM experiment was carried out to observe the transformation process in real time. This Ag-Pt compositional intermetallic phase showed much higher specific activity and stability for electrocatalytic oxidation of formic acid than the as-made Ag-Pt alloy nanoparticle and reference Pt catalysts at low overpotential ranges.

4.2 Experimental

4.2.1 Materials and chemicals

Platinum acetylacetonate ($Pt(acac)_2$, 98%) was purchased from Strem Chemical; silver stearate (99%) from Pfaltz & Bauer; oleylamine (OAm, 70%), oleic acid (OAc, 90%), diphenyl ether (DPE, 99%), 1,2-Hexadecanediol (1,2-HDD, 90%), and Nafion 117 solution from Sigma-Aldrich; chloroform (>99%) and methanol (>99%) from Macron; ethanol (200 proof) from Decon Labs; carbon black (Vulcan XC-72) from Cabot; perchloric acid (70%, VERITAS double distilled) and formic acid (88%) from GFS chemicals; propanol (LC-MS Reagent) from J. T. Baker; Pt/C catalyst (20% Pt on Vulcan XC-72) from BASF; argon gas (Ar, UHP grade) from Airgas; and nitrogen gas (C.P grade) from S J Smith. All chemicals were used as received without further purification.

4.2.2 Synthesis and processing of Ag_xPt_y nanoparticles

Ag_xPt_y alloy nanoparticles were synthesized through a wet chemical route. In a typical synthesis, designed amount of $Pt(acac)_2$ and Ag stearate (total of 0.191 mmol), 490 mg of 1,2-hexadecanediol (1,2-HDD 1.9 mmol), 0.3 mL of oleylamine, 0.3 mL of oleic acid, and 5 mL of diphenyl ether were mixed in a 15-mL three-neck round-bottom flask. The flask was connected to a Schlenk line through a condenser. The reaction mixture was preheated at 55 °C until metal precursors and 1,2-HDD were completely dissolved to form a homogeneous orange color solution. The flask was then evacuated with a rotary pump (Edward RV 12) and purged with Ar for six cycles. The temperature of the solution was ramped at a rate of 5 °C/min to 260 °C, maintained for 1 h, and then cooled down to room temperature under Ar. The solid products

were collected by centrifugation where ethanol was added into the synthesis solution to dissolve excess 1,2-HDD. The nanoparticles were re-dispersed in chloroform with ultra-sonication and separated from the solvent by centrifugation in a chloroform-ethanol mixture at 7000 rpm. This process was repeated two times. The final products were dispersed in chloroform for further characterization. The thermal treatments were carried out in a tube furnace (Lindburg Blue M, Thermo Scientific) with a quartz tube. The dry powders of nanoparticles were introduced into the tube furnace inside an alumina combustion boat. The heat treatment was conducted under N_2 atmosphere at 700 °C for 1 h with a ramp rate of 5 ºC/min and then cooled down naturally. The nanoparticles became sintered after this process.

4.2.3 Characterization

Powder X-ray diffraction (XRD) patterns were acquired on a Bruker D8 Venture diffractometer. Transmission electron microscopy (TEM) and high-resolution transmission electron microscopy (HR-TEM) micrographs were taken on a JEOL 2100 Cryo TEM with an accelerating voltage of 200 kV. High angle annular dark field scanning transmission electron microscopy (HAADF-STEM) micrographs were carried out on JEOL 2200 FS STEM with Schottky field emitter and a spherical aberration corrector (Cs-corrector) at an accelerating voltage of 200 kV. Scanning electron microscopy (SEM) and energy dispersive X-ray was performed on Hitachi S4700 SEM. X-ray photoelectron spectroscopy (XPS) data were acquired using PHI 5400 XPS (Physical Electronics) spectrometer with a Mg source. The XPS spectrum analysis was done using CasaXPS software with Shirley type baseline.

4.2.4 Electrochemical characterization

Electrochemical properties of Ag-Pt catalysts were characterized in a three-electrode cell. To prepare a working electrode, Ag-Pt particles were dispersed in an ethanol/water mixture (with 1:1 volumetric ratio) at a concentration of 3.4 mg/mL. A total of 30 μL was drop-cast onto the glassy-carbon rotating disk electrode (RDE, area: 0.196 cm^2). After deposition of Ag-Pt particles, a drop of Nafion solution (10 μL, diluted by five times from the supplier with ethanol) was drop-cast onto the RDE. A platinum foil (1 cm^2) was used as the counter electrode and a HydroFlex hydrogen electrode as the reference. Hydrogen evolution reaction (HER) was used to calibrate the hydrogen electrode before the tests. The electrochemical active surface area (ECSA), based on proton adsorption on Pt, was carried out by cyclic voltammetry (CV) under Ar saturated 0.1-M perchloric acid ($HClO_4$) and was determined by integrating the area accounted for proton adsorption in the potential range of 0.05-0.4V (vs RHE) with the following formula:

$$\text{ECSA } (cm^2_{Pt}) = \text{area}/[0.05\ (V/s) \times 210\ (\mu C/cm^2)]$$

Oxidation of formic acid was carried out in a mixture of 0.5-M formic acid (HCOOH) and 0.1-M $HClO_4$ by CV under Ar where the area specific activity was derived by normalizing the oxidation current by the ECSA. Data were used without *iR*-drop correction.

4.2.5 Density functional theory calculation

DFT calculation was performed using the CASTEP module with ultrasoft pseudopotentials.[24] The electron exchange and correlation energy was treated with generalized gradient approximation (GGA) and with the Perdew−Burke−Ernzerhof (PBE) functional using Tkatchenko-Scheffler (TS) dispersion correction.[25, 26] The plane-wave basis set cut-off energy

was set to 300 eV. The bulk energy of Ag and Pt was calculated based on a face-centered cubic unit cell whereas the cubic closely-packed (CCP) intermetallic was based on a cubic unit cell of 32 atoms and the hexagonal closely-packed (HCP) intermetallic was based on a hexagonal unit cell with 16 atoms. The slab energy for Ag and Pt (111} surfaces was calculated based on a slab with 12 atoms (1×1, 3 layers, 10 Å vacuum). The slab energy for CCP intermetallic (111) surface was calculated based on a slab with 96 atoms (1×1, 3 layers, 10 Å vacuum). The slab energy for HCP intermetallic (001) surface was calculated based on a slab with 96 atoms (2×2, 1 layer, 10 Å vacuum). The Monkhorst-Pack scheme k-point grid sampling was set to 3×4×1 for the surface. The tolerance for convergence was 1×10^{-5} eV/atom in energy, 3×10^{-2} eV/Å in force, and 1×10^{-3} Å in displacement. The surface energy was calculated using the following equation:[27]

$$\sigma = [E_{slab} - (N_{slab}/N_{bulk})E_{bulk}]/2N_{slab}$$

where σ is the surface energy per atom, E_{slab} is the total energy of the created metal surface, E_{bulk} is the total energy of the bulk metal, N_{slab} is the number of atoms in the created metal surface, and N_{bulk} is the number of atoms in the unit cell.

4.2.6 DIFFaX simulation of X-ray diffraction patterns

Simulation of X-ray diffraction pattern was conducted with the DIFFaX program which is designed for calculating diffraction intensity for crystals that contain planar defects, such as twins and stacking faults.[28] The simulation was built on a deformed hexagonal unit cell and the grain dimensions along three directions were assigned to reflect preferential orientation. Four different layers of closed-packed Pt and Ag were created to construct the stacks along *c*-axis either on the tetrahedral or octahedral sites, in which the probability of each layer stacking on

one another can be assigned. Ag-Pt CCP and HCP intermetallics without preferential orientation were simulated by building a hexagonal unit cell with alternating Ag and Pt layers. The DIFFaX structure data files for simulating the powder pattern of compositional intermetallic with faulted structures are listed as follows:

4.2.6.1 Structure data file for the compositional intermetallic

```
{data file for AgPt, with layer Ag on layer Pt interchangeably}
{probability of hexagonal stacking = 85%}

INSTRUMENTAL                          {Header for instrumental section}
X-RAY                                 {Simulate X-ray diffraction}
1.5418                                {X-ray wavelength}
PSEUDO-VOIGT 0.1 -0.036 0.009 0.6 trim {Instrumental broadening}

STRUCTURAL                            {Header for structural section}
2.67 2.80 2.38 120.0                  {unit cell coordinates}
Unknown                               {hexagonal, c axis = cubic [111]}
4                                     {111 sheet, plus its mirror}
1050    42                            {layer widths very wide in the a-b plane}

LAYER 1                               {cubic (111) layer, centrosymmetric}
CENTROSYMMETRIC
Pt    1  0.0   0.0   0.0  0.2   1.0  {name id# x_rel y_rel z_rel B_iso Occ}
                                      {B_iso = isotropic Debye-Waller factor}
                                      {Occ= occupancy factor}

LAYER 2
CENTROSYMMETRIC
Ag    1  0.0   0.0   0.0   0.2   1.0

LAYER 3
CENTROSYMMETRIC
Pt    1  0.0   0.0   0.0   0.2   1.0

LAYER 4
CENTROSYMMETRIC
Ag    1  0.0   0.0   0.0   0.2   1.0
```

```
STACKING                                {Header for stacking description}
recursive                               {Statistical ensemble}
100                                     {Infinite number of layers}

TRANSITIONS                             {Header for transitions}
{Transitions from layer 1}
0.01    1/3  2/3   1.0                  {layer 1 to layer 1, 1%   chance}
0.99    1/3  2/3   1.0                  {layer 1 to layer 2, 99% chance}
0.0     2/3  1/3   1.0                  {layer 1 to layer 3, 0 %  chance}
0.0     2/3  1/3   1.0                  {layer 1 to layer 4, 0%   chance}


{Transitions from layer 2}
0.145   1/3  2/3   1.0                  {layer 2 to layer 1, 14.5%  chance}
0.005   1/3  2/3   1.0                  {layer 2 to layer 2, 0.5%   chance}
0.845   2/3  1/3   1.0                  {layer 2 to layer 3, 84.5%  chance}
0.005   2/3  1/3   1.0                  {layer 2 to layer 4, 0.5%   chance}


{Transitions from layer 3}
0.005   1/3  2/3   1.0                  {layer 3 to layer 1, 0.5%   chance}
0.495   1/3  2/3   1.0                  {layer 3 to layer 2, 49.5%  chance}
0.005   2/3  1/3   1.0                  {layer 3 to layer 3, 0.5%   chance}
0.495   2/3  1/3   1.0                  {layer 3 to layer 4, 49.5%  chance}


{Transitions from layer 4}
0.495  1/3  2/3   1.0                  {layer 4 to layer 1, 49.5%  chance}
0.005  1/3  2/3   1.0                  {layer 4 to layer 2, 0.5%   chance}
0.495  2/3  1/3   1.0                  {layer 4 to layer 3, 49.5%  chance}
0.005  2/3  1/3   1.0                  {layer 4 to layer 4, 0.5%   chance}
```

4.2.6.2 Structure data file for intermetallic stacking in hcp structure

```
{data file for AgPt, with Ag layer on Pt layer interchangeably with hexagonal stacking}

INSTRUMENTAL                            {Header for instrumental section}
X-RAY                                   {Simulate X-ray diffraction}
1.5418                                  {X-ray wavelength}
PSEUDO-VOIGT 0.1 -0.036 0.009 0.6 trim  {Instrumental broadening}
```

```
STRUCTURAL                          {Header for structural section}
2.715 2.715 2.38 120.0              {unit cell coordinates}
unknown                             {hexagonal, c axis = cubic [111]}
2                                   {111 sheet, plus its mirror}
100  100                            {layer widths very wide in the a-b plane}

LAYER 1                             {cubic (111) layer, centrosymmetric}
CENTROSYMMETRIC
Pt    1  0.0   0.0   0.0  0.2   1.0   {name id# x_rel y_rel z_rel B_iso Occ}
                                    {B_iso = isotropic Debye-Waller factor}
                                    {Occ= occupancy factor}
LAYER 2
CENTROSYMMETRIC
Ag    1  0.0   0.0   0.0   0.2   1.0

STACKING                            {Header for stacking description}
recursive                           {Statistical ensemble}
700                                 {# of layers }

TRANSITIONS                         {Header for transitions}
{Transitions from layer 1}
0.0    1/3  2/3   1.0               {layer 1 to layer 1, 0%    chance}
1.0    1/3  2/3   1.0               {layer 1 to layer 2, 100% chance}

{Transitions from layer 2}
1.0    -1/3  -2/3   1.0             {layer 2 to layer 1, 100%  chance}
0.0    1/3  2/3   1.0               {layer 2 to layer 2, 0%      chance}
```

4.2.6.3 Structure data file for intermetallic stacking in fcc structure

```
{data file for AgPt, with Ag layer on Pt layer interchangeably with CCP stacking}

INSTRUMENTAL                        {Header for instrumental section}
X-RAY                               {Simulate X-ray diffraction}
1.5418                              {X-ray wavelength}
PSEUDO-VOIGT 0.1 -0.036 0.009 0.6 trim   {Instrumental broadening}

STRUCTURAL                          {Header for structural section}
2.715 2.715 2.38 120.0              {unit cell coordinates}
unknown                             {hexagonal, c axis = cubic [111]}
2                                   {111 sheet, plus its mirror}
500  500                            {layer widths very wide in the a-b plane}
```

```
LAYER 1                                  {cubic (111) layer, centrosymmetric}
CENTROSYMMETRIC
Pt   1  0.0   0.0   0.0  0.2   1.0       {name id# x_rel y_rel z_rel B_iso Occ}
                                         {B_iso = isotropic Debye-Waller factor}
                                         {Occ= occupancy factor}

LAYER 2
CENTROSYMMETRIC
Ag   1  0.0   0.0   0.0   0.2   1.0


STACKING                                 {Header for stacking description}
recursive                                {Statistical ensemble}
500                                      {Infinite number of layers}

TRANSITIONS                              {Header for transitions}
{Transitions from layer 1}
0.0    1/3  2/3   1.0                    {layer 1 to layer 1, 0%    chance}
1.0    1/3  2/3   1.0                    {layer 1 to layer 2,100% chance}

{Transitions from layer 2}
1.0    1/3  2/3   1.0                    {layer 2 to layer 1, 100%  chance}
0.0    1/3  2/3   1.0                    {layer 2 to layer 2, 0%      chance}
```

4.3 Results and Discussion

4.3.1 Discovery of intermetallic Ag-Pt absent of fcc phase

A range of Ag_xPt_y random alloy nanoparticles were synthesized by controlling the feeding ratio between the metal precursors of platinum acetylacetonate [$Pt(acac)_2$] and silver stearate in a mixture of diphenyl ether, oleylamine, oleic acid, and 1,2-hexadecanediol (see Experimental section for details).[29] Agreeing with previous study in our group, the morphology of the nanoparticles is dependent on the nominal ratio between Ag and Pt precursors. Spherical nanoparticles were formed when the feed is rich is Ag. However, when the feed is rich is Pt, worm like morphology was observed (Figure 4.1).[23]

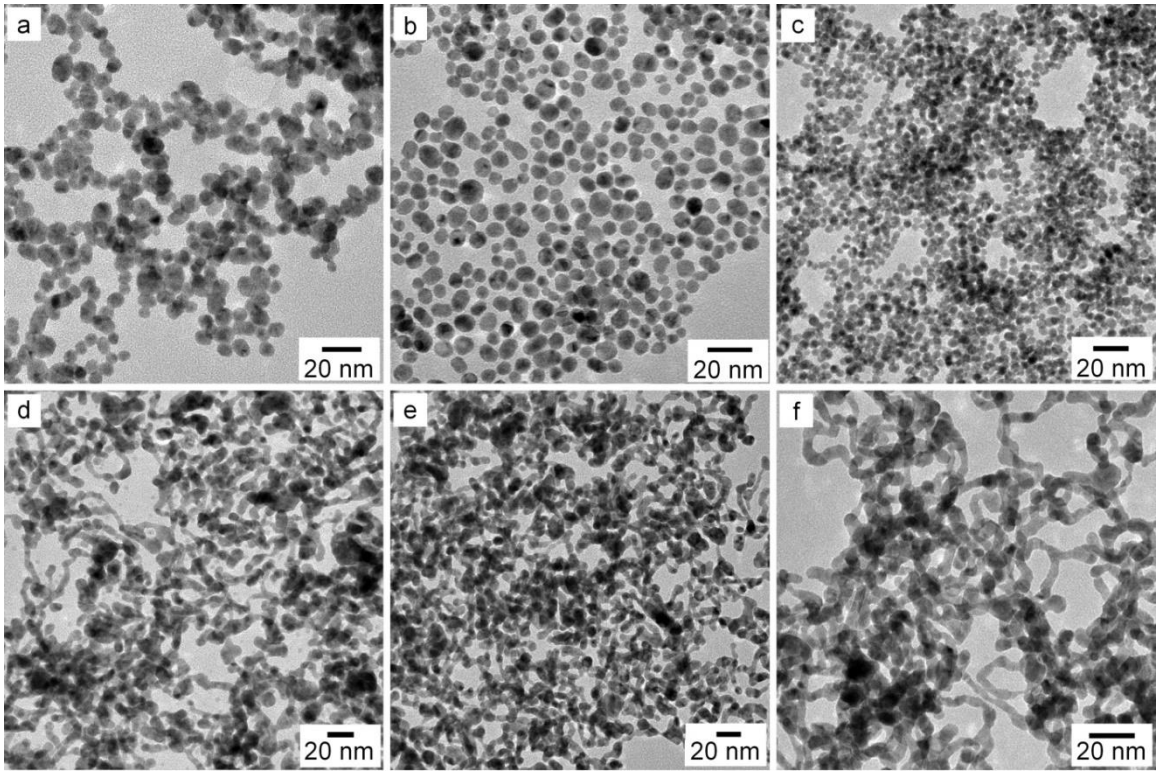

Figure 4.1 TEM micrographs of as-made Ag-Pt alloy nanoparticles at the nominal composition of (a) $Ag_{75}Pt_{25}$, (b) $Ag_{60}Pt_{40}$, (c) $A_{53}Pt_{47}$, (d) $Ag_{48.4}Pt_{51.6}$, (e) $Ag_{47}Pt_{53}$, and (f) $Ag_{33}Pt_{67}$, respectively.

These nanoparticles were then subjected to thermal treatment under N_2 atmosphere at 700 ºC to allow the sintering and phase transformation to occur. PXRD study shows that by using the nanoparticles with a nominal composition of $Ag_{48.4}Pt_{51.6}$, a new set of unique diffractions, absent of fcc-related peaks, was observed (Figure 4.2). The new diffraction peak at 18.58º 2θ was most intriguing and characteristic, corresponding to a *d*-spacing of 4.77 Å, which is about double the unit length of (111) lattice of fcc Ag (Figure 4.2a). This result indicates the closely packed Ag planes have a long range order, that is, an intermetallic-like structure in composition, separated by planes of Pt atoms.

We analyzed the structural details of this Ag-Pt compositional intermetallic, especially twinning and stacking fault, using the DiFFAX program.[28] Unit cell dimension (*a, b, c*), grain size, and probability of closely-packed planes stacking on different sites are the main parameters to be considered in the simulation of powder diffraction pattern that best resembles the experimental measurement. Figure 4.2b shows simulated XRD patterns of Ag-Pt compositional intermetallic in three types of packing structures, *i.e.*, cubic closely packed (CCP), hexagonal closely packed (HCP) and mixed CCP/HCP phases. The experimental data matched very well with the Ag-Pt intermetallic that has the closely packed layers of Ag and Pt as *ab* plane of slightly deformed hexagonal unit cell, stacking interchangeably along *c* direction with 85% on the tetrahedral sites (HCP) and 15% on the octahedral sites (CCP) (top panel of Figure 4.2b). This particular pattern was generated based on stacking 100 layers of 105 nm × 4.2 nm atom sheet in *ab* plane along *c* direction. From the DiFFAX simulation, the unit cell dimensions were determined to be 2.67 Å for *a*, and 2.80 Å for *b*, with the distance between the Ag and Pt layers of 2.38 Å, which is half of the value obtained from the experimental data (*d*-spacing of 4.77 Å at 18.58º 2θ).

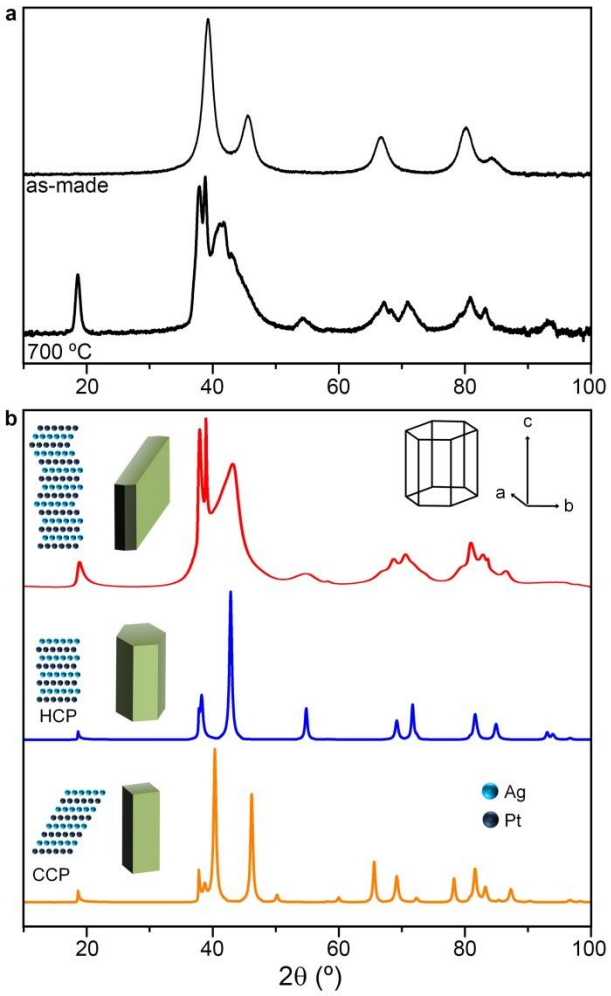

Figure 4.2 (a) Experimental XRD data of as-made and thermally-treated samples of $Ag_{48.4}Pt_{51.6}$ alloy nanoparticles. (b) Simulated XRD patterns of highly-faulted stacking of Pt and Ag interchanging layers with (top) mixed HCP/CCP, (middle) HCP and (bottom) CCP phase. The Ag-Pt intermetallic with mixed HCP/CCP phase was with 85% stacking on tetrahedral sites and 15 % on octahedral sites based on a deformed hexagonal unit cell.

4.3.2 Electron microscopy characterization of the Ag-Pt compositional intermetallic

Electron microscopy was used to experimentally examine the rather unique stacking structure of this Ag-Pt compositional intermetallic (Figure 4.3). After thermal treatment at 700 ºC, a film of porous network composed of sintered particles (~100 nm in diameter) was formed (Figure 4.3a). Dark field TEM (DFTEM) study shows the sintered particles were composed of tens of lamellar stacks with a characteristic thickness of around 3.9 nm along the normal direction (Figure 4.2b). Such value in thickness is in close agreement with the grain dimensions in the powder pattern simulation, which is 4.2 nm (Figure 4.2b). The intermetallic Ag on Pt layers was also clearly revealed by high angle annular dark field scanning transmission electron microscopy (HAADF- STEM) (Figure 4.3c). The bright lines, corresponding to Pt planes, were separated by the darker lines of Ag planes, which could also be seen in the intensity profiles (Figure 4.3d). The spacing between adjacent Pt planes or Ag planes was measured to be ~4.30 Å, also in excellent agreement with the simulated structure. The orders of these Ag-Pt compositional intermetallics could be highly anisotropic (Figure 4.3e). While the stacks had long range ordering in one direction, irregularity of such slab-like structures was observed along the near orthogonal direction. Both HCP and CCP stacks were also readily observed in close proximity, resulting in a wavy interwoven structure (Figure 4.3e).

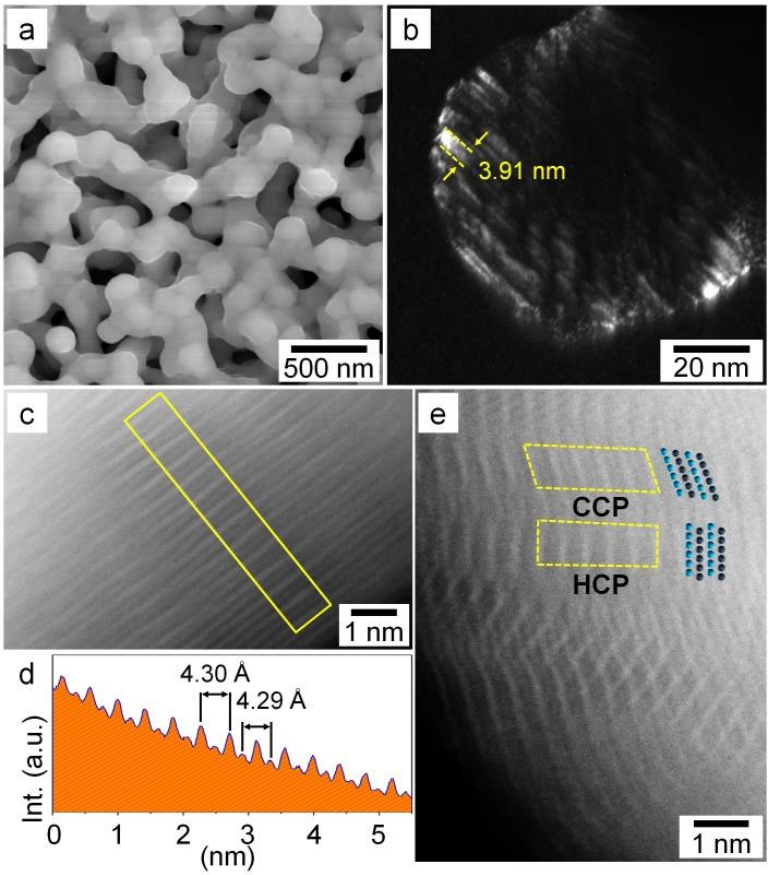

Figure 4.3 (a) SEM micrograph of thermally-treated sintered $Ag_{48.4}Pt_{51.6}$ particle. (b) DF-TEM showing the ~4-nm thick stacks of nanostructured layers within a sintered particle. (c) HAADF-STEM showing the alternating Pt (bright contrast lines) and Ag (light gray contrast lines) atom layers. (d) Intensity profile of boxed area in (c), showing the intermetallic lattice spacing of ~4.3 Å. (e) HAADF-STEM showing the complex interwoven structures of Ag-Pt compositional intermetallic that had both CCP and HCP stacks in close proximity. (DFTEM was constructed based on the 2.38 Å diffraction spot in Figure S2)

4.3.3 Investigation on the composition of Ag-Pt compositional intermetallic

This compositional intermetallic is unique in that it represents a new type of intermetallic compound with mixed hcp and fcc structure having a composition in the middle of miscibility gap of bulk phase diagram and that such an ordered phase was obtained only through the bottom-up approach using nanoparticles as starting materials. To further investigate the composition window of this unique intermetallic phase, we examined the crystal phase behavior upon thermal treatment using a series of Ag_xPt_y nanoparticles with different nominal Ag/Pt ratio based on the amount of precursors used (Figure 4.4). All as-made nanoparticles had fcc phase, indicating the formation of Ag-Pt random alloys (Figure 4.4a). After thermal treatment at 700 ºC, only two compositions ($Ag_{75}Pt_{25}$ and $Ag_{48.4}Pt_{51.6}$) were single phase, either the compositional intermetallic or the pure fcc alloy; while the rest had mixed crystal phases (Figure 4.4b). When the amount of Pt in the nanoparticle precursor was above the feeding ratio of $Ag_{48.4}Pt_{51.6}$, the annealed bimetallic separated into Pt-rich fcc alloy phase and the compositional intermetallic, judging by 2θ values of the characteristic fcc (200) diffraction peaks in the XRD for the as-made (black square) and thermally-treated (red circle) samples (Figure 4.5). On the other hand, if the Pt feeding ratio went below $Ag_{48.4}Pt_{51.6}$ but above $Ag_{75}Pt_{25}$, mixed compositional intermetallic and an Ag-enriched fcc phase were obtained, in agreement with a previous observation.[21] The composition of this intermetallic should be centered at 49% Ag and 51 % Pt feeding ratio, where the black solid line (as-made samples) and red dashed line intersected (thermally-treated samples).

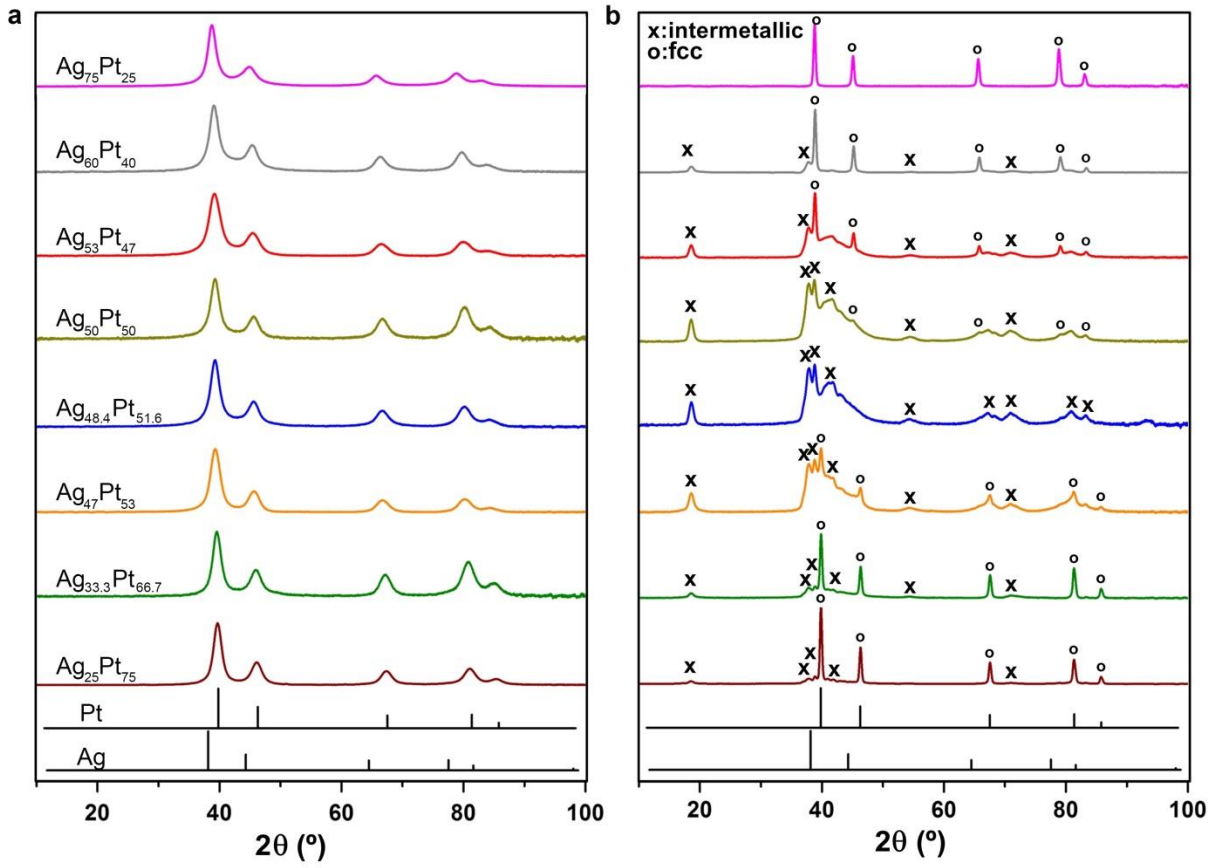

Figure 4.4 XRD of as-made $Ag_{100-x}Pt_x$ nanoparticles (a) and thermally-treated samples (b).

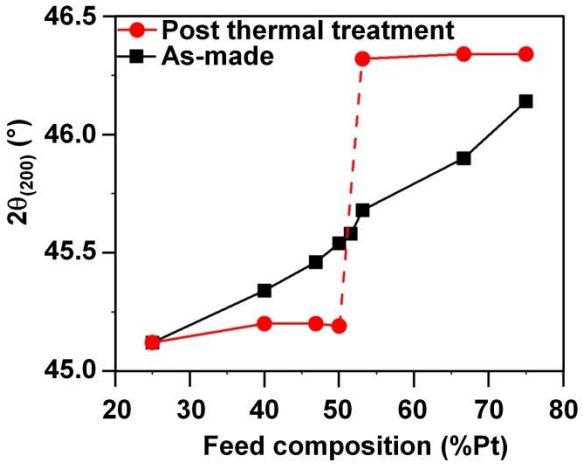

Figure 4.5 Position of fcc (200) diffraction of as-made and thermally-treated $Ag_{100-x}Pt_x$ samples as a function of feeding ratio in %Pt.

To further narrow down the exact composition of the compositional intermetallic compound, both the surface and bulk compositions were measured on thermally-treated samples with the Ag/Pt feeding ratio ranging from 53/47 to 47/53 by X-ray photoelectron spectroscopy (XPS) and energy dispersive X-ray spectroscopy respectively (Figure 4.6-4.9, Table 4.1). Enrichment of Ag took place at the surface after thermal treatment with a nearly constant atomic Ag/Pt ratio of 68/32 for these samples except for the sample with Ag/Pt feeding ratio of 47/53, in which case the Ag/Pt surface composition was measured to be 52/48. This observation suggests that a crossover of composition from left to right of the intermetallic phase.

Table 4.1 Analysis of surface composition using XPS

Entry		1	2	3	4
Composition	nominal	$Ag_{53}Pt_{47}$	$Ag_{50}Pt_{50}$	$A_{48.4}Pt_{51.6}$	$Ag_{47}Pt_{53}$
	XPS analysis	$Ag_{69}Pt_{31}$	$Ag_{68}Pt_{32}$	$Ag_{67}Pt_{33}$	$Ag_{52}Pt_{48}$

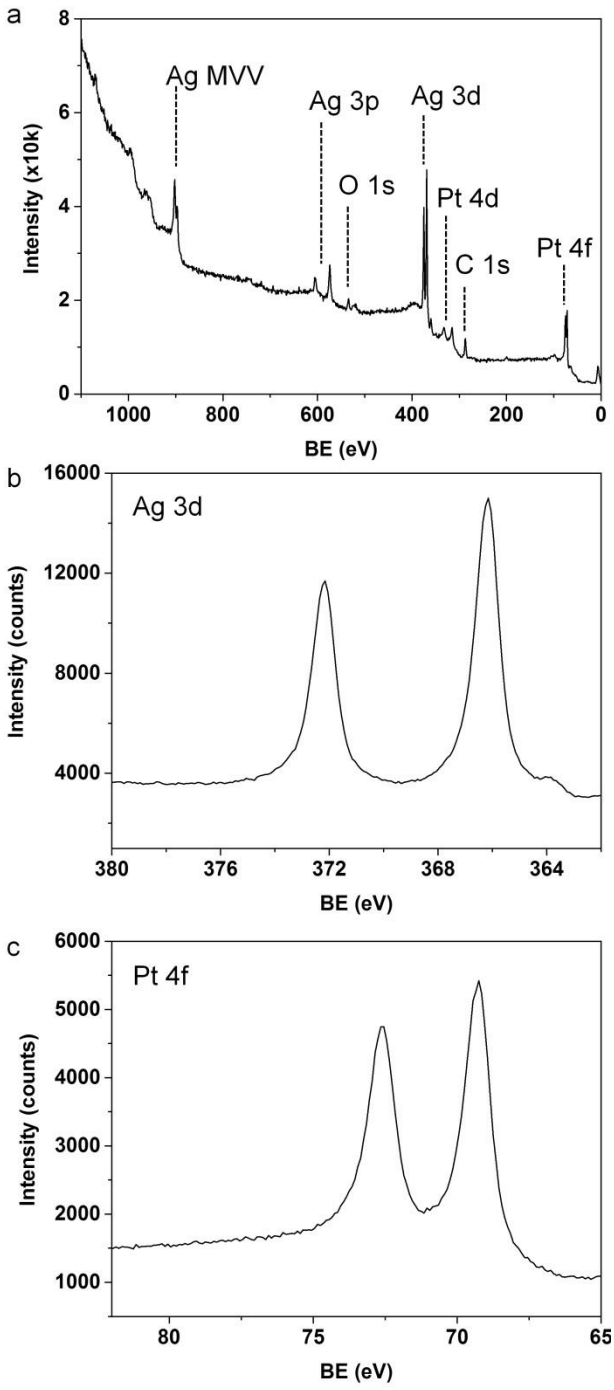

Figure 4.6 XPS spectra of the thermally treated $A_{53}Pt_{47}$ sample: (a) survey scan, (b) Ag 3d, and (c) Pt 4f regions.

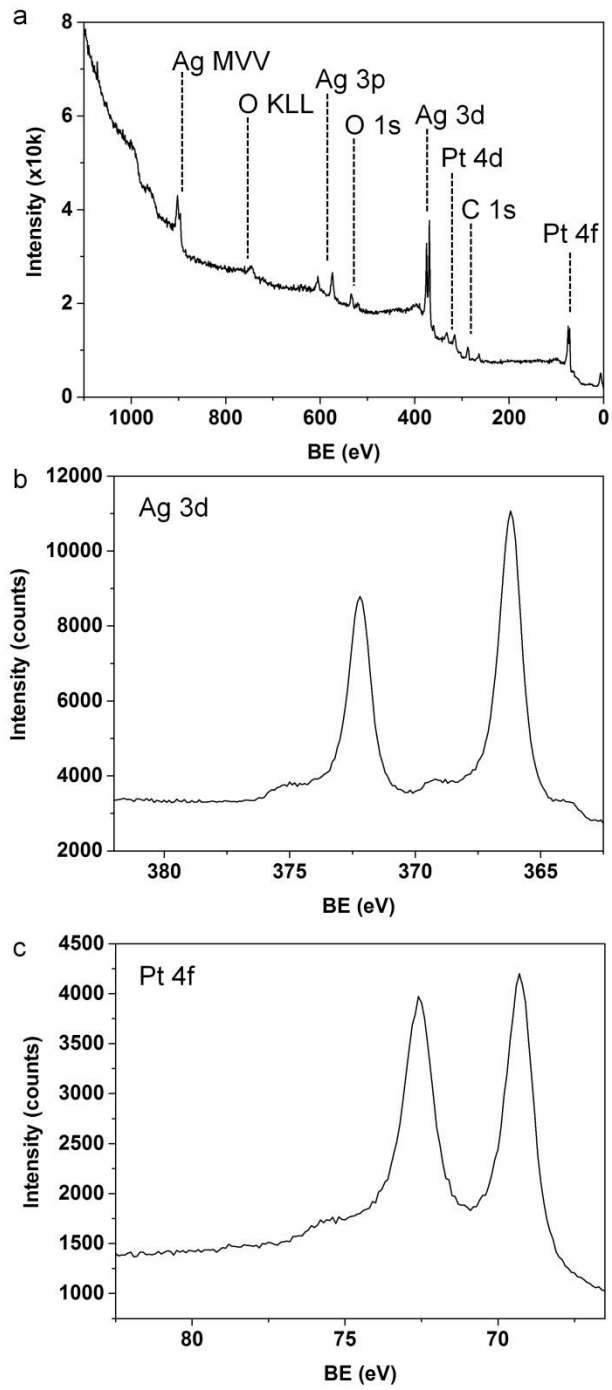

Figure 4.7 XPS spectra of the thermally treated $Ag_{50}Pt_{50}$ sample: (a) survey scan, (b) Ag 3d, and (c) Pt 4f regions.

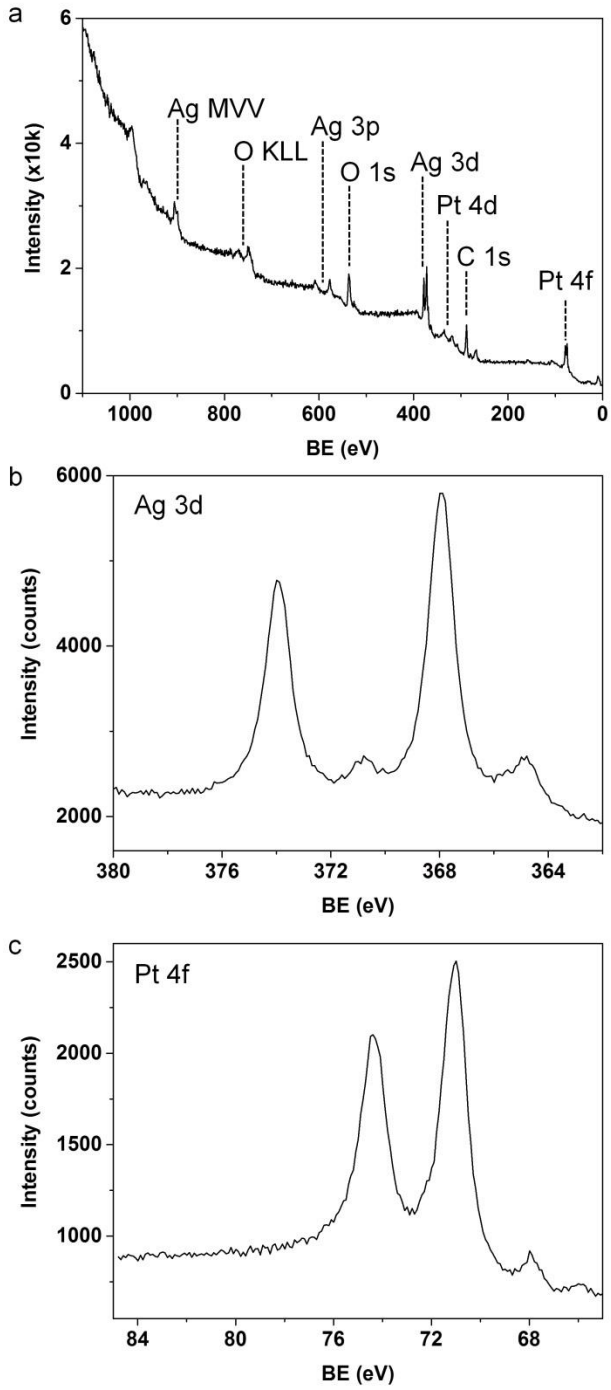

Figure 4.8 XPS spectra of the thermally treated $Ag_{48.4}Pt_{51.6}$ sample: (a) survey scan, (b) Ag 3d, and (c) Pt 4f regions.

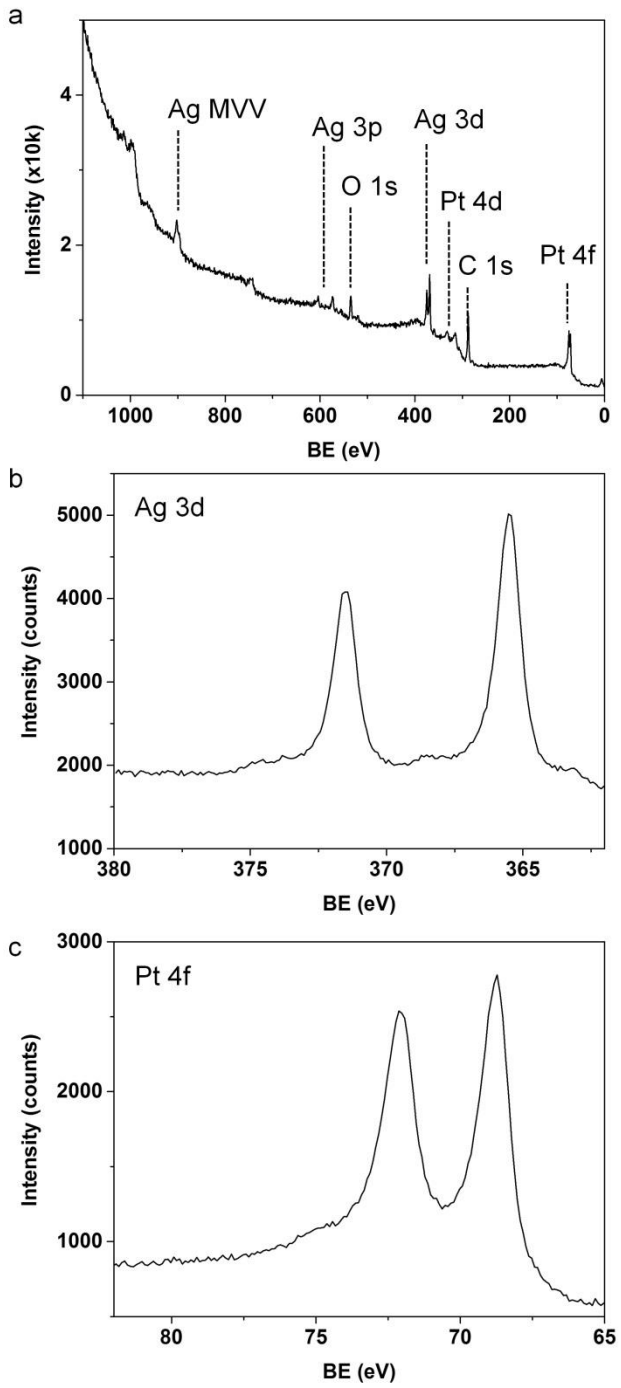

Figure 4.9 XPS spectra of the thermally treated $Ag_{47}Pt_{53}$ sample: (a) survey scan, (b) Ag 3d, and (c) Pt 4f regions.

From our density functional theory calculations, the intermetallic phase should exhibit intermediate surface energy in between a pure Ag and Pt surface which indicates the ratio of 52/48 closely represents the composition of the intermetallic phase (Figure 4.4b orange pattern, Figure 4.9, 4.10 and Table 4.1 entry 4). By treating the sample electrochemically in acidic electrolyte, the final Ag/Pt ratio became to 53/47 from 57/43 for the sample having the nominal ratio of $Ag_{48.4}Pt_{51.6}$ (Figure 4.2a, Table 4.2). Thus, the composition window for the intermetallic phase lies in between 52/48 and 53/47 for the Ag/Pt ratio.

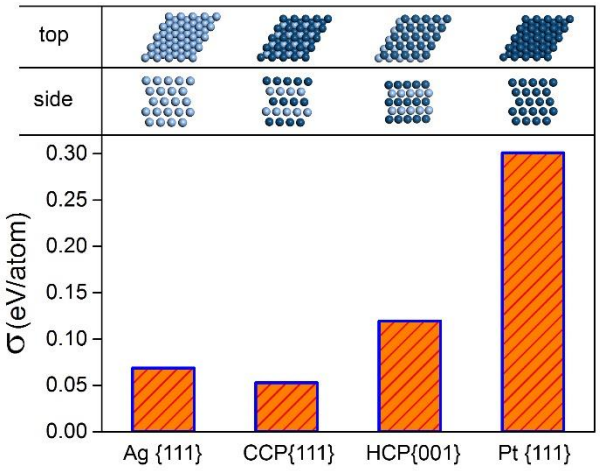

Figure 4.10. Surface energy of Ag, Pt, Ag-Pt CCP, and Ag-Pt HCP intermetallics obtained by DFT calculation.

Table 4.2 Analysis of composition of the sintered $Ag_{48.4}Pt_{51.6}$ catalysts before and after formic acid oxidation (FAOR) using EDX and XPS

	Composition	
	SEM-EDX	XPS
Prior to FAOR	$Ag_{57}Pt_{43}$	$Ag_{67}Pt_{33}$
After FAOR	$Ag_{53}Pt_{47}$	$Ag_{49}Pt_{51}$

The phase relationship between as-made and sintered Ag-Pt alloy at 700 ºC is summarized in Figure 4.11 based on the analysis of powder XRD patterns. There are three stable composition regions, corresponding to Ag-enriched fcc phase (light blue color), the compositional intermetallic (orange color), and Pt-enriched fcc phase (navy color). Our data show if the composition of Ag-Pt alloy nanoparticles (black stars) laid outside these three regions, phase separation took place upon thermal treatment, resulting in materials of two phases.

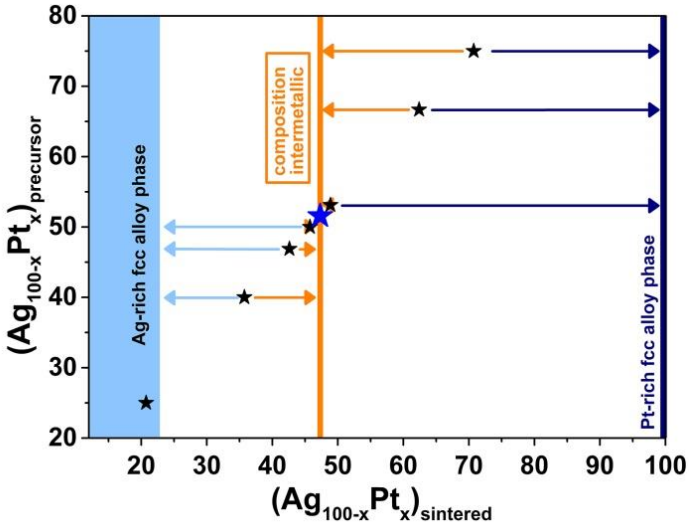

Figure 4.11 Composition phase diagram for Ag-Pt bimetallic showing the changes before and after the thermal treatment at 700 ºC.

4.3.4. Performance testing for electrochemical formic acid oxidation

The formation of intermetallic phase should impact on the performance of Ag-Pt bimetallic catalysts, especially towards those reactions sensitive to the surface composition and structure, such as formic acid oxidation reaction (FAOR).[30] Cyclic voltammetry (CV) was performed to study the activity towards FAOR using as-made $Ag_{48.4}Pt_{51.6}$ random alloy nanoparticles and compositional intermetallic catalysts. The current density had its maximum at 0.476 V for the intermetallic and 0.506 V for the as-made random alloy after the same initial cycling treatment (Figure 4.12).

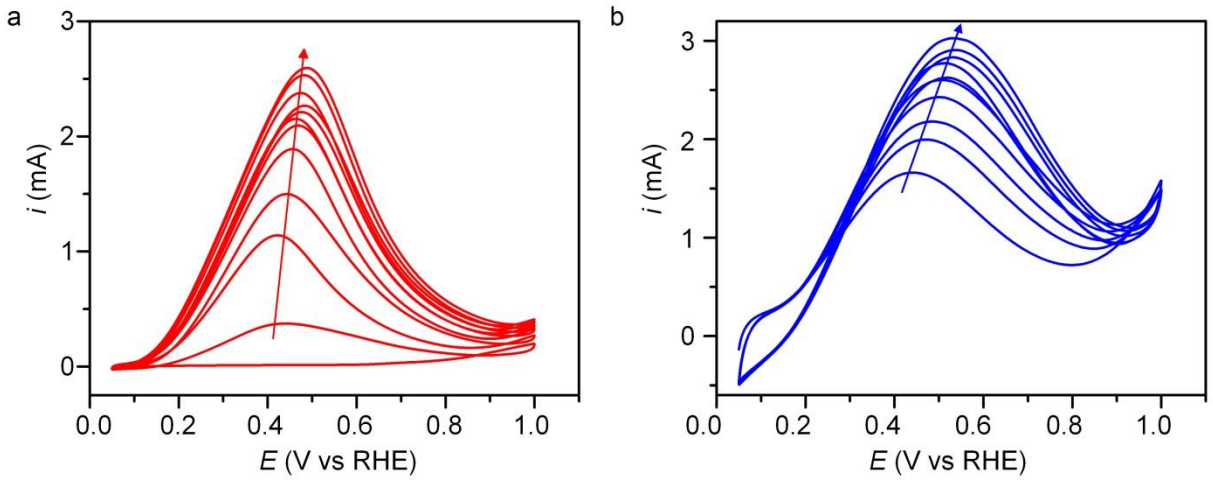

Figure 4.12 Initial 5 cycles of CV scan for (a) composition intermetallics and (b) $Ag_{48.4}Pt_{51.6}$ random alloy nanoparticles in 0.1M $HClO_{4(aq)}$ and 0.5M $HCOOH_{(aq)}$.

The convergent evidence from PXRD, SEM-EDX, and XPS studies shows the unstable, excess surface Ag could be removed after five potential cycles between 0.05 and 1.0 V for both Ag-Pt random alloy and compositional intermetallic. The X-ray diffraction patterns show no change for the intermetallic, demonstrating its excellent structural stability. The surface Ag

content for the random alloy nanoparticle catalyst, however, decreased from 66% to 49% based on the XPS analysis (Figure 4.13-14, Table 4.2).

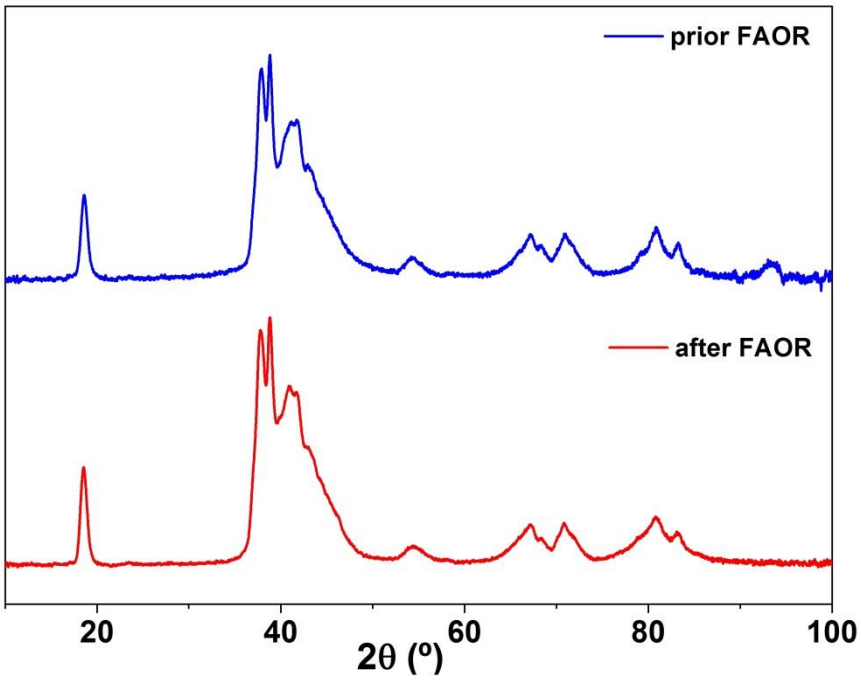

Figure 4.13 Powder XRD patterns of the compositional intermetallic catalyst before and after FAOR tests. (Nominal composition was $Ag_{48.4}Pt_{51.6}$)

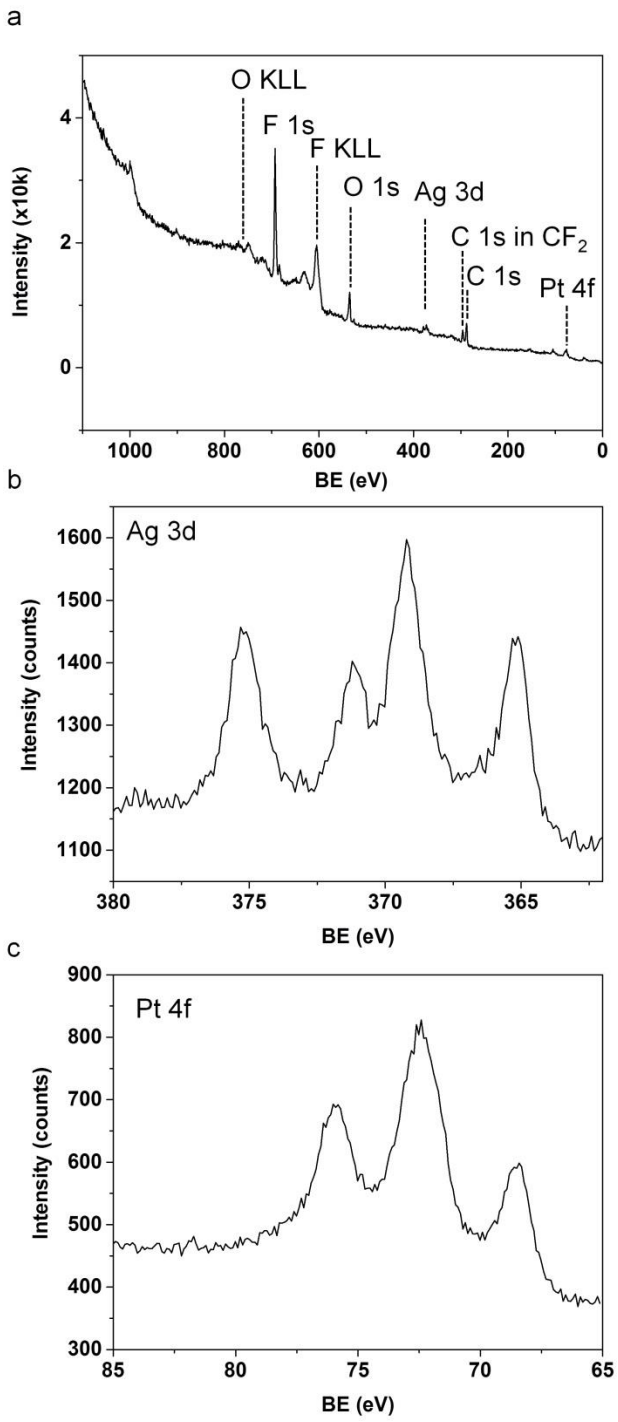

Figure 4.14. XPS spectra of thermally treated $Ag_{48.4}Pt_{51.6}$fter FAOR test. The extra peaks for the Ag 3d and Pt 4f regions were due to charging from the Nafion coating.

The electrochemical active surface area (ECSA) for proton adsorption was calculated from the CV curves scanned in 0.1M $HClO_{4(aq)}$ (Figure 4.15, Table 4.3) .

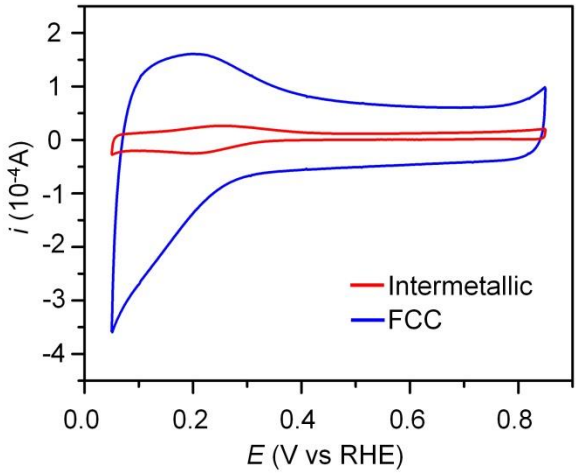

Figure 4.15 CV curves for intermetallic and alloy $Ag_{48.4}Pt_{51.6}$ random alloy nanoparticles in 0.1M $HClO_{4(aq)}$ after the initial 5 CV scans in 0.1M $HClO_{4(aq)}$ 0.5M $HCOOH_{(aq)}$.

Table 4.3 Integrated area and calculated ECSA based on the CV measurements*

	as-made	intermetallic	Pt/C
area (w)	3.13×10^{-5}	5.23×10^{-6}	5.50×10^{-5}
ECSA (cm^2)	2.98	0.498	5.24

*: The ECSA values were obtained based on the integrated area between 0.05 and 0.4V for proton adsorption.

The area specific activity was calculated by normalizing the FAOR current with ECSA which shows 3.75 mA/cm^2_{Pt} for the intermetallic and 0.75 mA/cm^2_{Pt} for fcc random alloy nanoparticles at 0.4 V (Figure 4.16). Similarly, at 0.5 V (near the peak potential in current

density), the area specific activity was 4.36 mA/cm^2_{Pt} for the Ag-Pt compositional intermetallic and 0.87 mA/cm^2_{Pt} for the random alloy. All these performance values were much higher than those for the reference Pt/C catalyst (Figure 4.17). The high FAOR activity of this Ag-Pt compositional intermetallic was attributed to a high degree of even dispersion of Pt atoms, the type of catalyst surface favoring the direct pathway for the oxidation of formic acid, which is the kinetically faster one of the two.[31, 32]

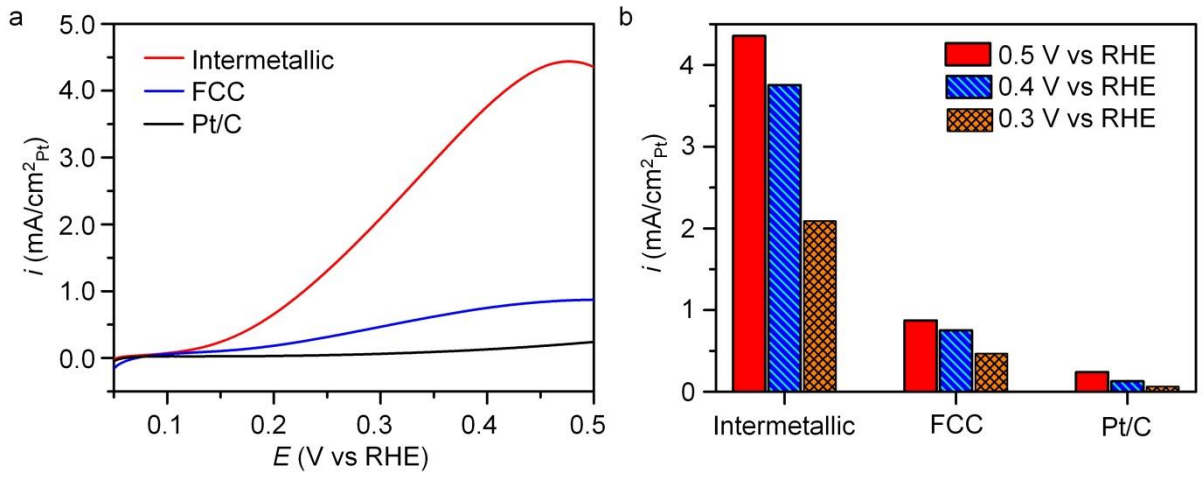

Figure 4.16 (a) current density-potential curves and (b), comparison of area-specific activity at given potentials for Ag-Pt intermetallic and fcc random alloy, and the reference Pt/C catalysts. The representative curves showed the 5th CV cycle for all catalysts in 0.5-M $HCOOH_{(aq)}$ with 0.1-M $HClO_{4(aq)}$ as the supporting electrolyte. The nominal ratio of Ag-Pt catalysts was 48.4% Ag and 51.6% Pt.

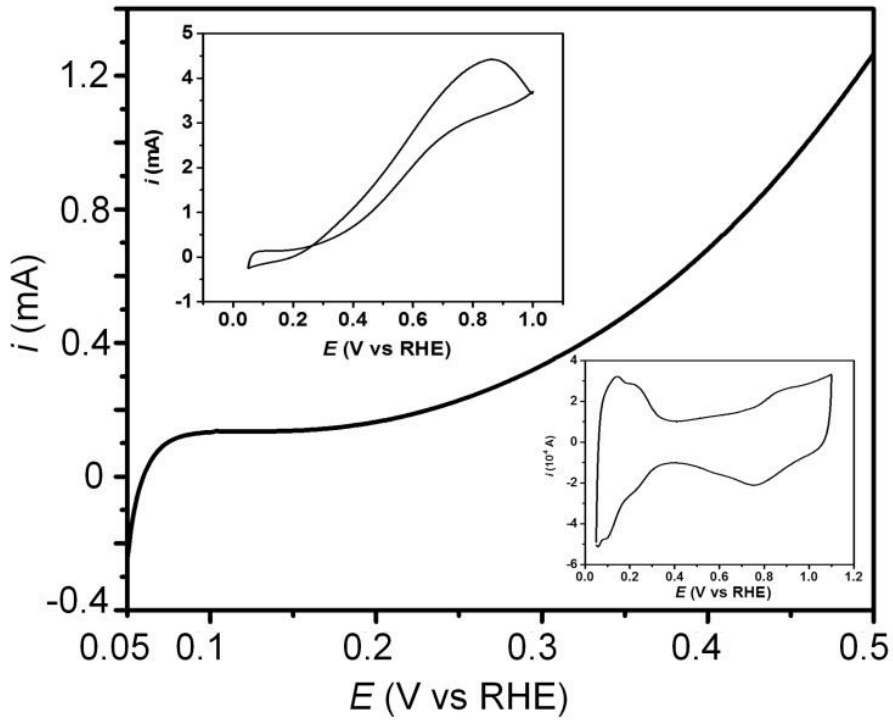

Figure 4.17 FAOR catalyzed by reference Pt/C catalyst. Inset at the upper left shows the full CV scan for FAOR from 0.05 to 1.0 V and inset at the lower right the proton adsorption/desorption in 0.1-M $HClO_{4(aq)}$ solution.

4.4 Conclusions

In summary, Ag-Pt compositional intermetallic phase was synthesized experimentally in the middle of bulk miscibility gap. The convergent results from XRD, STEM, XPS and X-ray diffraction simulation all point to a rare intermetallic structure of interchangeable close-packed Ag and Pt planes with long-range compositional order stacking with 85% on the tetrahedral symmetry sites and 15% on the octahedral symmetry sites. Ag-Pt alloy nanoparticles are necessary for the generation of such compositional intermetallic between the two immiscible metals because of the complex nanostructures, the final stable size of the stacks, and the narrow

composition window. Using modulated chemistry from nanoparticles to create atomic ordering between immiscible metals opens a new way for creating unusual nanostructured metals with superior properties.[7]

4.5 References

1. Gabor A. Somorjai, Y. L., *Introduction to surface chemistry and catalysis*. 2 ed.; John Wiley & Sons, Inc: Hoboken, New Jersey, 2010.

2. Peterson, A. A.; Nørskov, J. K. *J. Phys. Chem. Lett.* **2012,** 3, 251-258.

3. Reddington, E.; Sapienza, A.; Gurau, B.; Viswanathan, R.; Sarangapani, S.; Smotkin, E. S.; Mallouk, T. E. *Science* **1998,** 280, 1735-1737.

4. Greeley, J.; Mavrikakis, M. *Nat. Mater.* **2004,** 3, 810-815.

5. Sankar, M.; Dimitratos, N.; Miedziak, P. J.; Wells, P. P.; Kiely, C. J.; Hutchings, G. J. *Chem. Soc. Rev.* **2012,** 41, 8099-8139.

6. Mukherjee, P.; Manchanda, P.; Kumar, P.; Zhou, L.; Kramer, M. J.; Kashyap, A.; Skomski, R.; Sellmyer, D.; Shield, J. E. *ACS Nano* **2014,** 8, 8113-8120.

7. Freakley, S. J.; He, Q.; Harrhy, J. H.; Lu, L.; Crole, D. A.; Morgan, D. J.; Ntainjua, E. N.; Edwards, J. K.; Carley, A. F.; Borisevich, A. Y.; Kiely, C. J.; Hutchings, G. J. *Science* **2016,** 351, 965-968.

8. Chiritescu, C.; Cahill, D. G.; Nguyen, N.; Johnson, D.; Bodapati, A.; Keblinski, P.; Zschack, P. *Science* **2007,** 315, 351-353.

9. Ding, Y.; Fan, F.; Tian, Z.; Wang, Z. L. *J. Am. Chem. Soc.* **2010,** 132, 12480-12486.

10. Shao, L.; Zhang, W.; Armbrüster, M.; Teschner, D.; Girgsdies, F.; Zhang, B.; Timpe, O.; Friedrich, M.; Schlögl, R.; Su, D. S. *Angew. Chem. Int. Edit.* **2011,** 50, 10231-10235.

11. Armbrüster, M.; Kovnir, K.; Behrens, M.; Teschner, D.; Grin, Y.; Schlögl, R. *J. Am. Chem. Soc.* **2010,** 132, 14745-14747.

12. Armbrüster, M.; Wowsnick, G.; Friedrich, M.; Heggen, M.; Cardoso-Gil, R. *J. Am. Chem. Soc.* **2011,** 133, 9112-9118.

13. Armbrüster, M.; Kovnir, K.; Friedrich, M.; Teschner, D.; Wowsnick, G.; Hahne, M.; Gille, P.; Szentmiklósi, L.; Feuerbacher, M.; Heggen, M.; Girgsdies, F.; Rosenthal, D.; Schlögl, R.; Grin, Y. *Nat. Mater.* **2012,** 11, 690-693.

14. Ota, A.; Kunkes, E. L.; Kasatkin, I.; Groppo, E.; Ferri, D.; Poceiro, B.; Navarro Yerga, R. M.; Behrens, M. *J. Catal.* **2012,** 293, 27-38.

15. Fiordaliso, E. M.; Sharafutdinov, I.; Carvalho, H. W. P.; Grunwaldt, J.-D.; Hansen, T. W.; Chorkendorff, I.; Wagner, J. B.; Damsgaard, C. D. *ACS Catal.* **2015,** 5, 5827-5836.

16. Xiao, C.; Wang, L.-L.; Maligal-Ganesh, R. V.; Smetana, V.; Walen, H.; Thiel, P. A.; Miller, G. J.; Johnson, D. D.; Huang, W. *J. Am. Chem. Soc.* **2013,** 135, 9592-9595.

17. Wang, D.; Xin, H. L.; Hovden, R.; Wang, H.; Yu, Y.; Muller, D. A.; DiSalvo, F. J.; Abruña, H. D. *Nat. Mater.* **2013,** 12, 81-87.

18. Chung, D. Y.; Jun, S. W.; Yoon, G.; Kwon, S. G.; Shin, D. Y.; Seo, P.; Yoo, J. M.; Shin, H.; Chung, Y.-H.; Kim, H.; Mun, B. S.; Lee, K.-S.; Lee, N.-S.; Yoo, S. J.; Lim, D.-H.; Kang, K.; Sung, Y.-E.; Hyeon, T. *J. Am. Chem. Soc.* **2015,** 137, 15478-15485.

19. Kim, J.; Lee, Y.; Sun, S. *J. Am. Chem. Soc.* **2010,** 132, 4996-4997.

20. Zhang, L.; Roling, L. T.; Wang, X.; Vara, M.; Chi, M.; Liu, J.; Choi, S.-I.; Park, J.; Herron, J. A.; Xie, Z.; Mavrikakis, M.; Xia, Y. *Science* **2015,** 349, 412-416.

21. Durussel, P.; Feschotte, P. *J. Alloy Compd.* **1996,** 239, 226-230.

22. Marcel H. F. Sluiter, C. C., Alain Pasturel. *Phys. Rev. B* **2006,** 73, 174204.

23. Peng, Z.; You, H.; Yang, H. *ACS Nano* **2010,** 4, 1501-1510.

24. Clark Stewart, J.; Segall Matthew, D.; Pickard Chris, J.; Hasnip Phil, J.; Probert Matt, I. J.; Refson, K.; Payne Mike, C. *Kristallogr.* **2005,** 220, 567.

25. Tkatchenko, A.; Scheffler, M. *Phys. Rev. Lett.* **2009,** 102, 073005.

26. Yin, X.; Liu, X.; Pan, Y.-T.; Walsh, K. A.; Yang, H. *Nano Lett.* **2014,** 14, 7188-7194.

27. Methfessel, M.; Hennig, D.; Scheffler, M. *Phys. Rev. B* **1992,** 46, 4816-4829.

28. Treacy, M. M. J.; Newsam, J. M.; Deem, M. W. *P. Roy. Soc. Lond. A Mat.* **1991,** 433, 499-520.

29. Peng, Z.; Yang, H. *J. Solid State Chem.* **2008,** 181, 1546-1551.

30. Peng, Z.; You, H.; Yang, H. *Adv. Func. Mater.* **2010,** 20, 3734-3741.

31. Zhang, S.; Shao, Y.; Liao, H.-g.; Liu, J.; Aksay, I. A.; Yin, G.; Lin, Y. *Chem. Mater.* **2011,** 23, 1079-1081.

32. Kristian, N.; Yan, Y.; Wang, X. *Chem. Commun.* **2008**, 353-355.

Chapter 5

Double-Layered Rh-on-Pd Nanocatalysts for Selective CO_2 Methanation

5.1 Introduction

Atomically thin metal shells often show the largest effect on their surface electronic structures by the core metal which may exhibit drastically different adsorption affinity towards reactant molecules from their parent bulk metals, leading to exceptional activity and/or selectivity when applied as catalysts.[1-6] Monolayer metal-on-metal single crystal surfaces has been extensively studied based on this strategy, both theoretically and experimentally, for the hydrogenation and decomposition of alkenes,[7-8] reforming of oxygenates,[8] dehydrogenation of cyclohexene,[9] and reaction of C-OH and C=O functional groups.[10] A number of density functional theory (DFT) calculations have also been carried out for a wide variety of bimetallic catalyst for electrochemical reactions on metal surfaces such as Pt monolayers for oxygen reduction reaction (ORR),[11-13] and hydrogen evolution reaction (HER),[1, 3] etc. Adsorption energetics of key adsorbates can be computationally acquired relatively easily on a wide variety of metallic surfaces and served as a useful predictive tool for the development of catalyst.

From a practical standpoint, it is desirable to prepare monolayer metal-on-metal surfaces in the form of nanoparticles based on single crystal surface studies. However, direct synthesis of such monolayer-based core-shell nanoparticle system is a challenging task due to the structural complexity of real catalyst particles, which contain varied amounts of high energy step and kink sites. Solution phase synthesis was used successfully in limited cases where core-shell

nanoparticles closely resemble those structures of metal-on-metal surface.[14-15] A few known examples include core-shell structures of Pd@Pt cube,[13] Pd@Pt[16] and Au@Pd[17] octahedral, and Au-Pt star-shaped decahedron,[18] which were made through two-step process with controlled injection of shell precursors.

Besides the synthetic challenges, structural stability of as-synthesized, core-shell nanocrystal catalysts remains unclear. Since they often change their structures under reactive environments,[19-22] spherical core-shell nanoparticle catalysts often exhibit unpredictable performance over time with the loss of core-shell features.[14] Thus, there also is a need to gain further understanding on the behaviors of these temperature-sensitive catalysts with atomically thin shells under thermal and chemical reactive environments. For heterogeneous catalysis, optimization of reaction conditions becomes critical for the design and processing of bimetallic core-shell nanocatalysts to have the appropriate structures for high performance.

In this chapter, we demonstrate the preparation of Rh-on-Pd nanoparticles composed of a Pd core with double-atomic layered Rh shell and investigate their structure-performance relation for catalytic hydrogenation of carbon dioxide (CO_2). Conversion of CO_2 into hydrocarbons is a major research focus in recent years due to the growing concern of its impact on climate change.[23-24] In this conversion process, activation of CO_2 to CO intermediate occurs, therefore, the competition between the dissociation and desorption of CO on and from the catalyst surface often determines the CO/hydrocarbon selectivity. In general, if CO adsorbs preferably as molecular species on a catalyst surface, the reaction tends to result in high selectivity in CO production.[25-26] On the other hand, if the intermediate CO species preferentially dissociates over the catalyst surface, high selectivity towards CH_4 can often be achieved. Bimetallic core-shell catalysts with the monolayer metal-on-metal structures have been studied in overcoming the

intrinsic limitation of monometallic systems in tuning the dissociative adsorption energy of CO and in the product selectivity of CO_2 hydrogenation reaction.[27-28] However, due to the requirement of high reaction temperature, the stability of core-shell nanocatalyst under reaction conditions is an important subject matter that needs to be addressed. Thus, herewith we investigated the structural dynamics of Rh-on-Pd catalysts in hydrogen atmosphere under different temperature using the in situ environmental transmission electron microscope (ETEM).[29] The relationship between reaction temperature and CO/CH_4 selectivity was examined for the hydrogenation of CO_2 in real time at different reaction temperatures. Density functional theory (DFT) calculations were carried out to provide further understanding on the structural origin for the performance.

5.2 Experimental

5.2.1 Materials and chemicals

Palladium acetylacetonate ($Pd(acac)_2$, Strem Chemical, 99%); rhodium acetylacetonate ($Rh(acac)_3$, Strem Chemical, 99%); 1,4-butanediol (Sigma-Aldrich, 99%); polyvinylpyrrolidone (PVP, Sigma-Aldrich, MW: 10k); hexadecyltrimethylammonium bromide (CTAB, Sigma-Aldrich, >96%); α-alumina (α-Al_2O_3, Alfa-Aesar, 99%); acetone (Macron, >99%); ethanol (Decon Labs, 200 proof); 5% H_2 (balanced with N_2, Airgas); carbon dioxide (CO_2, SJSmith, research grade). All chemicals were used as received without further purification.

5.2.2 Synthesis of Rh-on-Pd nanoparticles

Synthesis of Rh-on-Pd nanoparticles was carried out modified polyol synthesis method.[21] 7.6 mg of $Pd(acac)_2$, 9.4 mg of $Rh(acac)_3$, 100 mg PVP10k, and 15 mg of CTAB, and 9 mL of 1,4-butanediol were mixed in a 25-mL three-neck round bottom flask. The flask was connected to a Schlenk line through a condenser. The reaction mixture was preheated at 55 °C until all species were completely dissolved to form a homogeneous yellow-orange color solution. The flask was then evacuated with a rotary pump (Edward RV 12) and purged with Ar for 6 cycles to remove air and moisture. The temperature of the solution was then ramped up to 220 °C (10 °C/min), maintained for 1 h, and cooled down to room temperature under Ar. The solid products were collected by centrifugation where acetone was added into the synthesis solution to precipitate out the nanoparticles. The washing steps of nanoparticles included re-dispersing in ethanol by ultra-sonication for 1 min and precipitation by centrifugation in an ethanol-acetone mixture at 9000 rpm for 20 min. The washing process was repeated five times. The final products were dispersed in ethanol for further characterization. Synthesis of Rh and Pd monometallic nanoparticles was carried out with procedures identical to that for the synthesis of Rh-on-Pd, except that the mixed metal precursors were replaced with one of the corresponding precursors.

5.2.3 Characterization

Powder X-ray diffraction (XRD) patterns were acquired on Bruker D8 Venture (DUO) diffractometer. Transmission electron microscopy (TEM) and nanobeam electron diffraction (NBD) was taken on a JEOL 2100 Cryo TEM. Scanning transmission electron microscopy

(STEM) and energy dispersive X-ray was carried out with JEOL 2010F microscopy with an accelerating voltage of 200 kV.

5.2.4 Density functional theory calculation

DFT calculation was performed using the CASTEP[30] module with ultrasoft pseudopotentials.[31] The electron exchange and correlation energy was treated with generalized gradient approximation (GGA) with the Perdew−Burke−Ernzerhof (PBE) functional[32] was applied to treat the electronic exchange and correlation with Tkatchenko-Scheffler (TS) dispersion correction was accounted.[33] The plane-wave basis set cut-off energy was set to 300 eV. The lattice constant of a Pd and Rh unit cell was first optimized and used for building Rh and Pd 3x3 periodic 3 layer (111) slab. Mono to tri-layers of Rh on Pd(111) was built by replacing the Pd surface layers with Rh on a 3x3 periodic 6 layer Pd(111) slab. The total energy of clean and CO adsorbed Rh and Pd(111) slab was calculated with the bottom two layers fixed while the bottom three layers were fixed for the calculation of mono to tri-layer Rh on Pd(111). Energy of single CO molecule was calculated in a 8.2Å×8.2Å×24.8Å box (same dimension as the for the triple-layered slabs). The Monkhorst-Pack scheme k-point grid sampling was set to 1×1×1 for the 3 layer slabs, 5×5×1 for the 6 layer slabs, and Gamma point for single CO molecule. The tolerance for convergence was 1×10^{-5} eV/atom in energy, 3×10^{-2} eV/Å in force, and 1×10^{-3} Å in displacement. The same settings were applied for calculation both in vacuum and with adsorbed CO molecule. The CO adsorption energy was calculated using the following equation:

$$E_{ad} = E(CO_{ad}/surface) - E(CO_{(g)}) - E(surface)$$

where E_{ad} is the adsorption energy, E(molecule) is the energy of the free molecule, E(surface) is the energy of the surface in vacuum, and E(molecule/surface) is the energy of the surface with molecular and dissociative adsorbed CO.

5.2.5 In Situ ETEM study

In situ TEM studies were carried out in a Hitachi H9500 Environmental Transmission Electron Microscope (ETEM) at an accelerating voltage of 200 kV (3μA) under Nano mode with a current density of 1.6×10^{-12} A/cm^2. The Rh-on-Pd/Al_2O_3 catalyst suspension in ethanol were deposited using fine tip brush onto a tungsten heating wire which served as a heating element in the variable temperature gas injection holder. The holder was then introduced into the Hitachi H9500 ETEM and connected to a DC power supply for resistive heating. Temperature of the heating element was referred to the current-temperature relation chart (Hitachi). Nano beam diffraction (NBD) on selected particles was carried out with increasing temperatures under hydrogen through a mass flow controller (Brooks Instrument, SLA 5850S1SAB1C2A1). The probe size is 3 nm and maintained throughout the course of the experiment. TEM and NBD micrographs were recorded using the Gatan Orius SC200 CCD camera, and Gatan digital micrograph software. Polycrystalline aluminum film (TED PELLA. INC.) was used as a standard to calibrate the diffraction micrographs. Electron irradiation was kept minimized during the course of experiment in which the gun valve was opened only during image acquisition. The sample was then left in dark before the next imaging cycle. Image analysis and processing was done using Digital Micrograph (DM, Gatan).

5.2.6 Catalytic performance test

As-synthesized Rh-on-Pd, Rh, and Pd NPs were supported on α-Al_2O_3 by physically mixing the Al_2O_3 powders in a suspension of NPs in ethanol; a typical recipe included 100 mg of Al_2O_3 with 1 mg of NPs suspended in 10 mL of ethanol. The Al_2O_3 supported NPs were than drop casted on a glass slide where the amount was measured with a balance. The glass slide was then placed into a 22 mL homemade stainless steel reactor where CO_2 and H_2 balanced with N_2 was flowed through with a total flowrate of 21 mL/min with a ratio of 2:1:18 using mass flow controllers (Brooks). The temperature of the reactor was controlled by a hotplate and the products were analyzed online by a GC (SRI, Multigas #3) with a TCD and FID detector equipped with a methanizer with He as the carrier gas.

5.3 Results and Discussion

5.3.1 Synthesis and characterization of Rh-on-Pd nanoparticles

Rh-on-Pd nanoparticle was synthesized by a modified wet-chemical route.[21] In a typical synthesis process, $Pd(acac)_2$ and $Rh(acac)_3$ was sequentially decomposed in a solution of 1,4-butanediol containing PVP and CTAB at 200 °C under Ar. The as-synthesized Rh-on-Pd nanoparticles possessed an icosahedral geometry (Figure 5.1a) with an estimated average diameter of 5.8 nm based on a spherical model (Figure 5.1a, inset).

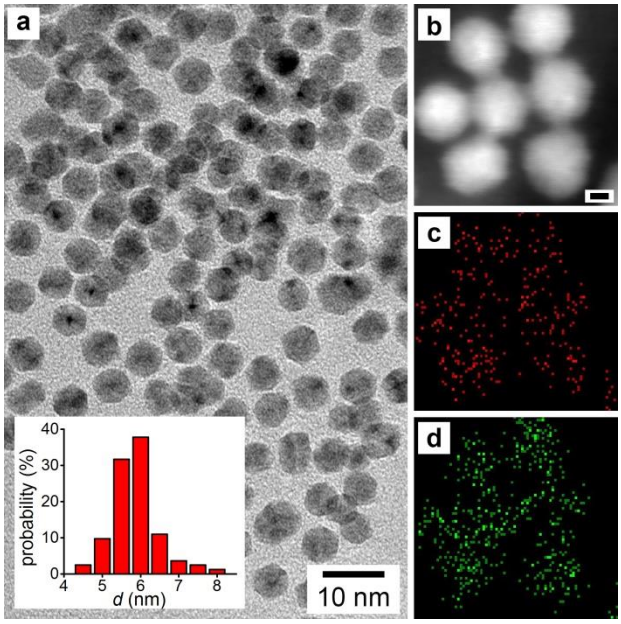

Figure 5.1 EM characterization of as-made Rh-on-Pd nanoparticles: (a) TEM, (b) STEM (Scale bar is 2 nm) and (c, d) EDX maps of Rh and Pd metals, respectively. Inset shows the size distribution of Rh-on-Pd particles.

Dark field scanning transmission electron micrograph (STEM) and its corresponding energy dispersive X-ray spectroscopy (EDS) mapping suggested the coexistence Rh and Pd atoms on individual particles (Figure 5.1b-d). Quantitative elemental analysis of the as-synthesized particles shows these nanoparticles had an average composition of 44 at% Rh and 56 at% Pd (Figure 5.2).

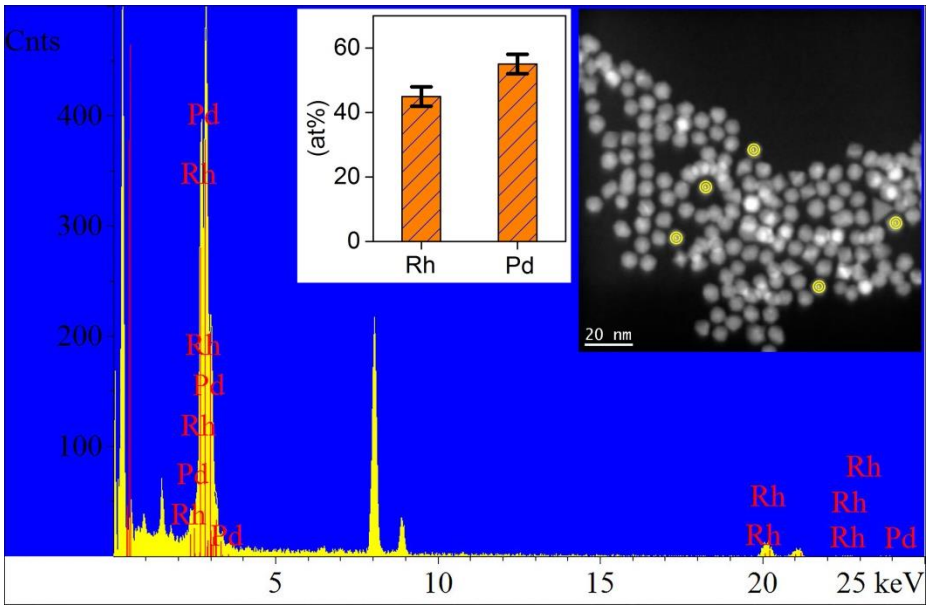

Figure 5.2 STEM-EDX spot analysis spectrum of as-synthesized Rh-on-Pd nanoparticles. (Inset bar chart shows the average composition over 5 measurements in the STEM micrograph)

PXRD pattern shows the as-synthesized particles had a face-center-cubic (fcc) phase structure with all peaks corresponding explicitly to Pd metal (Figure 5.3). No Rh diffraction signals were observed, although EDX analysis clearly shows Rh distributed evenly on the nanoparticles. We note that Rh and Pd metals are immiscible, thus the convergent data suggest that Rh atoms should deposit on the surface of these nanoparticles.

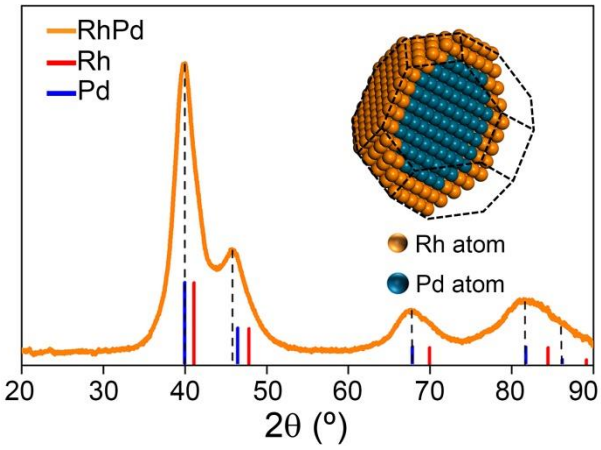

Figure 5.3. PXRD of as-made Rh-on-Pd core-shell nanoparticles

Since lattice constants are similar between Pd (3.89 Å) and Rh (3.80Å), we modelled the size of Rh-on-Pd core-shell nanoparticles using Pd icosahedral nanoparticle. The atomic fraction of shell is derived as a function of particle size of Pd by considering the volumetric percentage of shell over the entire particle. For an icosahedral nanoparticle, its volume V can be calculated by the following equation:

$$V = \frac{5}{12}(3+\sqrt{5})a^3 \approx 2.182a^3 \quad (1)$$

where a is the edge length of icosahedral nanoparticle. The volume of shell V_{shell} is calculated by subtracting V_{core} from the total volume V:

$$V_{shell} = V - V_{core} \quad (2)$$

The edge length of core (a_{core}) is obtained assuming that an icosahedral (Ih) particle is composed of 20 tetrahadras (Td) with the same edge length, that is, $a_{Ih} = a_{Td} = a$. Thus, for a tetrahedron, the height h has the following relation with edge length:

$$h = \sqrt{\frac{2}{3}}a \tag{3}$$

likewise, and the height (h_{core}) and edge length (a_{core}) of the core is given by:

$$h_{core} = \sqrt{\frac{2}{3}}a_{core} \tag{4}$$

Since the height of the core is equal to the height of the original tetrahedron subtracted by the thickness of the shell, *i.e.*, n layers of the (111) plane, as the following:

$$h_{\text{core}} = h - nd(111) \tag{5}$$

where $d(111)$ is the d-spacing of Pd (111) plane. The edge length of core a_{core} can then be derived by substituting h_{core} in Eq. (4) with Eq. (5):

$$h - nd(111) = \sqrt{\frac{2}{3}}a_{core} \tag{6}$$

which h can further be substituted by Eq. (3):

$$\sqrt{\frac{2}{3}}a - nd(111) = \sqrt{\frac{2}{3}}a_{core} \tag{7}$$

Where a_{core}:

$$a_{core} = a - \sqrt{\frac{3}{2}}nd(111) \tag{8}$$

And $V_{\text{core:}}$

$$V_{core} = 2.18[a - \sqrt{\frac{3}{2}}nd(111)]^3 \tag{9}$$

For a spherical particle, its atomic fraction of shell is calculated based on the following equation:

$$r_{\text{core}} = r\text{-n}\times d(111) \tag{10}$$

where r is the radius of the core and shell used to calculated the volumes accordingly. Assuming the shell is made of Rh due to the immiscibility between the two metals, Rh/Pd molar ratio can thus be directly estimated from $V_{shell}/(V- V_{shell})$ and can be calculated as a function of particle size and thickness of Rh shell (Figure 5.4).

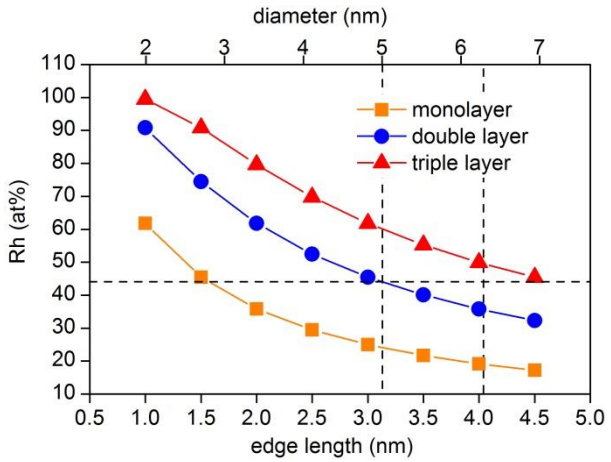

Figure 5.4 Modeled atomic layer thickness of Rh shell as a function of edge length of Rh-on-Pd core-shell icosahedron.

In this treatment, the calculated atomic fraction of shell is similar between an icosahedral and a spherical particle for a given particle (Figure 5.5) and the size distribution of as-made icosahedral Rh-on-Pd nanoparticles were used. For a Rh-on-Pd core-shell particles with diameters spanning from 5-6.5 nm, equivalent of edge lengths of 3.2-4.2 nm, and an overall composition of $Pd_{56}Rh_{44}$ (Figure 5.1a, 5.2), the shell should be composed of 2 or 3 atomic layers of Rh (Figure 3). Such thin layer did not have repeat lattice and thus could not be detected using PXRD, which explains the absence of diffraction signals.

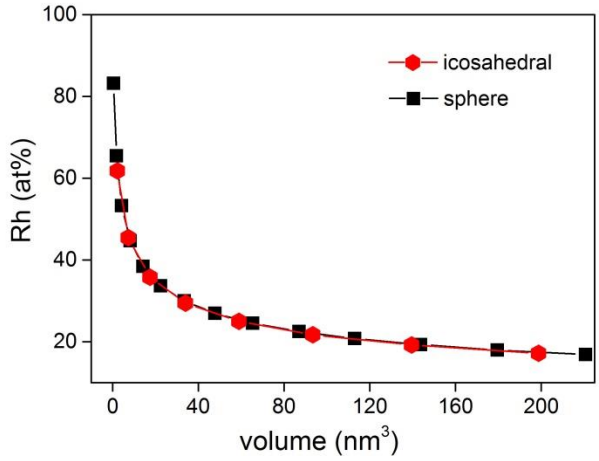

Figure 5.5 Calculated atomic fractions of a monolayer (n=1) shell for Pd icosahedral and spherical particle as a function of volume (*V*).

From the synthesis of monometallic Pd and Rh nanoparticles (Figure 5.6), a significant difference in the particle formation temperature can be observed (Figure 5.7). The nucleation of Pd nanoparticles can be initiated at 60~80 °C and was completed at 110 °C while it was not until 160 °C that the nucleation of Rh nanoparticles started taking place (Figure 5.8). This experimental observation further supports the successful one-pot synthesis of Rh-on-Pd nanoparticles through the sequential formation of Pd core followed by the growth of Rh shell due to the intrinsic difference in reducibility between the Pd and Rh metal salt precursors.

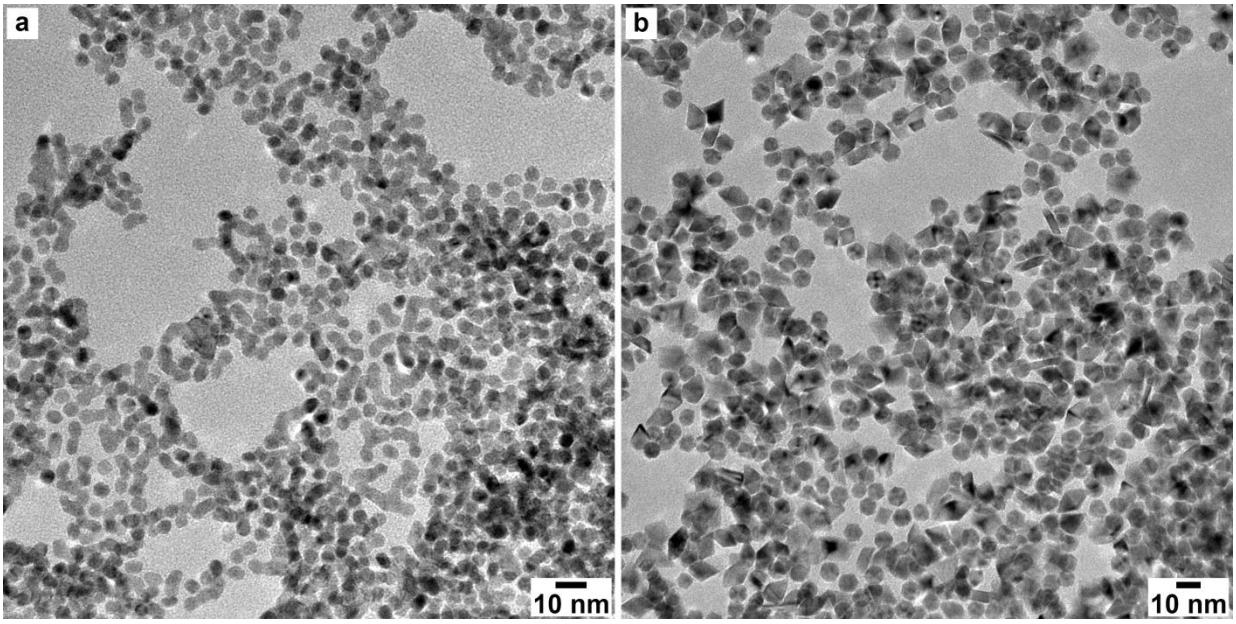

Figure 5.6 TEM micrograph of as-synthesized (a) Pd and (b) Rh nanoparticles.

Figure 5.7 Photographs of reaction solution showing the decomposition of $Pd(acac)_2$ (top rows) and $Rh(acac)_3$ (bottom rows) under different reaction temperatures.

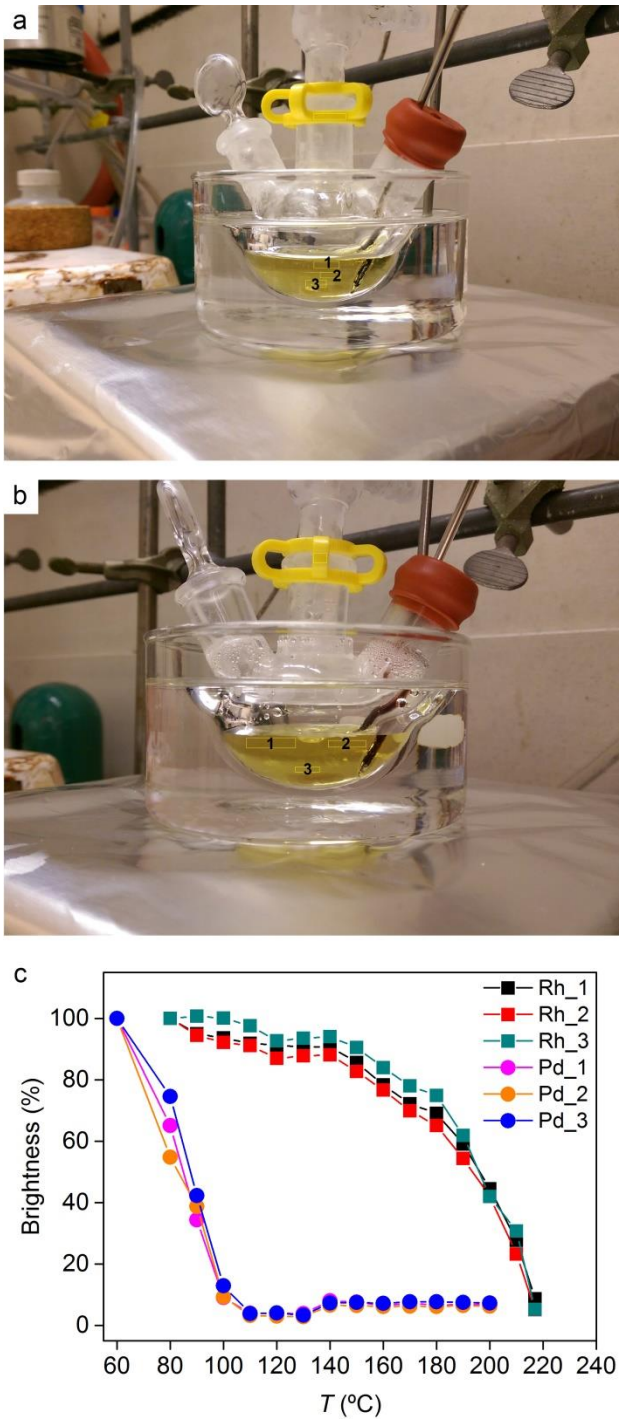

Figure 5.8 Locations where histogram as measured for (a) Pd, (b) Rh, and (c) summary of the brightness of the synthesis solution in Figure 5.7.

5.3.2 Structure evolution of Rh-on-Pd nanoparticles under reducing thermal environment

To investigate the thermal stability, α-Al_2O_3 supported Rh-on-Pd nanoparticles as catalyst was subjected to thermal environments under H_2 and studied in the ETEM. Images were acquired at different temperatures to estimate the particle size (Figure 5.9) and nanobeam electron diffraction (NBD), with a 3-nm probe (Figure 5.10), was applied to investigate the composition distribution.

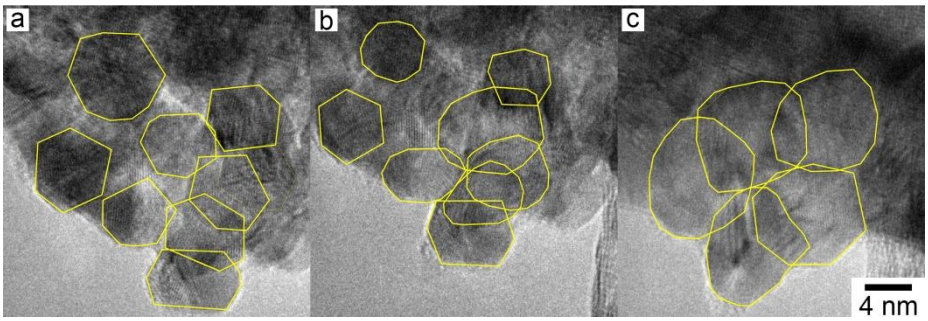

Figure 5.9 TEM micrographs of $RhPd/Al_2O_3$ catalyst acquired in situ under H_2 atmosphere at 50 °C (a), 100 °C (b), and 150 °C (c). The particles selected for size analysis are highlighted in yellow.

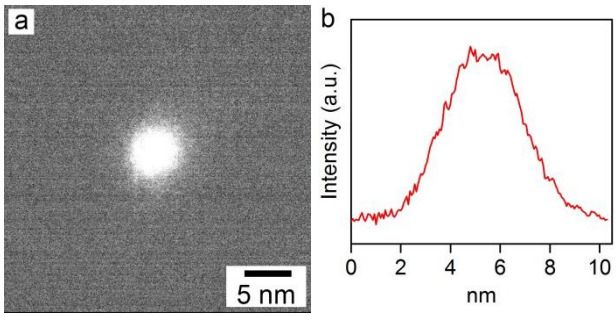

Figure 5.10 NBD probe (a) and FWHM (b) for in situ ETEM experiment and the SAED of Al diffraction standard (c) and calibration of measured distance in reciprocal space (d).

At 50 and 100°C, although aggregated on α-Al_2O_3 surface, individual icosahedral particles can be clearly observed where the NBD shows multiple spots forming a ring. When calculated back in to real space, the spots reflected a spacing of 2.225-2.24Å that corresponds to the (111) diffraction of Pd from multiple particles (Figure 5.11a,b). Sintering was initiated when the temperature was increased to 150 °C. Although difficult to distinguish the boundaries between individual particles, it is clear that the sintered particles remained polycrystalline with only the fcc Pd phase observable (Figure 5.11c). At 200 °C, the sintered particles evolved in to fewer single crystal domains with larger grain size (Figure 5.11d, inset). The NBD patterns taken at regions close to the surface started showing hints of the fcc Rh phase, the elongated spot highlighted is a results of the overlapping of the Pd and Rh(111) diffraction (Figure 5.11e) whereas only Pd related diffraction spots were observed at regions near the substrate (Figure 5.11f). Figure 5.11g summarizes the relation between temperature, particle size, and number of observed phases showing a critical temperature in between 150 and 200 °C and a threshold diameter around 10 nm where the second Rh (111) phase became observable.

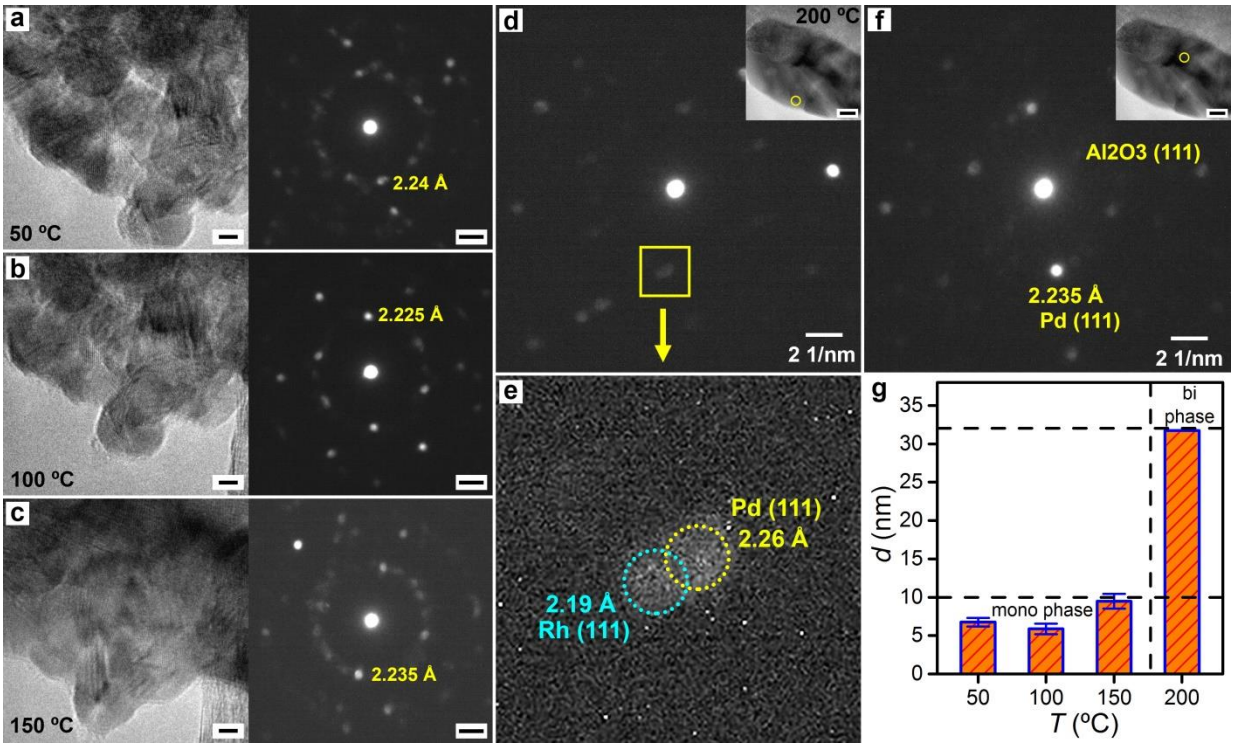

Figure 5.11 In situ ETEM-NBD observations of Rh-on-Pd nanoparticles under H_2 environment at different temperatures. (a-c) 50, 100, 150 °C respectively, scale bar 5 nm in TEM and 2 1/nm in ED; (d,e) 200 °C, NBD acquired at highlighted positions in inset TEM with 5 nm scale bar; (f) enlarged image of boxed area in (d) showing the overlapping of two diffraction spot from Rh and Pd; (g) relation of particle size, temperature, and phase summarized of from in situ NBD observations.

To confirm the phenomenon observed in situ, ex situ thermal treatments experiments was carried out under H_2 atmospheres in a tube furnace followed by characterization by TEM-NBD. The Rh-on-Pd particles were stable at 200 °C but started showing sintering and hints of detectable Rh phase at 250 °C which became more apparent at 300 and 350 °C (Figure 5.12-19).

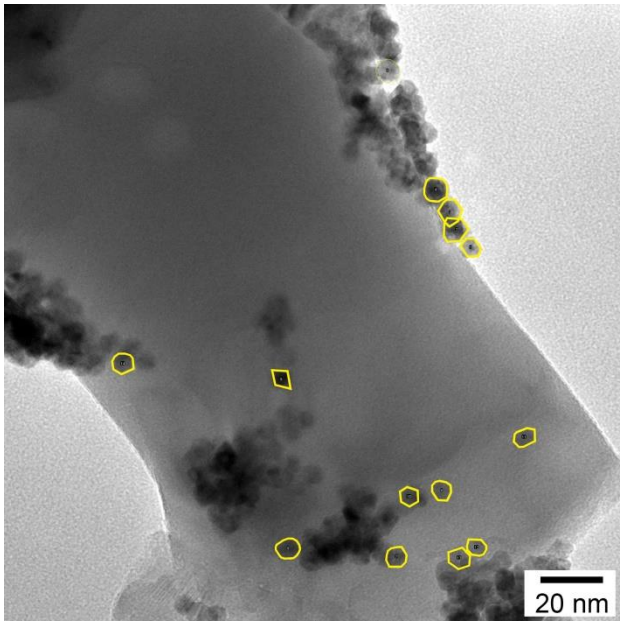

Figure 5.12 TEM micrographs of $RhPd/Al_2O_4$ catalyst treated in H_2 at 200 °C for 1 h. The particles selected for size analysis are highlighted in yellow.

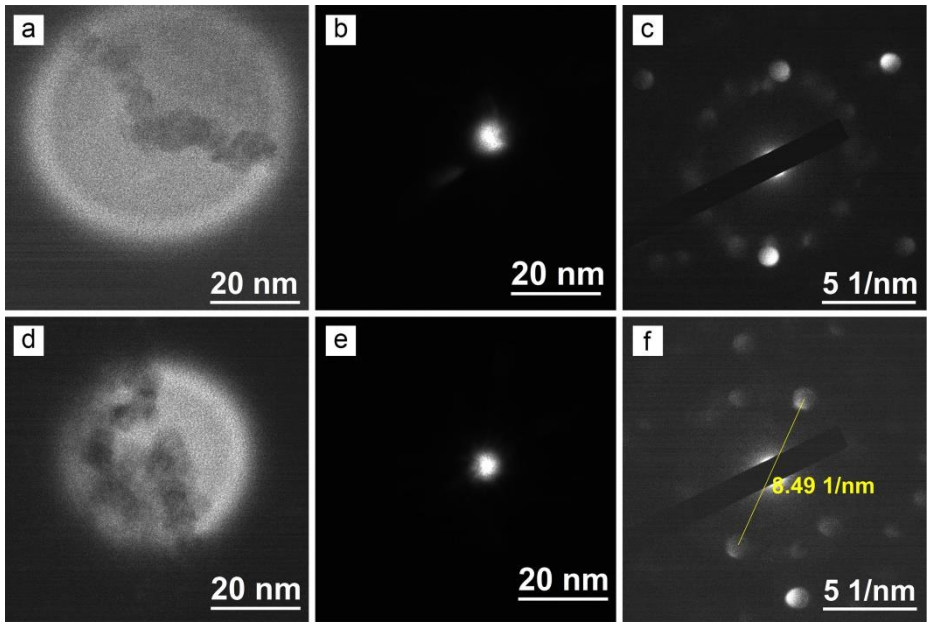

Figure 5.13 Nano mode imaging of $RhPd/Al_2O_4$ catalyst (a,d) with corresponding probe size and position (b,e), and NBD (c,f) treated in H_2 at 200 °C for 1 h.

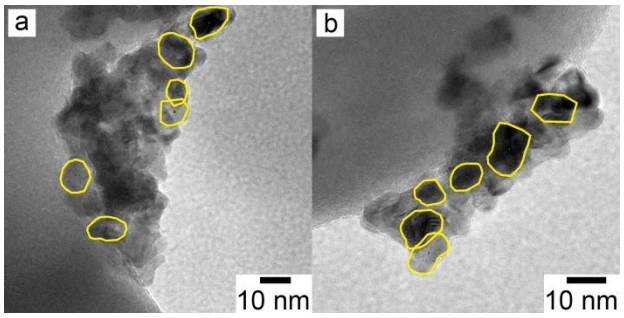

Figure 5.14 TEM micrographs of $RhPd/Al_2O_4$ catalyst treated in H_2 at 250 °C for 1 h. The particles selected for size analysis are highlighted in yellow.

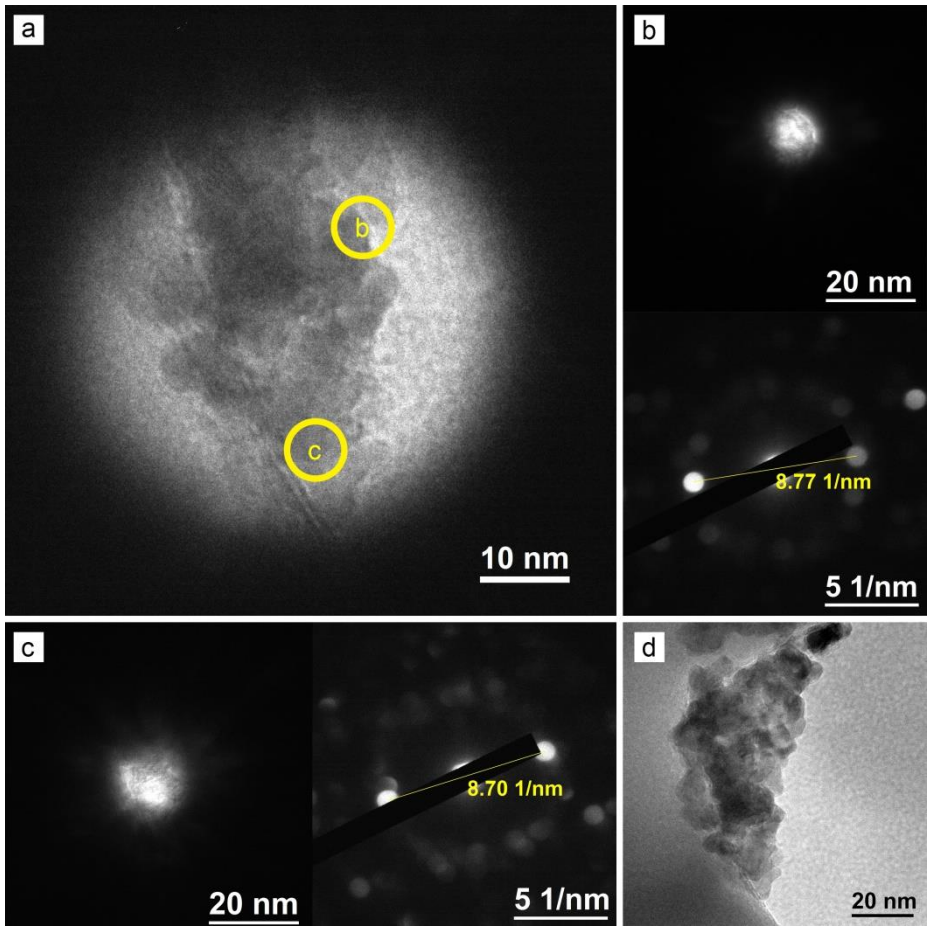

Figure 5.15 Nano mode imaging of $RhPd/Al_2O_4$ catalyst treated in H_2 at 250 °C for 1 h (a) with corresponding probe and NBD (b,c) together with low mag TEM micrograph (d).

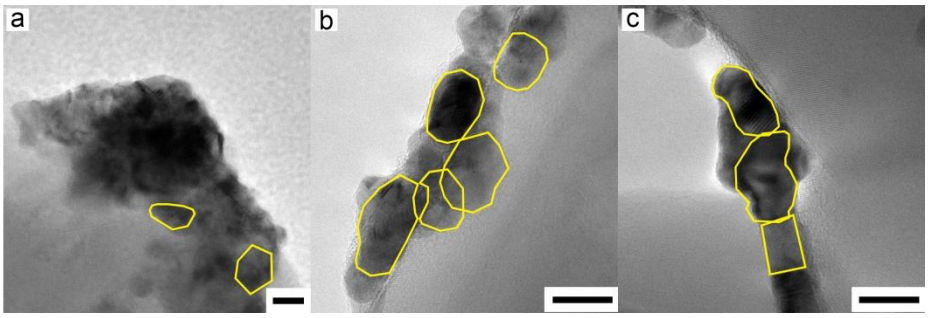

Figure 5.16 TEM micrographs of $RhPd/Al_2O_4$ catalyst treated in H_2 at 300 °C for 1 h. The particles selected for size analysis are highlighted in yellow. Scale bar are 10 nm.

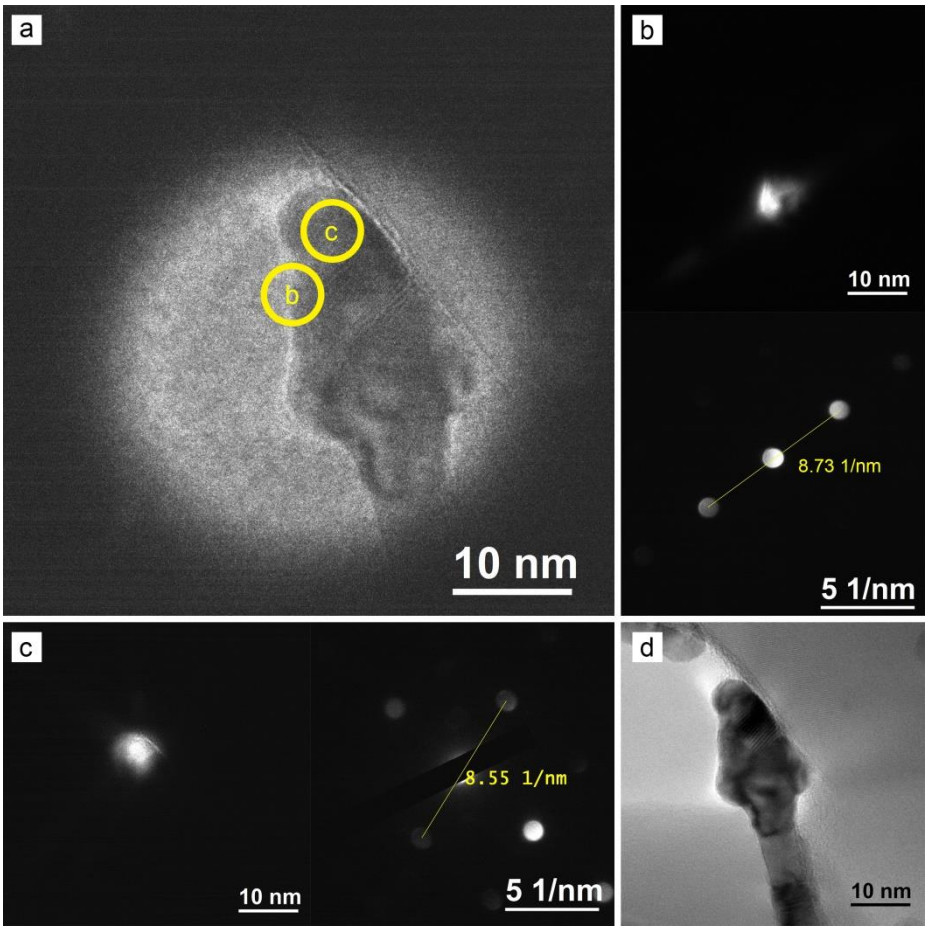

Figure 5.17 Nano mode imaging of $RhPd/Al_2O_4$ catalyst treated in H_2 at 300 °C for 1 h (a) with corresponding probe and NBD (b,c) together with low mag TEM micrograph (d).

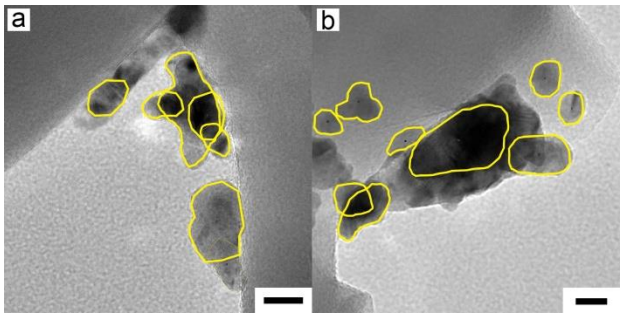

Figure 5.18 TEM micrographs of $RhPd/Al_2O_4$ catalyst treated in H_2 at 350 °C for 1 h. The particles selected for size analysis are highlighted in yellow. Scale bar are 10 nm.

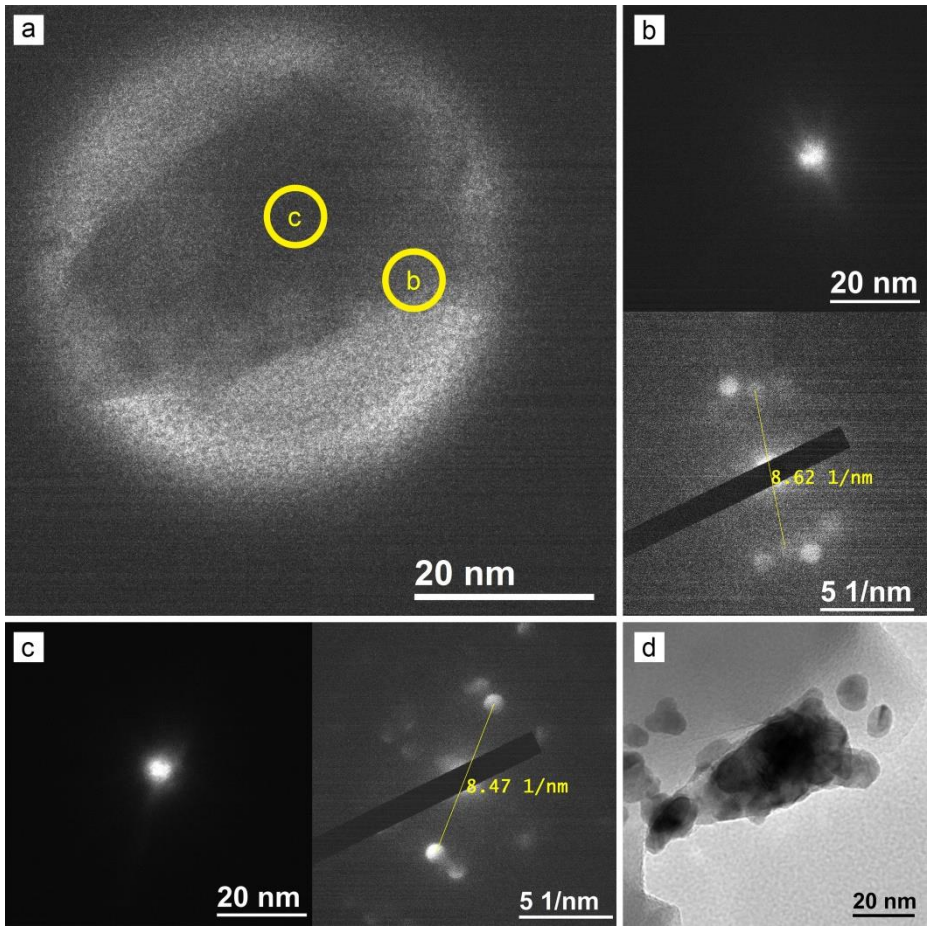

Figure 5.19 Nano mode imaging of $RhPd/Al_2O_4$ catalyst treated in H_2 at 350 °C for 1 h (a) with corresponding probe and NBD (b,c) together with low mag TEM micrograph (d).

The results for both in situ and ex situ study are summarized in Figure 5.20. Considering the measurements were much more reliable in ex situ experiments, the temperature for in situ heating might be underestimated by 50-100 °C. Nonetheless, both ex situ and in situ data indicate there exists a threshold size of around 10 nm, above which a separate Rh metal phase becomes observable. This threshold value corresponds to four atomic layers of Rh metal on the outer surface of these nanoparticles, and is approximately 1 nm thin (Figure 5.21).

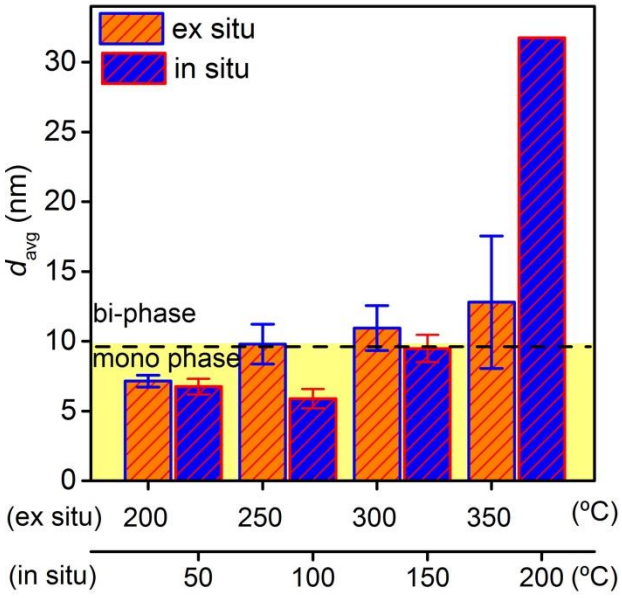

Figure 5.20 Summary of particle size and number of phases observed as function of temperature for both in situ and ex situ thermal treatments.

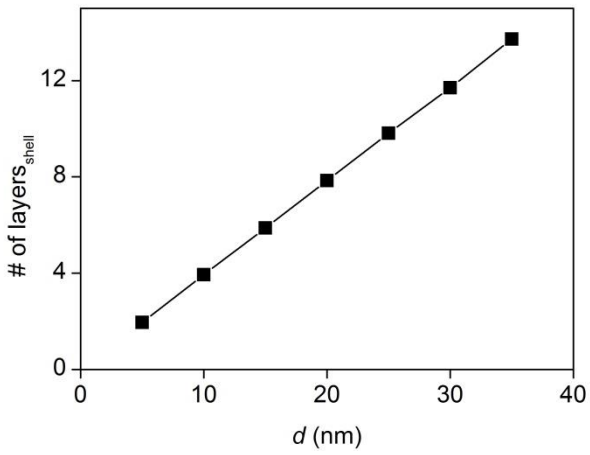

Figure 5.21 Modeled shell thickness as a function of particle diameter for a Rh-on-Pd core-shell nanoparticle with an overall composition of $Pd_{56}Rh_{44}$.

When temperature increased further, these particles could turn into single crystal. We further examined a particle formed in situ in ETEM chamber after heating the specimen at 300 ºC under hydrogen (Figure 5.22). At this in situ temperature under hydrogen gas, extensive sintering happened, resulting in the formation of large single crystal (Figure 5.22a).NBD was acquired at three regions, including the two locations near the right and bottom surface (Figure 5.22b, c) and one in the center (Figure 5.22d). The NBD patterns indicate this single crystal was made of fcc metal viewed from [011] zone axis (Figure 5.22e).The diffraction spots in the NBD patterns acquired from the surface regions (Figure 5.22b, c) are all further away from the center beam compare to those acquired from the center of the of the particle (Figure 5.22d). The calculated d-spacing from the (111) diffraction are 2.19Å (Figure 5.22b,c) and 2.23Å (Figure 5.22d) which correspond to the (fcc) Rh and Pd respectively (Figure 5.22f). Detailed examination suggests this nanocrystal was composed of a 10 atomic layers thick Rh shell epitaxially grown on a Pd metal core, judging by the (111) d-spacing of the acquired NBD

(Figure 5.21). This observation agrees very well with the trend in structural changes previous observations. This indicates that the surface composition in the current studied system was more likely to be governed by sintering of adjacent particles, which occurred much faster than the counter diffusion of Rh and Pd atoms within a single particle[21]. Considering the non-alloying nature and the much smaller diffusivity of Rh than Pd, reflected by their melting point, it is likely Rh atoms will remain on the shell.

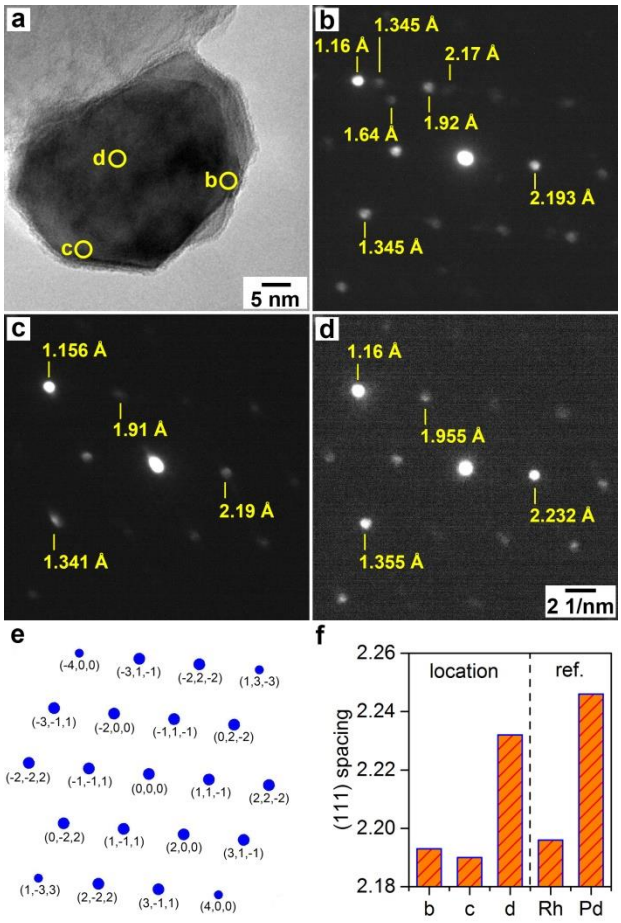

Figure 5.22 Electron microscopy characterization of Rh-on-Pd after in situ thermal treatments at 300 ºC under H_2. (a) TEM, (b, c, d) NBD acquired at position b, c, d in (a) respectively with d-spacing measurements, (e) simulated ED pattern of FCC crystal viewed from [011] zone axis, (f) measured d-spacing from NBD at highlighted locations in (a) with pure Rh and Pd as a reference.

5.3.3 CO_2 hydrogenation

Tunable performance the two-layered Rh-on-Pd nanocatalysts supported on Al_2O_3 was examined for hydrogenation of CO_2 gas at a constant CO_2/H_2 ratio. All experiments were carried out at a predetermined temperature between 180 and 340 ºC in a homemade continuous flow reactor monitored by an online GC. Pure Pd and Rh catalysts were also examined in comparison. The metal loading was estimated to be about 1% for Rh-on-Pd core-shell catalysts based on the SEM-EDX measurement (Table 5.1).

Table 5.1 metal loading of Al_2O_3 supported catalyst

Catalyst	Metal loading (wt%)
Pd/Al_2O_3	0.65
Rh/Al_2O_3	0.45
$Rh\text{-}on\text{-}Pd/Al_2O_3$	0.87

CO and CH_4 were the only detectable products for all the catalyst applied. Figure 5.23 shows the initial production rate of CO_2 hydrogenation products at reaction temperatures ranging from 180 ºC to 340 ºC. The Rh-on-Pd catalyst showed a high production rate of 0.679 ($mmol/g_{metal}\cdot s$) at 180 ºC, which was 3.5 and 72.7 times higher than pure Rh and Pd catalyst at the same temperature. As the reaction temperature increases, the production rate for CO_2 hydrogenation increased for Rh and Pd catalyst an Arrhenius like behavior while exhibiting level feature for Rh-on-Pd. The unvarying feature is attributed to the temperature dependent structural variations of the Rh-on-Pd catalyst as revealed by ETEM-NBD where the sintering of catalyst particles resulting in the decrease of surface area, leading to lower production rate at temperatures above 300 ºC comparing to Rh catalyst.

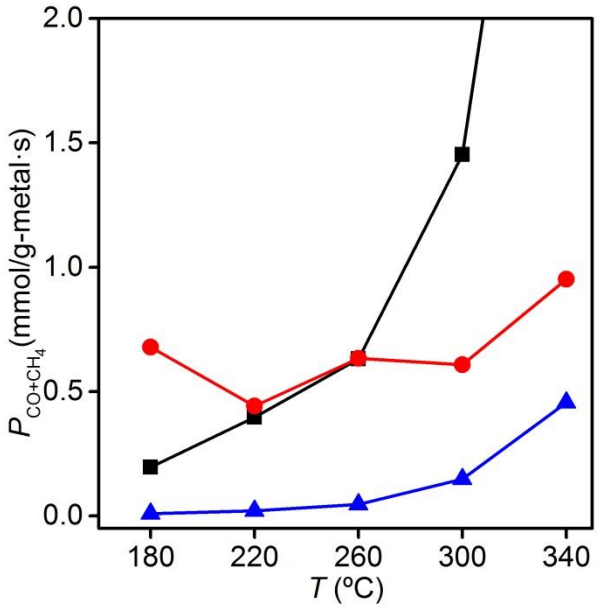

Figure 5.23 Initial production rate of CO_2 hydrogenation products (CO + CH_4) catalyzed by Rh-on-Pd (red circle), Rh (black square), and Pd (blue triangle) catalysts supported on Al_2O_3 (inset shows the methane selectivity respectively)

The selectivity of the α-Al_2O_3 supported Rh-on-Pd, Rh, and Pd nanoparticles towards catalyzing CO_2 hydrogenation was investigated at a constant CO_2 to H_2 ratio at various temperatures ranging from 180 to 340 °C in a homemade continuous flow reactor. For Rh-on-Pd catalyst, high selectivity towards methane was observed maintaining 88% at 300 °C (Figure 5.24a) which is even higher than the 68% of pure Rh (Figure 5.24b). The difference of methane selectivity between the Rh-on-Pd and Rh catalyst became much smaller at 340 °C due to the thickening of the Rh shell on the sintered Rh-on-Pd catalyst. Pd catalyst exhibited a much lower selectivity towards methane, and started favoring the formation of CO at 260 °C (Figure 5.24c). The experimentally observed selectivity for CO_2 hydrogenation showed great agreement with the DFT calculations as well as the (E)TEM-NBD thermal stability studies.

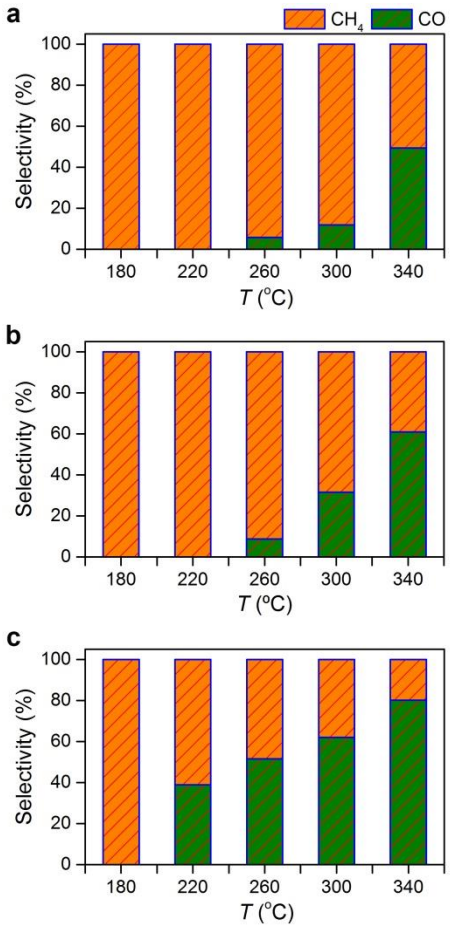

Figure 5.24 Selectivity towards CH_4 and CO from CO_2 hydrogenation reaction catalyzed by M/Al_2O_3 catalyst. **a**. as-synthesized Rh-on-Pd supported on Al_2O_3, **b**. Rh/Al_2O_3 pretreated under H_2, **c**. Pd/Al_2O_3 pretreated under H_2, **d**. Rh/Al_2O_3 pretreated under H_2.

5.3.4 CO dissociation studied by density functional theory calculations

To gain further understanding on the structure-selectivity relation, DFT calculations were carried out to investigate the energetics of CO dissociation since it acts as a descriptor for the CO/hydrocarbon selectivity for the hydrogenation of CO_2 on metal surfaces. Calculations were performed on the hollow sites of Pd(111), Rh(111), and monolayer to triple-layers of Rh on Pd(111) (Figure 5.25). Four configurations of CO including one molecularly, two dissociatively adsorbed CO, and the transition state (TS) on (111) surface were considered. For Pd(111), the CO molecule adsorbs strongly on the (111) surface but the dissociation of CO is non-favorable compare to desorption, evidenced by both the large activation barrier for the transition state and the positive adsorption energy as compared to gas phase CO (Figure 5.25, green lines). For Rh (111), strong molecular adsorption of CO is also presented. Although overall slightly exothermic, the large activation barrier suggest CO dissociation is not feasible on Rh (111) either. (Figure 5.25 red lines). Our calculation results indicate CO_2 hydrogenates mainly to CO through the RWGS reaction and desorbs from Pd and Rh (111) surfaces, in good agreement with literature reported observations.[26, 34] The dissociation of CO however, does occur favorably on under-coordinated sites such as step edges or kinks, which explained the high methane selectivity at low temperatures.[35] As temperature increased, contribution of CO desorption from the (111) surfaces gradually increased and became the primary product at 260 and 300 ºC for Pd and Rh catalyst respectively (Figure 5.24).

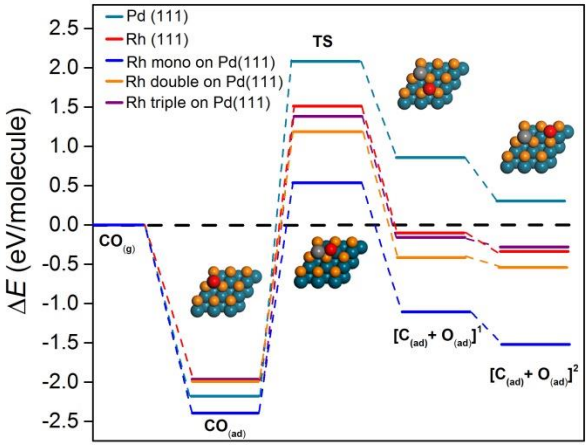

Figure 5.25 Calculated adsorption energies of CO on hollow sites of Pd(111), Rh(111), and atomic layers of Rh on Pd(111).

When the metal surface is composed of a monolayer of Rh on Pd(111), a significant decrease in both the transition state and dissociative adsorption energies of CO is observed (Figure 5.25, blue lines). The activation barrier was 0.5 eV larger than desorption suggesting CO dissociation becomes appreciably competitive. The dissociation of CO is very exothermic on the Rh monolayer which shows great potential for high selectivity towards hydrocarbons such as methane or even the production of C_{2+} chemicals.[27, 28, 36] If the thickness of the Rh surface on Pd(111) increases to 2 atomic layers, the dissociation of CO is still appreciably more favorable compare to a pure Rh(111) surface (Figure 5.25, orange lines). However, when it comes to three layers of Rh on Pd(111), the adsorption energetics for CO becomes almost indistinguishable from a Rh(111) surface. Based on our calculation on the (111) surfaces, the Rh-on-Pd catalyst should exhibit a stronger ability to dissociate CO and hence a higher initial production rate at 180 ºC. It also explains the overall higher methane selectivity of the Rh-on-Pd catalyst over pure Rh and Pd catalyst. When the reaction temperature increased to 340 ºC however, due to the severe

sintering and thickening of the Rh shell, the dissociation energy of CO approached to the level of pure Rh leading similar selectivity.

5.4 Conclusions

The successful preparation of the delicate Rh-on-Pd nanoparticles catalyst was demonstrated through a solution phase synthesis. Moreover, the connection between the reaction conditions to the structure and product selectivity variations was thoroughly investigated by correlating discoveries from in situ observations in the ETEM, CO/methane selectivity measurements for CO_2 hydrogenation reactions, and DFT calculations on the dissociation energetics of CO. This works points out the promising aspects of metal-on-metal bimetallic core-shell catalyst as well as its challenges in terms of structure stability in stringent thermal conditions. Methods to prevent sintering are most critical for the future development of these delicate core-shell nanocatalysts.

5.5 References

1. Calle-Vallejo, F.; Koper, M. T. M.; Bandarenka, A. S. *Chem. Soc. Rev.* **2013,** 42, 5210-5230.

2. Shao, M. H.; Huang, T.; Liu, P.; Zhang, J.; Sasaki, K.; Vukmirovic, M. B.; Adzic, R. R. *Langmuir* **2006,** 22, 10409-10415.

3. Esposito, D. V.; Hunt, S. T.; Kimmel, Y. C.; Chen, J. G. *J. Amer. Chem. Soc.* **2012,** 134, 3025-3033.

4. Greeley, J.; Mavrikakis, M. *Nat. Matter.* **2004,** 3, 810-815.

5. Wu, J.; Li, P.; Pan, Y.-T.; Warren, S.; Yin, X.; Yang, H. *Chem. Soc. Rev.* **2012,** 41, 8066-8074.

6. Friebel, D.; Mbuga, F.; Rajasekaran, S.; Miller, D. J.; Ogasawara, H.; Alonso-Mori, R.; Sokaras, D.; Nordlund, D.; Weng, T.-C.; Nilsson, A. *J. Phys. Chem. C* **2014,** 118, 7954-7961.

7. Zellner, M. B.; Goda, A. M.; Skoplyak, O.; Barteau, M. A.; Chen, J. G. *Surf. Sci.* **2005,** 583, 281-296.

8. Chen, J. G.; Menning, C. A.; Zellner, M. B. *Surf. Sci. Rep.* **2008,** 63, 201-254.

9. Hwu, H. H.; Eng, J.; Chen, J. G. *J. Amer. Chem. Soc.* **2002,** 124, 702-709.

10. Yu, W.; Barteau, M. A.; Chen, J. G. *J. Amer. Chem. Soc.* **2011,** 133, 20528-20535.

11. Karan, H. I.; Sasaki, K.; Kuttiyiel, K.; Farberow, C. A.; Mavrikakis, M.; Adzic, R. R. *ACS Catal.* **2012,** 2, 817-824.

12. Zhang, Y.; Hsieh, Y.-C.; Volkov, V.; Su, D.; An, W.; Si, R.; Zhu, Y.; Liu, P.; Wang, J. X.; Adzic, R. R. *ACS Catal.* **2014,** 4, 738-742.

13. Xie, S.; Choi, S.-I.; Lu, N.; Roling, L. T.; Herron, J. A.; Zhang, L.; Park, J.; Wang, J.; Kim, M. J.; Xie, Z.; Mavrikakis, M.; Xia, Y. *Nano Lett.* **2014,** 14, 3570-3576.

14. Park, J.-I.; Kim, M. G.; Jun, Y.-w.; Lee, J. S.; Lee, W.-r.; Cheon, J. *J. Amer. Chem. Soc.* **2004,** 126, 9072-9078.

15. Ferrer, D.; Torres-Castro, A.; Gao, X.; Sepúlveda-Guzmán, S.; Ortiz-Méndez, U.; José-Yacamán, M. *Nano Lett.* **2007,** 7, 1701-1705.

16. Zhang, L.; Roling, L. T.; Wang, X.; Vara, M.; Chi, M.; Liu, J.; Choi, S.-I.; Park, J.; Herron, J. A.; Xie, Z.; Mavrikakis, M.; Xia, Y. *Science* **2015,** 349, 412.

17. Lee, Y. W.; Kim, M.; Kim, Z. H.; Han, S. W. *J. Amer. Chem. Soc.* **2009,** 131, 17036-17037.

18. Bian, T.; Zhang, H.; Jiang, Y.; Jin, C.; Wu, J.; Yang, H.; Yang, D. *Nano Lett.* **2015,** 15, 7808-7815.

19. Mayrhofer, K. J. J.; Juhart, V.; Hartl, K.; Hanzlik, M.; Arenz, M. *Angew. Chem. Int. Ed.* **2009,** 48, 3529-3531.

20. Beaumont, S. K.; Alayoglu, S.; Pushkarev, V. V.; Liu, Z.; Kruse, N.; Somorjai, G. A. *Faraday Discuss.* **2013,** 162, 31-44.

21. Tao, F.; Grass, M. E.; Zhang, Y.; Butcher, D. R.; Renzas, J. R.; Liu, Z.; Chung, J. Y.; Mun, B. S.; Salmeron, M.; Somorjai, G. A. *Science* **2008,** 322, 932-934.

22. Yoshida, H.; Kuwauchi, Y.; Jinschek, J. R.; Sun, K.; Tanaka, S.; Kohyama, M.; Shimada, S.; Haruta, M.; Takeda, S. *Science* **2012,** 335, 317-319.

23. Wang, W.-H.; Himeda, Y.; Muckerman, J. T.; Manbeck, G. F.; Fujita, E. *Chem. Rev.* **2015,** 115, 12936-12973.

24. Saeidi, S.; Amin, N. A. S.; Rahimpour, M. R. *J. CO2 Util.* **2014,** 5, 66-81.

25. Yaccato, K.; Carhart, R.; Hagemeyer, A.; Lesik, A.; Strasser, P.; Volpe Jr, A. F.; Turner, H.; Weinberg, H.; Grasselli, R. K.; Brooks, C. *Appl. Catal. A* **2005,** 296, 30-48.

26. Leitenburg, C. d.; Trovarelli, A.; Kašpar, J. *J. Catal.* **1997,** 166, 98-107.

27. Cheng, J.; Hu, P.; Ellis, P.; French, S.; Kelly, G.; Lok, C. M. *J. Phys. Chem. C* **2008,** 112, 6082-6086.

28. Cheng, J.; Hu, P.; Ellis, P.; French, S.; Kelly, G.; Lok, C. M. *Top. Catal.* **2010,** 53, 326-337.

29. Wu, J.; Shan, H.; Chen, W.; Gu, X.; Tao, P.; Song, C.; Shang, W.; Deng, T. *Adv. Mater.* **2016**.

30. Clark Stewart, J.; Segall Matthew, D.; Pickard Chris, J.; Hasnip Phil, J.; Probert Matt, I. J.; Refson, K.; Payne Mike, C. *Kristallogr.* **2005,** 220, 567.

31. Vanderbilt, D. *Phys. Rev. B* **1990,** 41, 7892-7895.

32. Perdew, J. P.; Burke, K.; Ernzerhof, M. *Phys. Rev. Lett.* **1996,** 77, 3865-3868.

33. Tkatchenko, A.; Scheffler, M. *Phys. Rev. Lett.* **2009,** 102, 073005.

34. Panagiotopoulou, P.; Kondarides, D. I.; Verykios, X. E. *Appl. Catal. A* **2008,** 344, 45-54.

35. Mavrikakis, M.; Bäumer, M.; Freund, H. J.; Nørskov, J. K. *Catal. Lett.* **2002,** 81, 153-156.

36. Porosoff, M. D.; Yan, B.; Chen, J. G. *Energ. Environ. Sci.* **2016,** 9, 62-73.

Chapter 6

Structure Evolution of Core@Shell Cu@CuAg Nanocatalyst and Product Selectivity under Propylene Epoxidation Reaction Conditions

6.1 Introduction

The direct epoxidation of propylene (PP) by molecular oxygen (O_2) is of great interest for the industry since the current process utilizes the costly hydrogen peroxide (H_2O_2) as the oxidant to produce propylene oxide (PO). Many researches have been carried out searching for an effective catalyst with high conversion rates and selectivity. Silver (Ag) catalyst has been extensively studied due to its good catalytic property for ethylene epoxidation, however, a high selectivity towards PO is difficult to achieve except with ultra-small, *i.e.*, Ag_3 clusters (*i.e.*, Ag_3 clusters on Al_2O_3).[1] Catalysts of metallic copper (Cu) were reported to be much more selective towards the production of PO than Ag. The oxidation state of Cu species plays an important role in the product selectivity and maintaining the active metallic state under working conditions post a great challenge.[2-9] Cu nanoparticles were also reported to catalyze the formation of PO with much higher selectivity under illumination condition, and the metallic state was critical to the selectivity. [10] CuAg bimetallic catalyst was proposed to exhibit high performance for ethylene epoxidation[11] where the surface composition and oxidation states were discovered to be dependent on the ethylene to O_2 ratio. The surface was slightly richer in Cu and Cu^{2+} was suggested to be the valence state of the working catalyst (ethylene:O_2 = 1:1).[9, 12]

While AgCu bimetallics was proposed to be active towards catalyzing the epoxidation of ethylene and propylene,[7] the structure of an AgCu catalyst under working conditions is

experimental non-resolved, *i.e.*, a clear structure-performance relationship is currently not available. Ag and Cu are shown to be largely immiscible in bulk phase under 1000 K, [13-14] and experimental evidence for the formation of alloy phase in nanoscale is lacking. [15-18] It is likely that segregated structures, such as a core-shell nanoparticle, are the existing stable forms executing the catalytic epoxidation reactions.[9, 19]

Despite many attempts had been made, it remains challenging to synthesize monodisperse and structurally well-defined Cu@Ag core-shell nanoparticle catalysts with mean diameters less than 20 nm through solution phase synthesis methods.[20-23]

In this work, we studied the structure variations and performance of well-defined Cu@CuAg core-shell nanocatalyst for propylene epoxidation reaction. The successful preparation of the core-shell nanoparticle was achieved via the assistance of carbon monoxide (CO) and controlled infusion of metal precursors in a two-step solution phase synthesis process.[24] In situ ETEM was applied to study the structural behavior of the Cu@CuAg catalyst under varying PP/O_2 ratios at constant temperature through in situ imaging and detailed analysis on the crystal lattices and Moirè fringes in the high resolution micrographs. The core-shell structured catalysts were examined together with pure Cu and Ag catalyst for the production of propylene oxide from propylene epoxidation reaction. The Cu@CuAg catalyst not only showed the highest production rate of PO but also exhibited a volcano relation between the PO selectivity with the PP/O_2 ratio. Combining the discoveries from ETEM and catalyst testing, a relation between the reaction environment, the structure, and the performance of the Cu@CuAg catalyst was clearly revealed.

6.2 Experimental

6.2.1 Materials and chemicals

Copper acetylacetonate ($Cu(acac)_2$, 99.98%), silver trifluoroacetate ($AgCF_3COO$, 99.99%), oleylamine (OAm, 70%), and hexane (96%) were purchased from Sigma-Aldrich. Ethanol (200 proof) was purchased from Decon Lab. α-Al_2O_3 was purchased from Alfa-Aesar. Carbon monoxide (CO, 99.99%), oxygen (O2, compress grade), heleium (He, compress grade), argon (Ar, 99.9%) and propylene (PP, 99.9%) was purchased from Airgas. All chemicals were used as received without further purification.

6.2.2 Synthesis of Cu@CuAg nanoparticles

Synthesis of Cu@CuAg nanoparticles was carried out by a two-step process including the synthesis of the Cu core followed by the galvanic replacement/growth of CuAg shell. In the synthesis of the Cu core, 26 mg of $Cu(acac)_2$ was dissolved in OAm in a three-neck flask immersed in a 100°C oil bath. Oxygen was removed by 6 cycles of evacuation and Ar refill via the vacuum glass manifold. CO was then introduced into the flask with a flowrate of 90 mL/min while temperature of oil bath was increased with a ramp rate of 10°C/6min until 220°C. The synthesis solution was kept at 220°C for 2h and cooled down to 30°C under CO. $AgCF_3COO$, dissolved in OAm (5.5 mg/5 mL) was then introduced into the flask using a syringe pump with a infusion rate of 0.5 mL/h and was allowed to sit 1h after injection under CO at 30°C. The final products collected by centrifugation. The excess OAm was washed away by redispersing the particles in hexane followed by precipitation by centrifugation. The final products were dispersed in hexane for characterization and further applications.

6.2.3 Characterization

Powder X-ray diffraction (XRD) patterns were acquired on Bruker D8 Venture (DUO) diffractometer. Transmission electron microscopy (TEM) was carried out on a JEOL 2100 Cryo TEM. Scanning transmission electron microscopy (STEM) and energy dispersive X-ray was carried out with JEOL 2010F microscopy with an accelerating voltage of 200 kV.

6.2.4 Catalyst preparation

As-synthesized Cu@CuAg NPs were supported on α-Al_2O_3 by physically mixing the Al_2O_3 powders in a suspension of NPs in hexane for 12h; a typical recipe included 500 mg of Al_2O_3 with 5mg of NPs suspended in 50 mL of hexane. The Al_2O_3 supported NPs were kept in hexane as the stock solution for the ETEM experiment. The rest were precipitated by centrifugation and dried under Ar. The dry powders were then made into a pellet by hydraulic press and crushed into small grains as the catalyst for the packed bed reactor.

6.2.5 In situ ETEM study

In situ TEM studies were carried out in a Hitachi H9500 Environmental Transmission Electron Microscope (ETEM) at an accelerating voltage of 200 kV with a current density of 3.8×10^{-12} A/cm^2. The Cu@CuAg/Al_2O_3 catalyst suspension in ethanol were deposited using fine tip brush onto a tungsten heating wire which served as a heating element in the variable temperature gas injection holder. The holder was then introduced into the Hitachi H9500 ETEM and connected to a DC power supply for resistive heating. Temperature of the heating element was referred to the current-temperature relation chart (Hitachi). Propylene and oxygen were

introduced into the specimen area through a mass flow controller (Brooks Instrument, SLA 5850S1SAB1C2A1). TEM micrographs were recorded using the Gatan Orius SC200 CCD camera, and Gatan digital micrograph software. Electron irradiation was kept minimized during the course of experiment in which the gun valve was opened only during image acquisition. The sample was then left in dark before the next imaging cycle. Image analysis and processing was done using Digital Micrograph (DM, Gatan) and ImageJ software.

6.2.6 Catalytic performance test

Propylene epoxidation was carried out in a ¼" diameter quartz tube packed with catalyst grains. The quartz tube reactor was covered with a sand-bath heated by a hot plate. PP and O_2 balanced with He with a total flowrate of 20 mL/min (PP+O_2 = 2.5%) was passed through the reactor. The ratio of PP to O_2 and the reaction temperature are control variables. The products were analyzed online by a GC (SRI, Multigas #3) with a TCD and FID detector equipped with a methanizer. He was used as the carrier gas. Propylene oxide (PO) and acrolein analytical standards were purchased from Sigma-Aldrich for GC calibration.

6.3 Results and Discussion

6.3.1 Synthesis and characterization of Cu@CuAg nanoparticles

Cu@CuAg was synthesized through a two-step process. In the first stage of synthesis, Cu core nanoparticles were synthesized by thermally decomposing $Cu(acac)_2$ in oleylamine (OAm) under CO atmosphere. CO showed significant impact in alternating the reaction pathway resulting in a reduction in the temperature required for Cu nanoparticle synthesis, which can be evidenced qualitatively from the color of the synthesis solution at different temperatures (Figure 6.1). When absent of CO, the solution color changed from transparent green to colloidal brown, black, and finally turned into a wine color at temperatures above 210 °C indicating the formation of Cu_2O (brown), to CuO (black), and finally to metallic Cu (wine) nanoparticles. On the other hand, under the presence the CO, the solution color changed from transparent green to yellow and directly to colloidal red/wine color at a much lower temperature of 140 °C indicating the direct formation of metallic Cu nanoparticles from the CO coordinated Cu precursors.

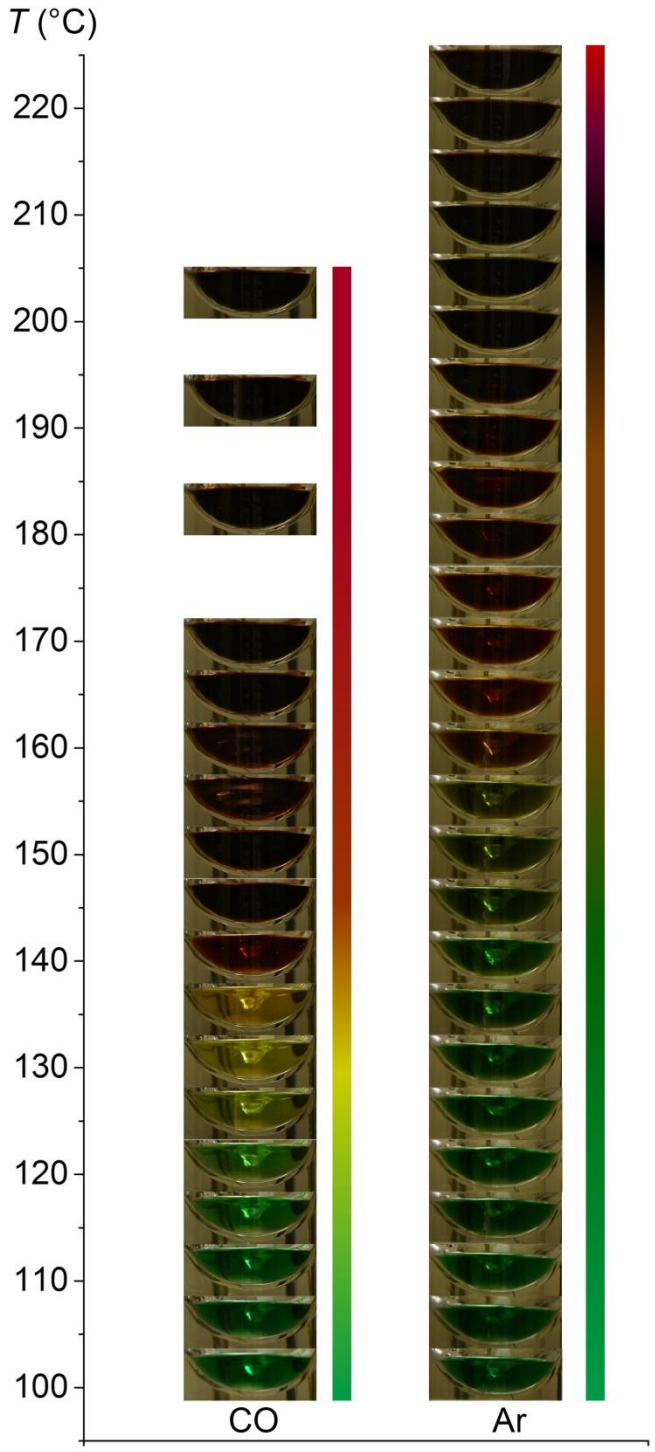

Figure 6.1 Photographs of solutions during copper nanoparticle synthesis with and without the presence of CO.

After cooling down, $AgCF_3COO$ dissolved in OAm was introduced into the Cu colloidal solution by a syringe pump. The infusion rate and the temperature of the Cu colloid were critical for the successful coating of Ag to form core-shell particles where the optimum condition we identified was 0.5 mL/h at 30 °C (Figure 6.2, 6.3). In general, a slower infusion rate at lower temperature favors the successful synthesis of Cu core with a Ag enriched shell.

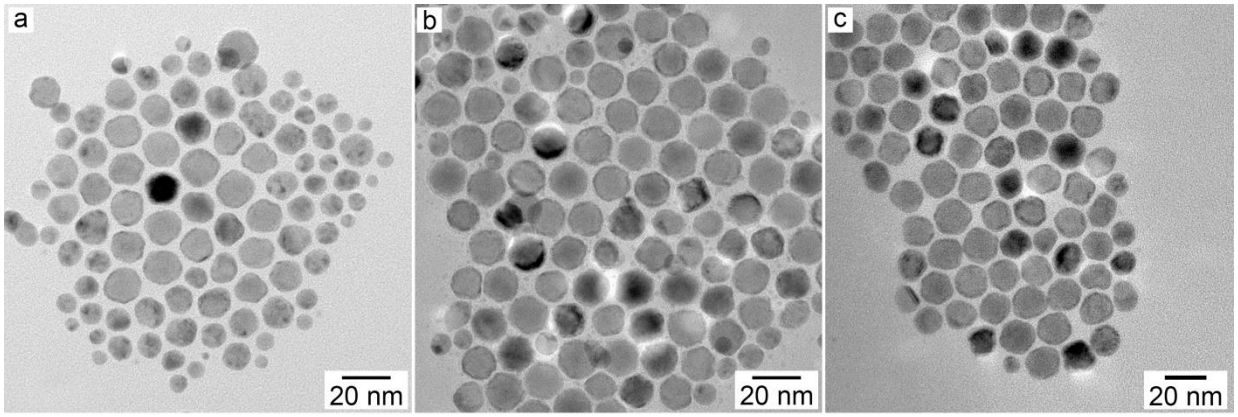

Figure 6.2 TEM micrographs of as-synthesized Cu@CuAg nanoparticles with a Ag precursor infusion rate of (a) 2.5 mL/h, (b) 1.25 mL/h, (c) 0.5mL/h with the Cu colloid temperature of 30 °C.

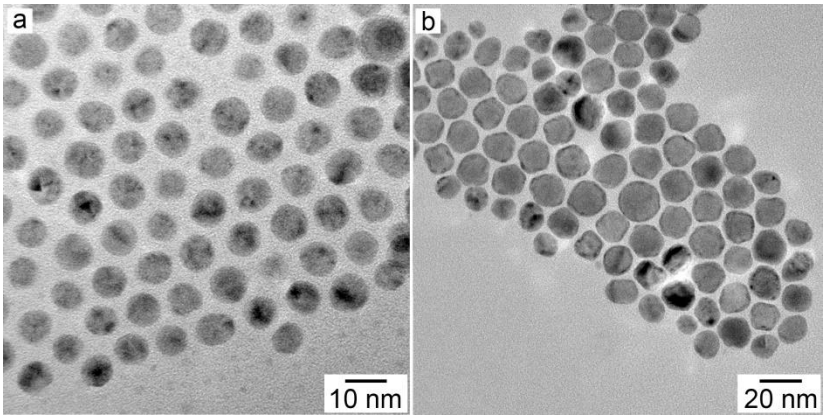

Figure 6.3 TEM micrographs of as-synthesized Cu@CuAg nanoparticles with the Cu colloid temperature of (a) 40 °C, (b) 30 °C and Ag precursor infusion rate of 0.5 mL/h.

The successful synthesis of core-shell particles with Cu core and Ag enriched shell was directly revealed by the Z-contrast high angle annular dark field (HAADF) STEM micrograph showing bright shells covering the dark cores (Figure 6.4a). The STEM-EDX line scan unambiguously showed the bimodal distribution of Ag and the Gaussian like distribution of Cu along the trajectory (Figure 6.4b). The core-shell nature was also showed in the high resolution (HR) TEM micrographs where the lattices of the shell layer can be observed and measured from the diffraction spots in the FFT (Figure 6.4c,d). The 0.22 nm spacing corresponded to a Cu_1Ag_1 alloy based on Vegard's law. The collective evidence from (S)TEM characterizations showed the as-synthesized nanoparticles were composed of a Cu core with a CuAg shell.

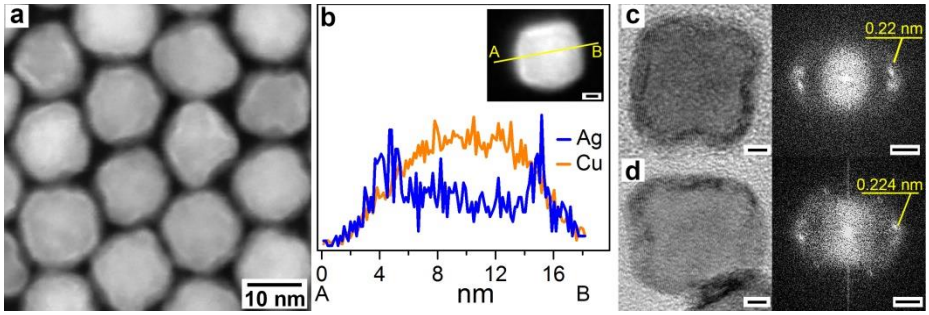

Figure 6.4 TEM characterizations of as-synthesized Cu@CuAg nanoparticles. (a) HAADF-STEM, (b) STEM-EDX line scan of the inset micrograph from A to B. (Inset scale bar is 5 nm) (c,d) HR-TEM showing the lattices fringes of the shell as well as the corresponding FFT. (Scale bar in HRTEM is 2 nm and 2.5 1/nm in the FFT)

6.3.2 Structure evolution of Cu@CuAg nanoparticles under propylene epoxidation conditions

The Cu@CuAg nanoparticles were applied as catalyst to study their structure variations under propylene epoxidation reaction conditions and how that affects catalyst performance, especially on product selectivity. In situ investigation of Cu@CuAg was carried out in the ETEM at a constant temperature of 155 °C according to the provided current temperature chart. Based on our previous work, the chart was likely to underestimate the temperature by 50-100 °C. The ratio between the propylene and oxygen served as the control variable to study the structural and elemental rearrangements of a single Cu@CuAg nanoparticle at fixed temperature. HRTEM micrographs were acquired sequentially at PP/O_2 ratios increasing from 4:1, to 2:1, 1:1, and 1:2 (Figure 6.5).

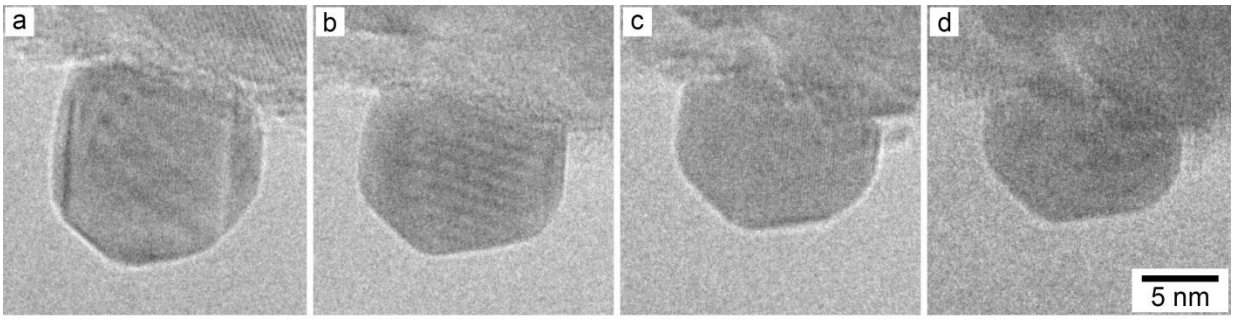

Figure 6.5 In situ TEM micrographs of Cu@CuAg nanoparticles acquired at 155 °C under different PP to O_2 ratios of: (a) PP:O_2 = 4:1, (b) PP:O_2 = 2:1, (c) PP:O_2 = 1:1, (d) PP:O_2 = 1:2.

The core-shell structure was maintained under propylene rich atmosphere evidenced by the observed Moirè patterns (Figure 6.5a,b). The observed Moirè patterns were a result of rotational mismatch between the Cu core and CuAg shell. When the PP/O_2 ratio was 4:1, a set of Moirè fringes could be observed having a 2.25 nm spacing (Figure 6.5a & 6.6a,b). The rotational mismatch resulted in the observed included angle of 57° between the substrate Cu (111) lattice

and Moirè fringes (Figure 6.6a and inset). Our model suggested this particular set of Moirè fringes is a result of the superposition of rotationally mismatched (111) lattices of CuAg shell (0.22 nm) and Cu core (0.21 nm) with a 5° ration of the shell with respect to the core. This resulted in a 2.37 nm spacing between the Moirè fringes, which is in good agreement with the observed value (Figure 6.6c,d).

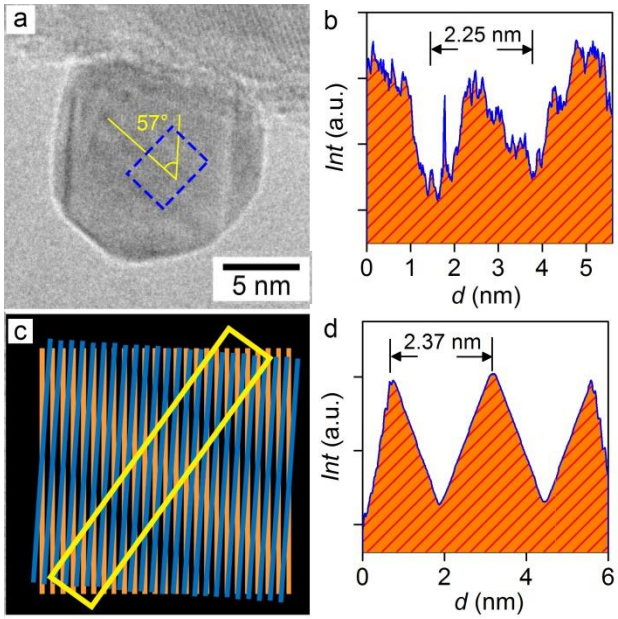

Figure 6.6 (a) TEM micrograph of Cu@CuAg nanoparticle under PP/O_2 = 4/1 showing the Moire fringes. (b) Corresponding intensity profile along dashed box in (a). (c) Schematic illustration of Moire fringes formed by rotational mismatch of 5°. The orange lines in the schematics reflects the Cu(111) fringes with a 2.1 unit distance (Å) while the blue lines represents AgCu(111) fringes with a 2.2 unit distance. (d) Corresponding intensity profile along yellow box in (c).

When PP/O_2 ratio decreased to 2/1, the Moirè fringes observed showed an increase in number accompanied with decrease in the spacing from 2.25 nm to 1.02 nm and a counter-

clockwise rotation, *i.e.*, increase of included angle from 57° to 80° (Figure 6.5b and 6.7a,b). Based on our model, this was due to the increase in the angle between the (111) lattices of the CuAg shell and Cu core from 5° to 10°. This resulted in a 1.18 nm spacing between the Moirè fringes, which is in good agreement with the observed value suggesting the core-shell structure was maintained in propylene rich environments agreeing with previous reported in situ observations (Figure 6.7c,d).[19]

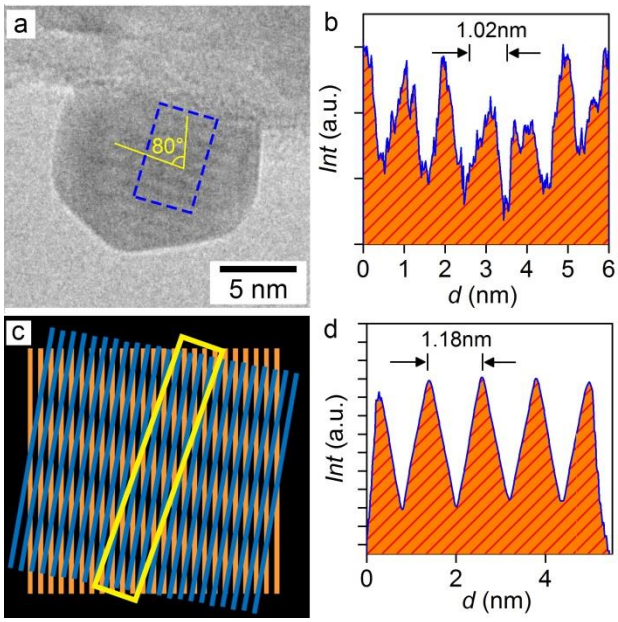

Figure 6.7 (a) TEM micrograph of Cu@CuAg nanoparticle under PP/O_2 = 2/1 showing the Moire fringes. (b) Corresponding intensity profile along dashed box in (a). (c) Schematic illustration of Moire fringes formed by rotational mismatch of 10°. (d) Corresponding intensity profile along yellow box in (c).

The spacing $d_{\text{Moirè}}$ of Moirè patterns arising from the rotational mismatch of two identical lattices (with spacing p) could be mathematically correlated to the included angle between the substrate lattice, *i.e.*, the lattice not rotated, and the Moirè fringes using the following equations:

$$d = \frac{p}{\sin\alpha} \qquad \text{Eq.1}$$

$$\alpha = 2\times(90°\text{-included angle}) \qquad \text{Eq.2}$$

By setting p to the Cu (111) and Ag(111) spacing, *i.e.*, 0.21 and 0.235 nm, the relation between $d_{\text{Moirè}}$ and the included angle was plotted for pure rotational mismatch together with the measured angle and $d_{\text{Moirè}}$ from in situ TEM micrographs (Figure 6.8). When PP/O_2 = 4/1, the position of the measured values (Figure 6.8, red triangle) was far from the black and red curves showing that the observed Moirè fringes was originated from the rotational mismatch of two lattices of different d-spacing. Although the position of the measured values became much closer to the curves, it is still fairly far away at PP/O_2 = 2/1 (Figure 6.8, blue circle). Considering the extremely close proximity of the black and red curve, the position of the blue circle still suggests a difference in the lattice spacing between the core and shell.

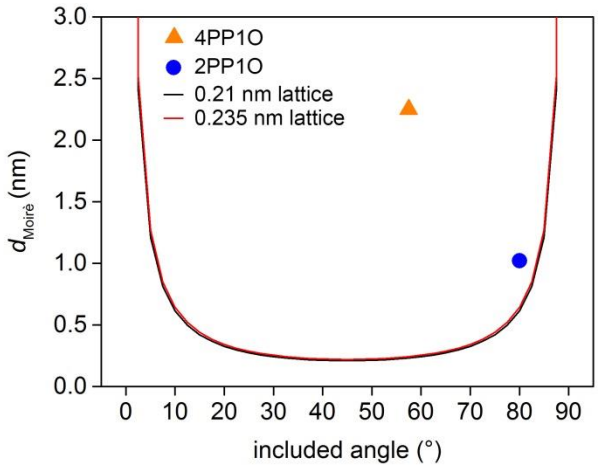

Figure 6.8 Calculated spacing of Moirè fringes as a functional included angle between Moirè fringes and Cu (111) lattices. ▲and ●are observed values in situ at PP/O_2 = 4/1 and 2/1 respectively.

The simultaneous disappearance of Moirè fringes and the appearance of a single set of lattices fringes in the interior of the particles were observed when the PP/O_2 ratio was decreased to 1/1 (Figure 6.9a). From the diffraction spots in the FFT, the spacing between the lattice fringes was calculated to be 2.16 Å and corresponds to an alloy with a composition of Cu_3Ag indicating the inward diffusion of Ag atoms from the shell into the core (Figure 6.9b). When the PP/O_2 ratio was further decreased to 1/2, neither Moirè nor lattice fringes were observable potentially due to the formation of disordered surface CuO_x species (Figure 6.5d).

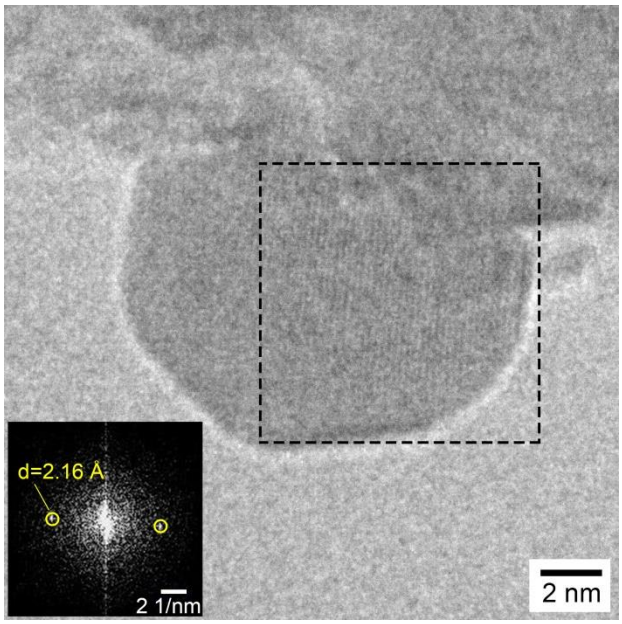

Figure 6.9 HRTEM (a) and corresponding FFT (b) of Cu@CuAg nanoparticle at $PP:O_2$ = 1:1.

6.3.3 Propylene epoxidation reaction: propylene oxygen ratio and product selectivity

Propylene epoxidation was performed using Al_2O_3 supported Ag, Cu, and Cu@CuAg catalyst at a constant temperature of 220 °C to examine the effects of PP/O_2 feeding ratio to

productivity and selectivity. The metal loading was characterized based on SEM-EDX measurements and listed in Table 1.

Table 6.1 Metal loading of Al_2O_3 supported catalyst measured by EDX

Catalyst	Cu (at/wt%)	Ag (at/wt%)
Cu@CuAg	3.20/2.01	2.94/3.15
Cu_H_2	2.18/2.70	0
Cu_O_2	1.78/2.20	0
Ag	0	1.60/3.31

The consumption rate of PP (molPP ·molemetal-1 ·min-1) as well as the production rate of PO at different PP/O2 ratios is presented in Figure 6.10. Production yields for PO, CO, CO2 and acrolein are showed in Table 6.2. At high PP/O2 ratio, the H2 pretreated Cu catalyst showed the highest consumption rate of PP as well as the highest rate of PO production. As the fraction of O2 increased, Cu@CuAg catalyst became the most active catalyst exhibiting the highest rate of PP consumption followed by H2 pretreated Cu, Ag catalyst, with O2 pretreated Cu catalyst being least active. The Cu@CuAg catalyst showed a volcano shaped relation between the PO selectivity with the PP/O2 ratio starting from a moderate PO selectivity when PP/O2 = 10:1, reaching a maximum of at PP/O2 = 2:1 and dropping to a plateau at PP/O2 = 1:1. Although the Cu@CuAg catalyst showed high consumption rate of PP, H2 pretreated Cu catalyst exhibited the highest selectivity towards PO at different PP/O2 ratios evidenced by the similar trend of the relation between PP consumption and PO production with PP/O2 ratios (Fig. 6b). The O2 pretreated Cu catalyst showed moderate PO selectivity when PP/O2 = 10:1 but decreased

considerably with increasing O2 ratio (Fig. 6c). Ag catalyst was least selective for PO showing no production of PO as soon as PP/O2 decreased from 10:1 to 4:1.

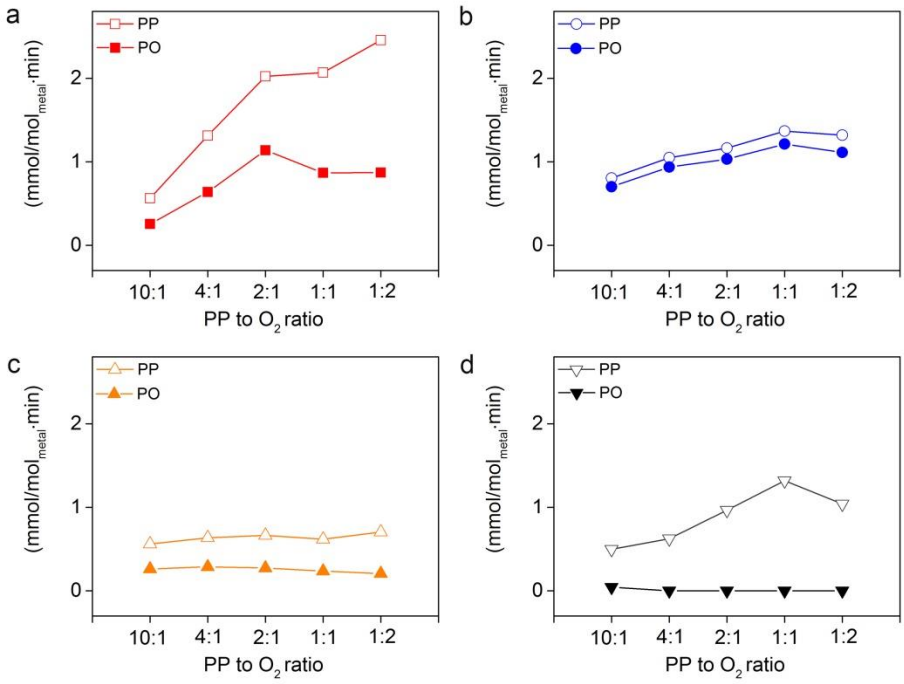

Figure 6.10 Consumption rate of PP (open symbols) and production rate of PO (closed symbols) for PER using (a) Cu@CuAg, (b) H2 pretreated Cu, (c) O2 pretreated Cu, and (d) Ag catalyst supported on Al2O3.

Table 6.2 Product yields for propylene epoxidation

PP: O_2	Catalyst	Y_{PO} (%)	Y_{CO} (%)	Y_{CO2} (%)	Y_{Acro} (%)
10:1	Cu@CuAg	0.19	0.075	0.15	0
	Cu_H_2	0.25	0.07	0.03	0
	Cu_O_2	0.09	0.06	0.05	0
	Ag	0.02	0.1	0.1	0
4:1	Cu@CuAg	0.54	0.15	0.41	0
	Cu_H_2	0.38	0.09	0.04	0
	Cu_O_2	0.12	0.07	0.07	0
	Ag	0	0.13	0.15	0.02
2:1	Cu@CuAg	1.15	0.21	0.69	0
	Cu_H_2	0.50	0.13	0.06	0
	Cu_O_2	0.13	0.09	0.1	0
	Ag	0	0.28	0.26	0.02
1:1	Cu@CuAg	1.17	0.34	1.28	0
	Cu_H_2	0.79	0.2	0.09	0
	Cu_O_2	0.15	0.09	0.15	0
	Ag	0	0.50	0.5	0.03
1:2	Cu@CuAg	1.76	0.59	2.62	0
	Cu_H_2	1.09	0.32	0.16	0
	Cu_O_2	0.2	0.23	0.26	0
	Ag	0	0.89	0.29	0.03

Although being a good catalyst for ethylene epoxidation, Ag did not serve as a good catalyst for propylene epoxidation since it was prone to allylic oxidation [25-28] and hence favored the formation of acrolein which readily oxidized into CO and CO_2. Our results on Ag catalyst supported on Al_2O_3 was in good agreement with the literature where PO was only observed in very small quantities at high PP/O_2 ratio with CO, CO_2, and acrolein as the primary product at increased PP/O_2 ratios (Figure 6.10b, Table 6.2). On the other hand, Cu was widely reported to be much more selective towards propylene oxide formation compare to Ag.[2, 4, 7-9, 29-30] The Cu and Cu^{1+} species were both reported to favor PO whereas Cu^{2+} favor acrolein formation. Our results on Cu catalyst were also in good agreement with literature where the H_2 pretreated

catalyst showed much higher yields for PO compare to O_2 pretreated Cu catalyst (Figure 6.10b,c).

Interestingly, when Cu@CuAg nanoparticles were applied as propylene epoxidation catalyst, the PO selectivity showed a volcano shape relation with respect to PP/O_2 ratio (Figure 6.10a). The variations in product selectivity can be qualitatively connected with the structure variations of the Cu@CuAg observed in situ. When the PP/O_2 ratio was high, the surface composed of a mixture of Ag and Cu which exhibited moderate selectivity of 57% towards PO. When the partial pressure of O_2 increased, due to the inward diffusion of Ag, the surface became dominated with Cu most likely in the form of Cu^0 or Cu^{1+} which were both reported to be more selective than Ag resulting in a maximum yield of 65% of PO at a PP/O_2 ratio of 2:1. However, further increase of O_2 partial pressure resulted in the formation of Cu^{2+} species on the surface and the formation of PO became non-favorable which is in good agreement with the O_2 pretreated Cu catalyst. The formation of Cu^{2+} species on the surface was theoretically and experimentally observed to be more favorable on an Ag substrate compare to a Cu substrate.[9, 12-14, 31-32]

From our selectivity measurements, it is clearly suggesting that the Cu atoms serve as the active sites for PP epoxidation. Although Cu@CuAg did not show the highest selectivity, it did exhibit the highest PO productivity per Cu atom which revealed the benefit of the bimetallic catalyst. This suggested isolated Cu site may be much more active compare to a continuous Cu surface. Future research should focus on creating these isolated Cu sites by selecting metals other than Ag to alloy with Cu that are inert towards oxygen activation but possess the ability to stabilized Cu towards oxidation.

6.4 Conclusions

Cu@CuAg nanoparticles were synthesized by Bimetallic CuAg catalyst for the epoxidation of propylene by molecular oxygen was revisited with well-defined Cu@CuAg core-shell nanoparticles synthesized through a two-step solution phase process starting from the synthesis of Cu nanoparticle under CO followed by the injection of Ag precursor solution at low temperature and infusion rate. The use of ETEM realized the in situ investigation of the structural behaviors of the Cu@CuAg nanocatalyst under working conditions. The collective discoveries from ETEM and catalyst testing suggested the presence of an optimum surface composition and arrangements of Ag and Cu elements that outperformed pure Cu catalyst for propylene epoxidation. This optimized composition is most likely dominated with Cu with small amounts of Ag on the surface. Finally, this work points out how an in-depth understanding of the interrelations between the working environments and the structure of bimetallic catalyst can facilitate the design of more active catalytic materials.

6.5 References

1. Lei, Y.; Mehmood, F.; Lee, S.; Greeley, J.; Lee, B.; Seifert, S.; Winans, R. E.; Elam, J. W.; Meyer, R. J.; Redfern, P. C.; Teschner, D.; Schlögl, R.; Pellin, M. J.; Curtiss, L. A.; Vajda, S., *Science* **2010,** *328*, 224-228.

2. Torres, D.; Lopez, N.; Illas, F.; Lambert, R. M., *Angew. Chem. Int. Ed.* **2007,** *46*, 2055-2058.

3. Düzenli, D.; Atmaca, D. O.; Gezer, M. G.; Onal, I., *Appl. Surf. Sci.* **2015,** *355*, 660-666.

4. Torres, D.; Lopez, N.; Illas, F., *J. Catal.* **2006,** *243*, 404-409.

5. Vaughan, O. P. H.; Kyriakou, G.; Macleod, N.; Tikhov, M.; Lambert, R. M., *J. Catal.* **2005,** *236*, 401-404.

6. Kizilkaya, A. C.; Senkan, S.; Onal, I., *J. Mol. Catal. A: Chem.* **2010,** *330*, 107-111.

7. Zheng, X.; Zhang, Q.; Guo, Y.; Zhan, W.; Guo, Y.; Wang, Y.; Lu, G., *J. Mol. Catal. A: Chem.* **2012,** *357*, 106-111.

8. Cropley, R. L.; Williams, F. J.; Urquhart, A. J.; Vaughan, O. P. H.; Tikhov, M. S.; Lambert, R. M., *J. Amer. Chem. Soc.* **2005,** *127*, 6069-6076.

9. Piccinin, S.; Zafeiratos, S.; Stampfl, C.; Hansen, T. W.; Hävecker, M.; Teschner, D.; Bukhtiyarov, V. I.; Girgsdies, F.; Knop-Gericke, A.; Schlögl, R.; Scheffler, M., *Phys. Rev. Lett.* **2010,** *104*, 035503.

10. Marimuthu, A.; Zhang, J.; Linic, S., *Science* **2013,** *339*, 1590-1593.

11. Linic, S.; Barteau, M. A., *J. Amer. Chem. Soc.* **2003,** *125*, 4034-4035.

12. Piccinin, S.; Stampfl, C.; Scheffler, M., *Phys. Rev. B* **2008,** *77*, 075426.

13. Ozoliņš, V.; Wolverton, C.; Zunger, A., *Phys. Rev. B* **1998,** *57*, 6427-6443.

14. Sanchez, J. M.; Stark, J. P.; Moruzzi, V. L., *Phys. Rev. B* **1991,** *44*, 5411-5418.

15. Shin, K.; Kim, D. H.; Yeo, S. C.; Lee, H. M., *Catal. Today* **2012,** *185*, 94-98.

16. Kim, N. R.; Shin, K.; Jung, I.; Shim, M.; Lee, H. M., *J. Phys. Chem. C* **2014**.

17. Ren, F.; Jiang, C. Z.; Zhang, L.; Shi, Y.; Wang, J. B.; Wang, R. H., *Micron* **2004,** *35*, 489-493.

18. Valodkar, M.; Modi, S.; Pal, A.; Thakore, S., *Mater. Res. Bull.* **2011,** *46*, 384-389.

19. Lu, P.; Chandross, M.; Boyle, T. J.; Clark, B. G.; Vianco, P., *APL Mater.* **2014,** *2*, -.

20. Tsuji, M.; Hikino, S.; Sano, Y.; Horigome, M., *Chem. Lett.* **2009,** *38*, 518-519.

21. Tsai, C.-H.; Chen, S.-Y.; Song, J.-M.; Chen, I.-G.; Lee, H.-Y., *Corros. Sci.* **2013,** *74*, 123-129.

22. Changsoo, L.; Na Rae, K.; Jahyun, K.; Yung Jong, L.; Hyuck Mo, L., *Nanotechnology* **2015,** *26*, 455601.

23. Kim, C. K.; Lee, G.-J.; Lee, M. K.; Rhee, C. K., *Powder Technology* **2014,** *263*, 1-6.

24. Teng, X.; Black, D.; Watkins, N. J.; Gao, Y.; Yang, H., *Nano Lett.* **2003,** *3*, 261-264.

25. Monnier, J. R., *Appl. Catal. A* **2001,** *221*, 73-91.

26. Khatib, S. J.; Oyama, S. T., *Catal. Rev.* **2015,** *57*, 306-344.

27. Geenen, P. V.; Boss, H. J.; Pott, G. T., *J. Catal.* **1982,** *77*, 499-510.

28. Lu, J.; Bravo-Suárez, J. J.; Takahashi, A.; Haruta, M.; Oyama, S. T., *J. Catal.* **2005,** *232*, 85-95.

29. Monnier, J. R.; Hartley, G. W., *J. Catal.* **2001,** *203*, 253-256.

30. Cowell, J. J.; Santra, A. K.; Lambert, R. M., *J. Amer. Chem. Soc.* **2000,** *122*, 2381-2382.

31. Duan, X.; Warschkow, O.; Soon, A.; Delley, B.; Stampfl, C., *Phys. Rev. B* **2010,** *81*, 075430.

32. Soon, A.; Todorova, M.; Delley, B.; Stampfl, C., *Phys. Rev. B* **2006,** *73*, 165424.

Chapter 7

Conclusion and Future Work

Synthetic methods for making monodisperse bimetallic nanoparticles with well-defined geometry and overall composition are available thanks to more than a decade of research and development. However, when applying bimetallic nanoparticles as catalysts, it is the near surface composition and elemental arrangements that play the most critical role determining both the activity and selectivity towards electrochemical and chemical reactions. In other words, it is essential to develop methodologies to fine tune the near surface elemental distribution of bimetallic nanocatalysts, in addition to any desired features, *i.e.,* size and shape. Another grand challenge lies in the prediction and characterization of the actual structures of a bimetallic nanocatalyst under reaction conditions, especially under harsh conditions because more and more studies show the surface composition reversibly responses to its changing surroundings.

In this dissertation, we focus on studying the behaviors of bimetallic nanoparticle catalyst under thermal and reactive gaseous environments where in situ investigations were carried out extensively by the ETEM. Our goal is to gain a fundamental understanding on the factors governing the near surface elemental arrangements. Such discoveries can be further utilized to design parameters for post-synthesis thermal processing for optimization of surface structure as well as prediction of the true state of a working bimetallic nanocatalyst.

We have developed low temperature post-synthesis processing protocols to manipulate the surface composition of octahedral Pt-Ni nanocatalyst. We discovered chemical vapor induced reversible segregation and homogenization of Pt and Ag atoms on the near surface regions of

Ag-Pt octahedral nanoparticles. We identified the, for the first time, a phase pure Ag-Pt compositional intermetallic compound through a high temperature process. We also investigated the Rh-on-Pd and core@shell Cu@CuAg nanocatalyst for hydrogenation and epoxidation, respectively. Here we aim at the understanding of relation among reaction environment, catalyst structure, and product selectivity for CO_2 methanation and for propylene epoxidation reactions.

All in situ ETEM studies were carried out at pressures typically in the 10^{-1} Pa range, which is much lower than the actual reaction conditions. The temperature control, based on resistive heating of the tungsten heating wire, was also not ideal due to potential operational error introduced by uncontrollable contact resistance. For future studies, it is recommended to carry out these in situ TEM studies with dedicated holders design to carry out experiments at ambient pressure and MEMS-based electronics for better control over temperature.

The chemical vapor-assisted process is in principle widely applicable to other bimetallic systems, especially with one component from group XI elements (Cu, Ag, Au) and the other from group VIII to group X elements. This process can be applied in the future to study catalytic properties of a variety of bimetallic nanocatalyst with controlled elemental distributions. The ultimate goal is to construct a library of bimetallic catalysts showing the interrelation between their geometrical structure and compositional landscape with the environment as a reference for catalyst processing and structure prediction.

Appendix A

In situ acquired high resolution transmission electron micrograph of a single AgPt octahedral nanoparticle under CO atmosphere and vacuum

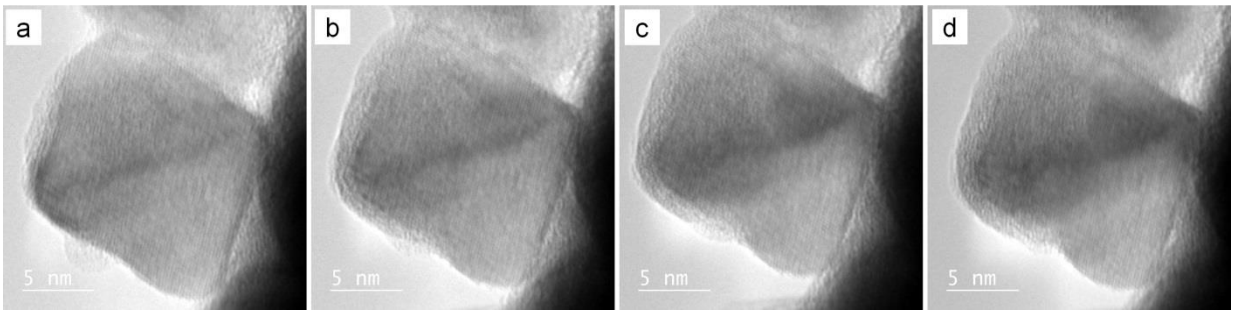

Figure A.1 In situ ETEM micrographs showing the evolution of the Ag-Pt octahedral nanoparticle under vacuum at 50 ºC (110 mA) as a function of time: (a) 0, (b) 1, (c) 3, and (d) 7 min, respectively. The first micrograph was taken 6 min after initiation of the experiment.

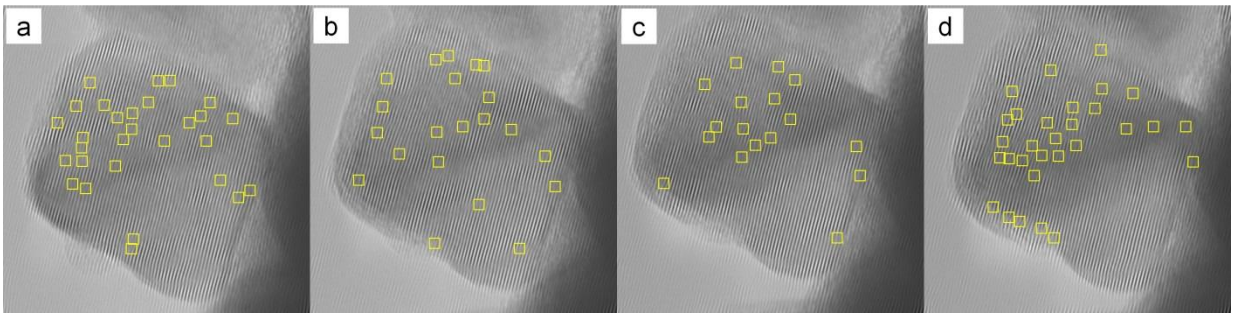

Figure A.2 FFT enhanced images (lattice set #1) highlighting dislocations in representative ETEM micrograph shown in Figure S20 acquired under vacuum at 50 ºC (110 mA) as a function of time: (a) 0, (b) 1, (c) 3, (d) 7 min, respectively.

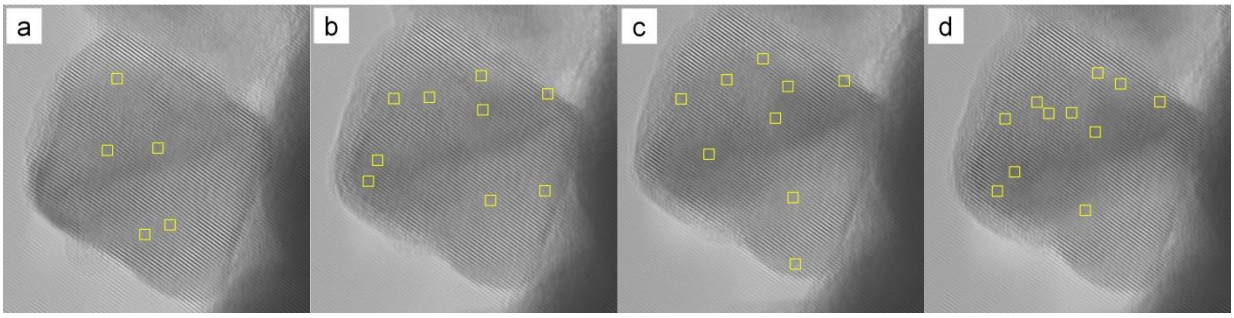

Figure A.3 FFT enhanced images (lattice set #2) highlighting dislocations of representative ETEM micrographs in Figure S20 acquired under vacuum at 50 ºC (110 mA) as a function of time: (a) 0, (b) 1, (c) 3, (d) 7 min, respectively.

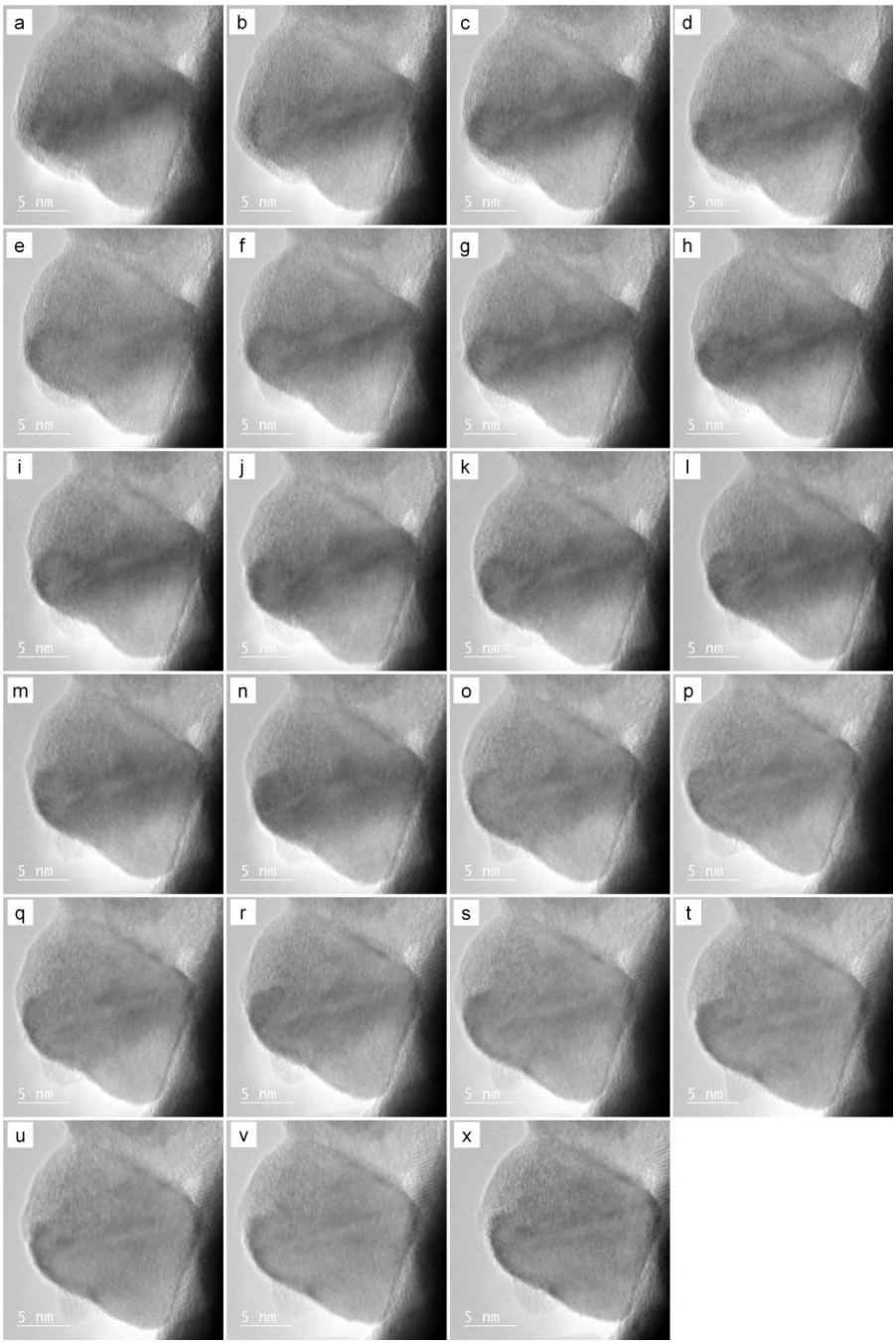

Figure A.4 In situ ETEM micrographs showing the evolution of the Ag-Pt octahedral nanoparticle under CO at 50 ºC (110 mA) as a function of time: (a) 10, (b) 13, (c) 18, (d) 23, (e) 26, (f) 29, (g) 33, (h) 36, (i) 38, (j) 41, (k) 51, (l) 53, (m) 59, (n) 65, (o) 70, (p) 76, (q) 84, (r) 97, (s) 102, (t) 109, (u) 109, (v) 116, and (x) 125 min, respectively, after initiation of the experiment.

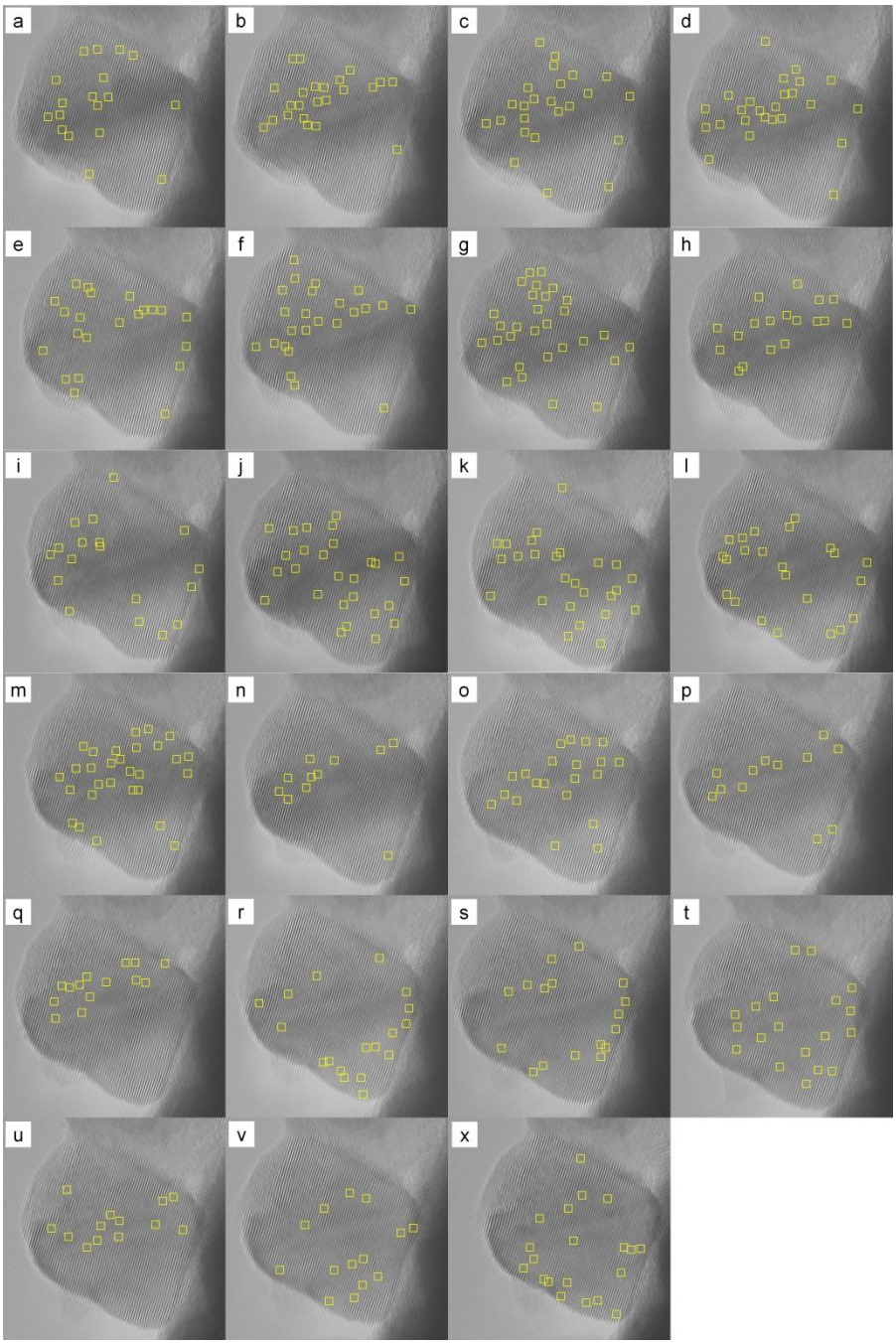

Figure A.5 FFT enhanced images (lattice set #1) highlighting dislocations of representative ETEM micrographs in Figure S22 acquired under CO at 50 ºC (110 mA) as a function of time: (a) 10, (b) 13, (c) 18, (d) 23, (e) 26, (f) 29, (g) 33, (h) 36, (i) 38, (j) 41, (k) 51, (l) 53, (m) 59, (n) 65, (o) 70, (p) 76, (q) 84, (r) 97, (s) 102, (t) 109, (u) 109, (v) 116, (x) 125 min, respectively, after initiation of experiment.

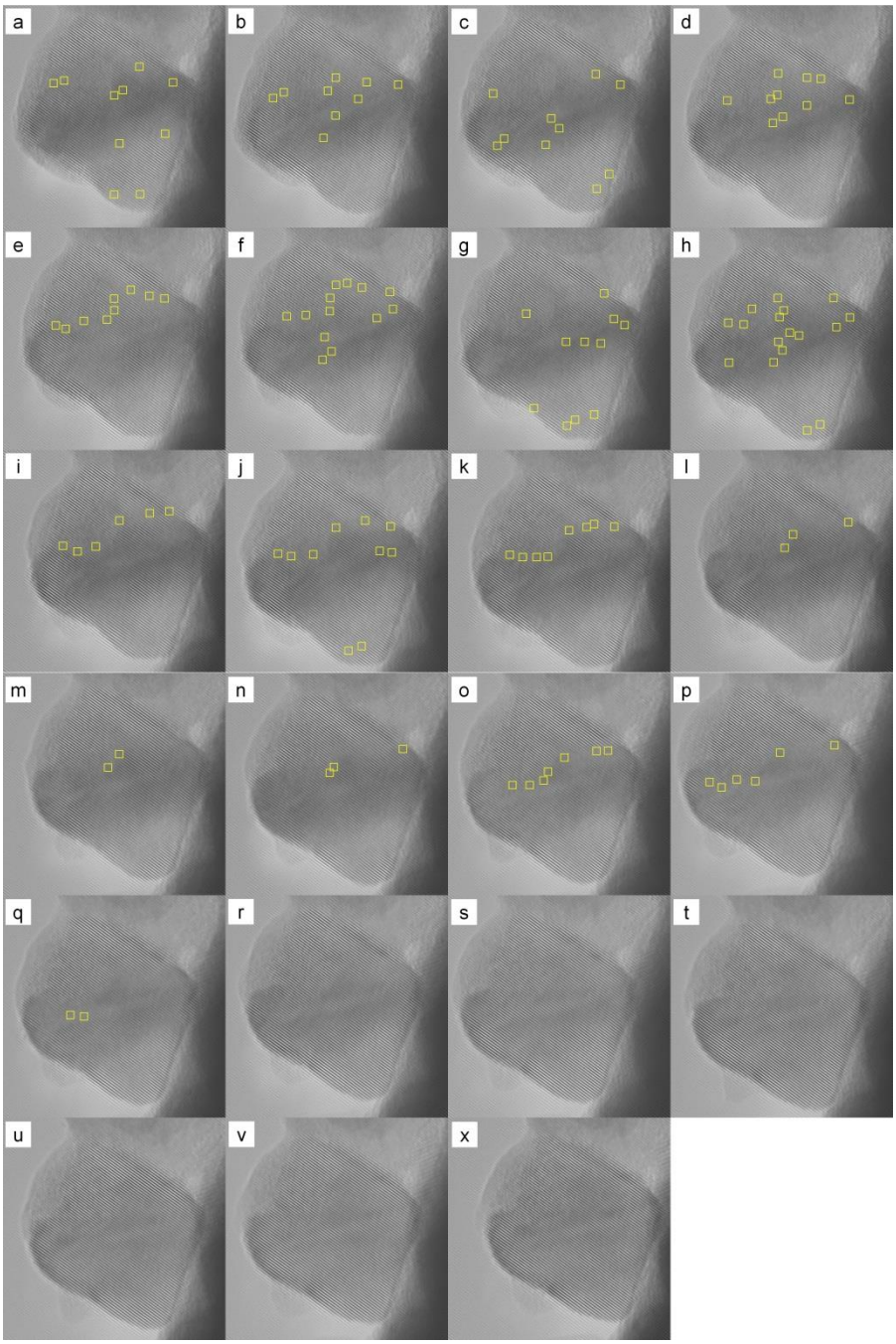

Figure A.6 FFT-enhanced images (lattice set #2) highlighting dislocations of representative ETEM micrographs in Figure S22 acquired under CO at 50 ºC (110 mA) as a function of time: (a) 10, (b) 13, (c) 18, (d) 23, (e) 26, (f) 29, (g) 33, (h) 36, (i) 38, (j) 41, (k) 51, (l) 53, (m) 59, (n) 65, (o) 70, (p) 76, (q) 84, (r) 97, (s) 102, (t) 109, (u) 109, (v) 116, (x) 125 min, respectively, after initiation of the experiment.

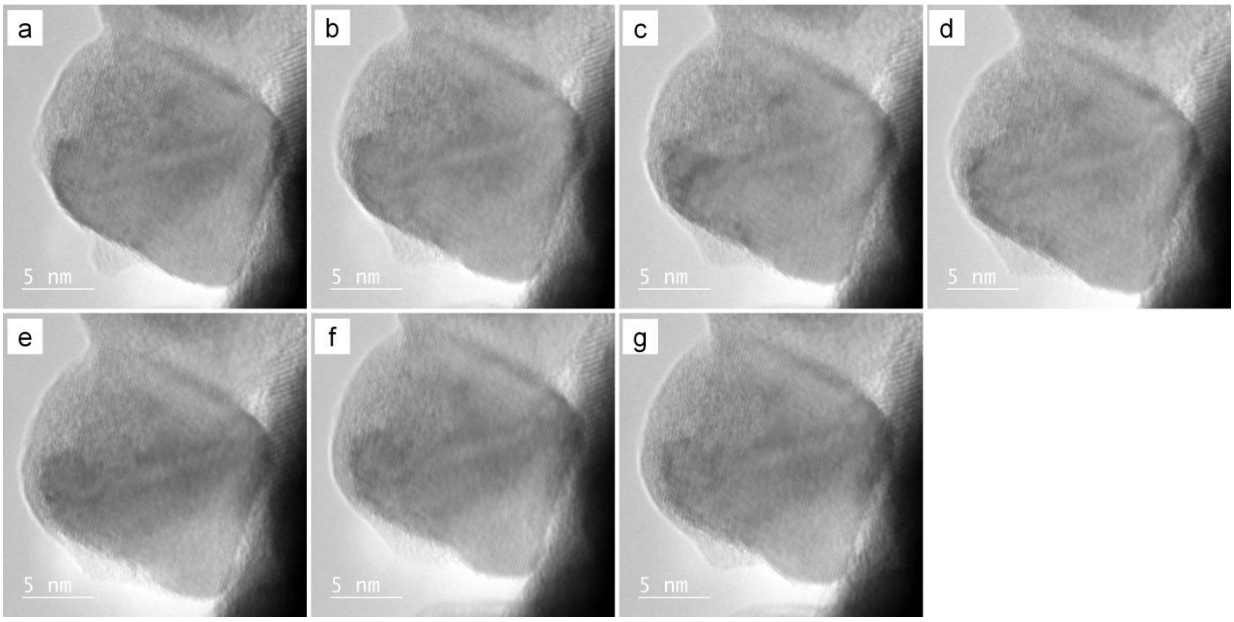

Figure A.7 In situ ETEM micrographs showing the evolution of the Ag-Pt octahedral nanoparticle under vacuum at 50 ºC (110 mA) as a function of time: (a) 128, (b) 130, (c) 131, (d) 132, (e) 140, (f) 141, (g) 142 min, respectively, after initiation of the experiment.

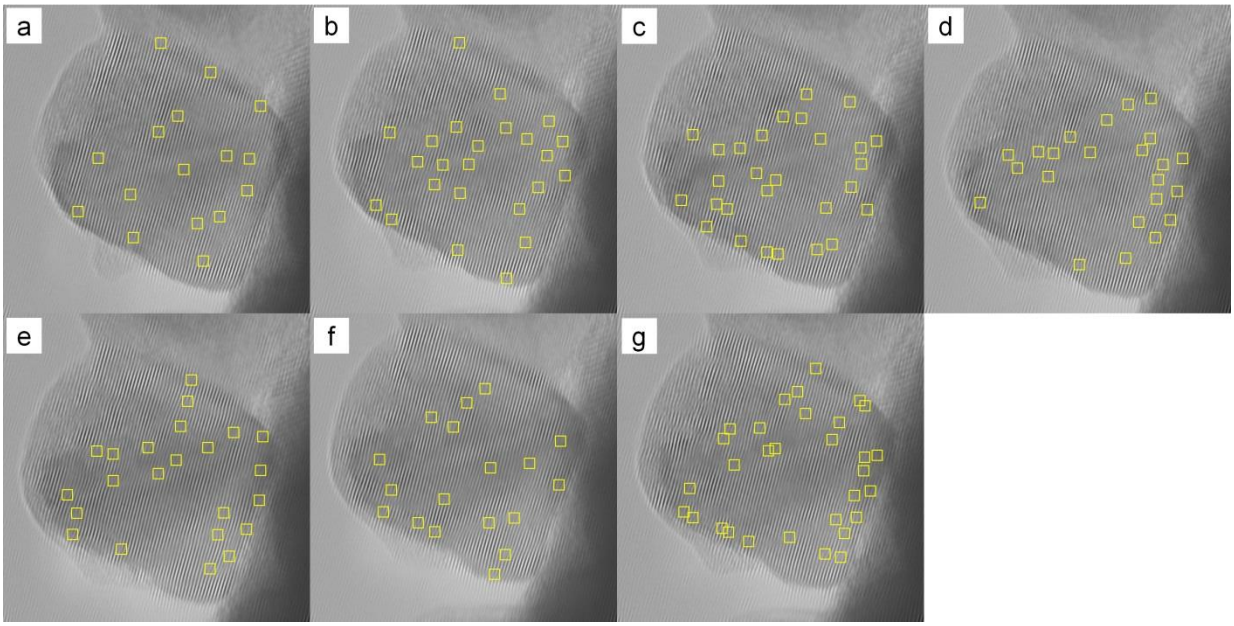

Figure A.8 FFT-enhanced images (lattice set #1) highlighting dislocations of representative ETEM micrographs in Figure S25 acquired under vacuum at 50 ºC (110 mA) as a function of time: (a) 128, (b) 130, (c) 131, (d) 132, (e) 140, (f) 141, (g) 142 min, respectively, after initiation of experiment.

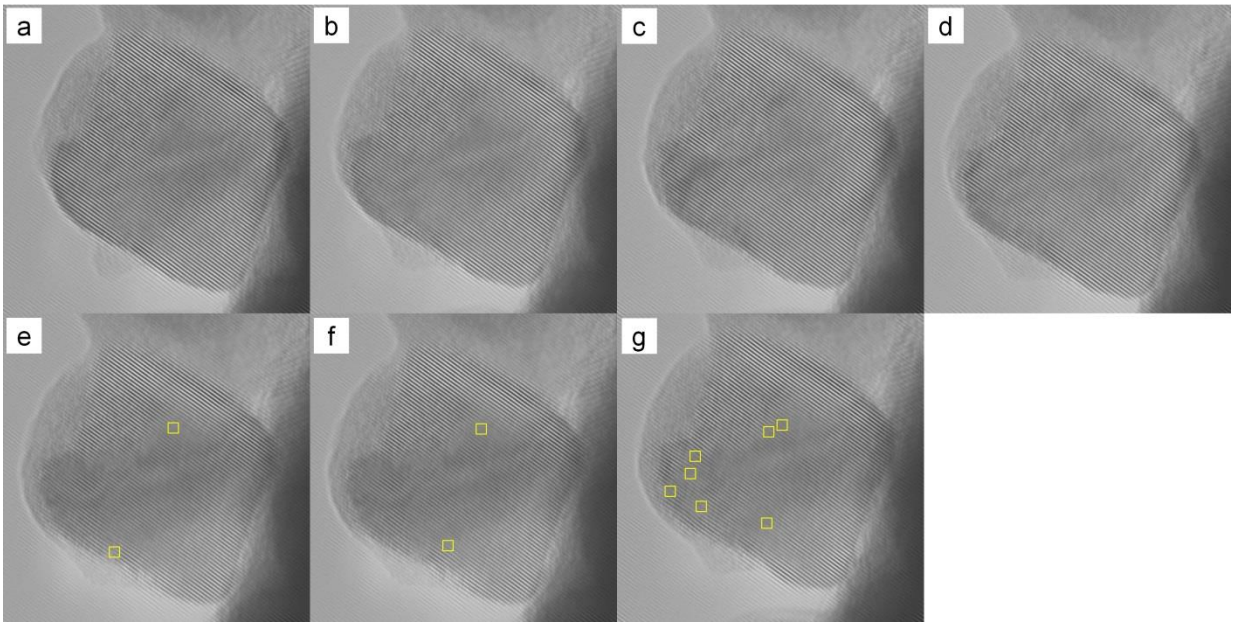

Figure A.9 FFT-enhanced images (lattice set #2) highlighting dislocations of representative ETEM micrographs in Figure S25 acquired under vacuum at 50 ºC (110 mA) as a function of time: (a) 128, (b) 130, (c) 131, (d) 132, (e) 140, (f) 141, (g) 142 min, repsctively, after initiation of the experiment.

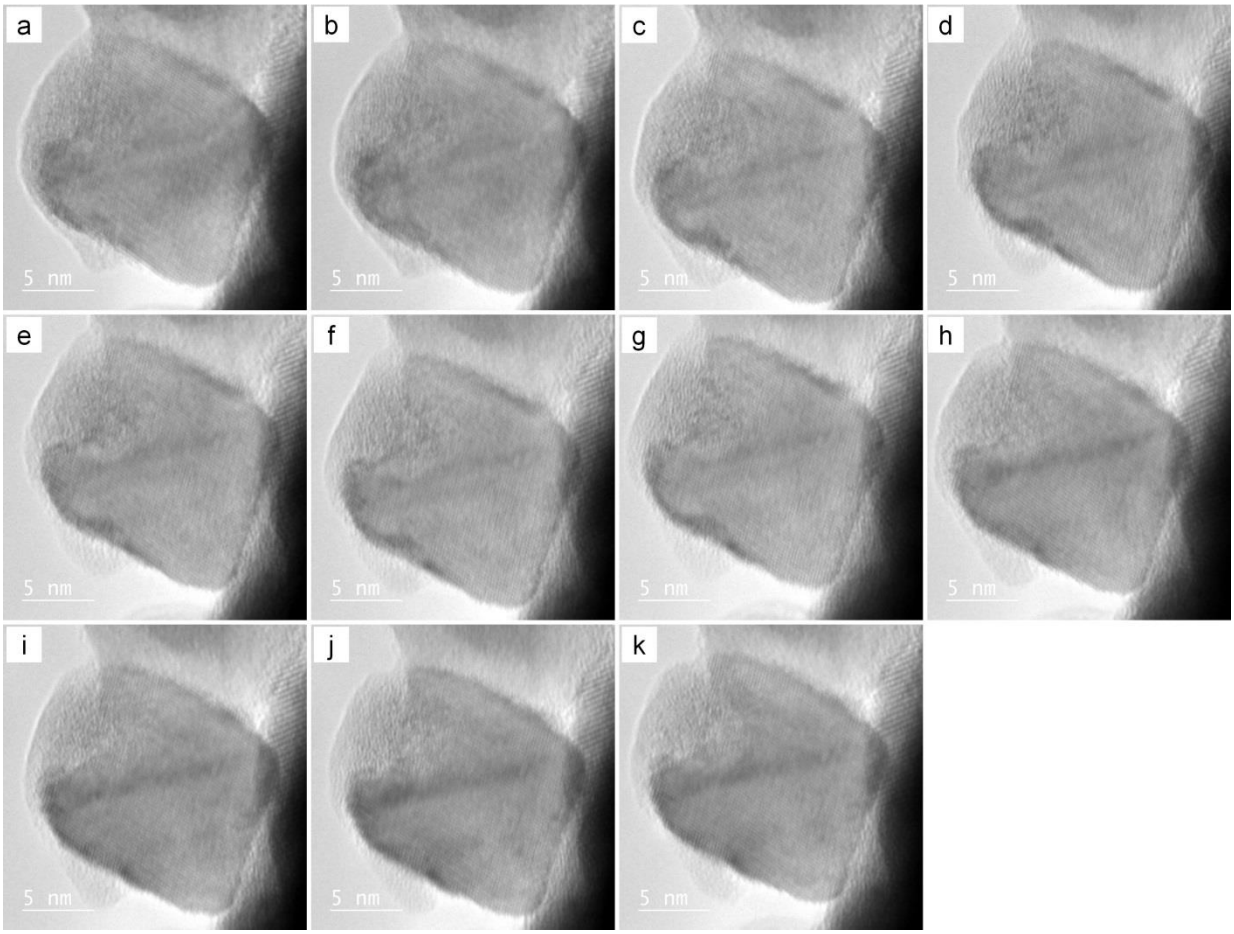

Figure A.10 In situ ETEM micrographs showing the evolution of the Ag-Pt octahedral nanoparticle under CO at 50 ºC (110 mA) as a function of time: (a) 146, (b) 148, (c) 153, (d) 159, (e) 164, (f) 169, (g) 174, (h) 181, (i) 187, (j) 192, (k) 196 min, respectively, after initiation of the experiment.

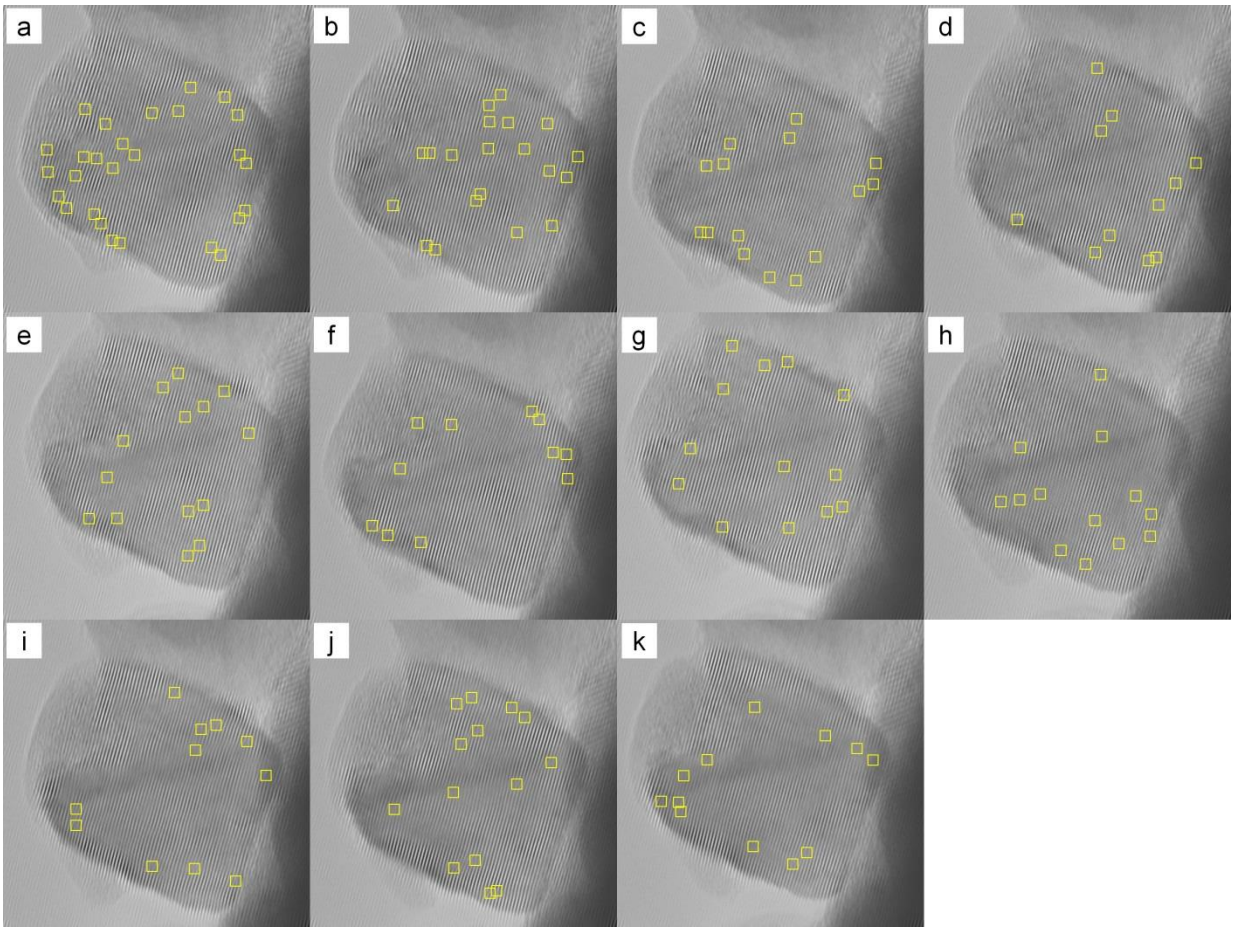

Figure A.11 FFT-enhanced images (lattice set #1) highlighting dislocations of representative ETEM micrographs in Figure S25 acquired under vacuum at 50 ºC (110 mA) as a function of time: (a) 146, (b) 148, (c) 153, (d) 159, (e) 164, (f) 169, (g) 174, (h) 181, (i) 187, (j) 192, (k) 196 min, respectively, after initiation of the experiment.

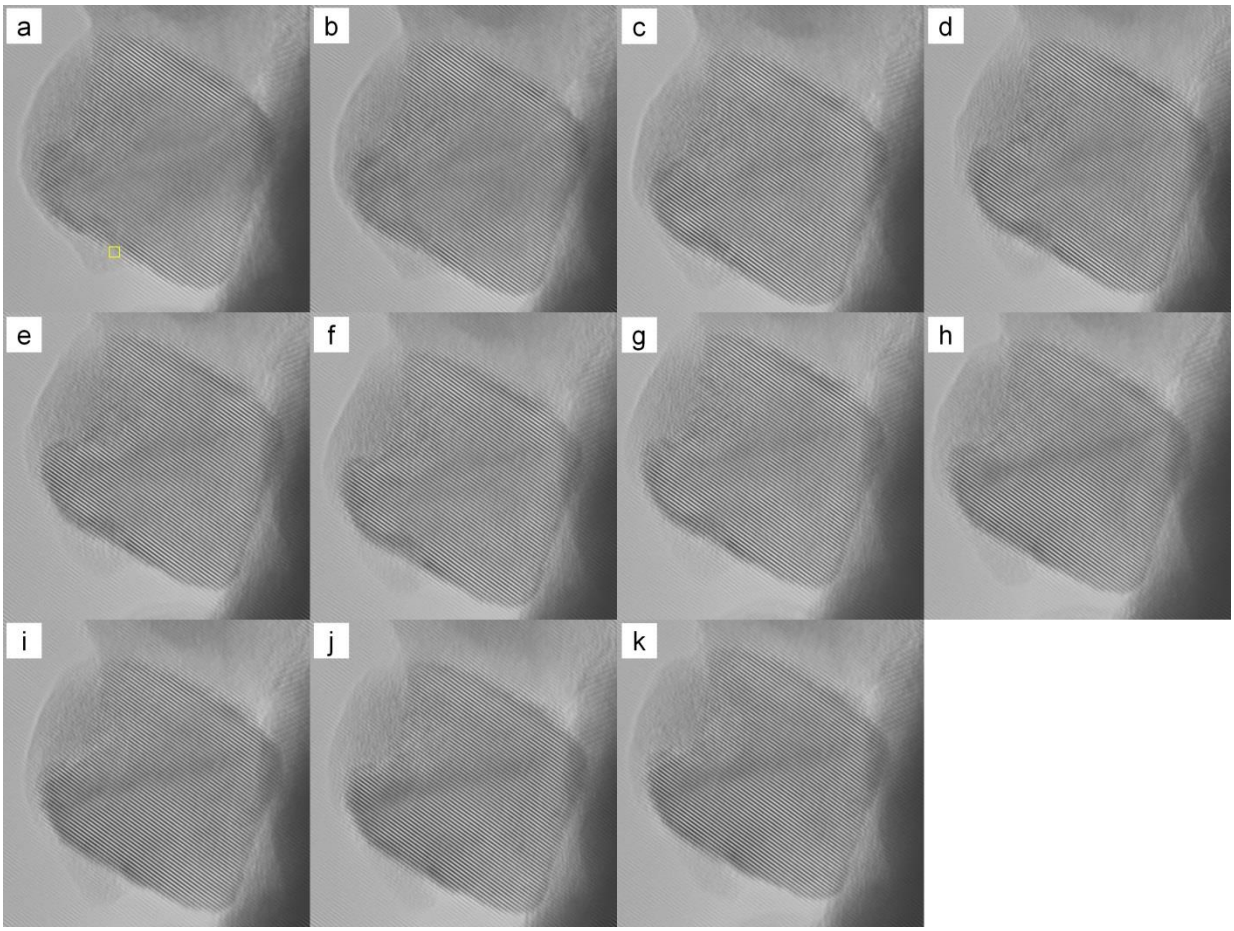

Figure A.12 FFT-enhanced images (lattice set #2) highlighting dislocations of representative ETEM micrographs in Figure S25 acquired under vacuum at 50 ºC (110 mA) as a function of time: (a) 146, (b) 148, (c) 153, (d) 159, (e) 164, (f) 169, (g) 174, (h) 181, (i) 187, (j) 192, (k) 196 min, respectively, after initiation of the experiment.

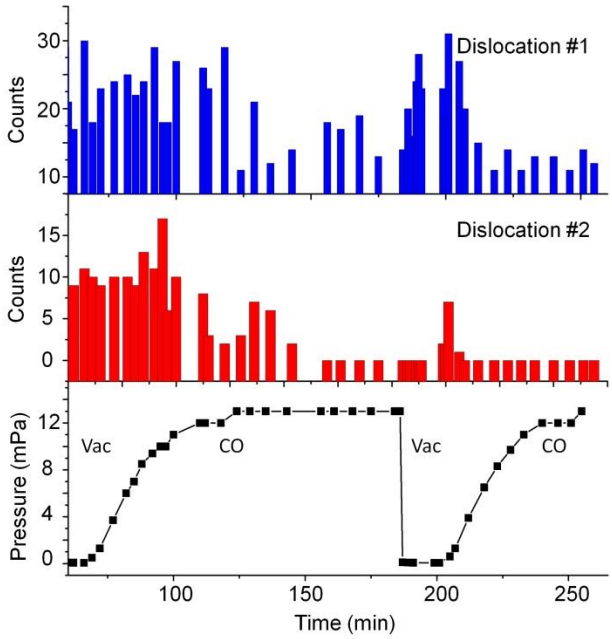

Figure A.13 Repeating experiment showing the evolution of dislocations in an octahedral Ag-Pt nanocrystal under alternating CO and vacuum vapor atmospheres. The initial treatment in vacuum caused the growth of amorphous surface of AgCl where it decomposed in the first exposure to CO. The data points were extracted from a series of micrographs following same image analysis procedure as shown in chapter 3.

Appendix B

Simulating X-Ray diffraction pattern for Ag-Pt compositional intermetallic compound using DIFFaX

DIFFaX is a Fortran based program that is designated to calculate diffraction intensities of crystals with coherent planner defects such as twin plans and stacking faults. In other words, the spirit of this program is used to model real world materials. In the DIFFax program, an end user provides can define many structural parameters from defining the type and dimensions of the unit cell, to the preferential orientation of the single grain, all the way to the probability of twining and stacking faults occurring within the single grain.

In this appendix, I would like to show how an end user can use this program to not only model a real material but also improve our understanding towards how the structure of a true material, *i.e.*, with preferential orientation and twin planes, can be reflected by its diffraction pattern.

The simulation of the AgPt compositional intermetallic compound will be used as an example to provide the step by step tutorial on constructing the structure data file which will then be input into the DIFFaX program to generate a simulated diffraction pattern. This tutorial focuses on how the designated structure is reflected by the simulated pattern and not on the specific commands for running the software. One can find the thorough instructions in the original manual provided for DIFFaX online.

B.1 Structure data file

A structure data file is a text file that contains information about the type of radiation, the structure of the layers, and details of the interlayer connectivity. The structure data file for the AgPt compositional intermetallic will be given as an example:

```
{data file for AgPt, with random intergrowths of hexagonal intergrowths}

INSTRUMENTAL                              {Header for instrumental section}
X-RAY                                     {Simulate X-ray diffraction}
1.5418                                    {X-ray wavelength}
PSEUDO-VOIGT 0.1 -0.036 0.009 0.6 trim    {Instrumental broadening}

STRUCTURAL                                {Header for structural section}
2.67 2.80 2.38 120.0                      {unit cell coordinates}
Unknown                                   {hexagonal, c axis = cubic [111]}
4                                         {111 sheet, plus its mirror}
1050    42                                {layer widths very wide in the a-b plane}

LAYER 1                                   {cubic (111) layer, centrosymmetric}
CENTROSYMMETRIC
Pt    1  0.0   0.0   0.0  0.2   1.0

LAYER 2
CENTROSYMMETRIC
Ag    1  0.0   0.0   0.0   0.2   1.0

LAYER 3
CENTROSYMMETRIC
Pt    1  0.0   0.0   0.0   0.2   1.0

LAYER 4
CENTROSYMMETRIC
Ag    1  0.0   0.0   0.0   0.2   1.0


STACKING                                  {Header for stacking description}
recursive                                 {Statistical ensemble}
100                                       {Infinite number of layers}

TRANSITIONS                               Header for transitions}
{Transitions from layer 1}
0.01    1/3  2/3   1.0                    {layer 1 to layer 1, 1%  chance}
0.99    1/3  2/3   1.0                    {layer 1 to layer 2, 99% chance}
```

```
0.0     2/3  1/3   1.0          {layer 1 to layer 3, 0 % chance}
0.0     2/3  1/3   1.0          {layer 1 to layer 4, 0% chance}

{Transitions from layer 2}
0.145   1/3  2/3   1.0          {layer 2 to layer 1, 14.5%  chance}
0.005   1/3  2/3   1.0          {layer 2 to layer 2, 0.5%  chance}
0.845   2/3  1/3   1.0          {layer 2 to layer 3, 84.5%  chance}
0.005   2/3  1/3   1.0          {layer 2 to layer 4, 0.5%  chance}

{Transitions from layer 3}
0.005   1/3  2/3   1.0          {layer 3 to layer 1, 0.5%  chance}
0.495   1/3  2/3   1.0          {layer 3 to layer 2, 49.5%  chance}
0.005   2/3  1/3   1.0          {layer 3 to layer 3, 0.5%  chance}
0.495   2/3  1/3   1.0          {layer 3 to layer 4, 49.5%  chance}

{Transitions from layer 4}
0.495   1/3  2/3   1.0          {layer 4 to layer 1, 49.5%  chance}
0.005   1/3  2/3   1.0          {layer 4 to layer 2, 0.5%  chance}
0.495   2/3  1/3   1.0          {layer 4 to layer 3, 49.5%  chance}
0.005   2/3  1/3   1.0          {layer 4 to layer 4, 0.5%  chance}
```

In the structure data file, commands for the DIFFaX are in text format with descriptions in brackets. The structure data file can be break down into several parts including defining the instrument parameters, the structural parameters of the unit cell and grain, the element and coordinates of different layers, and finally, the probability of different layers stacking on one another.

B1.1 Instrument parameters

```
INSTRUMENTAL                          {Header for instrumental section}
X-RAY                                 {Simulate X-ray diffraction}
1.5418                                {X-ray wavelength}
PSEUDO-VOIGT 0.1 -0.036 0.009 0.6 trim {Instrumental broadening}
```

In the instrument parameters, the user will type in X-RAY in line 2 for the X-ray diffraction calculation. Since most diffractometers uses Cu source, the X-ray wavelength will be set to

1.5418Å in line 3. The instrument broadening can also be defined in line 4. As an end user, one needs to make sure the parameters here matches with those of your X-ray diffractometer.

B1.2 Structural parameters of the unit cell and grain

```
STRUCTURAL                      {Header for structural section}
2.67 2.80 2.38 120.0            {unit cell coordinates}
Unknown                         {hexagonal, c axis = cubic [111]}
4                               {111 sheet, plus its mirror}
1050    42                      {layer widths very wide in the a-b plane}
```

In this part of the structure data file, the user must first define the unit cell dimension in line 2 which includes the three vectors (a, b, c) along (x, y, z) directions and the angle α between the a and b vectors in the following sequence (a, b, c, α). From the experimental data, we already know c is 2.38 Å, which is the distance between the Ag and Pt layers. In line 3, the user can define the type of symmetry for the DIFFaX program to speed up the calculation. However, if the symmetry is not known, the user can simply put “Unknown”. In line 4, the user with enter the number of layer types that AgPt intermetallic compound contains. Layers which are structurally identical, but exhibit different stacking behavior, count as distinct layers. The AgPt intermetallic is formed of layers of Ag and Pt stacking either on the octahedral or tetrahedral sites, *i.e.*, two elements and two possible sites, leading to 4 distinct layers. In line 5, one can define the preferential orientation of a single grain along the a and b directions with Å units. Overall, the user is providing guesses for the dimension of the a and b vectors as well as the preferential orientation in the a and b directions.

B1.3 Elements and coordinates of different layers

```
LAYER 1                                  {cubic (111) layer, centrosymmetric}
CENTROSYMMETRIC
Pt    1  0.0   0.0   0.0  0.2   1.0

LAYER 2
CENTROSYMMETRIC
Ag    1  0.0   0.0   0.0   0.2   1.0

LAYER 3
CENTROSYMMETRIC
Pt    1  0.0   0.0   0.0   0.2   1.0

LAYER 4
CENTROSYMMETRIC
Ag    1  0.0   0.0   0.0   0.2   1.0
```

In this part of the structure data file, the user will define the elements in each layer together with their position with respect to the origin. In the present example, layer 1 is composed of Pt (entry 1) with the atom located at 0.0 relative to a in the x direction, 0.0 to b in the y direction, and 0.0 to c in the z direction (entry 3 to 5). The 2nd entry is simply a numeric specifier, (*i.e.* 1 for the first atom, 2 for the 2nd, etc…). The last two entries refer to the isotropic Debye-Waller factor and the occupancy factor. The Debye-Waller factor is a measure of the atomic vibration amplitude and must be a positive value in Å^2 units. The atom occupancy must be between 0 and 1.

B1.4 Stacking

```
STACKING                                 {Header for stacking description}
recursive                                {Statistical ensemble}
100                                      {number of layers stacked, in the c direction}

TRANSITIONS                              {Header for transitions}
{Transitions from layer 1}
0.01    1/3  2/3   1.0                   {layer 1 to layer 1, 1%  chance}
0.99    1/3  2/3   1.0                   {layer 1 to layer 2, 99% chance}
```

```
0.0     2/3  1/3   1.0                {layer 1 to layer 3, 0 % chance}
0.0     2/3  1/3   1.0                {layer 1 to layer 4, 0% chance}

{Transitions from layer 2}
0.145   1/3  2/3   1.0                {layer 2 to layer 1, 14.5%  chance}
0.005   1/3  2/3   1.0                {layer 2 to layer 2, 0.5%  chance}
0.845   2/3  1/3   1.0                {layer 2 to layer 3, 84.5%  chance}
0.005   2/3  1/3   1.0                {layer 2 to layer 4, 0.5%  chance}

{Transitions from layer 3}
0.005   1/3  2/3   1.0                {layer 3 to layer 1, 0.5%  chance}
0.495   1/3  2/3   1.0                {layer 3 to layer 2, 49.5%  chance}
0.005   2/3  1/3   1.0                {layer 3 to layer 3, 0.5%  chance}
0.495   2/3  1/3   1.0                {layer 3 to layer 4, 49.5%  chance}

{Transitions from layer 4}
0.495   1/3  2/3   1.0                {layer 4 to layer 1, 49.5%  chance}
0.005   1/3  2/3   1.0                {layer 4 to layer 2, 0.5%  chance}
0.495   2/3  1/3   1.0                {layer 4 to layer 3, 49.5%  chance}
0.005   2/3  1/3   1.0                {layer 4 to layer 4, 0.5%  chance}
```

In this section, the user will define the number of layers being stacked in line 3, which essentially is defining the preferential orientation in the c direction. In the TRANSITIONS section, the user will define the probability of one type of layer stacking on the others, including itself. The four entries in line 6 (0.01, 1/3, 2/3, 1.0) are referring to the (probability, stacking position in the x direction relative to a, stacking position in the y direction relative to b, and stacking position in the z direction relative to c.) Thus, for the stacking on octahedral sites, the coordinate of the stacked atom is (1/3, 2/3, 1.0) and would be (2/3, 1/3, 1.0) for the tetrahedral sites.

B.2 Key parameters for simulation

Once the user have the previous frame work set up in the structure data file, the variables in the simulation includes the magnitude of the a and b vectors of the unit cell, the preferential orientation of the single grain, and the probability of the 4 layers stacking on one another.

Appendix C

Setup and procedures for heterogeneous gas phase catalyst testing

C.1 Equipment and materials:

GC (SRI, multigas #3), hotplate (VWR,), mass flow controller (Brooks, GF100C, 0254 four channel power supply), thermometer (J-KEM, Model 210), thermometer (J-KEM, K-type thermocouple), copper tubing (1/8”), glass bubbler, glass wool, quartz tube (1/4”), hydraulic press (MTI), helium (He, Airgas), hydrogen (H_2, Airgas), catalyst powder (Al_2O_3 powder supported metal catalyst, 100-500 nm diameter)

C.2 Procedures

C2.1 Preparation of catalyst bed

Al_2O_3 powder supported metal catalysts are made into a pellet using the hydraulic press with a homemade setup. Typically, one would use the weighing paper to confine the powders into 1.5 cm × 1.5 cm area simply by folding the paper (Figure C.1).

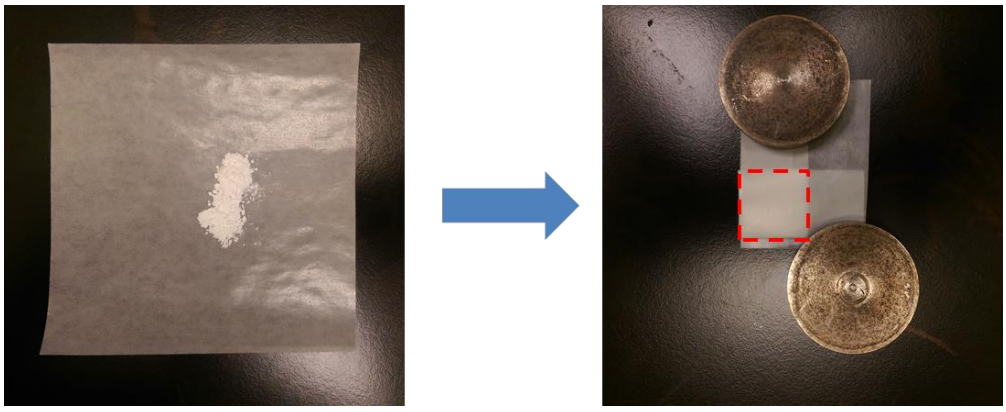

Figure C.1 Photographs showing the confinement of Al_2O_3 powders in a folded weighing paper.

The folded paper with powders inside will then be sandwiched in between two stainless steel plates. The sandwich is then placed in the hydraulic press to make a pellet at 3500 psi for 1 hr (Figure C.2).

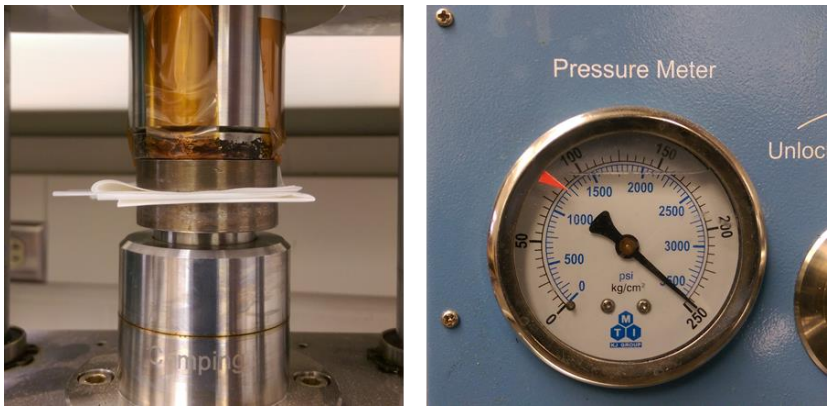

Figure C.2 Photographs showing the sandwich composed of two stainless steel plates and the catalyst powders situated in the hydraulic press (left) and the pressure applied (right).

The pellet is then crushed into small granules with sizes ranging from 1-3 mm (Figure C.3).

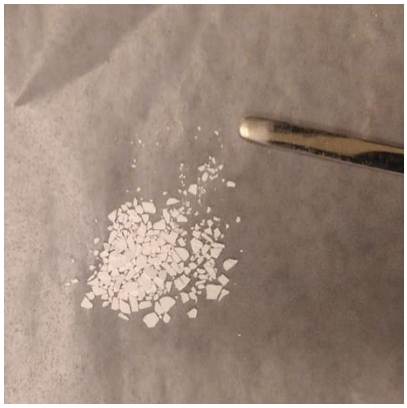

Figure C.3 Photograph showing the crushed Al_2O_3 pellet.

The small granules were packed in a 1/4” quartz tube using glass wools to secure both ends, as shown in scheme C.1.

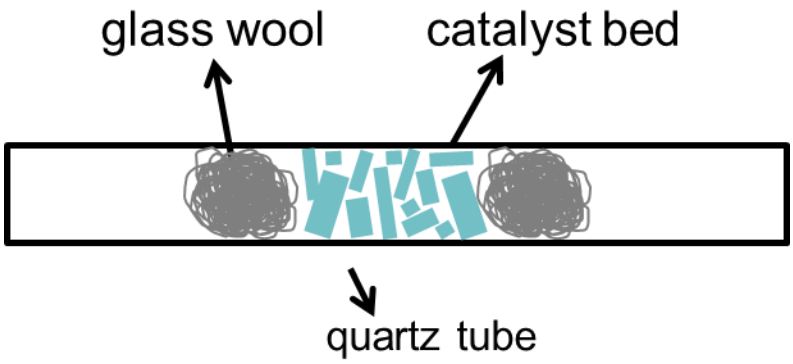

Scheme C.1

C.2.2 Setting up the reaction

Schematic of reaction setup

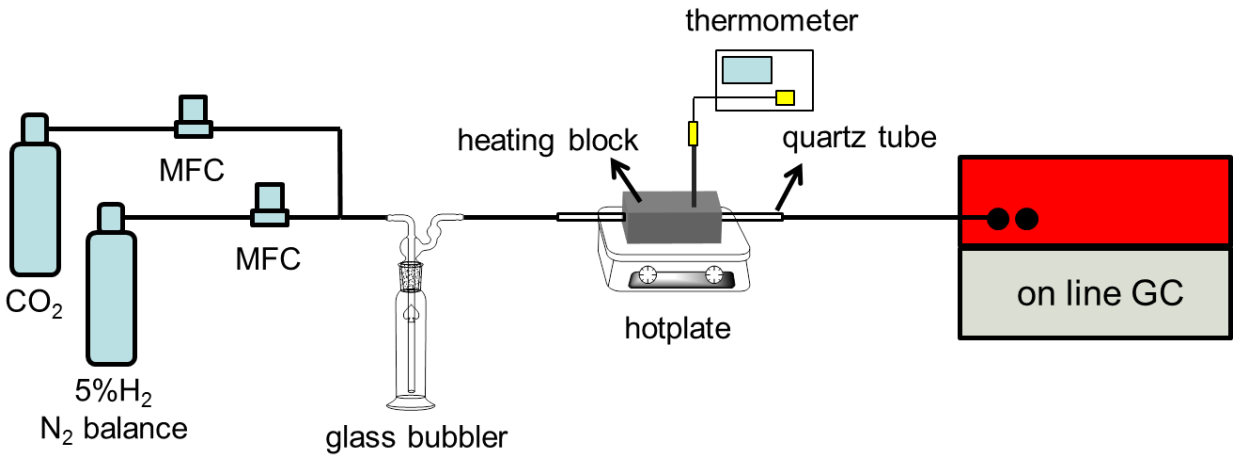

Scheme C.2

As shown above in scheme C.2, the reaction setup is composed of the compressed cylinders of the reactant molecules. The flowrates of different gases are controlled by mass flow controllers and was allowed for mixing in the glass bubbler prior entering the quartz tube where the catalyst bed is situated. The quartz tube passes through a stainless steel heating

block where the temperature is controlled by the hotplate and measured by the thermometer with the thermocouple directly inserted to sand bath in close proximity to the quartz tube.[1] The end products were directly analyzed by an online GC. In the current setup, all the components were wired together by copper tubing[2] with Swagelok tube fittings with the only exception at the quartz tube where adapters with tube fittings on one end and a compression fitting on the other.

[1] For future reference, it is recommended to use a tube furnace with accurate temperature measurements with programmable heating control.

[2] Copper might be active towards specific reactions, it is advised the copper tubing be replaced by stainless steel in the future provided heating in the wirings at the inlet and outlets of the reactor and GC is necessary.